

UNIVERSITY OF MARYLAND, COLLEGE PARK

Abstract

Faculty Name

Department of Astronomy

Doctor of Philosophy

**BETTII: A pathfinder for high angular resolution observations of
star-forming regions in the far-infrared**

by Maxime J. RIZZO

The Thesis Abstract is written here (and usually kept to just this page). The page is kept centered vertically so can expand into the blank space above the title too . . .

BETTII: A pathfinder for high angular resolution observations of star-forming
regions in the far-infrared

by

Maxime J. Rizzo

Dissertation submitted to the Faculty of the Graduate School of the
University of Maryland, College Park in partial fulfillment
of the requirements for the degree of
Doctor of Philosophy
2016

Advisory Committee:

Professor Lee G. Mundy, Chair/Advisor
Dr. Stephen A. Rinehart, Co-Advisor
Professor Andrew Harris
Dr. Mark Wolfire
Dr. Alison Nordt

To Michelle, my parents, and my brother.

Acknowledgements

The acknowledgments and the people to thank go here, don't forget to include your project advisor...

Contents

Acknowledgements	iii
Contents	v
List of Tables	ix
List of Figures	xi
List of Abbreviations	xiii
Physical Constants	xv
List of Symbols	xvii
I Star formation in clustered environments	3
1 Molecular Clouds	3
2 Star formation	5
2.1 Standard models	5
2.1.1 Gravitational collapse	5
2.1.2 YSO classification and characteristics	8
2.2 Mass accretion in clusters	12
3 Dust as a tracer of star formation	14
3.1 Dust populations and properties	15
3.2 Basics of dust extinction	17
3.3 Radiative transfer modeling	19
3.4 Observing star formation	20
II Star Formation in Clustered environments with SOFIA FORCAST	23
1 Introduction	23
2 Sample description and scientific goals	24
3 Observations	26
4 FORCAST characterization	29
4.1 PSF size	29
4.2 Aperture correction factor	31
4.3 Instrument response and overall uncertainty	32
5 Data reduction and photometry	33
5.1 Pre-treatment	34
5.2 Source flux extraction	35

5.3	Image sensitivity	37
5.4	Other photometry	37
6	Data products	37
6.1	Maps	37
7	SED fitting	38
7.1	A small grid of models	38
8	Application to four clusters	43
8.1	IRAS20050+2720	43
8.2	NGC 2071	47
III	The Balloon Experimental Twin Telescope for Infrared Interferometry	51
1	Towards higher angular resolution in the far-IR	51
2	BETTII description	52
3	Basics of interferometry	53
3.1	Fourier transform spectroscopy	54
3.2	Aperture synthesis	56
3.3	Double-Fourier interferometry	59
4	BETTII Instrument design	60
4.1	Stratospheric balloon environment	61
4.2	Mechanical design	63
4.3	Warm optical system	64
4.3.1	Optics layout	64
4.3.2	Optics manufacturing	65
4.4	Cryogenic instrument	67
4.5	Data products & analysis	68
5	Sensitivity analysis	70
5.1	Instrument and observing parameters	70
5.2	Far-IR background noise estimation	71
5.3	Interferometric visibility budget	74
5.4	Science channel estimated sensitivity	75
5.5	Tracking channel estimated sensitivity	77
6	Targets	80
6.1	Calibrators	81
6.2	Science targets	81
IV	Far-IR double-Fourier interferometers and their spectral sensitivity	83
1	Introduction	83
1.1	Spatio-spectral interferometry	85
1.2	The case study: BETTII	88
2	Mathematical formalism	89
2.1	Interferograms for a single baseline	90
2.2	Measured interferograms	93
3	Noise sources	95
3.1	Intensity noise	96
3.2	OPD noise	97
4	Spectral signal-to-noise ratio	99
4.1	Effects of Gaussian intensity noise	99
4.2	Effects of Gaussian OPD noise	101

4.3	Co-adding interferograms	104
4.4	Implications for spectroscopy	105
5	Spectral sensitivity analysis for BETTII	107
5.1	Noise sources and control system	108
5.2	Derived sensitivity and faintest detectable targets	110
6	Conclusion	112
V	Attitude estimation and control for BETTII	119
1	Control system architecture	119
1.1	Overall strategy	119
1.1.1	Requirements	119
1.1.2	Control loop design and operating modes	121
1.1.3	BETTII Coordinate systems	126
1.2	Subsystems	126
1.2.1	Gyroscopes	126
1.2.2	Star cameras	133
1.2.3	Azimuth control (CCMG)	136
1.2.4	Momentum dump mechanism	138
1.2.5	Elevation control (Rotators)	142
1.2.6	Delay lines	143
1.2.7	Tip/tilt	143
1.2.8	Fine guidance sensor	144
1.2.9	Clocks and timing	144
1.2.10	Computers	146
1.3	Software architecture	148
2	3D attitude estimation and sensor fusion	148
2.1	Sensor models	151
2.1.1	Gyroscope model	151
2.1.2	Star camera model	153
2.2	Continuous state equation and error	154
2.3	Integration of continuous equations	157
2.4	Discrete covariance matrices	157
2.5	Discrete Kalman filter setup	158
2.6	Kalman filter: prediction	160
2.7	Kalman filter: update	161
2.8	Delayed star camera solution	162
VI	Implementation and on-sky testing	163
1	Key pre-flight procedures	163
1.1	Inertia measurement	163
1.2	Sensor alignment and calibration	164
1.2.1	Gyroscope spectral analysis in flight configuration	164
1.2.2	Orthogonalization of gyroscope mount	164
1.2.3	Alignment of gyroscope mount to star camera mounts	164
1.3	Star camera	166
1.3.1	Tuning tests	166
1.3.2	Final parameters	172
2	Test setups and limitations	172

2.1	Talk about the way we test in the high bay, etc	172
2.2	List of test setups: gyro only, gyro+star camera, gyro+star camera+tip/tilts with CCD cameras, gyro+star camera with H1RG;	172
2.3	Explain the communication/data recording approach	172
2.4	Autofocus algorithm and performance	172
3	Estimator implementation	172
3.1	Gyro attitude estimator	172
3.1.1	Testing the Kalman filter software with simulated data . .	174
3.1.2	Test results when sitting on the ground	174
3.2	Telescope attitude estimator	174
3.3	Phase estimator [is that Arnab's realm?]	174
4	Operating modes	174
4.1	Track mode	174
4.2	Slew mode	174
4.3	Acquire mode [this one is contingent on the telescopes working, and is not perfectly representative when only using one single side of the payload]	174
5	Pointing tests and performance results	174
5.1	Gondola pointing stability	174
5.1.1	In the high bay	174
5.1.2	With the door open	175
5.2	Kalman filter performance	175
5.3	gyro+star camera+tip/tilts with CCD cameras	176
5.4	gyro+star camera with H1RG;	176
6	Using the test results to estimate the flight performance (have to think more about that section)	176
6.1	Perturbation rejection estimates	176
6.2	Pointing knowledge predictions	176
6.3	Pointing control predictions	176
VII	Conclusion	179
A	Attitude representation in three dimensions	181
1	Tait-Bryan/Euler angles	182
2	Rotation matrices	183
3	Quaternions	188
3.1	Quaternion multiplication	190
3.2	Relationship with matrices and elementary quaternions	192
4	Quaternion derivative and integration	193
5	Covariance matrices in different reference frames	194
5.1	Small angle approximation	195
5.2	Finding the rotation between two vectors	196
B	The PID control loop	199

List of Tables

II.1	List of desired sensitivities	26
II.3	List of targets	28
II.5	FORCAST Sensitivities	38
II.7	Spitzer photometry comparison	38
II.9	SOFIA photometry comparison	40
II.12	SED model grid	42
III.1	Instrument parameters	71
III.4	Thermal noise contributors	71
III.6	Power and NEP contributors	73
III.8	Interferometric visibility budget	75
IV.1	BETTII noise parameters	114
IV.2	BETTII sensitivity estimates	114
V.2	Operating modes	125
V.3	Gyroscope properties	134
V.4	Star camera properties	135
V.5	BETTII embedded computers	147
VI.1	Star camera tests	167

List of Figures

I.1	Early evolution of YSOs	10
I.2	Late evolution of YSOs	11
I.3	Scenarios of clustered star formation	14
II.1	Saturation and confusion	24
II.2	SOFIA bands	27
II.3	PSF size	30
II.4	PSF size of calibrators	32
II.5	aperture correction	33
II.6	Instrumental response	34
II.7	RGB images of select sample of sources	39
II.8	Spectral Index distribution of point sources	40
II.9	The core of IRAS20050+2720 is seen in the four bands of the <i>Spitzer</i> IRAS instrument, as well as with the four FORCAST bands. The increased resolution of FORCAST compared to previous instruments allows to match the long-wavelength emission with its short wavelength counterpart. The stretch in each image is adjusted for optimal readability. The white contours correspond to the FORCAST 37 μ m emission [mention the contour levels].	45
II.10	NGC2071 and IRAS20050+2720	46
II.11	The core of NGC2071 is seen in two bands of the <i>Spitzer</i> IRAS instrument ("I1" and "I4"), as well as with the four FORCAST bands. The increased resolution of FORCAST compared to previous instruments allows to match the long-wavelength emission with its short wavelength counterpart. The stretch in each image is adjusted for optimal readability. The white contours correspond to the FORCAST 37 μ m emission [mention the contour levels].	50
III.1	Michelson interferometer	54
III.2	Simple interferogram	55
III.3	Michelson Stellar interferometer	56
III.4	Aperture synthesis	58
III.5	FTS vs Double-Fourier	60
III.6	Balloon launch	62
III.7	Data processing	69
III.8	BETTII Transmission curves	72
III.9	Model atmospheric transmission, from Rizzo et al., 2012	78
III.10	Visibilities of calibrators	82

IV.1 WideField	115
IV.2 optics	116
IV.3 interfero	117
IV.4 BETTII Spectral SNR	117
V.1 Azimuth and elevation of a target	123
V.2 BETTII coordinate systems	126
V.3 The celestial sphere	127
V.4 The star camera reference frame	128
V.5 1000s of gyroscope data	129
V.6 Power spectral density	131
V.7 Normality analysis	132
V.9 Quantum efficiency of star camera CCD	135
V.10	139
V.11	140
V.12 Momentum dump assembly	141
V.13 Momentum dump PID	142
V.14 Software diagram	148
V.15 Control System Design	149
VI.1 Gyro PSD with payload on the ground	168
VI.2 Gyro PSD with payload on the ground - Main peaks	169
VI.3 Star camera example WISE	170
VI.4 Star camera individual star	171
VI.5 Integrated gyro time series while hanging	175
VI.6 Cross-elevation with control loop on	176
VI.7 Gyro PSD with payload lifted	177
VI.8 Gyro PSD with payload lifted, under azimuth control	178
A.1 Rotation of 30 degrees about K	185
A.2 Rotation of -30 degrees about K	186
A.3 Two consecutive elementary rotations	187
A.4 Three consecutive elementary rotations	187
B.1	200

List of Abbreviations

LAH List Abbreviations Here
WSF What (it) Stands For

Physical Constants

Speed of Light $c_0 = 2.997\,924\,58 \times 10^8 \text{ m s}^{-1}$ (exact)

List of Symbols

a	distance	m
P	power	W (J s^{-1})
ω	angular frequency	rad

Introduction

In order to improve the mind, we ought less to learn, than to contemplate.

R. Descartes

The work presented in this thesis is centered around the design, development, and testing of an astronomical balloon-borne telescope called BETTII: the Balloon Experimental Twin Telescope for Infrared Interferometry. Developed at NASA Goddard Space Flight Center, this instrument is exploring a new observation technique called "Double-Fourier" interferometry, which could lead to future space-borne telescopes with very high angular resolution in the far-infrared regime. Various fields in astronomy would benefit from such enhanced capability, as demonstrated by the success of far-infrared single-aperture telescopes such as *WISE*, *Spitzer* and *Herschel*.

More than just a pathfinder, BETTII is a scientific instrument in its own right. For its first flights, it will study regions of clustered star formation with unprecedented details, providing almost an order of magnitude better spatial resolution than any existing or past far-IR facility.

This thesis describes some aspects of my involvement with BETTII as well as my contributions to the scientific field of clustered star formation using the only existing far-IR facility, SOFIA. The document is organized as follows:

- Chapter I describes the framework and current understanding of how stars are forming in clusters, and lays out the key tools that we use to study these regions.

- Chapter II is a study of nearby star-forming clusters using new data that we obtained with the SOFIA observatory. SOFIA offers moderately high angular resolution, which we attempt to use to improve the study of the brightest, densest regions of star formation. This work is to be submitted for publication shortly after the conclusion of this dissertation.
- Chapter III describes the physical principles of interferometry which drive the design of the balloon instrument. We discuss how sensitive the instrument will be and identify scientific targets and calibrators that are suitable for our first flights.
- Chapter IV is a standalone, refereed publication that was published in 2015 on the spectral sensitivity of double-Fourier interferometers in general. It proposes a mathematical framework to analyze the sensitivity of such instruments to various types of noise sources. We apply those findings to the case of BETTII.
- Chapter V discusses the design of the control system for BETTII, which presents unique challenges compared to any other balloon-borne instrument. We also discuss the controls algorithm that is used in flight to properly estimate the orientation of the payload, a key requirement to achieve successful interferometry.
- Chapter VI shows results of the implementation that we discuss in the previous chapter. This consists of laboratory and on-sky testing of the observatory. We discuss the expected performance at float.
- Chapter VII summarizes our findings and discusses the path forward for the BETTII project.

Chapter I

Star formation in clustered environments

1 Molecular Clouds

Molecular clouds are the dense regions of the interstellar medium (ISM) where stars are forming. They contain about half the mass of the ISM in $< 2\%$ of its volume (Ferrière, 2001). High densities ($n > 100 \text{ cm}^{-3}$) of mostly molecular hydrogen and low temperatures ($< 20 \text{ K}$) distinguish molecular clouds from the various other components of the ISM in galaxies: the Warm Neutral Medium (WNM), the Warm Ionized Medium (WIM), and the other cold phase of the ISM, the Cold Neutral Medium (CNM), which is thought to be the parent region in which molecular clouds are formed (Kennicutt and Evans, 2012). In addition to molecular hydrogen, molecular clouds also contain Helium (10% by number), dust ($\sim 1\%$ by mass), CO ($\sim 1 \times 10^{-4}$ by number), and traces of many other molecules.

Observations of molecular clouds reveal that they are highly structured with often a filamentary pattern [cite shaye?]. While the literature proposes multiple classifications for the various structures found in molecular clouds, we choose to focus only on two structures

which are key to this work: clusters, which are more local associations of stars in virial equilibrium (Lada and Lada, 2003); and dense cores, which are sites where stars form individually or in systems of small multiples (Williams, Blitz, and McKee, 2000). Clusters are formed of multiple cores, but cores can also be found outside of clusters, in the field. In the classical picture, clouds are thought to fragment into clusters, which still contain many times the Jeans' mass - the minimum mass for gravitationally-bound cores (Larson, 1994) which are also called prestellar cores (Di Francesco et al., 2007).

Approximately 60% of all stars are thought to form in embedded, young stellar clusters of 1-3 Myr with 100 or more stars (Porras et al., 2003; Allen et al., 2007). These >100 star clusters have characteristic sizes of 2-4 parsecs (pc) with peak surface densities of 100-1000 stars per square parsec and a typical median distance between nearest neighbor young stellar objects (YSOs) of 0.03 to 0.06 pc (Gutermuth et al., 2009).

Because star-forming clusters are surrounded by interstellar matter from the parent molecular cloud, they usually cannot be studied at optical wavelengths, due to the large obscuration from dust grains along the line of sight. Infrared observations can be used to probe these structures since the dust can acquire sufficient temperature to emit thermally from the mid-infrared to millimeter and radio wavelengths.

The high density of YSOs within clusters, combined with their typical separations of few hundredths of parsecs requires a high angular resolution in order to capture the relevant spatial scales at which accretion mechanisms are occurring to give the star its final mass.

2 Star formation

2.1 Standard models

A considerable amount of literature exists on star formation and the various physical processes involved in forming stars. In this section, we review some of the most standard views that describe how stars are born and grow to acquire their final masses.

2.1.1 Gravitational collapse

A simple way to derive characteristic quantities related to the formation of stars is to consider a pre-stellar core as a spherical clump of uniform, isothermal gas in hydrostatic equilibrium. For such a system, the Virial theorem applies, which describes the balance between the gravitational potential and the kinetic thermal energy within the gas. In other words, in hydrostatic equilibrium, the core's self-gravity is compensated by the internal pressure caused by the temperature of the gas. For the same radius and temperature, a core with more mass will lead to a runaway collapse. While simplistic, this treatment leads to a handy derivation of critical timescales, sizes, and masses that form a good starting point for more elaborate theories.

First, it is important to determine what are the characteristic timescales of star formation. In the core with a uniform density, the simplest timescale to define is called the free-fall time: this is the time it takes for the total gravitational collapse of a spherically-symmetric clump of uniform density ρ if only the force of gravity is considered:

$$t_{\text{ff}} \sim \left(\frac{3\pi}{32G\rho} \right)^{-1/2} \sim 2 \times 10^5 \text{ yr} \left(\frac{\rho}{10^{-19} \text{ g cm}^{-3}} \right)^{-1/2}, \quad (\text{I.1})$$

where we have substituted a typical value for the gas density in clusters. The free-fall time is usually a lower limit on the collapse timescale, since there will always be some thermal pressure that will resist gravity and slow down the infall of gas into the potential well.

The other relevant quantity that involves time is the sound speed in the cloud, $c_s = (kT/(\mu m_H))^{1/2}$, where μ is the mean molecular weight of the gas and m_H the mass of hydrogen. For a given spatial scale R , the sound-crossing time is defined as $t_s = R/c_s = 4.9 \times 10^5 \text{ yr} \left(\frac{R}{0.1 \text{ pc}} \right) \left(\frac{c_s}{0.2 \text{ km s}^{-1}} \right)^{-1}$. This is the time it takes for a wave to cross the scale R while traveling at the sound speed. Intuitively, if the core has a size R such that $t_{\text{ff}} < t_s$, it will tend to collapse faster the gas in the cloud can compensate to maintain hydrostatic equilibrium. This corresponds to a characteristic sizescale that is called the Jeans' length, and corresponds to the characteristic sizescale of gravitational instability within a cloud (McKee and Ostriker, 2007):

$$\lambda_J = c_s \times t_{\text{ff}} = 0.04 \text{ pc} \left(\frac{c_s}{0.2 \text{ km s}^{-1}} \right) \left(\frac{\rho}{10^{-19} \text{ g cm}^{-3}} \right)^{-1/2}. \quad (\text{I.2})$$

The Jeans mass is the amount of mass within a sphere of diameter λ_J , and corresponds intuitively to the minimum mass a core needs to gather in order to trigger an gravitational collapse:

$$M_J = \frac{4\pi}{3} \rho \left(\frac{\lambda_J}{2} \right)^3 \quad (\text{I.3})$$

$$= 0.06 M_\odot \left(\frac{c_s}{0.2 \text{ km s}^{-1}} \right)^3 \left(\frac{\rho}{10^{-19} \text{ g cm}^{-3}} \right)^{-1/2} \quad (\text{I.4})$$

Note that this formalism completely ignores the material that surrounds the core while it collapses. In practice, the cloud exerts an external pressure on the core that needs to be taken into account when calculating the critical masses. This more elaborate case

of a clump of self-gravitating gas on the verge of collapse that is immersed in a medium of external pressure P_{ext} is called a Bonnor-Ebert sphere. It can be shown (McKee and Ostriker, 2007) that the sizescale is similar to the Jeans' length, and the mass scale is a few times smaller than the Jeans' mass, which stays well within the accuracy limits of our simple model.

Once the gas starts its gravitational collapse, nothing stops it until the central pressure and density reach values that trigger the ignition of nuclear fusion. This is the birth of the star. This new mechanism creates a large amount of radiation pressure that balances out the collapse and forms a new hydrostatic equilibrium.

In practice, it is likely that a single core fragments into multiple centers of collapse, each of them exceeding the local Jeans mass. This would create systems of binaries or small multiples instead of single stars, a scenario that is currently favored [LARSON?].

In the standard model, the collapse begins at the center of the core and propagates outward at the sound speed, so the density structure of the initial core will change as a function of time. Most models result in an infalling envelope with density profiles which follow power laws from $r_{\text{env}}^{-1.5}$ to r_{env}^{-2} , an important observable that can be useful to test these theories. Some models of slowly-rotating infalling clouds suggest more complex density profiles for the envelopes (e.g. Ulrich, 1976; Terebey, Shu, and Cassen, 1984) than simple power laws, but are observationally difficult to constrain due to the small differences with traditional power-law envelopes and the small scales at which those differences occur (a few 100's of AU).

Through conservation of angular momentum, some of the surrounding material naturally flattens into a centrifugally-supported flaring disk before it is fed to the star, and a bipolar cavity opens along the rotation axis of the system. The cavity opening can also be

bolstered by mechanisms such as stellar winds and jets [REFERENCE].

The object now has three characteristic components: the star itself; the flattened disk; and a diffuse envelope with an open cavity, which constitutes a mass reservoir for future accretion onto the star.

The accretion rate represents the speed at which the mass is transferred between different objects, and are important to set relevant timescales and to relate observables to the physics. For relatively low-mass star formation, the usually adopted accretion mechanism is called Shu accretion (“Self-similar collapse of isothermal spheres and star formation” 1977), and predicts a mass accretion rate of the envelope onto the disk $\dot{M}_{\text{env}} \propto c_s^3/G$, where c_s here represents the sound speed that includes turbulence, and G is the gravitational constant. Typical accretion rates for $c_s \sim 2.7 \text{ km s}^{-1}$ are $\dot{M}_{\text{env}} \sim 4.8 \times 10^{-6} M_{\odot} \text{ yr}^{-1}$ (Dunham et al., 2010).

Although most of the mass is contained in the H₂ gas, there is a small fraction of material in the form of dust grains of various sizes and populations. Despite their low mass, these grains play a very important role in determining the observable properties of YSOs, because of their tendency to absorb short wavelengths and radiate in the thermal infrared (see Section 3).

2.1.2 YSO classification and characteristics

We have determined that YSOs are composed of a star, a disk, and an envelope. The star is believed to be fairly well understood as a young object in hydrostatic equilibrium on its way to the main sequence. Depending on many parameters, the spatial distribution of gas in the disk and the envelope can be predicted by simple models, but in all likelihood is

very complex, inhomogeneous, and asymmetric. For clarity, we will discuss here the simple models that can be used to describe the YSOs in the multiple stages of their evolution.

In the most common model of the evolution of young stars, there are four stages in the lifetime of a YSO. The first stage consists of a dense core right after the YSO is born. The disk is almost nonexistent, the envelope still is dense and circularly symmetric. This is called Stage 0. As the system evolves, the cavity opening angle grows, the density of the envelope decreases, and the size of the disk increases. When a YSO is Stage III, both the disk and the envelope are almost entirely depleted.

The various stages of YSO (from 0 to III) have very distinct observational signatures, although are highly dependent on the viewing angle. The most commonly used tool to classify YSOs based on their SEDs is to use the spectral index, which corresponds to the mid-IR slope α in the log-log plots, with $\alpha = d(\lambda F_\lambda)/d\lambda$ between 2 to 20 μm (McKee and Ostriker, 2007). The four classes of YSOs are:

- Class 0: Most the of short-wavelength ($< 10 \mu\text{m}$) light is highly obscured by the dust in the massive envelope. Most of the emission is around 100 μm and into the sub-millimeter/radio regimes. If there is a disk, it is very small. Some authors (Dunham et al., 2010) classify a source as Class 0 as long as the amount of the mass in the envelope is at least half the total mass.
- Class I: Light scatters at short wavelength off the dust grains to give us a hint at the embedded object, but it still very obscured. The envelope's mass is lower, and the disk extends to larger distances. The typical spectral index α is positive.
- Class II: The YSO is now a pre-main sequence star, with a spectral index $-1.5 < \alpha < 0$ a significant circumstellar disk. This is traditionally referred to as a classical

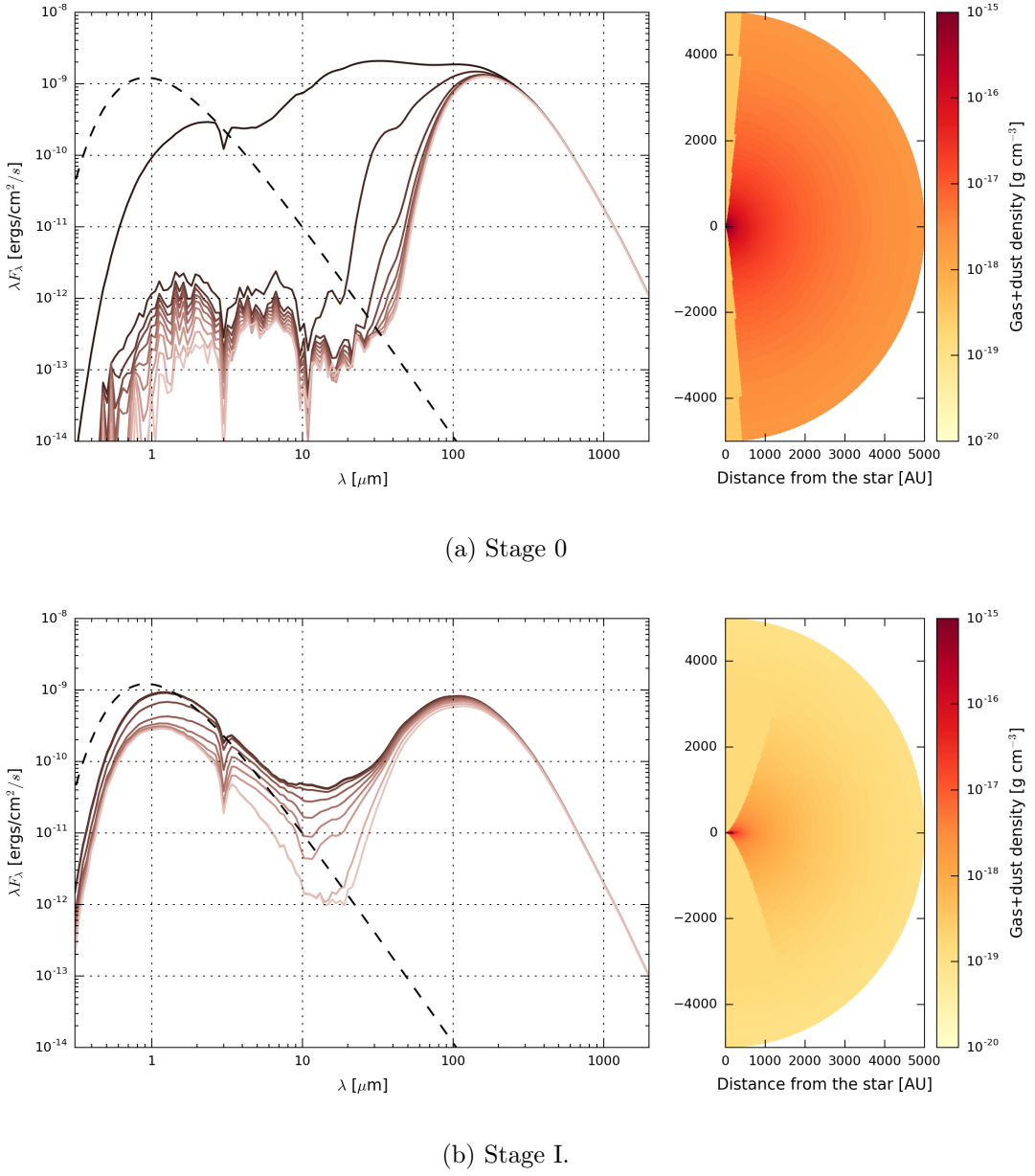


FIGURE I.1: Early evolution of YSOs.

T-Tauri star.

- Class III: Still a pre-main sequence star, but most of the accretion has stopped, and $\alpha < -1.5$. The envelope has almost completely disappeared, and so has most of the disk.

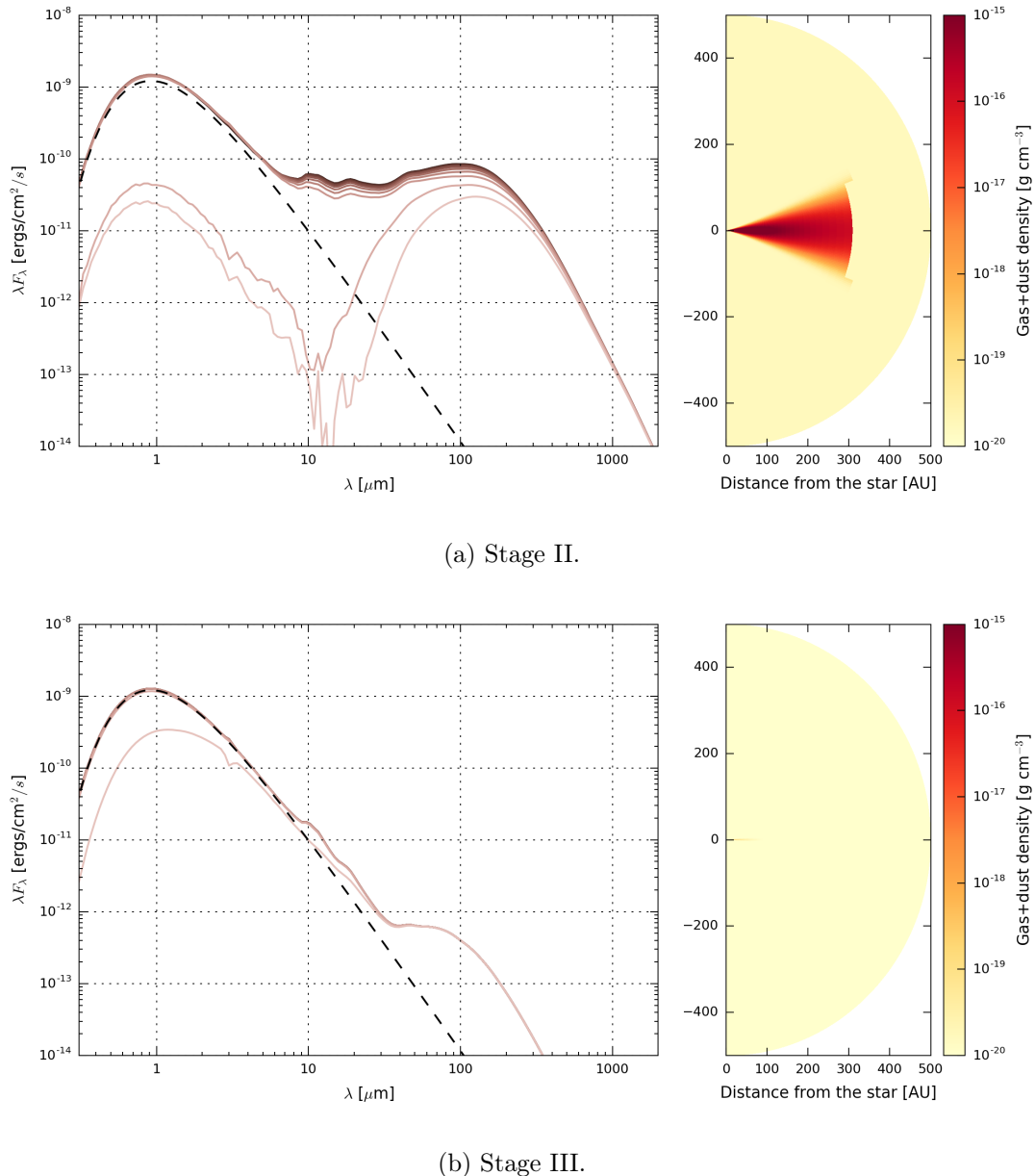


FIGURE I.2: Late evolution of YSOs.

An illustration of canonical spectral energy distributions (SED) and density structure is shown in Figs. ?? for the four main stages, with parameters taken in Whitney et al. (2003b). On the left of each picture, the SED is the measurable quantity when the YSO is unresolved at all wavelengths. The challenge is to estimate the density structure (to the right) by measuring the SED. The different lines plotted in the SEDs are different inclination angles, highlighting the enormous impact of the viewing angle on the potential interpretation of these SEDs. The dashed line corresponds to the Planck function from the central source. These models were run using the Hyperion software (Robitaille, 2011) with "OH5" dust (Ossenkopf and Henning, 1994), as discussed in more details in Section 3.

These SEDs are often characterized and classified with standard observational metrics, such as the bolometric temperature and luminosities (Myers and Ladd, 1993; Dunham et al., 2010):

$$L_{\text{bol}} = 4\pi d^2 \int_0^\infty S_\nu d\nu, \quad (\text{I.5})$$

$$T_{\text{bol}} = 1.25 \times 10^{-11} \frac{\int_0^\infty \nu S_\nu d\nu}{\int_0^\infty S_\nu d\nu} \text{ K}, \quad (\text{I.6})$$

where S_ν is the flux density in $\text{W m}^{-2} \text{Hz}^{-1}$.

2.2 Mass accretion in clusters

The discussion in the previous section represents a canonical view of how a single core collapses and forms a star. While it is convenient to assume that the original core forms a fixed reservoir of gas that will determine the star's final mass, it is likely too simplistic, since these YSOs are preferentially forming inside of clusters close to multiple other YSOs

and sharing a dense, often turbulent environment (Porras et al., 2003; Allen et al., 2007; Gutermuth et al., 2009).

The question of how stars acquire their final mass is key in studying star formation. Does dense gas fragment into isolated centers of collapse? Do young stars competitively accrete material from a surrounding common reservoir? Do gravitational interactions between forming young objects play a significant role in setting the final stellar mass function? Better observational understanding of these clusters is necessary to address these questions and to discriminate between the different models, as noted by Bonnell and Bate, 2006, Offner and McKee, 2011 and Myers, 2011.

Given the typical stellar separations in clusters with fully formed young stellar objects and the typical densities of gas in these cores, 1000's of astronomical units (au, 1 pc = 206 265 au - are the size scales over which forming stars must draw material to become 0.5-10 solar masses. Once the material is inside 100 au, it is strongly bound to the forming stellar system (which may be one or more stars) and its fate is determined. To give an idea of the possibilities for accreting material, Fig. I.3 sketches three scenarios for how stars could capture mass in the cluster environment: core collapse, competitive accretion, and collisional merging. In core collapse (CC) (Fig. ??, McKee and Tan, 2003; Myers, 2011), the cluster's gas fragments into cores which collapse individually to form single, binary, or small multiple star systems; the available mass is defined by the original fragment. In competitive accretion (CA) (Fig. ??, Bonnell et al., 1997), the initial core collapses but contains a small fraction of the star's final mass; additional mass is captured competitively with other forming stars from the surrounding dense core gas. In collisional merging (CM) (Fig. ??, Bonnell and Bate, 2002), the initial fragments interact gravitationally and form larger mass cores before and during the formation process.

Are all these processes observed at once in star forming clusters? What conditions favor one versus the other, and why? Are these processes observed at different stages in the cluster's history?

Recent studies by Offner and McKee, 2011 and **Myers:2011p1338** compared protostellar luminosity distributions with predictions of models based on these ideas. Offner and McKee, 2011 suggest that both CC and CA could work if the star formation rate in the cluster increases with time; (Myers, 2011) finds that a CA-type model with additional Bondi accretion to produce massive stars works best. As highlighted at the end of the Offner and McKee, 2011 paper, larger cluster samples and better data on massive stars are needed to improve the observational constraints on models.

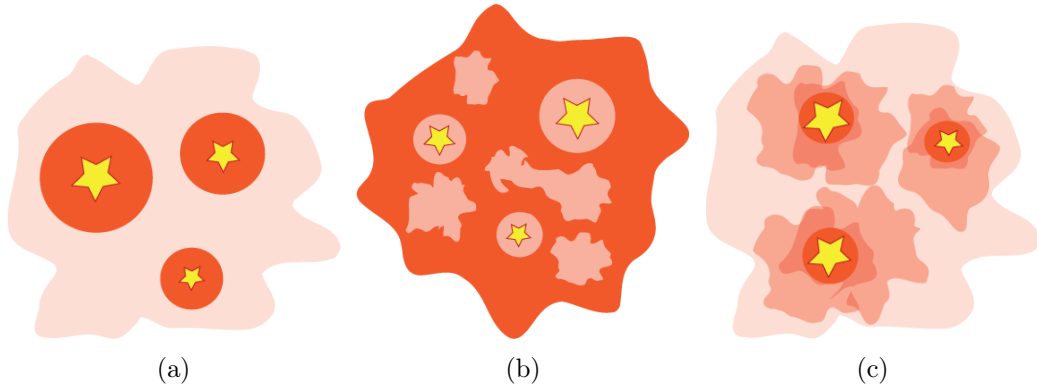


FIGURE I.3: Three scenarios of clustered star formation. Darker colors indicate higher densities.

3 Dust as a tracer of star formation

Despite being a small component by mass, interstellar dust is an important component of galaxies. Dust grains are heated up by absorbing the short wavelength emission from stars and re-radiate in the thermal infrared, accounting for $\sim 30\%$ of the total luminosity of the galaxy (Mathis, 1990).

Observationally, dust plays perhaps the most important role when it comes to studying star formation. It usually is assumed that dust is well mixed with the gas, which makes it an excellent tracer of the gravitational well and mass distribution in YSOs. Because H₂ and He molecules have very few spectral signatures, they are difficult to observe and study directly. Dust grains block UV and visible star light and emit continuum far-IR radiation, opening a large region of the electromagnetic spectrum for astronomers to study the properties of star formation. Alternative tools to study star formation are dedicated to observing spectral lines of the molecular compounds of the ISM such as CO and other dense gas tracers, a prospect that limits the study to the most dense regions since these compounds typically freeze out onto the surface of dust grains for sufficiently high densities [REF?]

3.1 Dust populations and properties

Perhaps the first understanding of the composition of dust grains in the ISM was described by Mathis, Rumpl, and Nordsieck, 1977, where they studied the absorption spectrum of the diffuse ISM, and found that the measurements were appropriately fitted with a dust grain composition of silicates and small graphite particles (Stecher and Donn, 1965). They were able to fit the observed extinction curve with canonical grain-size distribution, typically $n(a) \propto a^{-3.5}$, where a is the grain size (assuming spherical grains) and $n(a)$ corresponds to the number of grains of sizes $< a$. This assumes low and high cutoffs for the grain sizes, typically 50 Å and 0.25 μm, respectively.

This grain-size distribution model was later on enhanced by Cardelli, Clayton, and Mathis, 1989 to account for the difference in interstellar extinctions (hence size distributions) across different galactic lines of sight. These authors were able to successfully

parameterize this size distribution using a single parameter, R_V , which is the ratio of the total extinction $A(V)$ to selective extinction¹ (or color) $E(B-V) = A(B) - A(V)$. Smooth distributions of sizes of graphite and silicate grains between the less dense regions of the ISM, where $R_V = 3.1$, and the dense clusters, where $R_V = 5.3$ (Kim, Martin, and Hendry, 1994).

Observations in the thermal infrared from space telescopes have detected strong absorption lines at $9.7\text{ }\mu\text{m}$ and $18\text{ }\mu\text{m}$ which are attributed to stretching mode of Si-O and bending mode of O-Si-O, confirming the presence of silicates in dust compositions (Weingartner and Draine, 2001). Other emission features at 3.3 , 6.2 , 7.7 , 8.6 , and $11.3\text{ }\mu\text{m}$ (Sellgren, 1994) were attributed to bending and stretching modes of polycyclic aromatic hydrocarbons (PAH, see Gillett, Forrest, and Merrill, 1973; Allamandola, Tielens, and Barker, 1985), which are complex, planar organic molecules.

A consolidated model matching all-sky measurements by instruments on the COBE space observatory confirms the composition of amorphous silicates and carbonaceous grains with sizes ranging from large grains ($\approx 1\text{ }\mu\text{m}$) down to tens of atoms (Li and Draine, 2001), where the larger carbonaceous grains have graphitic properties and the smaller population have PAH-like properties.

[Molecular hydrogen is believed to form by recombination on the surface of dust grains [hollenbach and salpeter 1971, and are only able to survive from UV photodissociation within these obscured clouds.]

Knowing the dust composition and size distribution of grains is important to properly predict its observational behavior and relate it to the physical quantities of interest, since the goal of the exercise is to use dust as a tracer of star-forming mechanisms. A given

¹Extinction and colors are expressed in magnitudes

dust model needs to provide several key quantities that can be used in radiative transfer modeling (see Section 3.3), such as the albedo, the scattering function, and the opacity.

In the very cold regions surrounding a YSO, where the dust temperature typically never exceeds a few tens of K, it is expected that these dust grains are covered by a mantel of ices which can dramatically change their radiative properties, especially at short wavelengths.

3.2 Basics of dust extinction

Dust grains are responsible for the extinction within molecular clouds, inside of clusters, and also within each YSO; although these various extinctions could originate in different types of grain populations. The typical representation of this extinction uses the ratio of observed over expected flux, measured in V-band: $A_V \equiv A(V) = 2.5 \log(F_\nu^{\text{obs}}/F_\nu)$. The extinction, $A(\lambda)$, is a function of wavelength and is expressed in magnitudes. An alternative representation is to consider the extinction as being caused by an optical depth τ_{ext} such as $\exp(-\tau_{\text{ext}}) = F_\nu^{\text{obs}}/F_\nu$. We have the equivalence $A(\lambda) = 1.086\tau_{\text{ext}}(\lambda)$.

At sufficiently long wavelength, dust opacity models can usually be represented by a simple power-law, $\kappa_\nu = \kappa_0(\nu/\nu_0)^\beta$, with the index β depending on the specifics of the dust model. The opacity κ_ν is expressed in $\text{cm}^2 \text{g}^{-1}$, and can be interpreted as a extinction cross-section per unit mass. Most dust models assume a 1:100 dust-to-gas ratio, and derive opacities per unit gas+dust mass, instead of just dust mass. From a radiative transfer perspective, the observed specific intensity from a thermal source $B_\nu(T)$ in the optically thin regime is $I_\nu = \tau_\nu B_\nu(T)$, where the optical depth is $\tau_\nu = \kappa_\nu \int \rho_{\text{dust}} dl$. ρ is the density and the integral is calculated along the line of sight to the source.

A measure of the intensity from a source can thus lead to an approximation of the

total mass within a primary beam, for a given dust grain model. For a source with a measured sub-millimeter flux density S_ν , in the optically thin regime we can write $S_\nu = \tau_\nu B_\nu(T)\Omega$, where Ω is the solid angle of the source, $\Omega = A/d^2$, with A the area of the source and d its distance. We obtain a measure of the mass by writing $M \approx A \int \rho dl$, to obtain (Shirley et al., 2000):

$$M = \frac{S_\nu d^2}{B_\nu(T_{\text{dust}})\kappa_\nu}, \quad (\text{I.7})$$

with a dust temperature is usually taken to be between 10 to 20 K.

With only near- to far-IR wavelengths observations, however, it is more difficult to estimate the dust mass, because the system is usually not in the optically thin regime and very dependent on the local geometry and viewing angle. To use these observations, which are interesting because they naturally are at higher resolution than single-dish submillimeter data, detailed radiative transfer models are usually required (Section 3.3).

Dust grains can either scatter or absorb photons, and both of these processes have their own frequency-dependent efficiency. Large grains are usually considered in local thermal equilibrium (LTE), in which case the thermal emission balances out the absorption. However, small grains ($< 50 \text{ \AA}$) can be subject to stochastic heating, where single photons can heat up the grains to much higher temperatures for very short amounts of time. Scattering mechanisms can be much more complicated to represent, as they usually involve a scattering phase function, describing the deflection angle of incident photons (which also depends on wavelength). Most models show that dust grains are preferentially forward-scattering [CITE Draine?]. The scattering properties of the dust model exclusively influence the short-wavelength emission, while the absorption properties influence all wavelengths.

3.3 Radiative transfer modeling

Several radiative transfer codes exist in the literature, and we have explored a few of them. We opted for a recently-developed package called Hyperion (Robitaille, 2011), which is a Python interface to a 3D Monte-Carlo code by Whitney et al. (2013). The code is versatile, parallelized, can accept different dust models and can generate various types of geometries and density grids.

Hyperion functions in two steps. After choosing a discrete grid to represent a density model and adding energy sources, the temperature structure of the dust is calculated by propagating photon packets and determining the dust LTE temperature in each cell. Multiple iterations of this process are usually required to converge to a decent thermal structure.

Once the dust temperature is known, the dust becomes a source of thermal radiation. This type of radiation is modeled using ray tracing, which provides a very good signal-to-noise ratio (SNR). The light from the central source which was not absorbed, however, needs to be propagated and scattered off the dust grains, for example using a method called peeling-off (Yusef-Zadeh, Morris, and White, 1984). For non-isotropic scattering, this process has relatively low SNR, hence requires a lot of photons packets to function properly. While there are future plans to implement raytracing for scattering (Robitaille, 2011), we are currently forced to wait long times for simulating YSOs with massive envelopes because of this problem.

[Put models of YSOs with different masses here.]

These models usually present a large amount of degeneracies, especially when the entire range of wavelengths is not covered, as it is the case for most astronomical sources.

For example, an SED will look very different depending on the viewing angle. If we see down the throat of the cavity, the short-wavelength light from the central source will not exhibit a lot of extinction. If we observe this same source through the disk and envelope, these same wavelengths will show a lot of extinction. The short wavelength, up to the peak of the SED, are very geometry-dependent and highly degenerate parameters.

This realization helped us target our work using this code. Others (e.g Robitaille et al., 2006) have produced standardized grids of pre-computed models which randomly sample a very large number of source geometry parameters. These grids are routinely used by the community to fit a set of unresolved SED measurements at discrete wavelengths. However, most often the scatter in the parameters for the few best fit models prevents from drawing meaningful conclusions on the observations.

[Example?]

One of the key challenges of using this code is to determine which dust models to use. For this work, we choose to use exclusively OH5 dust (Ossenkopf and Henning, 1994), which represents grains with an ice mantle which are the result of a coagulation phase of an initial distribution of grain sizes following $n \propto a^{-3/2}$. This model was found to accurately represent some grain distribution in the ISM [NEED CITATION, CHECK OUT TRACY'S PAPER].

3.4 Observing star formation

In the past decade, space-based infrared observatories such as *Spitzer* and *Herschel* have really allowed the beginning of the detailed study of dust around forming stars, by sampling the SEDs in key spectral regions, such as the PAH region (with the IRAC instrument on

Spitzer), the mid-infrared (with the MIPS instrument, especially its 24 μm channel), and the far-IR (with the PACS instrument on *Herschel*).

However, these observatories lack the required angular resolution to observe the key physics of star formation in dense clusters in the key wavelength region between 30 μm and 200 μm. For a diffraction-limited single aperture telescope, the angular resolution and spatial resolutions R_θ and R_{linear} are:

$$R_\theta = 17.6'' \left(\frac{\lambda}{70 \mu\text{m}} \right) \left(\frac{D}{1 \text{m}} \right)^{-1}, \quad (\text{I.8})$$

$$R_{\text{linear}} = 0.04 \text{ pc} \left(\frac{d}{500 \text{ pc}} \right) \left(\frac{\lambda}{70 \mu\text{m}} \right) \left(\frac{D}{1 \text{m}} \right)^{-1}, \quad (\text{I.9})$$

which shows that even with *Herschel* and its 3.5 m primary mirror and its 70 μm channel, we can barely resolve clustered YSOs (typical separations of a few hundredths of pc), let alone study their structure in detail.

To further complicate the problem, most space observatories are tailored for very sensitive observations, so the brightest regions of clusters often cause saturation issues due to a lack of dynamic range. These two issues have continually prevented us from gathering a good picture of the physics in these dense and important regions of stellar birth.

[Image that shows the saturation/lack of resolution]

[Talk about SOFIA]

Chapter II

Star Formation in Clustered environments with SOFIA FORCAST

1 Introduction

Most stars in the Galaxy form in cluster environments of sizes 2-4 pc, often containing more than 100 young stellar objects (YSOs), with typical separations of <0.05 pc between stars near their centers (Porras et al., 2003; Allen et al., 2007; Gutermuth et al., 2009). Previous studies have been effective in elucidating the young stellar content and distribution in clouds on large scales (parsec down to 0.05 pc) (Kennicutt and Evans, 2012), but young cluster cores, born in dense portions of molecular clouds, are more difficult to observe. They are obscured at optical through near-IR wavelengths. At mid-IR through far-IR wavelengths, the material surrounding YSOs and involved in the stellar birth process emits due to heating by the young stars, but the resolution to date has not been sufficient to isolate individual stars in the cores of most nearby young clusters. »»»> Stashed changes

2 Sample description and scientific goals

Spitzer has tremendously helped our understanding of star formation, by providing sensitive observations in continuum bands from [] to 160 μm . In particular, the MIPS 24 μm channel provided a robust way to determine the spectral index of YSOs, hence leading to dramatic improvement of understanding of the YSO population in clusters (e.g., Gutermuth et al., 2009; Gutermuth et al., 2011).

However, the most dense regions of clusters still present a challenge for the MIPS instrument, as the YSOs are too bright and/or in too close proximity, which leads to saturation and confusion, as exhibited in Fig. ??.

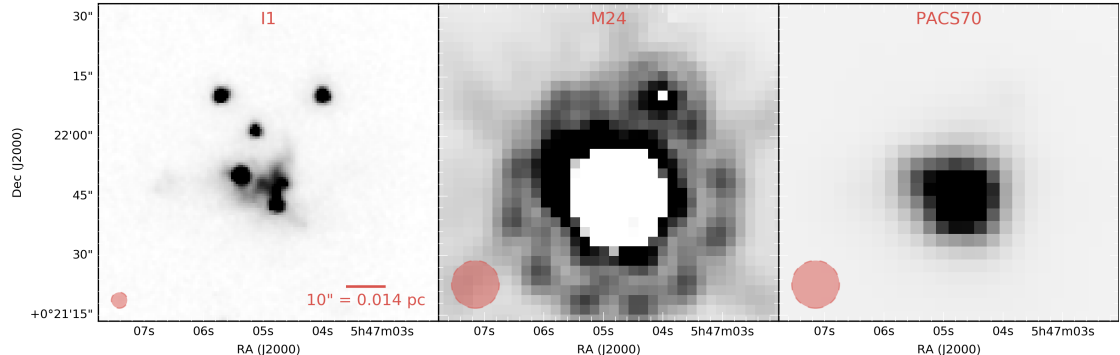


FIGURE II.1: Saturation and confusion in NGC2071.

BETTII will tackle the confusion problem at wavelengths from 30 to 100 μm , and will be complementary to *Herschel* observations of star-forming regions. SOFIA, however, can already start studying these dense regions with its FORCAST instrument, providing 2-3.5'' resolution between 10 and 37 μm .

We responded to SOFIA FORCAST's first science call with a proposal for a survey of nearby star-forming cluster cores. The clusters were selected from a list of dense young

clusters within 1 kpc of the Sun based on Porras et al. (2003) and Gutermuth et al. (2009).

From this list we selected clusters that were: (1) north of -25 degrees declination so that they could be done from a northern hemisphere flight; (2) included membership of >50 YSOs; and (3) included bright 8-24 μm sources within the dense cores based on *Spitzer* and/or WISE data.

In order to sample the most range of the SED, we proposed to observe in 4 of FORCAST’s science continuum bands: 11.1, 19.7, 31.5 and 37.1 μm . This wavelength coverage would be very complementary to archival data from *Spitzer* and WISE. Our focus on bright regions spread all across the sky is convenient for SOFIA, and our project would be observed as a gap-filler during the primary science flight legs.

The main objective of the survey is to gather statistics and fill the SED gap between *Spitzer*’s bands and *Herschel*’s bands. *Spitzer* is often unusable for these targets because of saturation and confusion, and *Herschel* is confused as well. As it is often the case, *Herschel* observations were not available for our targets, making these SOFIA observations the best attempt at observing those regions at mid-IR wavelengths, and our only opportunity to constrain the SED of very clustered YSOs in these regions to infer their physical properties.

Our strategy was successful and we were awarded time during the first and second science cycles of FORCAST (see Tab. II.3). The data analysis and scientific interpretation is presented in the next few sections. First, we describe our observations, as well as the archival datasets that we use to complement our observations. Second, we properly characterize the systematics of the FORCAST instrument and their variations over multiple science flights spanning multiple years. The data reduction process is then explained, followed by a snapshot of the data products themselves. We then discuss our SED fitting strategy, and fit the SEDs of three of our clusters to derive the physical properties of their embedded

YSOs.

3 Observations

The FORCAST camera has two separate 256×256 pixel infrared arrays that cover the wavelength range from $5.5\text{-}37\,\mu\text{m}$ in multiple bands with $0.768'' \times 0.768''$ pixels. The two arrays can observe simultaneously through a dichroic beam splitter that divides the wavelength range shortward and longward of $26\,\mu\text{m}$. Alternatively, the long wavelength array can be used by itself as the dichroic is removed from the light path, gaining a sensitivity of ~ 2.5 . We observe the 11.1 and $37.1\,\mu\text{m}$ together (hereafter "mode 1") and the 19.7 and $31.5\,\mu\text{m}$ together (hereafter "mode 2"). We set the 1σ sensitivity threshold to that of a moderately rising SED for a $1.5\,L_\odot$ source, which is scaled appropriately for the distance to the cluster. This is an attempt at probing the same luminosities at all distances and obtain a consistent sample of YSOs.

TABLE II.1: List of desired sensitivities

Distance (pc)	1 σ minimum detectable flux (Jy)				Corresponding minimum L_\odot
	11 μm	19 μm	31 μm	37 μm	
200.0	0.1	0.1	0.32	0.7	~ 0.5
400.0	0.1	0.1	0.32	0.6	~ 1.5
600.0	0.05	0.04	0.18	0.25	~ 1.5
800.0	0.02	0.02	0.1	0.12	~ 1.5
1,000.00	0.01	0.01	0.06	0.1	~ 1.5

List of desired sensitivities for different distances.

However, for the most nearby clusters, the corresponding observing time was so short that the overhead from the observatory was very costly. Hence, we put a lower threshold to the integration time of 30 s. Similarly, the sensitivity of the $37\,\mu\text{m}$ band is such that in order to be consistent with our sensitivity target, this band was heavily driving the

observing time using mode 1. Hence, we observe in this mode as long as is required to meet the sensitivity target for the 11 μm band, and request more observations in the 37 μm band on its own (hereafter "mode 3"). This allows us to request less total observing time while keeping our sensitivity self-consistent. A summary of our target sensitivities for various distances is shown in Table II.1.

Various observing techniques are available to the FORCAST user to deal with background subtraction. The most robust techniques are very costly in terms of overhead for the observatory, so we decided to be audacious and requested the cheapest observing mode: the Chop-Nod-Chop mode (CNC), combined with 9 ditherings for each field, which dramatically helps when co-adding images together. Most of our data was processed by the SOFIA automated pipeline that provided calibrated Level 2 images, except for the data from the first few flights, for which we received the help of one of FORCAST's Principal Investigator, Dr. Joe Adams, who processed the raw data through his own instrument pipeline.

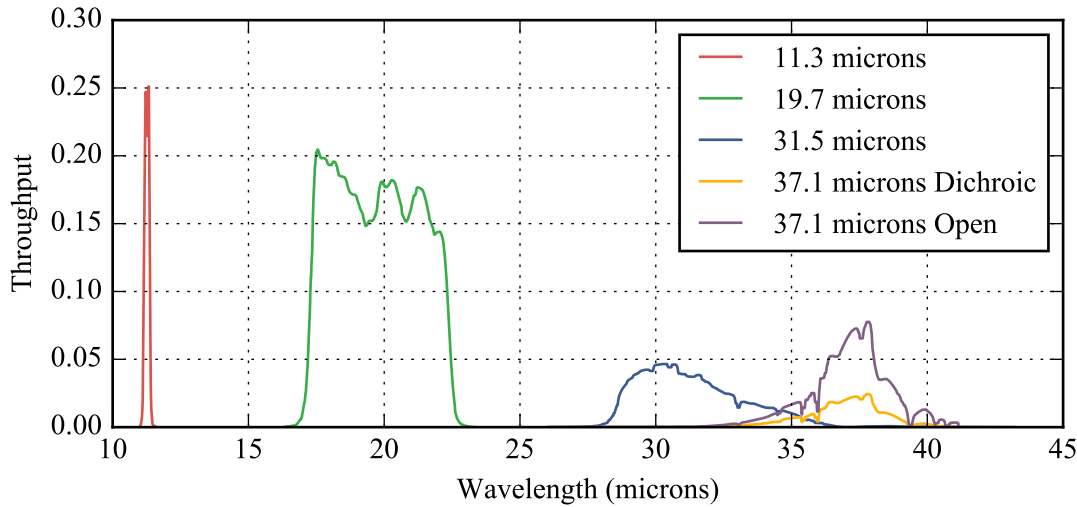


FIGURE II.2: SOFIA FORCAST bands.

The data were acquired over 10 SOFIA flights spanning multiple years, with the last batch dating from February 2015. The actual observing times for each band and cluster is shown in Table II.3. In that table, we have estimated the time for the 37 μm band using a composite formula that levels the observing time from mode 3 to that of mode 1, considering their respective sensitivities. We obtained about 10 h of on-sky data, and 10 out of our 12 original target clusters were observed.

TABLE II.3: List of targets

Cluster	Coordinates (J2000)	SOFIA Flight IDs	N_{Fields}	d (pc)	T_{11} (s)	T_{19} (s)	T_{31} (s)	T_{37} (s)
Cepheus A	22h56m10s +62d03m26s	F132 F109	2	730	206	234	235	490
Cepheus C	23h05m45s +62d30m05s	F132	1	730	150	121	121	286
IRAS20050	20h07m05s +27d28m51s	F166 F131	2	700	321	224	256	266
NGC1333	03h29m00s +31d17m20s	F129 F193 F190	9	240	530	558	467	446
NGC2071	05h47m06s +00d21m45s	F192	2	420	36	25	33	42
NGC2264	06h41m07s +09d33m35s	F156	4	913	495	300	331	587
NGC7129	21h43m07s +66d06m42s	F109	1	1000	383	214	214	709
Ophiuchus	16h27m05s -24d30m29s	F157	11	150	396	468	501	365
S140	22h19m23s +63d18m44s	F129	1	900	322	393	393	568
S171	00h04m01s +68d34m50s	F132	1	850	253	219	219	476

List of observed targets. For each cluster, we list the SOFIA flights on which the data was taken, the number of individual fields within the cluster, the distance, and the total integration time for each of the 4 observation bands, including all fields. Note that the 37 μm time quote is a composite time calculated by combining the exposure time of mode 1 with that of mode 3, as discussed in the text.

To complement our observations, we proceed to an archival search to find publicly available WISE, *Spitzer*, and *Herschel* images. Most of our targets have already available *Spitzer* IRAC and/or MIPS photometry (**Megeath:2012cn**; mostly from Gutermuth et al., 2009; Evans et al., 2009), which we use in the relevant cases. In the cases where no IRAC photometry was available, we applied our own photometry algorithms. We could not find published photometry for the targets with available *Herschel* images, hence we

also used our own photometry pipeline to derive fluxes. In some cases, we find previously published 1.3 mm continuum measurements to help constrain the long-wavelength behavior of the SEDs.

4 FORCAST characterization

In addition to the raw images, a number of calibrators were observed during each flight for different dichroic settings and wavelength bands. These calibrators are usually bright stars which guarantee to be point sources for SOFIA’s angular resolution, and have very predictable mid-IR fluxes, so they can be used both for flux and PSF calibration. We use them for two purposes: the first is to obtain a robust metric to determine whether sources are extended or not; the second is to determine the aperture correction factor which will later be used for aperture photometry.

4.1 PSF size

The size of the PSF can be defined in multiple ways, we adopt the approach of characterizing the PSF using its encircled energy distribution. Fig ?? shows the average of the normalized encircled energy distribution of the PSF, measured on all the calibrators of our sample. Each curve represents one of the five different combinations of bandpass filter and dichroic setting that we use for our observations. For each radius, the total energy is the sum of the pixels within the circular aperture of that radius, to which we subtract an estimate of the background in an annulus around the source (see Section [] for details on the background subtraction methods).

As expected, the PSF at 37.1 μm is larger than the PSFs at shorter wavelengths, but less than the traditional diffraction limit rule. This indicates that additional PSF smearing

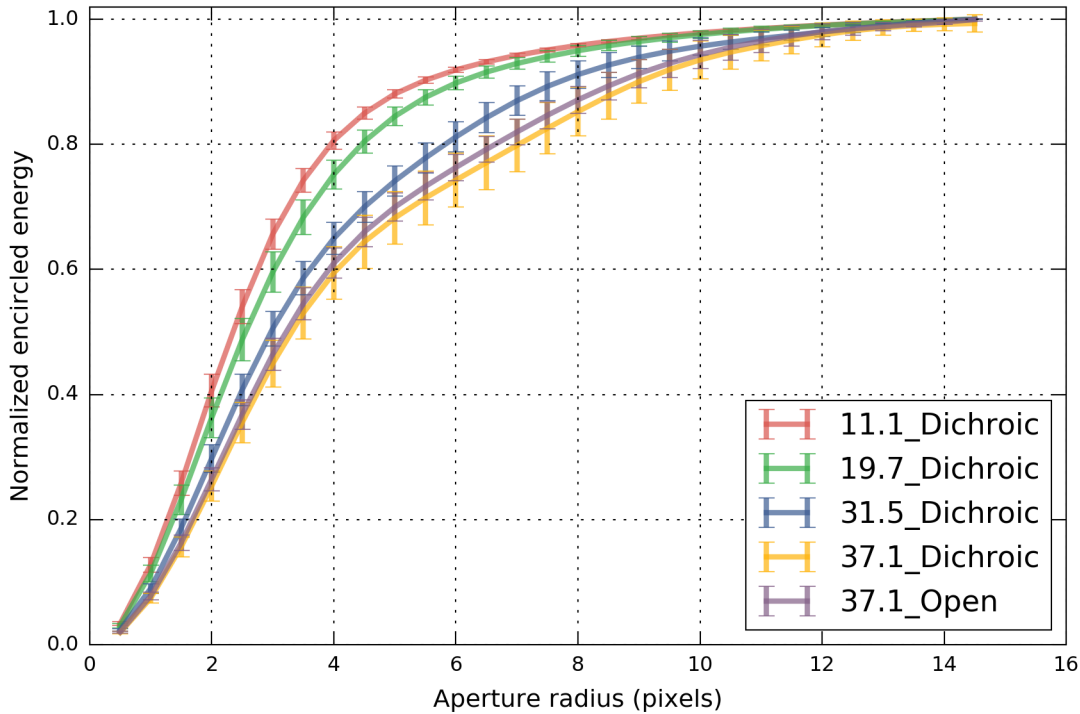


FIGURE II.3: Average PSF encircled energy distribution profile for all calibrator observations.

is occurring at short wavelengths, likely due to plane jitter and pointing errors, which is consistent with what other authors have found (e.g. Herter et al., 2013). Throughout all the flights, point source calibrators always have the same encircled energy distribution shape within $\sim 4\%$ rms.

To look at the behavior of the PSF in more detail, we can use the half width at half maximum of the encircled energy distribution, R_{50} as a proxy for PSF size. The variation of this quantity for the various flights, bandpass/dichroic setting, and calibrators used is showed in Fig ???. This shows the flight-to-flight differences and, for some calibrators, the in-flight variability. We find that the latter is usually small, except for the SOFIA flight on 05-02-2014, for which the spread is quite considerable and could have been caused by instrumental malfunction or abnormal levels of jitter. The variation from flight to

flight is larger than the variation within a given flight, which indicates variability in the observing conditions, systematics, or thermal radiation environment of the observatory between different flights. Even considering the flight-to-flight and calibrator-to-calibrator variations, the overall spread in R_{50} for a given observation setting is almost always less than 10%, making this metric a useful reference to compare with scientific data. In our analysis we will compute R_{50} for our sources and compare it to the R_{50} from the current flight for the same filter setting, if the calibration file exists. If no calibration file exists for a given setting, we use the mean R_{50} for that setting from calibrators observations in other flights. The ratio $R\%$ of these two quantities helps quantify the extension of the source, to within $\sim 10\%$.

4.2 Aperture correction factor

In Fig. ??, we observe that the encircled energy does not vary much by the time the aperture reaches a radius of 12 pixels, so we consider this fiducial aperture as our "total flux" aperture. The goal of aperture photometry is to estimate the amount of flux in this large aperture, which we consider to be the total amount of flux from the source, by only measuring flux within a much smaller aperture. This has the advantage of reducing contamination from other sources, and increases the signal-to-noise ratio of the flux estimate since the pixels near the tail of the PSF usually contain more noise than signal. In Fig ??, we plot the aperture correction factor that we compute from the ratio of the flux measured within an aperture of 4 pixels radius and this 12-pixel aperture. Not surprisingly, this graph follows very closely the plot of R_{50} from Fig ??, showing the close link between the aperture correction factor and the shape of the calibrator's PSF. We match each observation in our data to the mean of the aperture correction factors for the same observation

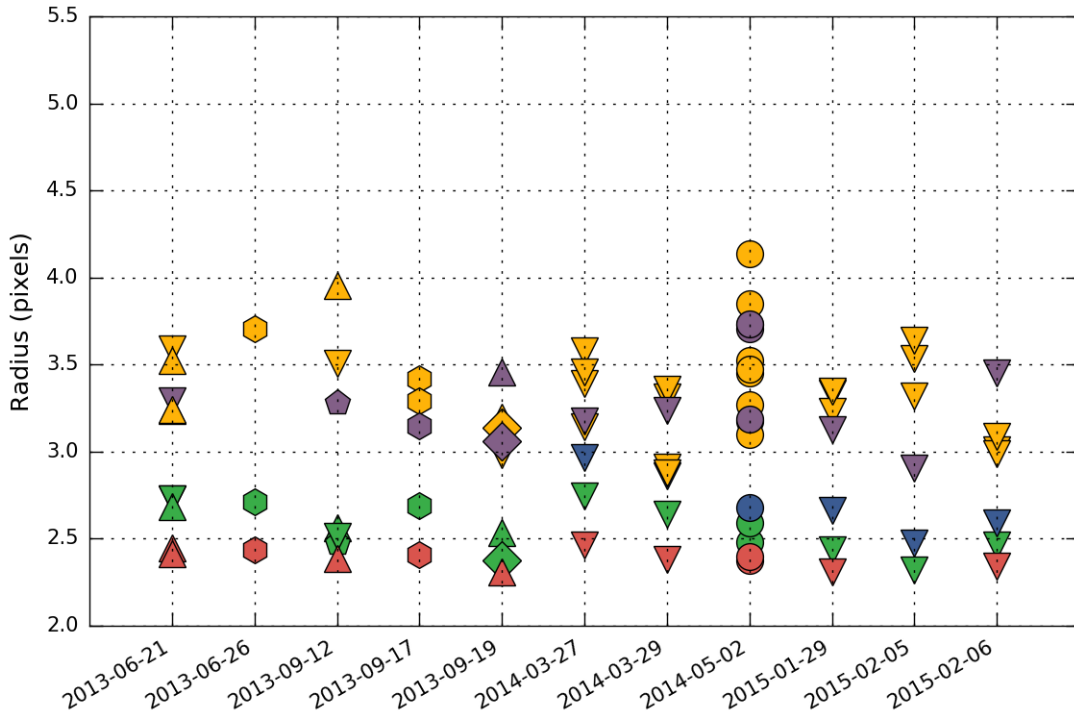


FIGURE II.4: Distribution of R_{50} for all calibrators observations within each bandpass. In red: $11\text{ }\mu\text{m}$ band, with dichroic; in green: $19\text{ }\mu\text{m}$ band, with dichroic; in blue: $31\text{ }\mu\text{m}$ band, with dichroic; in yellow: $37\text{ }\mu\text{m}$ band, with dichroic; in purple: $19\text{ }\mu\text{m}$ band, with dichroic. Down triangles: α Boo; Pentagons: α Cet; Diamonds: α Tau; Up triangles: β And; Hexagons: β Peg; Circles: β UMi;

setting and flight.

4.3 Instrument response and overall uncertainty

To validate our approach, we take a look at the calibrator fluxes after normalization by the calibration factor, which is provided directly by the FORCAST pipeline. This calibration factors converts the pixel digital value a physical flux density unit, and presumably is determined using the flux from calibrator stars as well. Here we re-measure the flux from each calibrator for each observation setting and each flight, using our standard aperture photometry method and background subtraction. Ideally, we would always obtain the

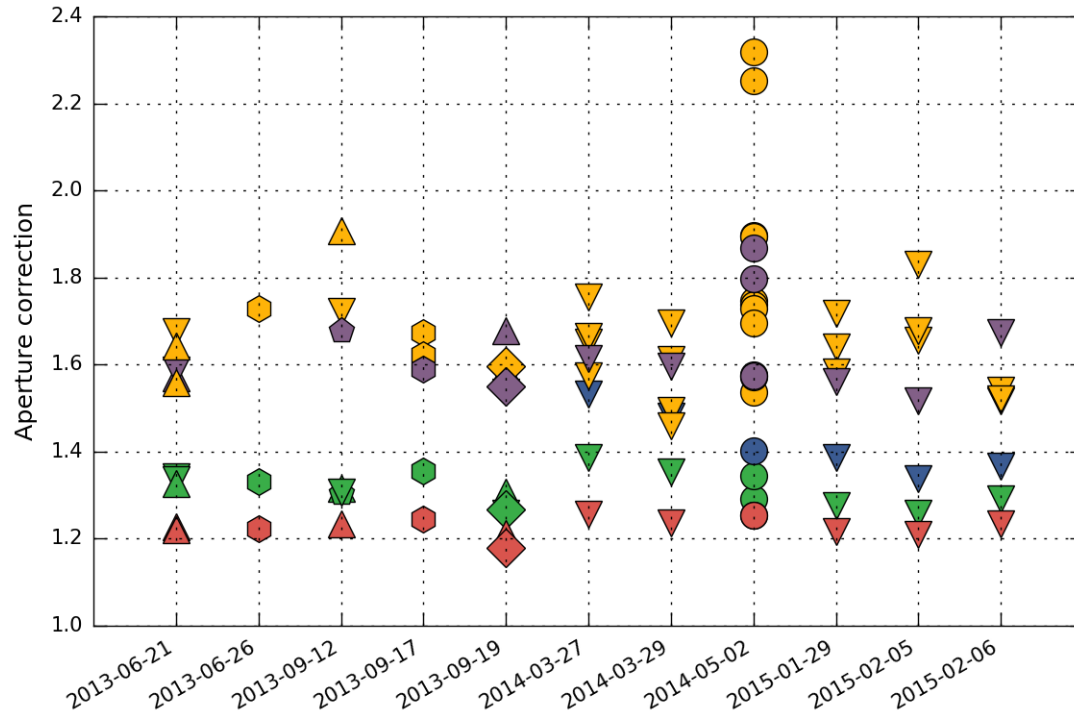


FIGURE II.5: Instrumental response and aperture correction

same flux for each setting and calibrator, independently of the flight, an assertion we find true to within $\sim 5\%$. The in-flight errors are typically lower than this. This validates our aperture photometry method, and we can trust that the instrument's systematics are well-behaved to within these levels.

This would suggest that we can adopt systematic 1σ uncertainties of $\sim 5\%$, a value which is consistent with the published uncertainties of $3\sigma \approx 20\%$ (DeBuizer:2012ie).

5 Data reduction and photometry

The data are processed through various versions of the online pipeline to yield Level 2 data products available on the archive (Herter et al., 2013). We apply our own reduction procedure and photometry pipeline on those products to derive final images, source positions,

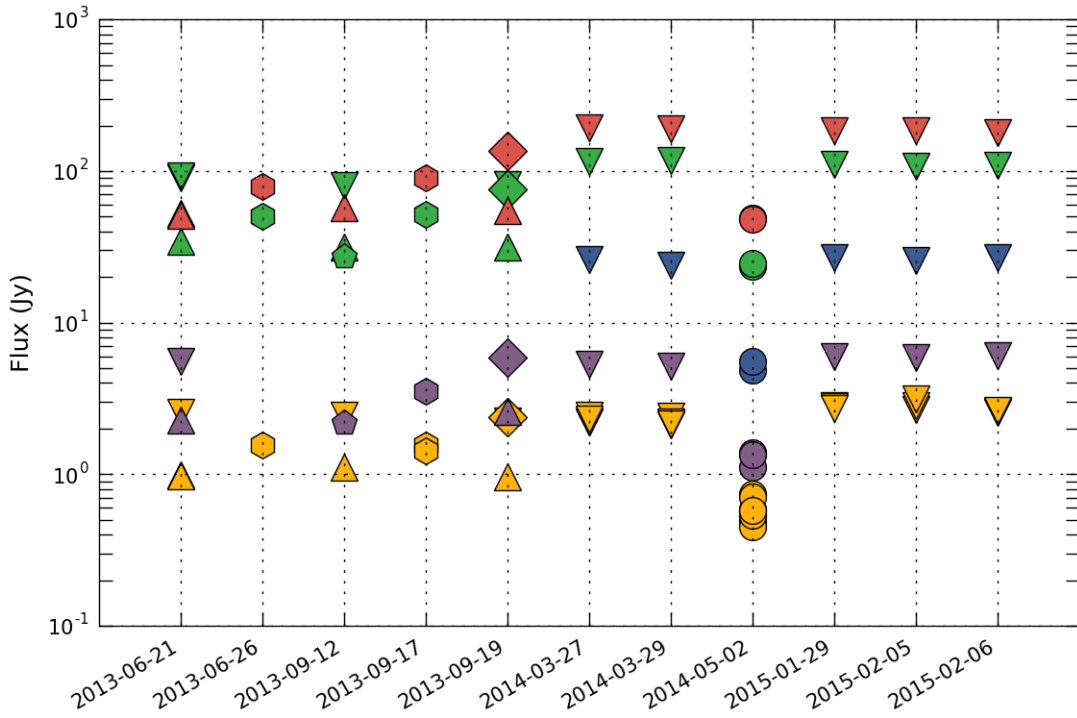


FIGURE II.6: Instrumental response

fluxes and sensitivities. Our software makes extensive use of the Python *astropy* package (Astropy Collaboration et al., 2013) and its associated modules *photutils* and *APLpy*.

5.1 Pre-treatment

Some manual treatment of each image is necessary before it can be analyzed by our software, which follows this procedure: a) visually aligning the WCS coordinate system, often 10-20" off, using point sources and archival data from other wavelengths and facilities such as IRAC 8 μm ; b) cropping the images to clean off the nodded fields, and c) identify the coordinates of each source, both point-like and extended.

After these manual steps, the Level 2 images are multiplied by the calibration factor provided by the online pipeline, which converts them to Jy/pixel. We do not proceed to

any systematic color correction, but the effects on the fluxes are very small (Herter et al., 2013).

1. Adjust WCS coordinates: use images at other wavelengths (2MASS, IRAC, MIPS, WISE) to re-align the (RA, DEC) position of the field. We estimate that this process is good to within one SOFIA pixel ($0.768''$) for the fields where one or more point sources can be identified. Extended fields are less trustworthy, since matching the extended emission to other wavelengths is harder. The rotation of the field produced by the SOFIA pipeline is correct for all of our data.
2. Crop each image, remove chopped fields, remove artifacts.
3. Identify and categorize sources: isolated point sources, clustered point sources, and extended sources. For extended sources, a circular or elliptical aperture is used to try to encompass the entirety of the emission.
4. Manually identify a location in the field that corresponds to a representative background.

5.2 Source flux extraction

We feed the adjusted FITS and associated metadata files to our photometry pipeline. For each identified source, we determine its flux in all bands using aperture photometry with local background subtraction. The aperture correction factor we use is the one determined from the calibrators observed for the same observation setting during this flight. If a calibrator was not available during the flight, we use the average aperture correction factor taken over 9 of our 10 flights (we choose to exclude the flight on 05/02/2014 which seems to have abnormal behavior).

We distinguish between 3 types of sources after manual identification: *isolated*, which are point sources with no nearby objects; *clustered*, which are point sources with nearby objects; and *extended*, which are not consistent with being point sources.

For point sources that are isolated, we use our standard aperture of 4 pixels at all wavelengths. We consider an annulus surrounding the source extending from 12 to 20 pixels radius (24 to 40 for clustered sources): the local background is determined from the mode of the pixels in the annulus, while the sensitivity is calculated by measuring the standard deviation of the flux values within 4-pixel apertures spread over that annulus [Cite Taro's paper and the Herschel photometry paper that Tracy gave us]. We apply the aperture correction derived from the calibrator observations taken during that flight.

For extended sources, an elliptical aperture is determined manually from the 37 μm images. The local background is determined from the mode of an elliptical annulus, with an inner boundary at the elliptical aperture and an outer boundary corresponding to an ellipse 20% larger. The sensitivity quoted is the point source sensitivity, and is determined following the same method as for point sources, using the standard deviation of apertures spread across the elliptical annulus.

The photometry from sources that were observed in different flights is then combined to increase the signal-to-noise ratio. This combination takes into account the sensitivity of each source by appropriately weighing each image.

The source sensitivity calculated this is added to the systematic uncertainty of the instrument, for which we follow the recommendation from (Herter et al., 2012) to adopt a 20%, 3σ uncertainty.

5.3 Image sensitivity

In order to determine the absolute sensitivity in the image, we use two methods. First, we manually determine a region in each cluster that visually appears devoid of flux. We calculate the sensitivity as if this background region was a source, by patching apertures in an annulus around this background location and calculating the standard deviation of the obtained fluxes. We call this sensitivity measurement σ^{man} . The main downside of this method is that it requires a manual operation to select the appropriate background field, and hence could have more variation depending on which field we select. Second, we use a routine that iteratively isolates the pixel values above 2σ of the image, in order to remove the contamination from our actual sources. The standard deviation of the resulting image is then calculated, and is multiplied by the square root of the number of pixels in an aperture of 4 pixel radius. This corresponds to a floor sensitivity σ^{std} . We present our results in Table II.5, where we also compare this sensitivity with the expected sensitivity σ^{th} obtained using the online calculator with the actual exposure time of our images. We note that usually, the theoretical values are more in agreement with our first method.

5.4 Other photometry

6 Data products

6.1 Maps

Explain map-making algorithm

Image of extended sources: CepA, NGC7129, NGC2264, NGC1333

Image of clustered sources: IRAS20050, NGC2071, S140

TABLE II.5: FORCAST Sensitivities

Cluster	F11			F19			F31			F37			Sources
	σ^{man}	σ^{std}	σ^{th}										
CepA	0.07	0.04	0.05	0.11	0.05	0.05	0.19	0.07	0.16	0.26	0.09	0.34	4
CepC	0.03	0.03	0.04	0.10	0.05	0.04	0.19	0.06	0.16	0.16	0.09	0.30	4
IRAS20050	0.04	0.03	0.04	0.08	0.04	0.05	0.13	0.05	0.16	0.30	0.11	0.32	7
NGC1333	0.12	0.04	0.07	0.07	0.07	0.07	0.22	0.08	0.25	0.48	0.13	0.52	11
NGC2071	0.19	0.10	0.12	0.32	0.15	0.15	0.21	0.22	0.49	0.45	0.28	0.81	6
NGC2264	0.07	0.03	0.05	0.19	0.05	0.06	0.28	0.07	0.20	0.21	0.09	0.43	21
NGC7129	0.07	0.03	0.03	0.10	0.04	0.03	0.26	0.09	0.12	0.17	0.08	0.19	5
Ophiuchus	0.11	0.05	0.08	0.16	0.07	0.08	0.31	0.09	0.27	0.41	0.18	0.65	19
S140	0.04	0.03	0.03	0.16	0.03	0.03	0.21	0.07	0.09	0.35	0.11	0.21	7
S171	0.04	0.03	0.03	0.07	0.04	0.03	0.07	0.05	0.12	0.16	0.06	0.23	2

For each band, we measure the 1σ sensitivity σ^{man} and σ^{std} in each field from the data using two different methods (see Section ?? for details), and present here the median of all fields. The theoretical sensitivity σ^{th} corresponds to the expected sensitivity for the effective integration time, using the SOFIA FORCAST observation planning tools. All sensitivity values are in Janskies.

TABLE II.7: Spitzer photometry comparison

SOFIA name	i1	i2	i3	i4
NGC2071.1	0.04	0.06	0.02	-0.03
NGC2071.3	-0.07	-0.10	-0.06	-0.09
NGC2071.4	0.04	-0.12	-0.01	-0.10
NGC2071.5	-0.05	-0.06	-0.11	-0.11
IRAS20050.1	-0.08	-0.06	-0.07	0.08
IRAS20050.3	0.19	0.10	0.05	0.10
IRAS20050.6	-0.07	-0.06	-0.12	-0.05
IRAS20050.7	-0.15	-0.07	-0.02	-0.07

Fractional difference between our own aperture photometry on *Spitzer* archival images and published *Spitzer* photometry from **Megeath:2012cn** for NGC2071, and Gutermuth et al. (2009) for IRAS20050+2720.

7 SED fitting

7.1 A small grid of models

SED fitting is prone to many degeneracies: usually many geometrical and physical parameters are used to construct detailed radiative transfer models, but only a handful of

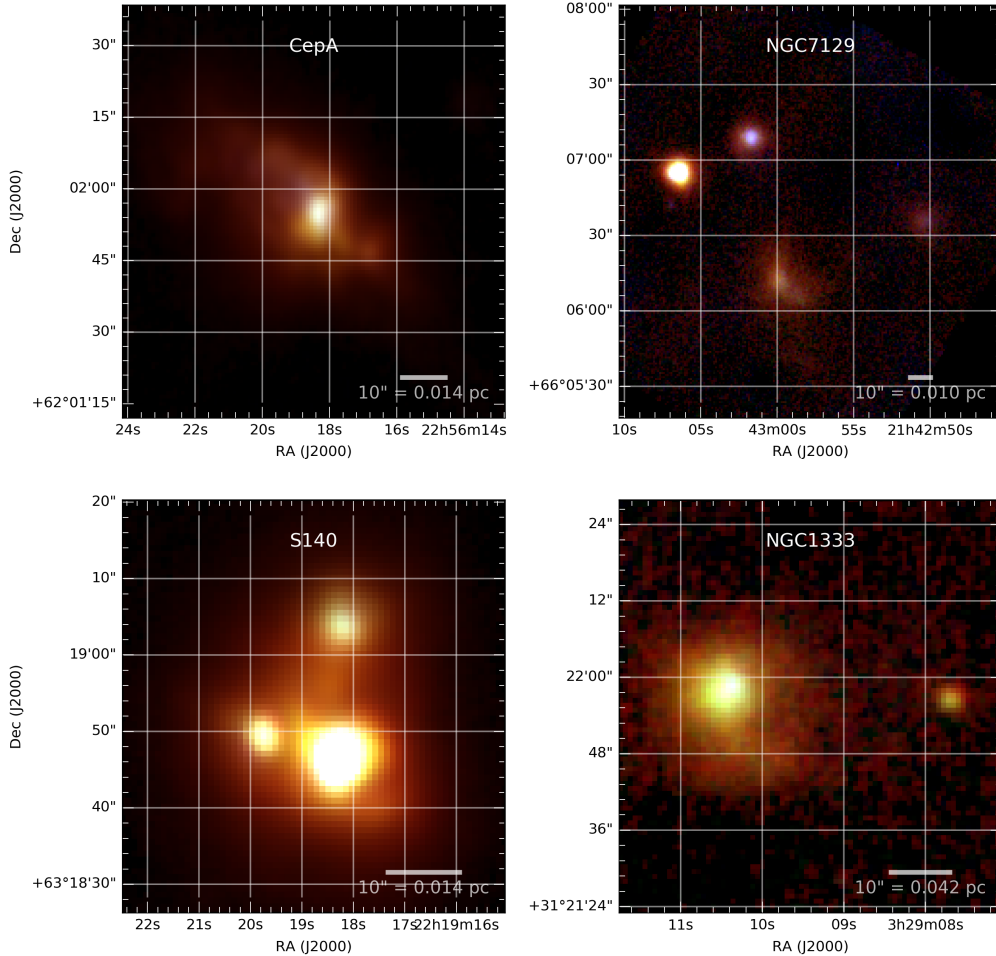


FIGURE II.7: Selected sample of sources

measurement points are available to fit, leading to a dramatically under-constrained problem. As our starting point of our investigation of the SEDs of these sources, we used the *sedfitter* tool from (Robitaille et al., 2006). These authors computed a large grid of tens of thousands of SED models using a radiative transfer code by (Whitney et al., 2003a), by varying 14 geometrical and physical parameters in the dust density grid such as the size of the disk, the accretion rates, the radius and mass of the envelope, etc. The models are then evaluated in the bands corresponding to our data, and a χ^2 metric is evaluated for

TABLE II.9: SOFIA photometry comparison

SOFIA name	F11	F11L	F19	F31	F31L	F37	F37L
S140.3	9.79	9.7	101.70	449.60	401.00	639.17	669.00
S140.4	3.62	4	91.09	357.63	368.00	367.35	485.00
S140.5	110.02	110	812.84	1857.33	1585.00	2000.94	2176.00
Sum of point sources in cluster	123.43	123.7	1005.63	2664.57	2354	3007.47	3330
Total cluster emission	135.26	145	1195.20	4450.31	3780.00	5910.26	6730.00
Error (%)	9.59	17.22	18.85	67.02	60.58	96.52	102.10

Comparison of SOFIA four-band photometry from **Harvey:2012kw** on S140. The author's "total emission" actually represents the total emission in the entire field of view, whereas our measurement corresponds to a manually-selected source region encompassing only the dense core. Note that in this cluster, there is a large amount of emission which is not due to the three identified sources.

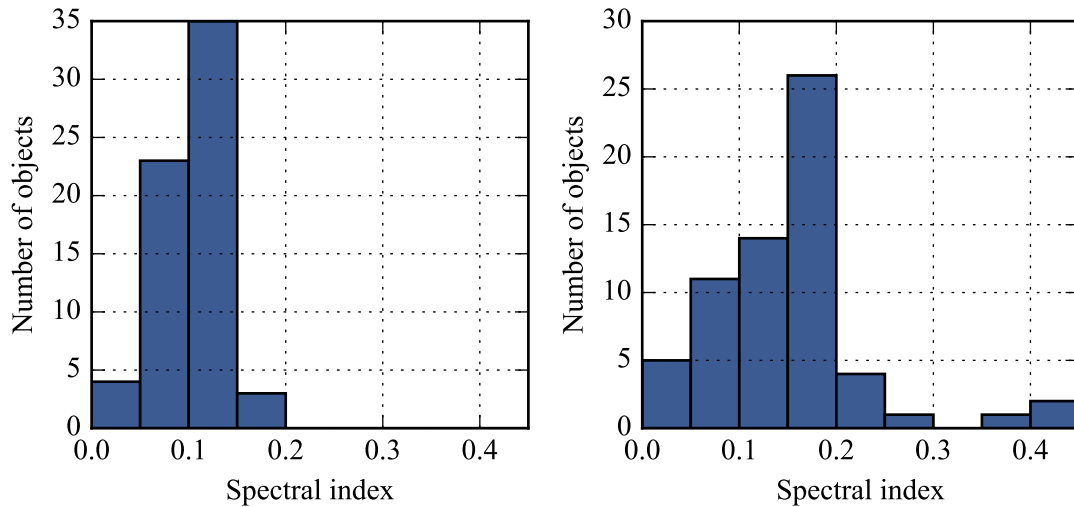


FIGURE II.8: Spectral Index distribution of point sources. *Left:* standard determination of the spectral index, using 2MASS and *Spitzer* from $2 \mu\text{m}$ to $24 \mu\text{m}$, when data is available. *Right:* Determination of the spectral index using data from 2MASS, *Spitzer* and our FORCAST data up to $37 \mu\text{m}$. The distribution changes significantly when you account for the longer fluxes in these clustered regions.

each model. By exploring the distribution of χ^2 , we noticed, as expected, the very large correlations between the parameters which is indicative of many local minimas in the grid. Hence, inferring geometrical and physical parameters from such a grid can be misleading.

We used a more modern version of the same core radiative transfer code, called Hyperion, to develop our own capability of simulating SEDs and understand the sensitivity of these parameters on the SED shape of our Class 0 and I sources. Based on our investigation, the degeneracy between viewing angle and multiple geometrical parameters is considerable. In particular, the sensitivity of the disk properties is minimal, as most of the SED properties are determined almost entirely by the envelope. In addition, parameters of the central source such as the mass, radius and temperature are irrelevant, as they are all combined into one single term, which is the central luminosity. Similarly, the luminosity created when simulating a disk accreting onto the central object can not be distinguished from a more luminous central object and a non-accreting disk. Finally, we find that there is very little difference between Ulrich envelope models and standard power-law envelopes (see for example Fig. 14 from Whitney et al. (2013)), except that the latter can more directly be related to physical parameters such as the mass.

From these findings, we created a simplified grid of models by significantly reducing the number of parameters. The resulting choices are presented in table []]. Note that unlike most authors, who use multiple kinds of dust models for different regions of the SED (which add complexity and number of parameters), we simply use the same dust model for both the envelope and the disk: OH5.

[Add radiative transfer table details.]

Parameter	Description	Values	Units
Constant parameters			
Central source			
M_\star	Stellar mass	1	M_\odot
T_\star	Stellar temperature	4000	K
Disk			
Type	Flared or alpha disk	Flared	
M_{disk}	Disk mass	0.01	M_\odot
R_{disk}^{\max}	Disk outer radius	100	au
R_{disk}^{\min}	Disk inner radius	sublimation radius	au
β	Flaring parameter	1.25	
p	Disk surface density exponent	-1	
r_0	Reference distance for scale height	R_{disk}^{\min}	au
h_0	Disk scale height at r_0	$0.01R_{\text{disk}}^{\min}$	au
d	Dust	OH5	
Envelope			
Type	Power-law or Ulrich	Power-law	
R_{env}^{\min}	Envelope inner radius	R_{disk}^{\min}	au
R_{env}^{\max}	Envelope outer radius	5000	au
α	Power	-1.5	
r_0^{env}	Reference radius	R_{env}^{\min}	au
d	Dust	OH5	
Cavity			
r_0^{cav}	Cavity outer radius	R_{env}^{\max}	au
θ_0	Opening angle at r_0^{cav}	10	degrees
	Flaring exponent	1.5	
ρ_0	Density at r_0^{cav}	0	g cm^{-3}
α_e	Density profile exponent	0	
Changing parameters			
i	Inclination angle	0 to 90 in 20 constant increments of $\cos(i)$	degrees
L_\star	Central luminosity	5×1.5^p for $p = -4, -3, \dots, 15$ (from 0.99 to 288)	L_\odot
M_{env}	Envelope mass	0.01×1.5^p for $p = -2, -1, \dots, 20$ (from 0.004 to 22.17)	M_\odot
A_V	External extinction	0, 1, ..., 15	
s	Scaling	0.7, 0.85, 1, 1.5, 1.3	

TABLE II.12: SED model grid.

8 Application to four clusters

8.1 IRAS20050+2720

IRAS 20050+2720 is part of an active site of intermediate-mass star formation in the Cygnus Rift located at 700 pc (Wilking et al., 1989), with the particularity that it doesn't seem to contain any massive stars (Günther et al., 2012). The main cluster core is associated with water and methanol masers (Palla et al., 1991; Fontani, Cesaroni, and Furuya, 2010) and multipolar molecular outflows observed at millimeter wavelengths (Bachiller, Fuente, and Tafalla, 1995; Anglada et al., 1998; Beltrán et al., 2008), suggesting that the region might have experienced a recent episode of star formation in the past 0.1 Myr which contrasts with the average age of the cluster of 1 Myr (Chen et al., 1997; Gutermuth et al., 2005). Gutermuth et al., 2009 have identified > 170 YSOs surrounding the core and measured their continuum fluxes up to $8 \mu\text{m}$ with IRAC. While measurements at longer wavelengths were able to provide estimates of the total mass of the cluster (e.g. using IRAS, Molinari et al., 1996, $388 L_\odot$), the measurements are confused in the densest region and it has not been possible to properly associate the far-IR emission with its short wavelength counterpart because of the small separation between IRAC-detected protostars. The IRAS point source was classified as a luminous class 0 protostar (Bachiller, 1996), and its emission associated with the bright millimeter source MMS1 to the northwest of the core (Chini et al., 2001). Beltrán et al., 2008 show strong evidence that this region has multiple generations of stars, and suggest that a group of low-mass stars first completed its main accretion phase, before setting the stage for the birth of new intermediate-mass stars at the core of this cluster.

We have observed two fields within the cluster (see Fig. ??), including the brightest

core at $20^h07^m06.70^s + 27^\circ28'54.5''$. Multiple sources in the core can be distinguished in the IRAC maps, but the core appears extended in *Spitzer* MIPS at 24 μm , and is identified as a single source with WISE. No good high resolution far-infrared continuum data longward of 24 μm was available for this source.

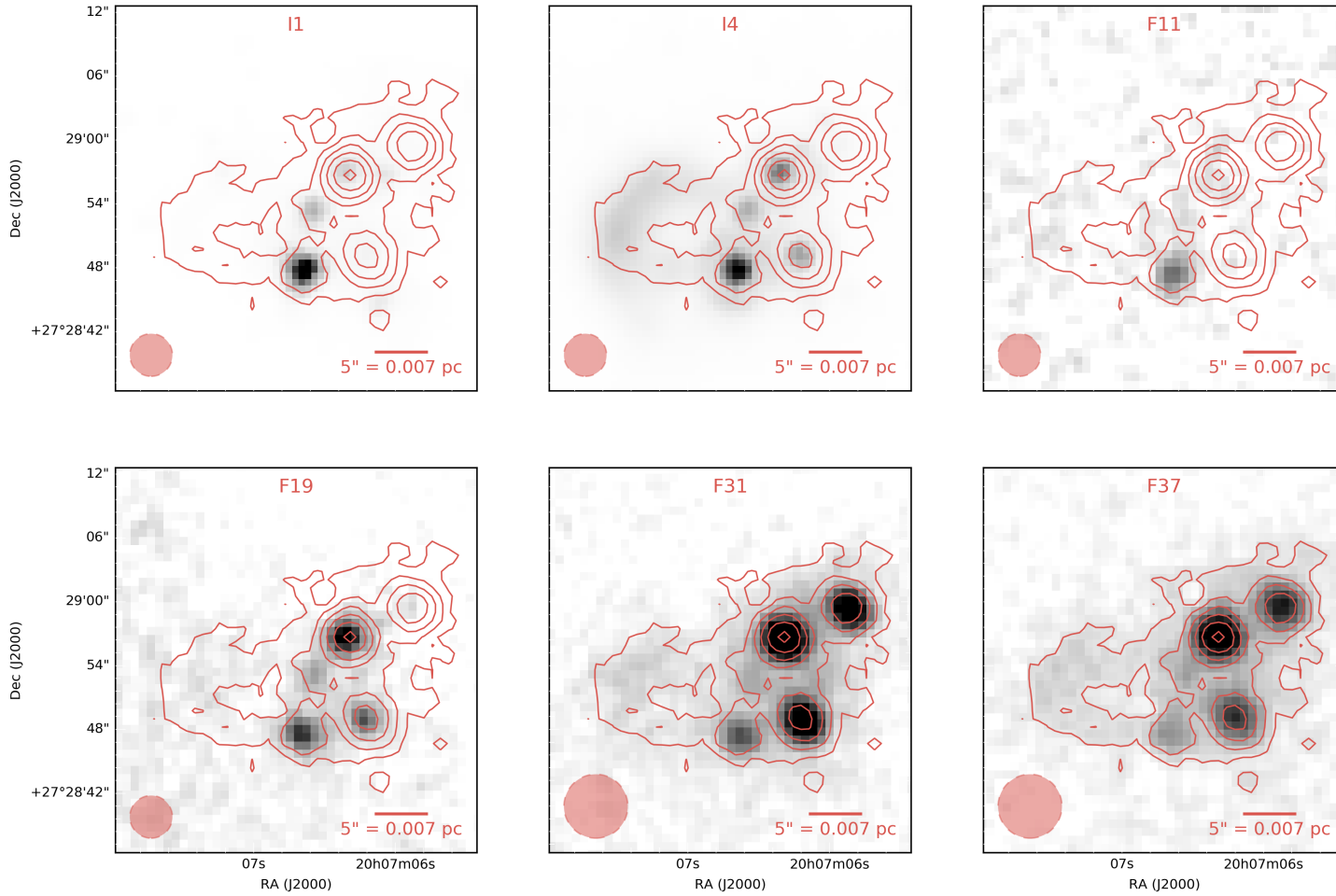


FIGURE II.9: The core of IRAS20050+2720 is seen in the four bands of the *Spitzer* IRAS instrument, as well as with the four FORCAST bands. The increased resolution of FORCAST compared to previous instruments allows to match the long-wavelength emission with its short wavelength counterpart. The stretch in each image is adjusted for optimal readability. The white contours correspond to the FORCAST 37 μ m emission [mention the contour levels].

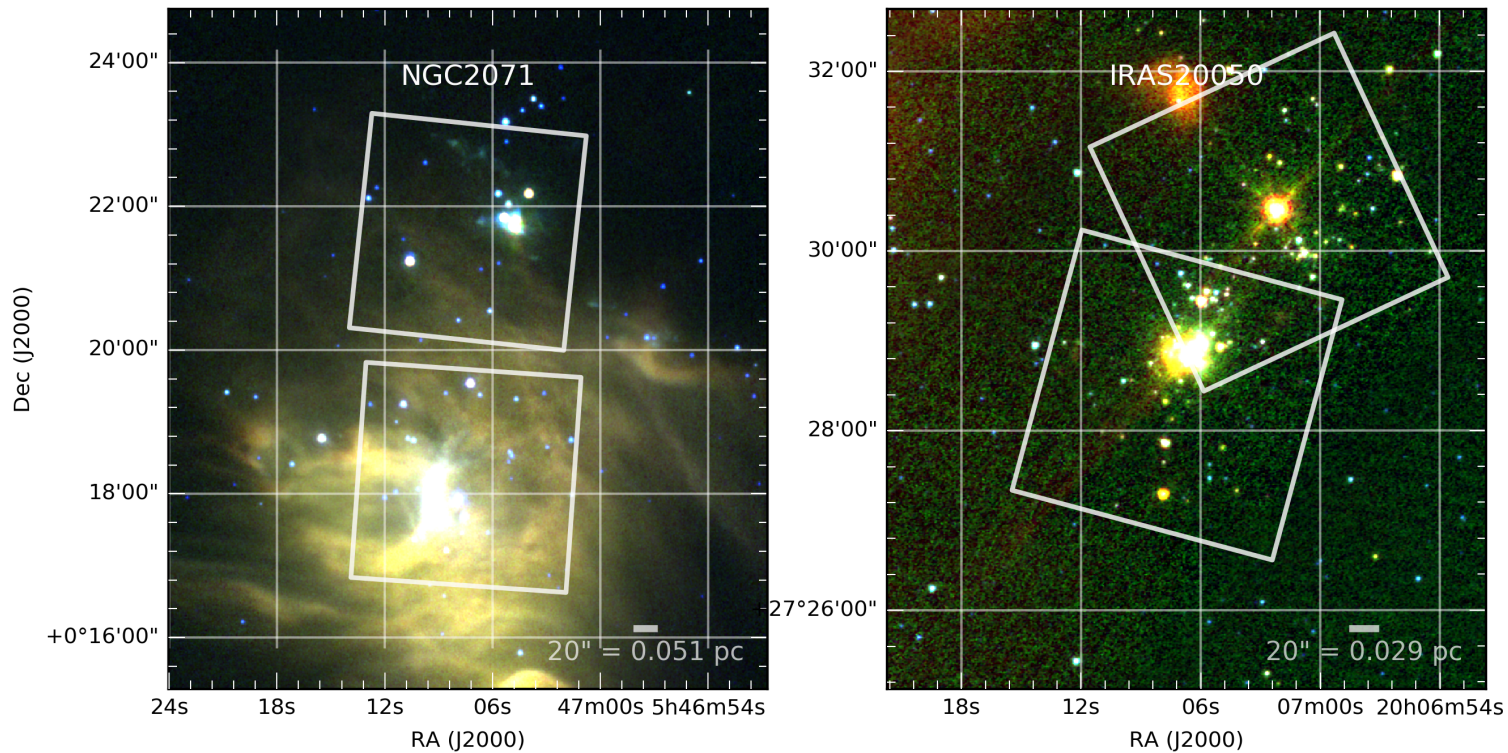


FIGURE II.10: IRAC 3-color images of NGC2071 and IRAS20050+2720.

8.2 NGC 2071

The NGC 2071 star-forming region is one of several active areas of star formation in the northern part of L1630 giant molecular cloud which is located at a distance of 390 pc (Anthony-Twarog, 1982). NGC 2071 itself is a reflection nebula. The NGC 2071 infrared cluster, located about 4' north of the reflection nebula, is a region of intermediate mass star formation (Strom, Strom, and Vrba, 1976; Persson et al., 1981; Butner et al., 1990). Maps of the cloud in CO and its isotopomers (Buckle et al., 2010) show a large scale clump with $\sim 1,000 M_{\odot}$ associated with the cluster. Dust continuum emission at $\lambda=0.85$ and 1.3 mm peaks on center of the cluster extending 1' in diameter containing $30 M_{\odot}$ of gas and dust (Johnstone et al., 2001; Mitchell et al., 2001; Launhardt et al., 1996). Emission from CS in the J=2-1 through J=7-6 indicate that the gas in this region is centrally condensed with a density of 10^6 cm^{-3} (Zhou, Evans, and Mundy, 1990).

There are a number of near infrared surveys of the young cluster (e.g., Strom, Strom, and Vrba, 1976; Lada et al., 1991; Megeath et al., 2012; Spezzi et al., 2015). Spezzi et al., 2015 identify 52 YSOs associated with the NGC 2071 cluster, with the majority Class II sources. Flaherty and Muzerolle, 2008 estimate an age of ~ 2 Myr for the cluster, consistent with the large fraction of Class II sources (Evans et al., 2009). The brightest far infrared emission from the cluster is associated with the IRS1 region (Harvey et al., 1979; Butner et al., 1990), which has an estimated total luminosity of $520 L_{\odot}$. The immediate region of IRS 1 is, in fact, home to a number of YSOs that are infrared, X-ray, and radio sources (Skinner et al., 2009; Carrasco-González et al., 2012; van Kempen et al., 2012). The radio (Carrasco-González et al., 2012) and H₂ emission line imaging indicate that IRS 1, IRS 2, IRS 3, and, perhaps, VLA 1 are YSOs with outflows. The larger scale molecular outflow

associated with this region is well studied in a number of molecules (Bally, 1982; Chernin and Masson, 1993; Stojimirović, Snell, and Narayanan, 2008).

Figure ?? shows the Spitzer 3.1 μm image of the IRS 1 region on the left (image from Spitzer Archive: Megeath et al., 2012) and the Herschel 70 μm image on the right (image from Herschel Archive: Gould Belt Project, P.I. André). The plus marks in both panels indicate the position of the brighter YSOs: IRS 1, IRS 2, IRS 3, IRS 4, and VLA 1. The inner red circle with a diameter of 26" indicates the extend of the saturated region in the Spitzer MIPS 24 μm image; the outer red circle, diameter 60", encompasses the region with strong imaging artifacts in the MIPS 24 μm image. The right panel shows Herschel 70 μm image which does not resolve the emission from IRS 1, IRS 2, IRS 3, and VLA 1. The centroid of the 24 μm and 70 μm emission is between IRS 1 and VLA 1 indicating that several of the sources are contributing to the total observed emission. Interferometric observations show that the millimeter wavelength dust emission is dominated by envelopes associated with IRS 1 and IRS 3, with estimated masses of 8.2 and 12.3 M_{\odot} material, respectively (van Kempen et al., 2012). The millimeter emission also reveals the presence of disks with radii ≤ 100 AU associated with IRS 1 and IRS 3 (van Kempen et al., 2012).

The luminosities and masses of the individual source, IRS 1, IRS 2, IRS 3, and VLA 1, are not known. The Spectral Energy Distributions (SEDs) shortward of 10 μm support their identification as embedded YSOS (Skinner et al., 2009). Skinner et al., 2009 gives a clear discussion of the possibilities for IRS 1 and concludes that it is likely a mid-to late B star. van Kempen et al., 2012 find luminosities of 10, 3.4, and $\leq 27 L_{\odot}$ for IRS 1, 2, and 3, respectively, and stellar masses of $\leq 1 M_{\odot}$ for each, based on SED fitting. These masses and luminosities are not consistent with estimate of the total luminosity of the region of $520 L_{\odot}$ (Butner et al., 1990). The far infrared images from Herschel reveal that

IRS 1 alone does not totally dominate, as seen in Figure N; IRS 1, VLA 1, and IRS 3 likely make substantial contributions to the emission with lesser emission from IRS 2 and IRS 4.

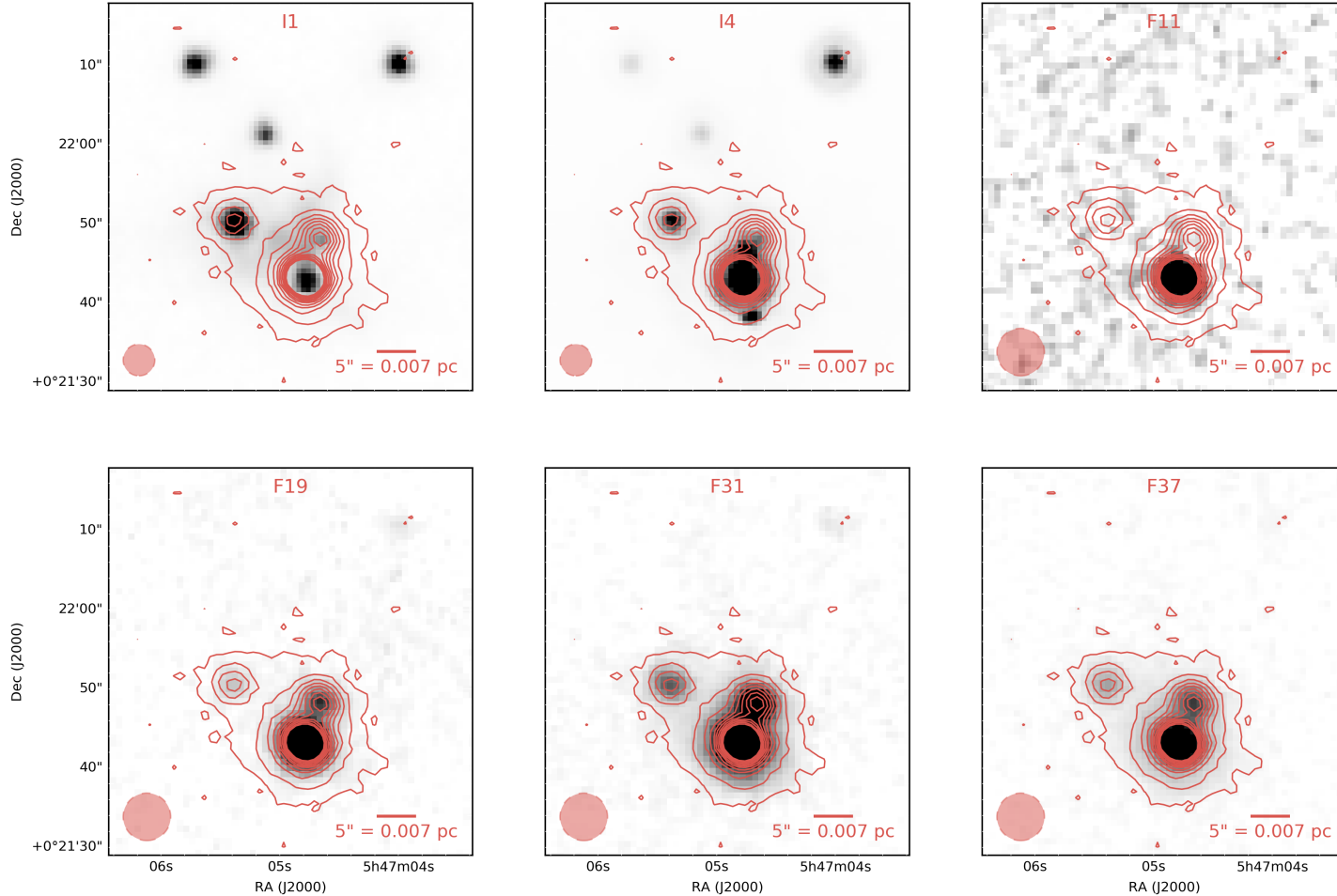


FIGURE II.11: The core of NGC2071 is seen in two bands of the *Spitzer* IRAS instrument ("I1" and "I4"), as well as with the four FORCAST bands. The increased resolution of FORCAST compared to previous instruments allows to match the long-wavelength emission with its short wavelength counterpart. The stretch in each image is adjusted for optimal readability. The white contours correspond to the FORCAST 37 μm emission [mention the contour levels].

Chapter III

The Balloon Experimental Twin Telescope for Infrared Interferometry

1 Towards higher angular resolution in the far-IR

Observations at mid- to far-infrared wavelengths from the Earth’s surface are extremely limited by the large atmospheric opacity in this region of the spectrum. Space-based telescopes like IRAS (12-100 μm ; Neugebauer et al., 1984), ISO (2.5-240 μm ; Kessler et al., 1996), *Spitzer* (3.6-160 μm ; Werner et al., 2004), AKARI (1.7-180 μm ; Murakami et al., 2007), WISE (3.4-22 μm ; Wright et al., 2010) and *Herschel* (55-672 μm ; Pilbratt et al., 2010) have demonstrated the scientific value of observations at these wavelengths; but the spatial resolution of space-based observatories is limited by the cost and complexity of building and flying progressively larger aperture telescopes.

High-altitude platforms are a good compromise between ground and space observatories: while less sensitive because of the surrounding thermal emission from the atmosphere, they can still feature larger optics and payloads, more experimental setups, and instrumentation that can be changed on a more frequent and significantly less costly basis.

BETTII is an experiment that aims at breaking from the single-aperture paradigm by using interferometry between 30 and 90 μm from a balloon platform. Interferometry is commonly used on the ground at other wavelengths such as optical and radio, and is a viable path forward to obtain much higher resolution than what single apertures can provide. In the rest of this introduction, we will briefly describe the fundamentals of interferometry and discuss key design points for BETTII.

In this work we focus on the particular technique called *spatio-spectral interferometry* (Mariotti and Ridgway, 1988), which is a way to achieve high angular and moderate spectral resolutions at far-IR wavelengths from above the atmosphere, without the cost and limitations of large single apertures.

2 BETTII description

As a cryogenic payload flying at an altitude of 37 km, BETTII is the first flying "direct detection" interferometer: it will attempt to coherently combine light from two different telescopes to provide increased angular resolution. Because it is operating from above the atmosphere, it can see the far-infrared universe between 30 and 90 μm , and provide 0.5"-1" spatial resolution at these wavelengths - a key region of parameter space well-suited to study protostars evolving in dense clustered environments.

To provide this resolution which matches that of JWST at 25 μm , BETTII needs to be have two collectors separated by $\sim 8 \text{ m}$; Because of its operating wavelength, it needs to have a cryogenic instrument; because it is an interferometer, it needs optics with exquisite surface quality; and because it flies on a balloon platform, it needs to be robust to large changes in temperature, large pointing errors, and severe shock resistance for the landing phase.

Throughout this chapter, we will first discuss the basics of double-Fourier interferometers, before presenting the general design of BETTII payload and most of its subsystems.

3 Basics of interferometry

Since the end of the 19th century with Michelson [reference], scientists have learned how to use the wave properties of light to learn about new astrophysical phenomena. It did not take long for what first started as a laboratory experiment by Michelson and Morley [cite] to be applied to astronomy, with the Michelson Stellar Interferometer experiment.

The principle of interferometry is simple. Because light behaves like a wave, two beams of light coming from the same source can be combined *coherently*, provided that their amplitudes and phases are controlled. The intensity of the combined signal is a function of a) the brightness of the light beam, but also b) the relative phase and wavefront of each beam, which can create a modulation of that brightness.

Michelson and Morley created what became the standard Michelson interferometer (Fig. III.1). It uses one single source of light and a beam splitter that creates two coherent light beams from that one source. The two light beams go through two separate *arms* before being recombined. While adjusting the length of one arm with respect to the other, we modulate the phase difference between the two arms, leaving everything else the same. This creates a modulation called an *interferogram*, which describes the measured intensity variation as a function of the phase difference between the two arms.

The phase difference is expressed in radians and depends on the wavelength of the light that is used. In this work, we will usually refer to this difference in terms of an actually physical distance instead: the optical path difference (OPD). This has the advantage of being wavelength-independent and relate more easily to opto-mechanical considerations.

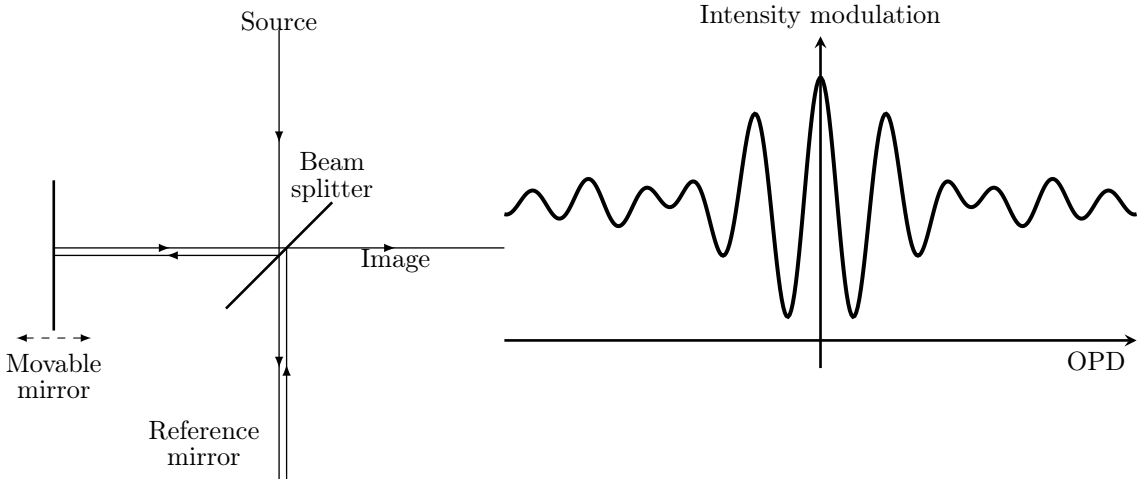


FIGURE III.1: A Michelson interferometer.

3.1 Fourier transform spectroscopy

One immediate consequence of the original Michelson experiment is to realize that the interferogram actually contains spectral information. For an ideally monochromatic source, the intensity modulation (or *fringe*) depends on the OPD only modulo a wavelength. This means that the modulation is identical whether we introduce an $\text{OPD} = \lambda$, or $\text{OPD} = n\lambda$, where n is an integer. This is because the monochromatic wave can essentially be represented by an amplitude times a cosine function of phase (or a cosine function of $2\pi\text{OPD}/\lambda$).

The intensity of modulation for a given wavelength is then a cosine wave as well, with an amplitude related to the intensity of the signal, and a wavelength equal to the wavelength of the incident light.

If we consider a polychromatic signal as a sum of monochromatic wavelengths, this phenomenon happens for each single wavelength, and the resulting intensity modulations add *coherently*: the total intensity is the coherent sum of the intensity modulations created by each individual wavelength. This has the effect of smearing the resulting modulation

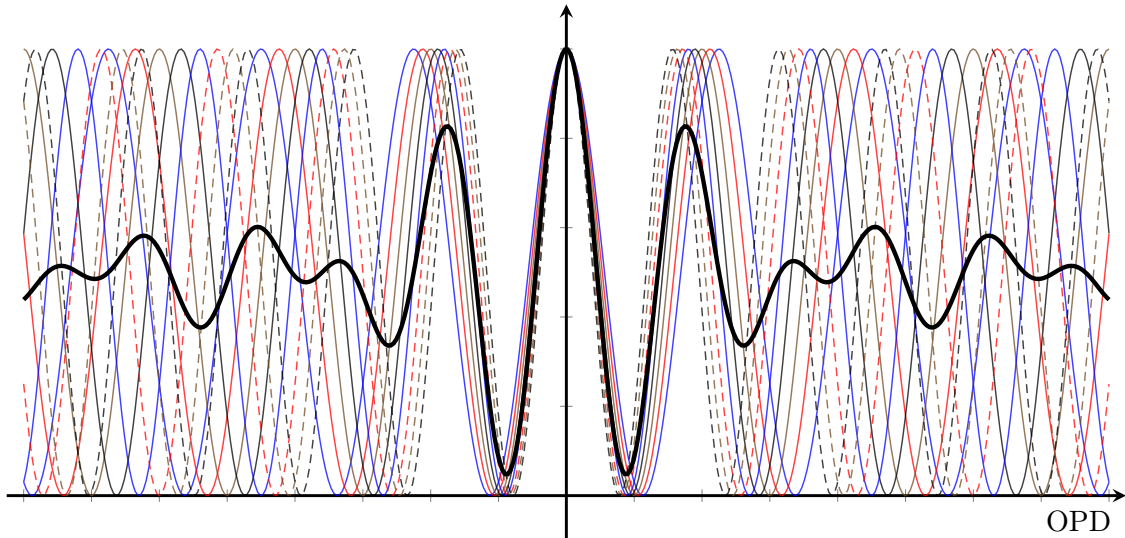


FIGURE III.2: An ideal interferogram here is shown as a sum of cosine waves of different frequencies.

in most places except around the precise location where the OPD is zero. Around this location, the modulation is not wavelength dependent, and fringes are always seen. These are commonly referred to as *white light fringes*. The range of wavelengths in which fringes can be seen is called the *coherence length* L_c . When all wavelengths are weighted equally in a bandpass $\Delta\lambda$, the coherence length can be expressed as:

$$L_c = \frac{\lambda^2}{\Delta\lambda}, \quad (\text{III.1})$$

and the interferogram can be represented by a carrier frequency modulated by an envelope function:

[add equation for the integral of interferograms]

Since the modulation is a coherent superposition of cosine waves, it contains spectral information. A cosine transform of the interferogram will decompose the contribution of each individual wavelength, hence reproducing the spectrum of the polychromatic source. This realization has led to many scientific discoveries in astronomy, chemistry and other

fields over the last 100 years.

[Add picture of Mach-Zehnder testbed from second year project]

3.2 Aperture synthesis

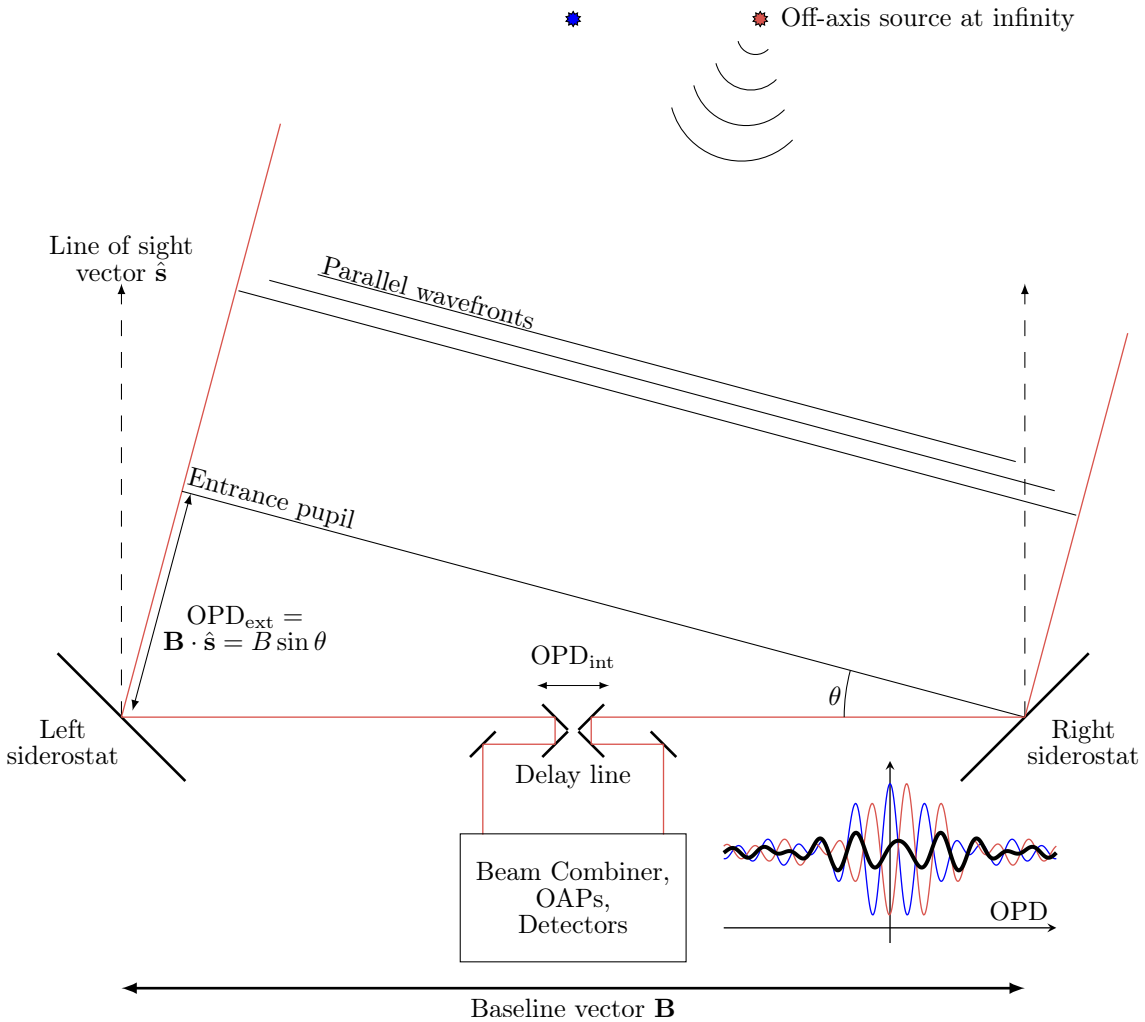


FIGURE III.3: A Michelson Stellar interferometer.

An interferogram is produced by coherently combining photons from one single source of light. This can be applied for example for an infinitely far astronomical source: as the light propagates from the source, by the time it reaches our instrument the radius of curvature of its wavefront is extremely large, and the latter can be approximated as being flat. The photons from this source nominally enter each arm of the interferometer

with the same phase, when the alignment is perfect. When combined, these photons would interfere and create an interferogram.

However, let's suppose that a second source is sufficiently far away from the first source that its wavefront enters the interferometer at an angle. This means the photons from the second source enter one arm slightly later than the other - or that photons need to cross more optical path in one arm than in the other. These photons would also create an interferogram, but the latter will be centered about a different position in OPD space than the interferogram created by the photons from the first source. Now let's suppose that the second source is exactly as bright as the first one, and that it is apart from the first by an angle θ such that $\mathbf{B} \sin \theta = \lambda/2$. In this case, the interferogram created by the photons from the second source has the same amplitude as the first interferogram, but is shifted by half a wavelength in OPD. As a result, the two interferograms would exactly cancel each other, and we would say that the *spatial degree of coherence* between the two sources is zero. Although the sources are not coherent in the strict sense because they are completely independent sources, the intensity modulation (or interferograms) caused by each source would, in this case, cancel out. If the angular separation was such that $\mathbf{B} \sin \theta = \lambda$, then the modulations would add up and the resulting modulation would have twice the amplitude of that with just one single source. We would say that the spatial degree of coherence between the two sources is unity.

One way to formalize this important property is to consider an interferometer with a given baseline length and angle as a filter of the source's spatial distribution on the sky. For a given baseline length and angle with respect to the sky, the interferometer is only sensitive to a single angular frequency in a single direction on the sky. Various sources observed simultaneously by the interferometer will all contribute to a single measured

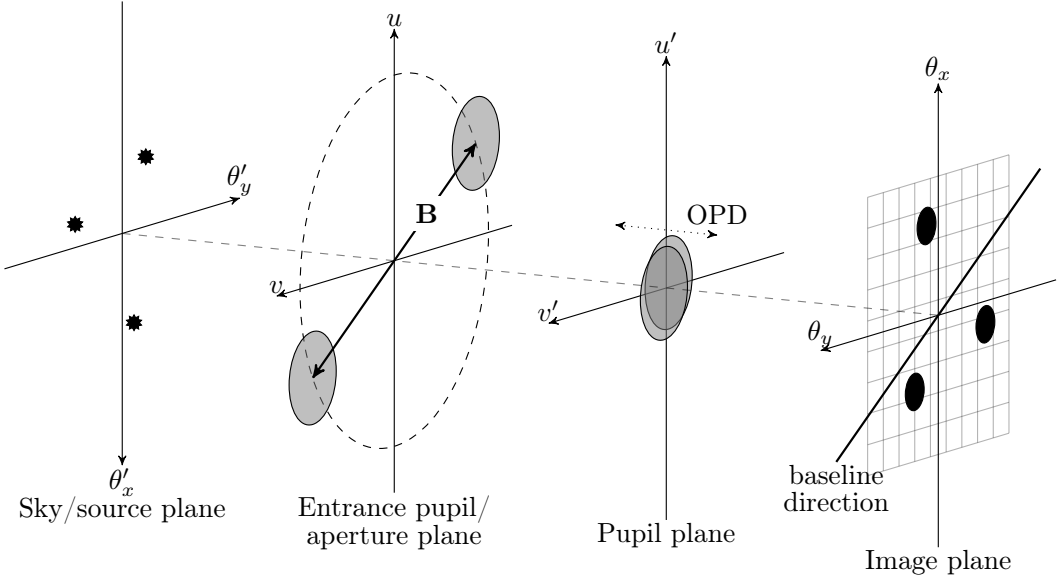


FIGURE III.4: Relevant planes in the optical train for aperture synthesis.

interferogram (or intensity modulation), which can be characterized in terms of the spatial degree of coherence, also called *complex visibility*, between the sources for a given baseline angle and length.

The generalization of this property is called the Van Cittert-Zernike theorem: the 2D Fourier transform of the intensity distribution on the sky is its complex visibility function. In other words, by mapping the complex visibility (through measuring interferograms) for all baseline angles and lengths, we can reconstruct the original image through an inverse Fourier transform. The plane of complex visibilities is commonly referred to as the (u,v) -plane [CITE THOMPSON 2008].

Interferometry and aperture synthesis is used commonly at radio wavelengths, where coherent detectors can obtain the direct phase of the incoming light by mixing the signal with a local oscillator. Both the amplitude and the phase of the signal can be recorded for each antenna, and can be combined with all the other antennas at a later time.

Aperture synthesis has also been achieved at optical and near-infrared wavelengths, where a nearby guide star is used to determine a reference phase of the incoming beam.

The fringe patterns measured for the science sources can then be non-ambiguously aligned with each other. This process requires very rapid imaging capabilities (on the order of 10 ms, a typical atmospheric coherence timescale) to freeze the atmospheric variations across the synthetic aperture. This requires bright guide stars. In addition, because of the large baselines, the field of view is very limited, so the targets accessible by optical interferometers are limited to scientific sources which are a few arcseconds of a bright guide star: this dramatically limits the capabilities of ground-based interferometry at these wavelengths.

3.3 Double-Fourier interferometry

In this work, we introduce the concept of Double-Fourier interferometry, which uses a standard Fourier Transform Spectrometer at the back-end of a Michelson stellar interferometer (see Fig. III.5 and Mariotti and Ridgway (1988)).

We adopt a Michelson interferometer configuration that we use in pupil-plane combination. Unlike image-plane combination, where fringes are seen across a single Airy disk in the image plane, no fringes are visible across the field of view for a given OPD. Instead, the intensity of the entire field of view is modulated as a function of OPD.

By scanning the OPD, we obtain a modulation of each pixel on the detector, which combines information on both the spectral (through the Fourier transform of the scan) and the spatial (through the amplitude of the fringe packet) content of the source, at that baseline orientation and length. By repeating the measurement over multiple baseline angles and lengths, one can unambiguously retrieve both the spatial and spectral content of the astronomical scene.

Pupil-plane combination allows for an interferometric response of the entire field of

view. The price we pay is that the OPD scans need to be longer in order to cover enough spectral range for each pixel in the field of view. For a single-pixel detector, the OPD scan would only need to cover enough stroke to obtain the desired spectral resolution over that one single pixel.

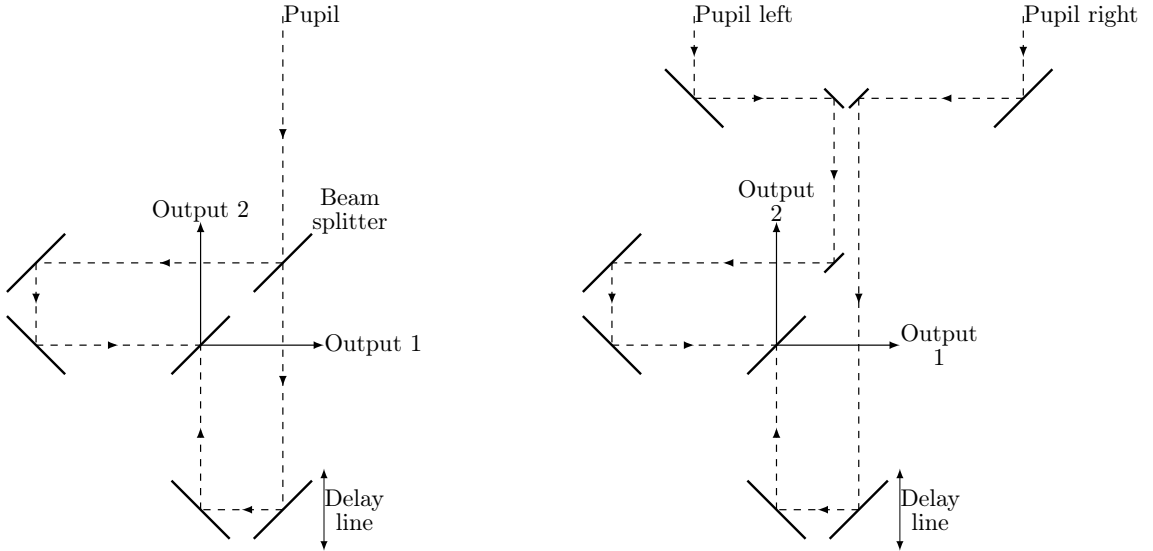


FIGURE III.5: Standard FTS telescope layout (left) versus double-Fourier telescope layout (right) (Mariotti and Ridgway, 1988).

4 BETTII Instrument design

The BETTII payload is an 8 m fixed-baseline interferometer, equipped with 2 50 cm siderostats. It operates in two wavelength bands, 30-55 μm and 55-90 μm . In these two bands, its theoretical angular resolution is 0.5'' and 1'', respectively. This is significantly better than all existing or previous facilities that operate in the far-infrared, which have traditionally been limited by the mirror size. In addition, this matches the resolution of JWST at 25 μm , hence providing a good continuity to probe astrophysical phenomena at longer wavelength but with the same linear resolution.

There are four major components to BETTII: the mechanical structure and design; the optics and their mounts; the cryostat and the detectors; and the control system. The latter will be discussed extensively in chapter V. In this section, we first describe the balloon environment and its constraints, before discussing the three remaining components of BETTII.

4.1 Stratospheric balloon environment

High-altitude balloons have for many years served as a test platforms for future space instruments, such as the FIRAS instrument on COBE (**Fixsen:2002jv**). These balloon platforms fly between 30 and 40 km, above more than 99% of the atmosphere, which make them particularly well suited for studying the universe at infrared, far-infrared and sub-millimeter wavelengths. Balloon launches occur year-round across all continents, including Antarctica. NASA and other agencies, which allows balloon flights that can last for multiple weeks.

For a typical launch, the scientific payload is attached on the bottom of a train of about 100 m that includes a parachute and a ladder. The top of the ladder attach to the bottom of the large helium-filled balloon.

At float altitude, the air temperature is between 230 K and 250 K, while the air pressure is down to 0.5% of the sea level pressure (about 5 mbar). Upper altitude winds are large-scale laminar flows that move the balloon and the payload as one. This can excite pendulum motions about the pivots underneath the balloon and at the top of the payload, which are typically of the order of a few arcminutes and have periods of a few to many tens of seconds (Fixsen et al., 1996a).

The payload's temperature and temperature distribution is influenced by the air



FIGURE III.6: Picture of a balloon launch. The payload is captured by the launch vehicle (in yellow) until the balloon is inflated and released. The parachute assembly, which is a part of the long train from the top of the payload to the bottom of the balloon, can be seen in red. Credit: NASA.

temperature, the infrared radiation of the Earth, and the sunlight, which can result in complex temperature gradients across the instrument. A better temperature uniformity is expected for night flights, which is what BETTII is expecting.

Balloon experiments can also be affected by cosmic rays which can damage the electronics, lead to data corruption and or failures of the software/control system. However, this becomes more of an issue for long-duration balloon flights around Antarctica, during which the payloads are exposed for many weeks to the cosmic ray environment.

BETTII is expected to launch from Fort Sumner, NM, for its first engineering flight. After a morning launch, we expect to wait until nightfall to achieve proper thermal stabilization and achieve our science goals. We expect the flight to last about 16 h, although this is highly dependent on the weather and wind patterns.

4.2 Mechanical design

BETTII has two main structures. The first is a carbon fiber and steel truss that is used as our optical bench. This was the first item that was designed in the project. The elements of this structure are built by bonding 7.5 cm carbon tubes to custom-made steel nosecones. The steel nosecones are lightweight and strong, and have a threaded hole on the axis: they attach to multi-faceted steel nodes like tinker toys. There are three lengths of tubes on the truss. At the interface between the nosecone and the nodes, spherical washers or polypropylene washers are used, depending on the location on the payload. The difference of material compensates for differential thermal contraction on the beams that form the long side of triangles.

The structure is about 9 m long. It is designed to be lightweight, strong, and have a first resonant mode above 20 Hz to ensure fast damping of residual mechanical oscillations. This property was measured and the predicted resonance was found to be within 1 Hz of its expected frequency, at 25 Hz.

The entire balloon payload needs to be robust to handle 10 g vertical force and 5 g force at 45 deg. With an expected total mass of 1000 kg, we need yield strength sufficient to hold 100 000 N of force.

The gondola is what holds the truss and attaches to the balloon train. It also holds the electronics, reaction wheels, batteries, and communications to the ground. The frame is made out of 80/20 T-slotted aluminum bars that are attached together using T-inserts, and reinforced by screwed-on corner plates. The precision of this payload is of no importance to the optical alignment.

[NEED annotated picture of BETTII]

The various electronic components of the system are attached to the gondola using aluminum or honeycomb aluminum plates, which are painted with white appliance paint for better thermal behavior. These plates act as radiator panels which allow us to dissipate the heat out to space.

The most critical portion of the gondola is the assembly that connects to the balloon train. This holds a single pin that needs to have the highest yield strength, since it is the only point of the payload that needs to support the entire weight. A more detailed description of the pin is presented in Section 1.2.4.

4.3 Warm optical system

The optical system was one of the most challenging design aspects of the project. It is beyond the scope of this work to go into details about all the considerations that went into the design, but we will review some of the main aspects: the overall optics layout, and the fabrication of the telescope assemblies.

4.3.1 Optics layout

Because the nature of balloon payloads, there can be extensive damage to the structure during parachute opening and landing. In order to minimize the repair costs from one flight to the next, it was decided to place the telescope assemblies - which are expensive, long lead-time items - away from the edges of the truss.

Instead, flat mirrors are used to redirect the light towards the telescope assemblies, which are kept close to the center of the truss where damage is expected to be minimal.

The telescope assemblies consist of 3 powered mirrors and a folding flat. They provide a 20:1 compression ratio of the beams with reasonable tolerance on the mirror

positioning. As an all-aluminum assembly, they shrink homologously as the temperature varies during the different phases of the flight, hence maintaining optical prescriptions.

In order to perform double-Fourier interferometry, an asymmetry needs to be introduced in the system in order to properly combine the polarizations of the light at the beam combiner. This asymmetry occurs after the telescope assemblies and before entering the cryostat. In one arm, a 3-mirror assembly (called the K-mirror assembly, or KMA) is used on a rotating stage to properly de-rotate the field of view as the telescopes change elevation. On the other side, a 4-mirror delay line assembly (called the Warm Delay Line, or WDL) is set at a fixed orientation. Its role is to compensate for the optical delays caused by the residual pointing errors.

On both the KMA and the WDL, one of the mirrors is actuated in tip and tilt, and provide the fine control required to properly overlap the two beams [discussed in section...]

[Show picture of the optics train]

The beams of light enter the cryostat through a thin polypropylene window. We tested different window thicknesses and selected the 15 μm thickness as our baseline design. Test pieces with this window have been shown to comfortably resist about 1.5 times the atmospheric pressure, even after 50 cycles of pressurization. The number is a little smaller when the pressurization occurs very rapidly and do leave time to the window to deform elastically. A number of tests were done on identical batches of windows to ensure the repeatability of our test method.

4.3.2 Optics manufacturing

Despite working at relatively long wavelengths, the tolerance in the surface figure of all the mirrors is an important consideration. Traditionally, figure errors are specified in

terms of the required beam quality at in the focal plane, which starts to degrade when the wavefront errors in the optical train are comparable with the wavelength of the light beam, or introduce specific aberrations such as coma. In interferometers, the fidelity of the final image is not a priority. However, differential wavefront errors between the two optical trains before combination will result in decreased contrast of the interferograms. As a result, the surface quality of the mirrors pre-combination needs to be much lower than a wavelength of light, since errors will stack after hitting many mirrors from both sides. For our specifications, we determine that a 300 nm r.m.s surface figure error over the entire aperture is sufficient to ensure decent scientific results. This requirement is difficult to match for the largest elements in our optical train (the siderostats and the primary mirror) - but smaller mirrors pose less of a challenge in their manufacture. It is important to mention that figure errors are a concern for us because we are using all-aluminum optics, as opposed to more traditional materials such as glass which are easier to polish.

The company Nu-Tek, in Aberdeen, MD manufactured all of our small optics out of aluminum. The procedure includes an initial milling process, heat treatment, followed by diamond turning and gold coating to avoid oxidation.

However, very few manufacturers in the United States were able to diamond-turn the siderostats and the primary mirror assembly, while ensuring the level of surface figure we needed. The diamond-turning process uses a slowly moving diamond blade that is controlled in 3 axes to carve out the required shape. This process requires extreme temperature stability, which is often not available in traditional machine shops.

The Department of Advanced Manufacturing at North Carolina State University was able to manufacture our mirrors by meeting all of our requirements. The results are published in [REF to JATIS paper]. Each telescope assembly has a stacked RMS surface

figure error of [], while the siderostats have []. The siderostats are more complicated because they did not exactly fit in their diamond-turning spindle. We decided to proceed with a two-step diamond turning, where they turned two sections of the ellipse consecutively. This does not guarantee that the two areas will be at the same height since they have to unmount the mirror off the spindle. However, our models show that even if different sections of the mirrors are at different heights, the beam combination can still be successful, as the parts of the pupil that are shifted in one arm are also shifted in the other.

4.4 Cryogenic instrument

The cryostat was designed by our team. Items were sent out for manufacturing to different companies and assembled in house. The cryostat is passive and does not require any mechanical cryo-cooler. It is designed to operate for a duration of 40 h, which should give us enough margin considering the typical lengths of balloon flights from the U.S. of about 16 h.

The fridge is a ($^3\text{He} + ^4\text{He}$) sorption refrigerator from Chase Research that cools down the main optical bench to 4 K. It also has an intermediate cold finger at 1 K and a final stage that brings down the detector temperature to 300 mK.

At the heart of the instrument are four 9×9 close-packed linear arrays of multiplexed superconducting transition edge sensors (TES) bolometers [REF Benford et al. 2008] incorporating the Backshort Under Grid (BUG) architecture [REF Allen et al. 2006]. These arrays are scaled versions of similar arrays already built for ground-based instruments (e.g., GISMO: REF Staguhn et al. 2006, 2014). Detectors are read out using advanced linear SQUID multiplexer and amplifiers. A 4×22 multiplexed readout is used for each array; the extra seven channels are used for calibration signals (unilluminated pixels, “dark

SQUID” channels, and an “always on” channel), allowing monitoring of all potential noise contributors [REF de Korte et al. 2003].

The optics inside the cryostat include two sections: a near-infrared fine guidance sensor, and the far-infrared channels which lead to the science detector. The incoming light beam is split right after entering the cryostat with a NIR/FIR dichroic beam splitter. This custom-made filter reflects off the far-IR and transmits the near-IR, and its recipe was suggested by P. Ade at Cardiff University. At the bottom of the cryostat, in the 77 K volume, the fine guidance sensor is composed of N optics and one H1RG detector [REFERENCE].

At the top of the cryostat and attached to the 4 K cold plate, there is a cold optics bench that holds all of the far-IR optics, filters, and the Cold Delay Line. All filters were manufactured by Cardiff University in the U.K. The layout of the optical system is shown in Figure [], and more details can be found in [REF ARNAB’s SPIE PAPER].

4.5 Data products & analysis

Once in flight the payload operations consist of pointing at a target, stabilizing the attitude motions, and scanning the delay while recording detector data. A number of operational modes are required to ensure we reach this stable observing stage, and are described in more details in Chapter V.

Individual scans will last for a nominal duration of 3 s, and consist of 1024 individual detector frames, which are matched to a given OPD. To increase the signal-to-noise ratio (SNR), we expect to stack 10 min worth of data, which corresponds to 200 scans. For this duration, we expect that the change in the baseline angle due to the rotation of the Earth

is negligible. It is critical to correctly stack the interferograms, as OPD errors from scan to scan can significantly reduce the fringe contrast (see Chap. IV).

To describe post-processing, let's consider a 10 min cube which is the OPD-corrected stack of images from the 200 individual scans. The cube has a crossection of 9×9 , and a depth of 1024 frames. For each frame, the intensity of each source in the detector is determined for each OPD, and combined into interferograms. We repeat the process for the same field observed at different baseline angles.

The set of cubes are fed to an inversion algorithm that was developed in Dr. Juanola-Parramon's Ph.D. thesis [REFERENCE], which provides a final datacube corresponding to the images as a function of wavelength, with the spectral resolution that the user chooses.

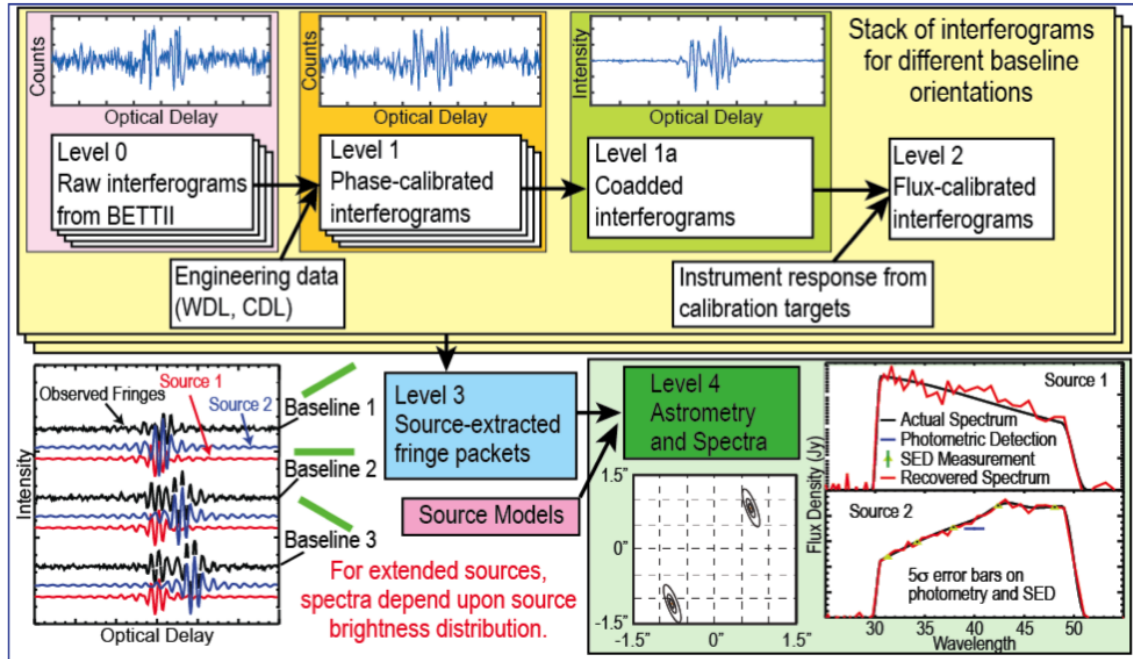


FIGURE III.7: BETTII data processing steps.

5 Sensitivity analysis

Early in my involvement with BETTII, I led the effort in trying to estimate the sensitivity of our instrument, in order to select relevant scientific targets, but also find astronomical calibrator objects which would help us understand the systematics of our payload.

In this section, we summarize our findings and give details on the methods and equations we used. Since only very few authors have approached the problem of double-Fourier interferometers, we were able to derive a new formalism to estimate the spectral sensitivity of double-Fourier interferometers for point sources. Our method uses propagation of gaussian errors through Fourier transforms, and is described in detail in Chap. IV. This can be useful to determine the sensitivity of other types of instruments, such as a space-based follow-up of BETTII, which we briefly discuss in the conclusion of this work.

5.1 Instrument and observing parameters

Table III.1 represents the key instrument parameters that are relevant for the sensitivity estimation of the two science channels of BETTII. Some of these parameters are user inputs (such as the aperture size), and some are already derived. A detailed, custom calculator tool uses a few user inputs to provide a number of instrumental properties, which in turn serve as design baseline for various subsystems. For example, the "OPD range required" is a derived output, depending on the baseline length, the field of view and the required spectral resolution.

TABLE III.1: Instrument design parameters for BETTII.

Parameter	Value	Units
Input aperture	0.196	m ²
Baseline length	8	m
Detector pixels	9 × 9	pixels
Detector quantum efficiency	70 %	
Integration time per full frame	2.5	ms
Number of data points in one scan	1024	points
OPD range required	8.2	mm
Time per u,v point	10	min
	Band 1	Band 2
Central wavelength	40	82
Fractional bandwidth	62.5 %	54.9 %
Etendue per pixel	8.2×10^{-10}	1.8×10^{-9}
Estimated efficiency	34 %	34 %
Required spectral resolution	10	$\lambda/\Delta\lambda$
Pixel angular size	13.32	arcsec
Full width half max	17.31	arcsec
Field of view	2.00	arcmin
Number of samples per fringe	4	8.2

5.2 Far-IR background noise estimation

We proceed to an estimation of the known far-IR background noise contributions from sources in thermal equilibrium. We assume that each source of noise emits like a Planck function B_ν with a certain emissivity ϵ . In Table III.4, we list the number of photons generated per second for the amount of sky seen by a single pixel. The thermal emission is weighted by the normalized transmission function, which was measured in the laboratory (Fig III.8). By far the strongest contributors from our system are the warm optics and the cryostat's polypropylene window.

Noise source	T (K)	Emissivity	Photons s ⁻¹ Band 1	Photons s ⁻¹ Band 2	Reference
Warm optics	240	0.1	1.38×10^{11}	9.97×10^{10}	Assumes 99% per

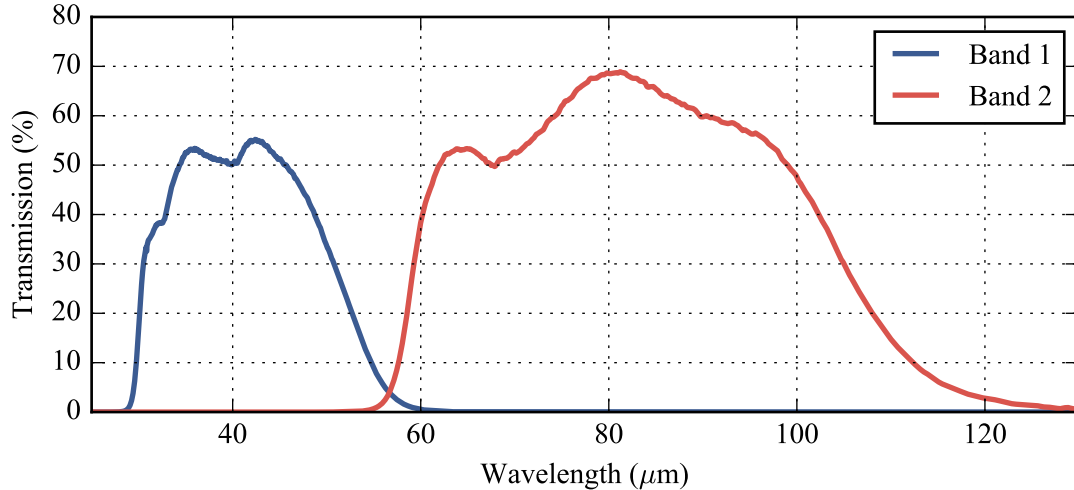


FIGURE III.8: BETTII total transmission curves from all cold filters, excluding the beam combiner, cryostat window, and NIR/FIR dichroic.

$0.07 \text{ W m}^{-2} \text{ sr}^{-1}$ for band 1 and 2 respectively. This corresponds to $2.6 \times 10^{10} \text{ photons s}^{-1}$ and $5.2 \times 10^{10} \text{ photons s}^{-1}$, respectively.

To know how much power is actually reaching the detectors, we need a measurement of our optical throughput. The throughput is the product of the efficiencies of the various elements along the optical train: the mirrors, the cryostat window, the NIR/FIR dichroic, and all the cold filters. The latter sum up to the transmission profile shown in Fig. III.8), which we call \mathcal{T}_{bp} . We write $f_{\text{arm1-}>\text{detN}}$ (resp. $f_{\text{arm2-}>\text{det1}}$) the throughput of light from arm M (resp. arm 2) falling on the detector N, where $N = 1,2$:

$$f_{\text{arm1,2-}>\text{det1,2}}(\lambda) = \tau_{\text{combiner}} \mathcal{T}_{\text{bp}}(\lambda) \tau_{\text{window}} \tau_{\text{dichroic}} r^{N_{\text{mirrors}}} \quad (\text{III.2})$$

$$\approx 0.38 \times \mathcal{T}_{\text{bp}}, \quad (\text{III.3})$$

where we have used lab measurements to estimate $\tau_{\text{window}} \approx 0.98$, $\tau_{\text{dichroic}} \approx 0.95$, $\tau_{\text{combiner}} \approx 0.5$ and $r \approx 0.99$ is the far-IR reflection of each warm mirror. There are

$N_{\text{mirrors}} = 9$ within the warm optics train on the left side, and 8 on the right side. Until we obtain precise measurement of the throughput of each element as a function of wavelength, we consider that this extra factor is wavelength-independent and represents an average over the band. This is valid since most of these materials do not have steep dependence at such a long wavelength. For a 50% mean bandpass transmission, this amounts to about to $\sim 15\%$ efficiency for the light coming from one arm falling onto one detector.

Noise source	Power reaching the detector (pW)		NEP ($10^{-16} \text{ W Hz}^{-0.5}$)	
	Band 1	Band2	Band 1	Band2
Warm optics	166	58	12.8	7.6
Atmosphere	33	30	5.6	5.5
Window	32	11	5.7	3.4
Detectors	-	-	3	3
Total	230	99	15	10

TABLE III.6: Estimated power and NEP contributors for a single detector pixel. Note that these are slightly different than the ones cited in Rinehart et al. (2014) and **Rizzo:2015gf** since we now have more precise measurements of the transmission as a function of wavelength.

We approximate the total power per pixel as:

$$P_{\text{pix}} = (f_{\text{arm1-}\rightarrow\text{detN}} + f_{\text{arm2-}\rightarrow\text{detN}}) N_{\text{Photons s}^{-1}} E_{\text{ph}} \text{QE}, \quad (\text{III.4})$$

where $N_{\text{Photons s}^{-1}}$ is the total number of photons per second per pixel from the warm optics, the window, and the atmosphere, which are the three main contributors of noise. We also use the photon energy E_{ph} and detector efficiency of the detector, $\text{QE} \approx 0.7$. Throughout most the design phase of BETTII, this equation was used for the band-averaged quantities, for lack of better knowledge of the exact wavelength dependence of the various optical

components. However, this is also valid on a finer scale and can be integrated over wavelength to provide more accurate estimates. In Table III.6, we used our knowledge of the bandpass transmission and integrate over the band. The Noise Equivalent Power (NEP), a common measure of noise in the far-IR, is calculated as $\text{NEP} = \sqrt{2P_{\text{pix}}E_{\text{ph}}}$. Note that the detectors are designed to contribute less than 30% of the total estimated photon NEP, so that their noise contribution is negligible.

5.3 Interferometric visibility budget

Estimating the noise from each arm separately can help us determine important quantities such as the photon loading and NEP, which can be used to design the detectors. However, the scientific signal from an interferometer also depends on how well the two arms combine. This is roughly a measure of how symmetric the optical system is. In table III.8, we identify two kinds of error contributions: the static contributors, which are caused by differential wavefront errors (WFE), amplitude mismatch, polarization errors and pupil area overlap. These are caused mostly by misalignments of the optics along each train, or by errors in the manufacturing of the mirror surfaces. Second, we have the dynamic contributors, which are caused by OPD errors and differential tip/tilt. These are errors which need to hold over the timescale corresponding to a single data point, so about 2.5 ms. The OPD errors correspond to fast uncorrected motion of the delay lines, while the differential tip/tilt corresponds to an error in co-aligning the two beams at the detector. Note that in Chap. IV, we discuss the various timescales involved with the OPD motions. In this table and for the calculation of the visibility, we only take into account the instantaneous, un-recoverable error in OPD. The error in OPD over longer timescales, resulting in a decrease in SNR as we co-add consecutive interferograms, is not taken into account here.

For reference, the equations are explicitly stated here, as we have found it handy to gather them all in one single place. The derivation for most equations can be found in Lawson (2000).

Term	Symbol	Alloc.	Effect on visibility	V_{loss}	
				Band 1	Band 2
Static contributors					
Total WFE in mirror surfaces	σ_{WFE}	2 μm	$\exp(-[2\pi\sigma_{\text{WFE}}/\lambda]^2)$	0.906	0.977
Amplitude mismatch	R	95 %	$2/(R^{1/2} + R^{-1/2})$	0.999	0.999
Polarization effects	θ	12°	$\cos(\pi\theta/180/2)$	0.995	0.995
Pupil area overlap	f_{overlap}	90 %	f_{overlap}	0.900	0.900
Dynamic contributors					
Error in OPD knowledge	σ_{OPD}	2 μm	$\exp(-[2\pi\sigma_{\text{OPD}}/\lambda]^2)$	0.906	0.977
Differential tip/tilt	σ_{tt}	1.5''	$2J_1(\pi D\sigma_{\text{tt}}/\lambda)/(\pi D\sigma_{\text{tt}}/\lambda)$	0.990	0.998
Total visibility		$\Pi(V_{\text{loss}})$		0.726	0.851

TABLE III.8: Interferometric visibility budget. The dynamic contributors need to hold true for 2.5 ms, and consist of the residual amount that cannot be corrected in post-processing.

5.4 Science channel estimated sensitivity

Now that we know the noise per pixel and the efficiency of the interferometric beam combination, we can determine the SNR for a single source of known flux. For this, we use the formalism by Michell (2005) who derive the proper equation for a matched filter representing a point-spread function (PSF) discretized on a noisy detector array. The efficiency η_{mf} of the matched filter is the inverse of the square root of the effective background area of the PSF, $\beta = 4\pi\mathcal{S}^2$, where \mathcal{S} is the standard deviation of the PSF in

pixels, $\mathcal{S} = \frac{0.42\lambda/D}{\theta_{\text{pix}}}$. We obtain $\eta_{\text{mf}} \approx 0.55$ and 0.39 for band 1 and 2 respectively.

This matched filter efficiency is due to the uneven spread of the light from a PSF onto multiple pixels, and corresponds to the error in fitting the detector to the PSF assuming an even noise floor among all pixels. Pixels with more photons will have more SNR, hence should be weighted more when attempting to extract the flux from the PSF. In this sense, using a matched filter is a best-case scenario. Another approach would consist of simply dividing the PSF area by the area of one single pixel, which is a worst-case alternative that would lead to efficiencies of 0.13 and 0.07 in band 1 and band 2 respectively. In what follows, we are using the optimistic approach and assume we can recover the flux from the PSF using matched filtering.

We define the Minimum Detectable Line Flux (MDLF) as the flux per pixel which corresponds to a $\text{SNR} = 1$:

$$\text{MDLF} = \frac{\text{NEP}}{(f_{\text{arm1->detN}} + f_{\text{arm2->detN}})\mathcal{A}\sqrt{2T_{\text{int}}}}, \quad (\text{III.5})$$

where $T_{\text{int}} = 2.5 \text{ ms}$ corresponds to the integration time per pixel (or detector frame). The MDLF is expressed in W m^{-2} .

The Minimum Detectable Flux Density (MDFD) is the MDLF divided by the bandwidth. This is expressed in $\text{W m}^{-2} \text{ Hz}^{-1}$ and can be converted to Jy.

The faintest detectable interferometric point source with $\text{SNR} = 1$ is then given by $S_{\text{min}} = \text{MDFD}/\mathcal{V}_i/\eta_{\text{mf}}$, where the MDFD is increased due to the interferometric visibility losses and the spreading of the photons onto multiple pixels of the detector. S_{min} represents the smallest flux density that leads to an $\text{SNR} = 1$ within a single scan.

Co-adding consecutive scans will improve the SNR considerably, but it will also

introduces errors and inefficiencies. We quickly realized the impact of systematic errors in co-adding scans, so a significant amount of effort went into understanding the behavior of the various error contributions, and analyzing mitigation strategies. The result of this investigation was published in **Rizzo:2015gf** and is shown here in Chap. ???. In that chapter, we discuss the meaning and importance of the phase noise or OPD noise, and quantify the impact on the sensitivity. The OPD noise arises when residual uncertainties in the knowledge and control of the OPD result in errors while co-aligning and co-adding consecutive interferograms. For the rest of this discussion, we will assume that the OPD noise amounts to $5\text{ }\mu\text{m}$ r.m.s over 200 consecutive scans.

Using the formulas derived in Chap. ???, we can now correctly determine the SNR in the co-added interferograms. However, co-added interferograms are not the only goal of BETTII. Although interferograms allow for the distinction between multiple, nearby point sources, most of the scientific information is retrieved by analyzing the spectrum of each source in the field by taking the Fourier transform of the interferogram. Hence, we want to characterize the spectral sensitivity of the instrument, and establish this metric as the default observing metric for our science.

A summary of the results is presented in Table [REF].

5.5 Tracking channel estimated sensitivity

A similar sensitivity analysis is done for the tracking channel. This is simplified somewhat since the tracking channels consists only of two cameras, and does not involve beam combination. The levels of background noise are less obvious to estimate. We primarily use the findings of Matsumoto, Matsuura, and Noda (1994), which measured $2\text{ }\mu\text{m}$ emission line strengths from balloon altitude. This emission is thought to arise from a thin layer

of OH radicals at ~ 100 km altitude, and is sometimes referred to as *airglow*. Using the measurements by these authors, who span multiple balloon flights in the 60s and 70s, we obtain an average radiance in the NIR bands of $R_{\text{NIR}} \approx 1 \times 10^{-4} \text{ W m}^{-2} \text{ sr}^{-1}$. According to our estimates, this is two orders of magnitudes lower than the brightest astronomical noise source in the NIR, which is the zodi scattering.

Balloon altitudes provide significantly better atmosphere transmission in the NIR wavelength region, compared to ground observatories. Fig. III.9 illustrates this difference using a modelling software called MODTRAN. The transmission from an altitude of 4 km shows transmission windows (J, H, K bands) that would limit the design of a ground-based interferometer. At float, the bands are not limited by the atmospheric transmission and thus we can use larger bands than the traditional J, H and K in order to optimize our photon signal.

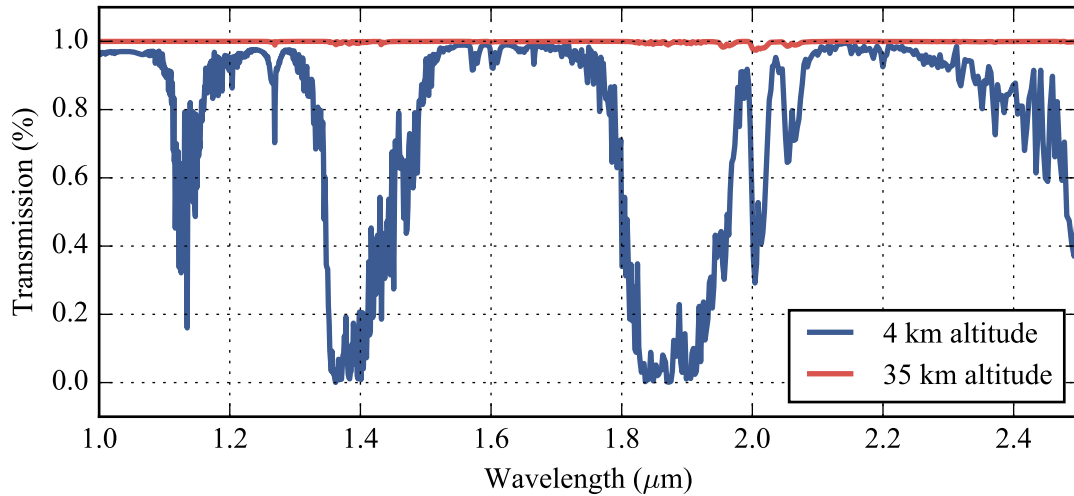


FIGURE III.9: Model atmospheric transmission, from Rizzo et al., 2012

Due to the prioritization of the science channels, the NIR tracking channel is less advanced at the time of writing. Hence, we use estimates for the transmission and reflection

efficiencies of the various components along the optical train. We estimate the efficiency of the major components: the mirrors (95% reflective), the cryostat window (90% transmissive), and the NIR/FIR dichroic (90% transmissive), which transmits the NIR light. There is an additional filter just in front of the detector, which limits the bands from 1 to $2.5\text{ }\mu\text{m}$. The detectors are not responsive for longer wavelengths. The total amount of efficiency for this channel is expected to be on the order of $\epsilon = 20\%$. Using this, a 1 Jy source will correspond to a number of photons N_{ph} within a PSF at the detector:

$$N_{\text{ph}} = \frac{1 \times 10^{-26}}{h} \mathcal{A} \times \text{FBW} \times \epsilon T_{\text{int}} \approx 8100, \quad (\text{III.6})$$

where $\text{FBW} \approx 0.67$ corresponds to the fractional bandwidth, and h is the Planck constant.

The detector is expected to have a read noise of $\sigma_{\text{RON}} = 18$ electrons r.m.s in up-the-ramp sampling, according the manufacturer specifications. Its frame rate changes throughout the acquire mode (REF appropriate CHAP), but the fastest mode will have a frame rate of $\sim 50\text{ Hz}$. Since the detector does not read destructively, saturation is an issue and needs to be addressed carefully - having to reset the pedestals to avoid saturation can complicate the software and might require a lot of tuning. Our calculations take into account a 20 ms integration time, a quantum efficiency of 70%, and a $0.6\text{ arcsec pixel}^{-1}$ plate scale, which provides an effective background area $\beta = 0.43$ for a diffraction-limited PSF of diameter $1.5''$ at $1.5\text{ }\mu\text{m}$. We consider that most of the photons will be spread on $1/\beta \approx 2.35$ pixels, so we expect about $N_{e^-} \approx 3440$ electrons per pixel from a 1 Jy source. A much more rigorous analysis is required once the efficiencies are measured.

For convenience, we express the SNR of a source using its flux S in electronss $^{-1}$:

$$\text{SNR} = \frac{S}{\sqrt{S + \beta(B + \sigma_{\text{RON}}^2)}}, \quad (\text{III.7})$$

where B is the number of electrons per pixel from the background. In our case, we calculate $B \approx 2.4$ electrons, which is negligible compared to the read noise, so we will ignore this term in the future.

The required flux density for a given SNR is then found by solving the previous equation for S :

$$S_{[\text{Jy}]} = \frac{\text{SNR}^2 + \sqrt{\text{SNR}^4 + 4\text{SNR}^2\beta\sigma_{\text{RON}}^2}}{2N_{e^-}}. \quad (\text{III.8})$$

For a $\text{SNR} = 10$, this corresponds to $\sim 0.13 \text{ Jy}$, or $\sim 9.66 \text{ H magnitude}$.

6 Targets

The science targets we seek have fluxes that are above the spectral sensitivities from table [], with a bright NIR guide star nearby. In addition, to correctly know the OPD, we need sets of bright calibrator targets which provide high-SNR fringes in one single scan of the delay line.

The science targets need to be available during our launch window, and preferably cover a large range of projected angles (so we can study the source at multiple angles to retrieve more of the spatial distribution). For this reason, we favor circumpolar sources, since they are the ones which change orientation at the fastest pace.

6.1 Calibrators

Calibrators ideally need to be point sources $\gg 100 S_{\min}$ Jy in our FIR bands, and it is not straightforward to identify which astronomical sources exist that would provide this kind of flux density. The planets of the solar system and their moons are usually bright enough, but they are often resolved by our instrument, which dramatically reduce their interferometric contrast. For example, we estimate the Uranus is > 1000 Jy, but because it is so resolved, the actual fringe contrast is very small, hence drastically reducing the SNR. Nearby, bright A stars such as Alpha Boo are most likely point sources, but are usually not as bright as we would want, especially not in Band 2 since they are essentially thermal sources with temperatures of thousands of Kelvin. It is possible to use actual science sources as calibrators, but of course it is unknown whether or not they actually are extended (this is the purpose of a mission like BETTII!).

We find that bright asteroids such as Ceres, Pallas and Vesta are the best candidates for bright calibrators. Because of their temperature and size, they should provide many hundreds of Jy in both our bands, while not being resolved. In addition, because of their albedo, they also reflect the sunlight so they would also be suitable for the tracking channels. Their only disadvantage is that they are not inertial targets - this complicates the pointing control system as their expected position moves across the sky, which requires the payload to have accurate timing capabilities to know where the object is at a given time.

6.2 Science targets

introduce the SOFIA work here

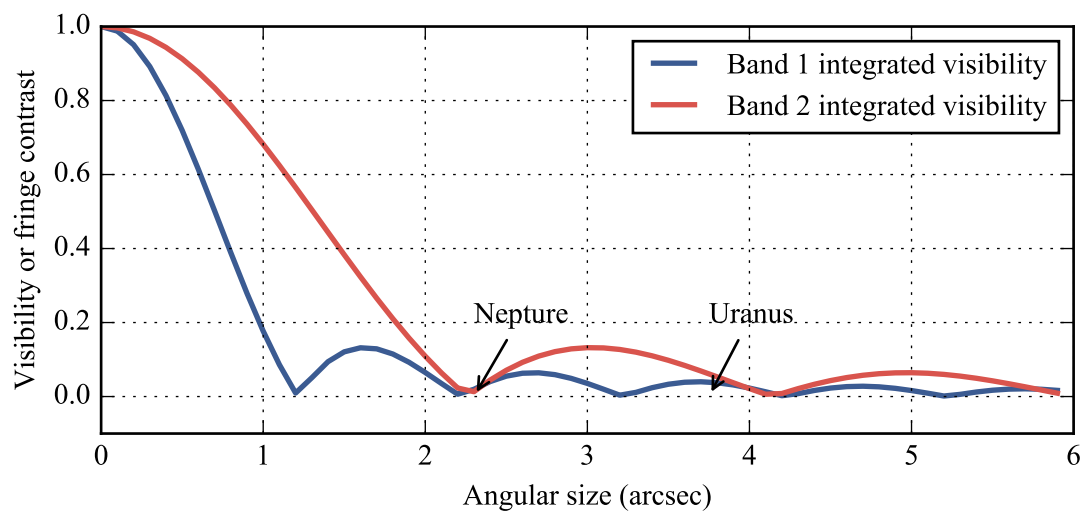


FIGURE III.10: Visibilities of calibrators.

Chapter IV

Far-infrared double-Fourier interferometers and their spectral sensitivity

1 Introduction

Observations at mid- to far-infrared wavelengths from the Earth's surface are extremely limited by the large atmospheric opacity in this region of the spectrum. Space-based telescopes like IRAS 12-100 μm ; Neugebauer et al., 1984, ISO 2.5-240 μm ; Kessler et al., 1996, *Spitzer* 3.6-160 μm ; Werner et al., 2004, AKARI 1.7-180 μm ; Murakami et al., 2007, WISE 3.4-22 μm ; Wright et al., 2010 and *Herschel* 55-672 μm ; Pilbratt et al., 2010 have demonstrated the scientific value of observations at these wavelengths; but the spatial resolution of space-based observatories is limited by the cost and complexity of building and flying progressively larger aperture telescopes. Interferometry is a common solution to this problem on the ground, and is a viable path forward to obtain much higher resolution than what single apertures can provide. In particular, spatio-spectral interferometry (Mariotti

and Ridgway, 1988) is a way to achieve high angular and spectral resolutions at far-IR wavelengths from above the atmosphere, without the cost and limitations of large single apertures.

Several space-based interferometer concepts, the Far Infrared Interferometer (FIRI; Helmich and Ivison, 2009), the Space Infrared Interferometer Telescope (SPIRIT; Leisawitz et al., 2007), and the Submillimeter Probe of the Evolution of Cosmic Structure (SPECS; Harwit, Leisawitz, and Rinehart, 2006), have been proposed and use spatio-spectral interferometry to achieve the much needed angular resolution to study astronomical processes such as the birth of stars and planetary systems, the activity in galactic nuclei and the formation of galaxies in the distant universe. The FIRI and SPIRIT concepts have two mirrors which are movable on one axis along a monolithic truss to provide a range of baseline lengths. SPECS consists of three spacecraft connected via tether to achieve baselines of order 1 km.

There are numerous engineering challenges to be addressed before such missions can become reality. A number of them can be tackled with testbeds (e.g. Leisawitz et al., 2012; Grainger et al., 2012) and small-scale pathfinder missions. These missions will likely be two-element, single baseline interferometers in space or on balloon platforms, such as the Balloon Experimental Twin Telescopes for Infrared Interferometry **2014PASP..126..660R** and to a certain extent the Far-Infrared Interferometric Telescope Experiment FITE; Kato et al., 2010. These pathfinders will have very limited baseline coverage and rather than producing full images, they will focus on reconstructing spectral information from closely-spaced sources. This paper explores aspects of the noise in spectral measurements specific to these instruments.

1.1 Spatio-spectral interferometry

In their pioneering paper, Mariotti and Ridgway, 1988 lay out the principles of spatio-spectral (or double-Fourier) interferometry. A spatio-spectral interferometer consists of a Fourier transform spectrometer (FTS), where a delay line mechanism modulates the optical path difference (OPD) between two independent light beams before combining them in the pupil plane. The instrument produces interferograms, which are arrays of power measurements as a function of the OPD. Unlike traditional FTS, where a single incoming beam is split, delay-modulated, and recombined, a double-Fourier interferometer utilizes multiple light collectors pointing to the same astronomical source and combines the incoming light from the collectors pairwise in the pupil plane. The orientation and magnitude of the baselines - the vectors between each pair of light collectors - determines which spatial frequency of the astronomical image the instrument measures. Longer baselines correspond to higher angular resolutions. The “double-Fourier” aspect comes from the fact that the interferogram measured on a given baseline is related to the Fourier Transform (FT) of the spatial and spectral distribution of the source emission. Two FTs are used to reconstruct the full spatio-spectral datacube representing the astronomical scene: the spectra which are more directly related to the power as a function of time delay difference between the two incoming beams (equivalent to the OPD) and the source 2D spatial structure on the sky which is more directly related to measurements accumulated from many different baseline vectors. The length of the baseline vectors can be changed by modifying the distance between the light collectors. The orientation of the vectors can be changed by rotating the baseline with respect to the source on the sky. The plane representing the source visibilities as a function of baseline vector is referred to as the (u, v) -plane and is a common

notion in ground-based submillimeter and radio interferometry. This paper focuses on the reconstruction of the spectrum from closely-spaced point sources using single-baseline measurements, and does not address the techniques and sensitivities involved in using multiple baseline lengths to produce an image of the scene; a mathematical formalism that covers imaging is already proposed in Elias et al., 2007.

Proposed double-Fourier instruments at far-IR wavelengths distinguish themselves from operating interferometers at sub-millimeter and radio wavelengths in several ways. First, they do not directly measure the phase information. The fundamental measurement is a time series of real-valued power as a delay line modulates the OPD in a controlled sequence (for example a linear ramp). The OPD from the delay line, as well as other OPD contributors in each arm of the instrument, and the external OPD created when the line of sight to a source is not perpendicular to the baseline vector, add up to the total OPD. In double-Fourier instruments, the OPD can be determined by measuring or estimating the various contributors to the total OPD. For a given detector location along the projected baseline vector, there exists a value of the OPD in the delay line that exactly compensates all other OPD contributors. This delay line position results in a zero net total OPD, and is called the Zero Path Difference (ZPD). At this value of OPD, an incoming plane wave traverses the two beam paths reaching the detector exactly with the same phase, for all wavelengths. ZPD corresponds to the center of an interferogram for that detector location. In the context of this paper, the phase for a given wavelength ϕ_λ is related to the OPD between the beams from each arm when they combine, at the time of a data point measurement: $\phi_\lambda = 2\pi \text{OPD}/\lambda$.

A second important difference for balloon and space interferometers is that collectors are not fixed to the Earth. In the case of BETTII and SPIRIT, the collectors are fixed

to a truss structure which is part of the mechanical system for pointing the collectors. Consequently, baseline length and external OPD, as relevant to an astronomical source, are not independent of pointing errors. The impact of errors in baseline length is modest because the relevant measure is in terms of fractions of the collector diameter. Errors in pointing translate into external OPD as the sine of the error angle times the baseline length, while the relevant measure is the wavelength. This can easily become significant; for example, a 1" pointing error for an 8 m long baseline corresponds to a 38 μm shift in OPD.

Third, bolometer-type detectors, such as being built for BETTII and envisioned for SPIRIT, are easily, and indeed typically, configured as two-dimensional arrays. With pupil plane combination, the entire field of view has an interferometric response; hence wide-field interferometry over multi-pixel arrays is straightforward. Fig. IV.1 shows this concept and sketches the instrumental response. For the configuration shown with the detector array columns aligned perpendicular to the baseline vector, ZPD is the same along lines perpendicular to the baseline vector projected on the detector. As the OPD is swept, it moves across ZPD for the different columns in the array, yielding interferograms with shifted centers corresponding to the changes in external OPD for each source location in the field.

By sweeping the OPD, the double-Fourier instrument measures interferograms which contain both spectral and spatial information over the detector array. The full spatial and spectral source information can be unambiguously recovered by repeating the delay line sweep over a range of baseline angles and lengths, which correspond to different spatial frequencies on the sky (Mariotti and Ridgway, 1988).

1.2 The case study: BETTII

The BETTII project ([2014PASP..126..660R](#)), is a motivation for this paper and a near-term application of spatio-spectral interferometry. BETTII consists of two 50 cm siderostats on a fixed 8 m baseline, with a far-IR beam-combining instrument at the center. It will observe the far-IR universe in two wavelength bands, 30-50 μm and 60-90 μm . The instrument is currently under construction at NASA Goddard Space Flight Center and is scheduled to launch in the Fall of 2016 on a stratospheric balloon from Fort Sumner, New Mexico, to an altitude of 35 km in order to be above most of the atmosphere. For its first flight, BETTII will focus on the study of dense star formation in nearby clusters. While a complete image reconstruction is not possible due to the static baseline length, BETTII will help resolve point source objects that are 0.5-1" apart in the short and long band, respectively, more than ten times the spatial resolution of *Spitzer* at 24 μm and six times the resolution of SOFIA at 37 μm . Combined with a modest spectral resolution of $\mathbf{R} = 10 - 50$, BETTII will measure the spectral energy distributions (SEDs) of clustered young stars to determine their evolutionary stage, locate the origin of the far-IR emission, and improve our understanding of how stars accrete their mass in these very dense regions of stellar birth e.g. see Tan et al., 2014, and references therein. For resolved sources, the fixed baseline will not completely lift degeneracies between the spectral and spatial information; however detailed source modeling can put constraints on the distribution of the far-IR emission ([2013ApJS..207...30W](#)).

In this paper, we study how various types of noise propagate to the derived spectrum in an instrument like BETTII or SPIRIT. In section 2, we establish a mathematical

formalism that can be used to represent interferograms. In section 3, we look at the dominant types of noise in the interferogram and define the relevant timescales associated with spatio-spectral interferometers. In section 4, we derive the spectral signal-to-noise ratio (SNR). In section 5, we apply these results to the special case of BETTII to derive its point source spectral sensitivity.

2 Mathematical formalism

The general optics layout for a double-Fourier system is shown in Fig. IV.2 for a single baseline. The combination of the siderostat and beam compressor acts as an afocal telescope which outputs a parallel beam with a diameter convenient for the rest of the optical train. The K-mirror in one beam path corrects for the pupil rotation so that the images of the sky from the two collectors are matched over the field of view. At the center of the instrument, there are optics for pupil re-imaging, filtering, and beam folding, as required by the specific implementation. The key components for our purpose are the delay line, beam combiner and detectors. The delay line introduces a controlled OPD between both arms. The two incoming beams are combined in the outputs from the beam combiner. We arbitrarily define one output as the “+” and the other as the “-”. To conserve photon energy, the two outputs must be complimentary such that the summed power of the two is independent of the OPD. In an ideal double-Fourier system, the two beam paths are symmetric about ZPD; hence, the power from the “+” and “-” outputs are equal at ZPD, and have odd symmetry about ZPD. In a traditional FTS at ZPD, one output has fully constructive interference while the other has fully destructive interference, with even symmetry about ZPD.

2.1 Interferograms for a single baseline

The interferogram for a single frequency of light measured at the outputs of the ideal double-Fourier instrument can be described in terms of the normalized intensity:

$$\hat{I}_{\pm}(x, \sigma) = \text{Re}(1 \pm i \mathcal{V}_{\mathbf{B}}(\sigma) e^{-2i\pi\sigma x}), \quad (\text{IV.1})$$

where $\sigma \equiv \frac{1}{\lambda}$ is the wavenumber of the light in cm^{-1} as per the convention for the FTS literature, x is the instrumental OPD created by the delay line with $x = 0$ corresponding to ZPD, and $\mathcal{V}_{\mathbf{B}}(\sigma)$ is the complex spatial visibility of the astronomical source for the baseline vector \mathbf{B} . “ $\text{Re}(f)$ ” indicates the real part of the complex-valued function f . The \pm indicates values for the two output beams: “+” and “-” in Fig. IV.2. The derivation of this expression is given in Appendix ??.

The normalized complex spatial visibility $\mathcal{V}_{\mathbf{B}}$ has a magnitude of 1 for all baselines for which the source is completely unresolved. For extended sources, the spatial visibility depends on the source geometry, intensity distribution, and the instrument baseline vector as described in Chapter 2 of **2000plbs.conf.....L** and Chapter 3 of Thompson, Moran, and George W Swenson, 2008. For a normalized source brightness distribution $\hat{\mathcal{F}}$, the spatial visibility with respect to a phase reference position on the sky can be written as:

$$\mathcal{V}_{\mathbf{B}}(\sigma) = \int_{\text{source}} d\Omega \hat{\mathcal{A}}(\xi) \hat{\mathcal{F}}(\xi) e^{-2i\pi\sigma\xi \cdot \mathbf{B}}, \quad (\text{IV.2})$$

where $\hat{\mathcal{A}}$ is the normalized reception pattern of the collecting area; \mathbf{B} is the baseline vector between the two collectors and ξ is the vector on the plane of the sky from the phase reference position to the infinitesimal solid angle $d\Omega$. The resulting visibility as a function

of baseline vector is the 2-dimensional FT of the source's sky distribution. Since $\hat{\mathcal{F}}$ does not have to be symmetric with respect to the chosen phase center, \mathcal{V}_B is in general complex and can be expressed as an amplitude and a phase, $\Phi_B(\sigma)$: $\mathcal{V}_B(\sigma) = |\mathcal{V}_B(\sigma)|e^{i\Phi_B(\sigma)}$.

Real instruments have asymmetries, imperfections, and measurement errors which can create phase-shifts between the two optical paths and across the pupils. Fixed instrumental effects can be represented by a normalized instrumental visibility loss term, $\mathcal{V}_i(\sigma)$ where the complex quantity $\mathcal{V}_i(\sigma) = |\mathcal{V}_i(\sigma)|e^{i\Phi_i(\sigma)}$, as described in details in Chapter 3 of **2000plbs.conf.....L** represents both amplitude losses and phase shifts (see Appendix ??). Additional phase errors can arise from imperfect knowledge of the real-time optical path lengths which we will represent as $e^{i\Phi_r(\sigma,x)}$, where $\Phi_r(\sigma,x)$ is the “phase noise”; this term depends on the OPD x through time-dependent phenomena such as mechanical jitters, temperature variations in the optics support, or pointing errors. In the rest of this paper, we will mostly talk about this “OPD noise”, which is the physical source of the noise, whereas phase noise represents its effects on the interferogram. The total complex visibility sampled at a single σ by the system is $\mathcal{V}_B(\sigma)\mathcal{V}_i(\sigma)e^{i\Phi_r(\sigma,x)}$, and it is normalized such that, for an ideal instrument observing a point source, this quantity is equal to 1 at ZPD.

Using Eq. IV.1 for the monochromatic source, the polychromatic interferogram is the integral over σ of this dimensionless response at each wavenumber. The total amount of power coming into the 2-aperture interferometer within a small wavenumber range $d\sigma$ is $2\mathcal{A}B(\sigma)cd\sigma$ where $2\mathcal{A}$ is the total aperture area in m^2 , $B(\sigma)$ is the spectral flux density in $\text{W}\cdot\text{m}^{-2}\cdot\text{Hz}^{-1}$ and c is the speed of light in $\text{cm}\cdot\text{s}^{-1}$. Filters and optics in an instrument cause a wavenumber-dependent transmission profile $\mathcal{T}_{bp}(\sigma)$. The quantum efficiency of the detector can depend on wavenumber, $\eta_D(\sigma)$. For multi-pixel detectors the interferogram is measured by matched filtering a point-spread function on a pixel array, which has some

efficiency η_{mf} .

The actual power measured by the instrument can be represented as:

$$I_{\pm}(x) = \mathcal{A}c \int_0^{+\infty} \eta_{\text{mf}} \eta_D \mathcal{T}_{\text{bp}} B \times \text{Re} [(1 \pm i\mathcal{V}_i \mathcal{V}_B e^{i\Phi_r} e^{-2i\pi\sigma x})] d\sigma, \quad (\text{IV.3})$$

where the factor of 2 for the two apertures is dropped because it is implicit in Eq. IV.1.

All quantities within the integral can be functions of wavenumber, and all the instrumental phase and interferometric loss terms are in \mathcal{V}_i and $e^{i\Phi_r}$.

Instead of considering each separate output, we use $\mathbf{I} = \mathbf{I}_+ - \mathbf{I}_-$ as our interferogram expression, which cancels out the constant term. We also introduce an interferometric instrument transmission function, which can be complex, which represents the normalized amplitude and phase of the interferogram for a point source of uniform spectrum and no phase noise:

$$T_{\text{inst}}(\sigma) \equiv \mathcal{A}c \eta_{\text{mf}} \eta_D \mathcal{T}_{\text{bp}} \mathcal{V}_i = |T_{\text{inst}}(\sigma)| e^{i\Phi_{\text{inst}}(\sigma)}, \quad (\text{IV.4})$$

We can then write the modulated signal as:

$$I(x) = \text{Re} \left(2 \int_0^{+\infty} i|T_{\text{inst}}| B \mathcal{V}_B e^{i\Phi_r + i\Phi_{\text{inst}}} e^{-2i\pi\sigma x} d\sigma \right), \quad (\text{IV.5})$$

where B is real and \mathcal{V}_B can be complex.

Eq. IV.5 can be turned into a Fourier transform by mirroring all quantities to negative wavenumbers. This convention is explained in detail in Davis, Abrams, and Brault (2001) for FTS instruments; the odd symmetry of the interferogram for a system with one beam combiner and the complex instrumental transfer function means that the incident spectrum on the detectors must be mirrored to $-\sigma$ as the negative of the complex conjugate of $+\sigma$:

$\mathcal{S}_e(\sigma) \equiv [T_{\text{inst}} B \mathcal{V}_{\mathbf{B}}]_e(\sigma) = \frac{1}{2} [T_{\text{inst}}(\sigma) B(\sigma) \mathcal{V}_{\mathbf{B}}(\sigma) - T_{\text{inst}}^*(-\sigma) B(-\sigma) \mathcal{V}_{\mathbf{B}}^*(-\sigma)]$. We use the subscript e to denote the reflected function, and will apply this convention in the rest of this paper; this reflection ensures that the integrals keep the same value when expressed from $-\infty$ to $+\infty$, and does not affect the SNR estimates: although the signal appears to be divided by a factor of two, so is the noise, as it is spread between positive and negative frequencies. The interferogram expression is then:

$$I(x) = \text{Re} \left(\int_{-\infty}^{+\infty} i \mathcal{S}_e e^{-2i\pi\sigma x + i\Phi_r} d\sigma \right). \quad (\text{IV.6})$$

2.2 Measured interferograms

In practice, the interferogram data are discrete measurements of a real-valued signal on the detectors. Like for most FTS instruments, each data point on the interferogram corresponds to an integration of the detector while the delay line is continually in motion. This decreases the amplitude of the interferogram due to the local smearing of the fringes, but it can be kept to low values by increasing the fringe sampling. At each delay x_n , the interferogram has a measured value $\mathcal{I}(x_n) = \frac{1}{dx} \int_{x_n-dx/2}^{x_n+dx/2} \mathbf{I}(x) dx$. To first order, this has the effect of multiplying the power at each wavenumber by $\text{sinc}(\pi\sigma dx)$. For the purpose of this paper, we consider this term to be included as part of the instrumental transmission T_{inst} . Note that the value of the optical delay x_n is the path difference from ZPD, not the physical location of the delay line, since there could be a multiplying factor between the two due to beam folding (e.g., for BETTII, a motion of 1 mm of the delay line creates 4 mm of OPD).

A discrete Fourier transform (DFT) is used to transform a discrete interferogram of N measurements into a complex discrete spectrum with N points. The resolving power

of the instrument, $\mathbf{R} = \lambda/d\lambda$, is dependent on the physical length scanned by the delay line L : $\mathbf{R} = L\sigma/2$ for a scan with symmetric length on both sides of ZPD. For these instruments where we scan through the whole interferogram, the data should be sampled at least at the Nyquist rate for the interferogram response frequency of $dx = \lambda/2$. For a sampling exactly equal to Nyquist, we have the relationship: $N = 4\mathbf{R}$.

For a double-Fourier instrument, as shown in Fig. IV.1, the ZPD for different columns on the array occurs at different delay positions x_{col} , related to the projected baseline length. The simplest way to express this is in terms of the angular offset on the sky of each column, ξ , along the direction of the baseline, \mathbf{B} :

$$x_{\text{col}} = |\mathbf{B}| \sin \xi \approx |\mathbf{B}| \xi = 48.7 \mu\text{m} \left(\frac{|\mathbf{B}|}{10 \text{ m}} \right) \left(\frac{\xi}{1 \text{ arcsec}} \right), \quad (\text{IV.7})$$

where we have filled in practical units for an infrared instrument. For a far-IR interferometer working at 50 μm , with 1-2 m diameter collectors, the delay shift across the collector point spread function (collector angular resolution) is several to ten wavelengths. Hence the scan length to cover a wide-field array detector is comparable to the scan length required to achieve \mathbf{R} 's of 100's to 1000's. This property is an important consideration for observation and data analysis strategies.

The ideal interferogram for a point source from a perfect instrument is an odd function of the OPD x , so its DFT is purely imaginary. The noise in the interferogram will be converted into spectral noise in both the real and imaginary axes so the real axis is a proportional measure of the noise. Referring back to Eq. IV.6, phase shifts caused by the instrumental transfer function and source spatial visibility will break the anti-symmetry; in practice, the DFT of a measured interferogram is complex and the real and imaginary

parts are of interest. The scientifically interesting quantities are the source spectrum and source spatial visibility: \mathbf{B} and $\mathcal{V}_{\mathbf{B}}$; the fixed instrumental terms have to be calibrated or properly modeled by observing a bright point source of known spectrum. The techniques for calibrating FTS systems are well developed (e.g. Davis, Abrams, and Brault, 2001), and there are many methods proposed to correct some phase and amplitude errors (e.g. Forman, Steel, and Vanasse, 1966; Sromovsky, 2003).

The phase noise term $\Phi_r(x, \sigma)$ in Eq. IV.6, and the SNR in the measured interferogram can have significant impact on the ability to recover the source spectrum with a real instrument. The upper panel in Fig. IV.3 shows an example of an interferogram (left), and the transformed $\mathcal{S}_e(\sigma_k)$ (right) for a source with flat power spectrum, multiplied by a flat bandpass function with smoothed edges. The middle panel of Fig. IV.3 shows the same source and instrument parameters as the upper panel, now with an assumed Gaussian OPD noise of standard deviation equal to 10% of the central wavelength of the band $\lambda_0 \equiv \frac{1}{\sigma_0}$ (*i.e.*, there is a $\lambda_0/10$ OPD uncertainty for each data point in the interferogram). The lower panel is the top panel observed with a incoherent background noise corresponding to $\text{SNR} = 10$ at the peak of the interferogram, and no phase noise. The next sections of this paper will analyze these noise contributions and quantify their impact on the derived spectrum.

3 Noise sources

The two primary types of noise in a double-Fourier instrument are intensity and OPD noise. The intensity noise consists of the astronomical and thermal background noise, the photon noise from the source, and the detector noise. The OPD noise arises primarily from uncertainties and changes in OPD, which would prevent us from accurately knowing the

x -values of measurements in the interferogram before the FT. For convenience, we usually refer to the OPD noise as a percentage of the carrier wavelength. In the rest of this paper, a “10% OPD noise” signifies that the OPD for each measurement in the interferogram is known to within an error of 10% of the carrier wavelength, or 10% of one full fringe cycle.

3.1 Intensity noise

The measured signal has units of power and can be represented as the interferometric signal with additive noise:

$$\mathbf{I}_{\text{measured}}(x_n) = \mathcal{I}(x_n) + n_{\mathcal{I}}(x_n), \quad (\text{IV.8})$$

with $n_{\mathcal{I}}$ being the difference of the noise in the two outputs of the interferometer, $n_{\mathcal{I}} = n_+ - n_-$. When the beam combiner, optical train, and detectors are symmetric, the residual $n_{\mathcal{I}}$ has zero mean. The total noise in $\mathbf{I}_{\text{measured}}(x_n)$, expressed in Noise Equivalent Power, NEP_{tot} , is the sum of the three noise variances:

$$\text{NEP}_{\text{tot}}^2 = 2\text{NEP}_{\text{ph}}^2 + 2\text{NEP}_{\text{det}}^2 + 2\text{NEP}_{\text{sou}}^2, \quad (\text{IV.9})$$

where NEP_{ph} and NEP_{sou} are the thermal noise from the background (e.g. sky and warm optics in the case of a far-IR instrument) and source photon noise, respectively, in one output, and NEP_{det} is the noise-equivalent power characterizing each detector’s noise (including phonon, readout and Johnson noise). The factor of 2 multiplies each term since we are considering the difference of both outputs. The relation between NEP_{tot} and the

variance $\sigma_{\mathcal{I}}^2$ of the noise $n_{\mathcal{I}}$ during an interval dt is (Sromovsky, 2003):

$$\sigma_{\mathcal{I}}^2 = \frac{\text{NEP}_{\text{tot}}^2}{2dt}. \quad (\text{IV.10})$$

For space instruments, the noise will likely be dominated by the sky background (zodiacal light, galactic cirrus emission, or optics thermal emission) and detector for a very large fraction of astronomical targets, which tend to be faint; for balloon instruments, emission from warm optics and the atmosphere sets the noise level in the far-IR.

3.2 OPD noise

Observing from the ground at optical wavelengths with a double-Fourier interferometer is limited by the phase coherence between the apertures, which is related to the atmospheric coherence time, as discussed by Mariotti and Ridgway, 1988. The short coherence time forces fast scan rates, which degrades the sensitivity of the instrument due to short integration times and phase shifts between sequential scans. This is not a problem for flying platforms, since even at balloon altitudes the atmospheric coherence is not a significant issue (Rizzo et al., 2012). The major concerns for balloon and space missions are overall instrumental stability, knowledge of ZPD, and pointing errors, which can all contribute to OPD noise.

OPD noise arises in an interferogram when the OPD at the time of a measurement is uncertain, hence compromising the reconstruction of the true x -value. Since this uncertainty is a physical delay δ_x , the error in phase is wavenumber dependent: $2\pi\delta_x\sigma$. δ_x is the difference between the estimated x and the true x . For single-beam FTS instruments, internal laser metrology can provide optical path length measurements to high accuracy (e.g. Griffiths and De Haseth, 2007), and the separate paths the split beams need to travel

can be kept small. For double-Fourier instruments, the entire optical paths upstream of the beam combiner affect the OPD, hence it is more challenging to accurately measure and estimate the OPD contributors. In addition, common-mode pointing errors of the collectors are directly converted to geometrical delay errors. Hence, it is critical to know the position and orientation of the baseline vector with respect to the astronomical target with high accuracy in order to properly reconstruct the interferogram.

For this analysis, we identify three timescales that can be used to examine the effects of OPD noise on the interferogram. These timescales are important to consider in the design of the OPD control system of any double-Fourier interferometer. Timescale 1 is the shortest and corresponds to the integration time for a single data point, typically a few milliseconds. In practice, this kind of OPD noise could be created by high-frequency mechanical jitters in the instrument (including the delay line bearing and motor, stick-slip behaviors and resonant modes, reaction wheels and other self-induced vibrations...). Timescale 2 is the time it takes to acquire one single interferogram over the full field of view and at the desired resolving power, typically on the order of seconds. The sources of noise that can affect this timescale include for example pointing errors and drifts, as well errors in the knowledge of the delay line position relative to a reference ZPD. Finally, the longest timescale to be considered, timescale 3, is the time it takes to complete one full "track" by co-adding several consecutive interferograms to achieve the desired SNR, typically a few minutes long. During this timescale, it is expected that the change in baseline orientation on the sky does not produce any significant change in the source spatial visibility function. The latter timescale is most importantly influenced by thermal variations and time-varying gradients that could change the optical alignment and mechanical configuration between the two arms.

4 Spectral signal-to-noise ratio

4.1 Effects of Gaussian intensity noise

In the presence of Gaussian intensity noise (thermal background and detector noise), the measured interferogram is of the form of Eq. IV.8. We suppose that the noise has a variance $\sigma_{\mathcal{I}}^2$ and zero mean, and is independent of delay position. In particular, this assumes that the source photon noise is negligible. The noise in the spectral domain is the transform of the noise in the interferogram domain:

$$dx \mathbf{DFT}(n_{\mathcal{I}}) = dx \sum_{n=-N/2}^{N/2-1} n_{\mathcal{I}}(x_n) e^{2i\pi nk/N}, \quad (\text{IV.11})$$

where the dx factor is to normalize the noise to a sampling bin (Press et al., 1992), and k indexes the N discrete wavenumbers in the spectral domain. The interferogram interval is symmetric with about ZPD ($n=0$). The noise variance is equal in the imaginary and the real domain, and can be expressed as the variance of the noise transform:

$$\sigma_{\mathcal{S}}^2 = dx^2 \mathbf{VAR}(\text{Re}(\mathbf{DFT}(n_{\mathcal{I}}))), \quad (\text{IV.12})$$

where **VAR** is the variance operation. By writing out the variance we obtain:

$$\sigma_{\mathcal{S}}^2 = dx^2 \sigma_{\mathcal{I}}^2 \sum_{n=-N/2}^{N/2-1} \cos^2(2\pi nk/N) = \frac{N}{2} dx^2 \sigma_{\mathcal{I}}^2, \quad (\text{IV.13})$$

where we used $\sum_{n=-N/2}^{N/2-1} \cos^2(2\pi nk/N) = N/2$ for $k \neq 0$.

The signal at wavenumber σ_k in the discrete spectrum $\mathcal{S}_e(\sigma_k)$ is:

$$\mathcal{S}_e(\sigma_k) = \frac{1}{\delta\sigma} \int_{\sigma_k - \delta\sigma/2}^{\sigma_k + \delta\sigma/2} \mathcal{S}_e(\sigma) d\sigma, \quad (\text{IV.14})$$

where $\delta\sigma = (Ndx)^{-1}$. A line of power P_e at σ_{k_0} will thus have an apparent flux density $\mathcal{S}_e(\sigma_k) = NdxP_e$ at $k = k_0$ and 0 for all other k . The signal-to-noise ratio in the spectrum can be expressed in general as:

$$\text{SNR}_k = \frac{\mathcal{S}_e(\sigma_k)}{\sigma_S} = \sqrt{\frac{2}{N}} \frac{\mathcal{S}_e(\sigma_k)}{dx\sigma_I}. \quad (\text{IV.15})$$

Using Eq. IV.10 and the definition $x_{\max} = Ndx/2$, this becomes:

$$\text{SNR}_k = \frac{\mathcal{S}_e(\sigma_k)}{x_{\max} \text{NEP}_{\text{tot}}} \sqrt{Ndt}, \quad (\text{IV.16})$$

where dt corresponds to the integration time of one data point on the interferogram. As expected the SNR improves as the square-root of the total integration time, \sqrt{Ndt} , and is adversely affected by increasing NEP and scan length.

Defining the central wavenumber of the band as σ_0 , the spectral resolving power of the transformed interferogram is $\mathbf{R} = dxN\sigma_0/2$. We introduce the sampling parameter $s = (\sigma_0 dx)^{-1}$ which is the number of data samples per fringe for the central wavenumber in the band. The spectral resolving power at the band center can now be written $\mathbf{R} = \frac{N}{2s}$. In practice one wants to pick a value of s that ensures Nyquist sampling on the fringe for all wavenumbers in the band so $s \sim 3$ or greater is typically preferred. For a given integration time per data point (given SNR_I), increasing the fringe sampling effectively increases the amount of time spent on the fringe, so the spectral SNR should increase with \sqrt{s} . Note

that as long as we Nyquist-sample the fringe, there is no difference between multiplying the fringe sampling by some factor, and increasing the integration time per data point by the same factor, since in both cases the effective time on the fringe is equally increased.

It is useful to relate SNR_k to the SNR in the interferogram at the location of maximum intensity of the fringe, using physical quantities. The noise in each discrete measurement of the interferogram is $\sigma_{\mathcal{I}}$. The signal at maximum intensity is $\mathcal{I}_{\max} = d\sigma \bar{\mathcal{S}}$, where $d\sigma$ is the width of the bandpass filter and $\bar{\mathcal{S}}$ is the average value of the signal in the band. Defining $\text{SNR}_{\mathcal{I}} = \mathcal{I}_{\max}/\sigma_{\mathcal{I}}$, and noting that $\sqrt{Ndx^2/2} = \frac{1}{\sigma_0} \sqrt{R/s}$, we obtain:

$$\text{SNR}_k = \frac{\mathcal{S}_e \sqrt{2}}{\sqrt{Ndx\sigma_{\mathcal{I}}}} = \frac{\mathcal{S}_e(\sigma_k)}{\bar{\mathcal{S}}} \sqrt{\frac{s}{\mathbf{R}}} \frac{\sigma_0}{d\sigma} \text{SNR}_{\mathcal{I}}. \quad (\text{IV.17})$$

Thus, the SNR in a channel of the final spectrum depends inversely on the square root of the resolving power \mathbf{R} and the fractional bandwidth $\frac{d\sigma}{\sigma_0}$; and it depends directly on the square root of the number of samples per fringe \sqrt{s} .

4.2 Effects of Gaussian OPD noise

This section derives analytic expressions for the effects of Gaussian-distributed OPD noise. We look at the general case in order to derive sensitivities for double-Fourier instruments. Here, we suppose that the OPD from the delay line, the OPD within each arm of the instrument, and the OPD caused by an off-axis source are all measured or estimated with some residual error. Hence, the data points measured in the interferogram are associated with a delay value relative to ZPD, and if necessary, resampled to produce an evenly-spaced delay axis. This is necessary to use the FT and retrieve the spectrum. The noise on the delay estimate can be characterized as a wavenumber-dependent phase error in the interference on the two beams. In the following, we quantify the impact of this noise on

the spectral SNR, in order to understand how good our knowledge of the OPD needs to be to make sure the OPD noise effects are not dominant.

Let's consider a single frequency signal first, so that the phase is proportional to the OPD. If we suppose that these residual phase errors $\Phi_r(x)$ are represented by a Gaussian distribution with zero mean and variance σ_Φ^2 , then the primary effect of the noise is to change the instantaneous power in $\mathbf{I}(x)$ by the factor $e^{i\Phi_r(x)}$. Now we consider a large ensemble of realizations of this noise distribution in order to predict its effect on the SNR. Using the expression from Richards, 2003, for sufficiently small phase errors ($< \pi$ radians), the intensity of the coherent signal is reduced, on average, by a factor $e^{-\sigma_\Phi^2/2}$. For Gaussian-distributed OPD uncertainties with standard deviation $\lambda/20$, where λ is the wavelength, the signal intensity is reduced by 5%; for $\lambda/10$ the amplitude is reduced by 18%. To give a practical example of the impact of this effect, we can consider the case of BETTII: if we assume that the uncertainty in the attitude of the payload is the only source of OPD noise, then knowing the attitude to within 0.1" rms will reduce the signal, on average, by 18% at 40 μm .

For the polychromatic case, the delay position uncertainty, δ_x , creates larger phase errors the shorter the wavelength, $\Phi_r(k) = 2\pi\delta_x\sigma_k$. A given error distribution of variance σ_{OPD}^2 in position yields a degradation across the band, $e^{-\sigma_\Phi^2(k)/2}$, with $\sigma_\Phi^2(k) = (2\pi)^2\sigma_{\text{OPD}}^2\sigma_k^2$.

Of course, the power lost from the coherent fringe pattern is still present in the scan; it becomes part of the incoherent signal seen by each output. In the limit where there is

no spectral noise from the background or detectors, defining $\mathcal{S}_k \equiv \mathcal{S}_e(\sigma_k)$ we have:

$$\text{SNR}_k = \frac{\mathcal{S}_k e^{-\sigma_\Phi^2(k)/2}}{\sqrt{\frac{1}{2s\mathbf{R}} \sum_{k'} [\mathcal{S}_{k'}^2 (1 - e^{-\sigma_\Phi^2(k')})]}}, \quad (\text{IV.18})$$

where k' designates an index on all positive wavenumber bins. Note that $N = 2s\mathbf{R}$. This relationship is identical to the one derived by Meynard (1992), and we suggest an alternate and more detailed justification for it (see Appendix ??). Studying this relationship, all the wavenumbers contribute to the white noise at a given wavenumber σ_k . The strongest lines (strongest $\mathcal{S}_{k'}^2$) and the shortest wavelengths (strongest $1 - e^{-\sigma_\Phi^2(k')}$) contribute the most to the overall noise. To summarize, considering an ensemble average of interferograms, OPD noise degrades the spectral SNR in two ways: first, it reduces the overall signal in the interferogram; second, it converts this lost power into white noise.

More realistically, observations will have both intensity and OPD-generated spectral noise. In this case, the intensity noise and the scattered power add in quadrature to give:

$$\text{SNR}_k = \frac{\mathcal{S}_k e^{-\sigma_\Phi^2(k)/2}}{\sqrt{\frac{1}{2s\mathbf{R}} \sum_{k'} [\mathcal{S}_{k'}^2 (1 - e^{-\sigma_\Phi^2(k')})] + s\mathbf{R}dx^2\sigma_I^2}}. \quad (\text{IV.19})$$

The numerator of Eq. IV.19 shows that any amount of OPD noise will reduce the spectral SNR. However, the impact of OPD noise is even greater when the power lost from the fringe is comparable to the intensity noise, as the first term of the denominator starts to matter. In fact, for arbitrarily large source fluxes, this equation reaches an asymptotical value which depends only on the OPD noise, and sets the maximum SNR achievable on average in a single scan. This is relevant for astronomical calibrators which can be so bright that the intensity noise term is negligible. In that case, assuming constant OPD noise,

more SNR is only achievable by co-adding consecutive scans, as we discuss in the next section and in Appendix C. For most astronomical applications, where targets are usually faint compared to the intensity noise, it is expected that the first term of the denominator will be negligible.

4.3 Co-adding interferograms

Eq. IV.19 is the general case of a single interferogram with OPD and intensity noise. In practice, we would co-add M interferograms in one “track” to build up SNR, but this puts stringent requirements on the performance of the control system and OPD estimator, because consecutive interferograms need to stay aligned with each other to within a small fraction of the carrier wavelength, to avoid causing OPD noise. The design and performance of the OPD estimator is highly implementation-specific, but most balloon and space designs will likely include an estimator that either directly measures the OPD, or indirectly infers it from the measurement of another quantity.

A direct OPD measurement can be achieved for example with a fringe-tracking instrument, while an indirect OPD estimate can be an attitude measurement, which can be related to the OPD by simple geometry by using some assumptions. The latter scheme only works if the OPD errors are only influenced by pointing uncertainties over the timescale of a track, and that all other OPD contributors are modeled and corrected with comparatively high fidelity. The spectral SNR over M scans can be determined from Eq. IV.19 by multiplying the whole equation by a factor of \sqrt{M} . The OPD noise term causing the phase noise variance σ_Φ^2 then corresponds to the variance of the OPD uncertainties for each point of a scan, plus the variance of the OPD estimation error in determining the position of the center of each scan, which is necessary to properly co-align them (Appendix

C).

4.4 Implications for spectroscopy

A primary application for BETTII and proposed missions like SPIRIT will be the measurement of the spectral energy distribution from warm dust associated with star formation in different environments. These types of measurements require broad wavelength coverage but not especially high spectral resolution since the emission can be characterized as a sum of Planck functions over a range of temperatures. For an instrument like BETTII, covering from 30-50 μm and 60-90 μm simultaneously, $\mathbf{R} \sim 10$ in each band is sufficient to accomplish much of the science.

Spectral measurement with $\mathbf{R} \sim 10$ requires covering a delay range of $\pm 10 \lambda_0$ for a single source. On the other hand, a delay range of 35-70 λ (see Eq. IV.7) is needed to move ZPD across 1 arc-minute of sky. Hence, typically, the delay requirements for spatial coverage creates interferograms with higher resolution than needed to measure the continuum, and the full scan needs to be cut into smaller arrays around each target in the field. The size of these smaller arrays depends on the desired spectral resolving power \mathbf{R} , and the required sensitivity, as shown in Eq. IV.17. However, the additional data can be used for higher-resolution spectroscopy, for example to measure specific atomic lines in the far-IR. The SNR for lines is actually increasing with the square root of the number of data points in the interferogram, as the broadband noise gets more diluted in increasingly narrower spectral bins (see Eq. IV.14, IV.15).

As discussed for FTS instruments (e.g. Davis, Abrams, and Brault, 2001), apodization, the weighting of the points of the measured interferogram before applying the DFT, is one method for optimizing the SNR in the spectrum. The weight scheme is optimized to

measure a specific type of spectrum: narrow line, broad features, continuum. The method relies on the fact that the data points close to the center or edges of a fringe packet contain information about low or high spectral frequencies, respectively. For example, if the purpose of an observation is to study continuum, it is appropriate to apply smaller weights to data points far away from the central fringe, since they add noise and very little SNR.

A common low-resolution spectroscopy case can be derived analytically if a source has a spectrum following a power law distribution over the covered band. We can write $\mathcal{S}(\sigma) \propto \sigma^\alpha$ where the exponent α is the quantity of interest. Several methods have been developed to properly fit these power laws using maximum entropy and other techniques (e.g. Clauset, Shalizi, and Newman, 2007). Here we use a simple estimator and provide a ready-to-use formula to help quantify the sensitivity of double-Fourier instruments.

By taking the logarithm of the spectrum, the problem is turned into a weighted linear fit in log-log space, where we want to determine the slope of a line. The noise in the new domain is $\sigma_L = \left| \frac{d(\ln(\mathcal{S}))}{d\mathcal{S}} \right| \sigma_{\mathcal{S}} = \sigma_{\mathcal{S}}/\mathcal{S} = 1/\text{SNR}_{\mathcal{S}}$. The weights $w_k = 1/\sigma_k^2$ of the linear fit are then simply the values of the spectral SNR squared at each data point, SNR_k^2 . The error on the weighted least square estimate of the slope is (Bevington and Robinson, 2003):

$$\sigma_\alpha^2 = \frac{\sum w_k}{\sum w_k \sum w_k X_k^2 - (\sum w_k X_k)^2}, \quad (\text{IV.20})$$

where $X_k \equiv \ln(\sigma_k)$ is the natural logarithm of the wavenumber for data point k . In the case of uniform spectral signal-to-noise ratio $\text{SNR}_{\mathcal{S}}$ over m points of the spectrum, this expression simplifies to:

$$\sigma_\alpha^2 = \frac{1}{m \times \text{SNR}_{\mathcal{S}}^2 \times \text{VAR}(X_k)}. \quad (\text{IV.21})$$

This equation indicates that the variance of the spectral index estimate decreases with

the number of points used to calculate the estimate, the spectral SNR squared, and the variance of the points distribution on the logarithmic wavenumber axis. For example, for 10 data points spread evenly from 30 to 55 μm , each with a spectral SNR of 5, we obtain an error on the slope determination $\sigma_\alpha \sim 0.3$.

5 Spectral sensitivity analysis for BETTII

This section applies elements of the above discussion to BETTII. A general discussion on the details of BETTII can be found in **2014PASP..126..660R**. On BETTII, two mirrors collect light with an altitude-azimuth pointing system. The truss that holds the two mirrors moves in azimuth and determines the baseline vector, while the mirrors themselves move only in elevation. While BETTII does not physically rotate about the line of sight to cover different baseline angles, the payload always stays horizontal and the projection of its baseline vector changes as a source moves across the sky, hence covering different angles in the (u, v) -plane. The absolute OPD and ZPD of the instrument cannot be measured, maintained, or known with perfect accuracy, especially during the flight itself, due to attitude estimation errors leading to our inability to perfectly estimate the orientation of the baseline vector in real time. In fact, a significant component of the mission's design and implementation involves the selection and coordination of the suite of instruments which provide attitude measurements to construct the OPD estimator.

A second relevant aspect of BETTII is that the detectors are cryogenic bolometers see Staguhn et al., 2014, for similar architectures with $1/f$ noise which sets an optimal read-out time for the detectors of around 2.5 milliseconds (timescale 1). With BETTII's designed field coverage of 2 arcminutes, full field scans consist of 1024 points and take 3 seconds to complete (timescale 2). Due to thermal emission from the atmosphere, warm

mirrors, and cryostat windows, BETTII will be in the background noise limited case for all science targets. It is anticipated that 200 scans will typically be co-added to create one single visibility measurement over 10 minutes (timescale 3). For most source locations, the variation of the baseline orientation due to change in parallactic angle is not significant over this period.

5.1 Noise sources and control system

Table IV.1 shows our estimates of the background power levels associated with the atmosphere, warm optics, and windows in the two BETTII bands. The detectors themselves have been designed to have a noise level comparable to the background to optimize the use of the dynamic range of the devices. The total NEPs of the short and long bands are expected to be $\sim 2 \times 10^{-15} \text{ W.Hz}^{-0.5}$ and $\sim 1 \times 10^{-15} \text{ W.Hz}^{-0.5}$, respectively. The source photon noise is negligible compared to the total NEP.

Balloon instruments are subject to low frequency ($< 0.5 \text{ Hz}$) pendulum modes and other oscillations introduced by the system's geometry and mass distribution, which make pointing a challenge. However, it is expected that the balloon environment is free of perturbations at any higher frequency (other than the instrument specific perturbations). Hence, sensors with high electrical bandwidth can robustly estimate the pendulum modes to gain accurate knowledge of the attitude, which can be used as our indirect OPD estimator since it is geometrically related to the phase on sufficiently short timescales.

The BETTII control system is organized with three different levels of control loops (**2014SPIE.9143E..3HR**): the coarse pointing loop, the fine pointing loop, and the OPD loop. The coarse pointing loop uses gyroscopes and star cameras to keep the baseline oriented within 10-15" of an appropriate near-IR guide star. A dichroic splits the near-IR

(1-2 μm) from the far-IR (30-90 μm) inside the cryostat before the scanning delay line. The guide star is imaged through each of the two arms on two separate readout windows of a near-IR detector array that shares most of the optical path with the science channels. The fine control loop uses fast-steering tip-tilt mirrors, located at the pupils of each arm, to control the guide star image on each window and maintain good overlap of the beams at the science detectors. This loop reads the near-IR detector and generates a tip/tilt correction at 100 Hz. We expect to achieve beam overlap to within better than 1.5" at all times when a guide star is available. The spatial resolution of an individual BETTII beam is 17" in the short wavelength band so this is a little better than 1/10th of a resolution element. The interferometric visibility loss for this overlap error is anticipated to be less than 0.5%.

We do not expect to be able to maintain the three dimensional orientation of the truss, and hence the baseline vector, to much better than 10" rms, due to the various pendulum modes mentioned above and large inertia of the payload. However, the errors in OPD introduced by pointing errors can be corrected directly using a delay line. BETTII uses a delay line external to the cryostat to correct the OPD at the entrance of the cryogenic volume. This delay line is completely separate from the science delay line which scans the OPD to produce the interferogram. Two delay lines are not a requirement for a double-Fourier instrument in general as the job can be done in theory by a single mechanism, with sufficient range and mechanical bandwidth. The external delay line on BETTII allows for the possible future upgrade of correcting and monitoring the OPD outside of the cryostat using the near-IR channel by implementing a fringe tracker (Rizzo et al., 2012).

For the OPD loop on BETTII, the angles of the tip/tilt mirrors which are used to maintain overlap of the beams act as an estimator of the baseline orientation, and hence

as an indirect estimator of the OPD. The attitude estimates computed from these angles are fed to the external delay line so that the OPD at the entrance of the cryostat stays as constant as possible. Because the pendulation modes have periods of a few to tens of seconds and should be well-behaved, we expect to be able to trust the control signals and estimate the attitude of the baseline vector to $\sim 0.12''$ rms, which corresponds to a fifth of a detector pixel in the near-IR tracking array. A $0.12''$ attitude error indirectly corresponds to a delay uncertainty of $5 \mu\text{m}$, or 12% of a wavelength at 40 microns. This is a critical consideration when co-adding consecutive interferograms. With this amount of OPD noise, we expect, on average, a $\sim 25\%$ degradation in SNR for all sources in the short band, simply from the effects of phase noise in reducing the coherent signal (see Eq. IV.19).

Even with a stable OPD estimator, the absolute ZPD of the instrument must be measured during flight and tracked over long timescales as the instrument and the truss cool down to ambient temperatures (~ 240 K). This can be accomplished by observing a bright point source with known position periodically during a flight and identifying the center of the interferogram response (see Appendix II).

5.2 Derived sensitivity and faintest detectable targets

Incorporating these sources of noise with the formulas derived in the previous sections leads to the sensitivity values shown in Table IV.2. In this table we show the sensitivity in the two bands. The minimum detectable flux density (MDFD), which is the flux that provides $\text{SNR}_{\mathcal{I}} = 1$ in a single interferogram, is 15 Jy and 26 Jy in band 1 and 2 respectively. For 200 scans averaged with a OPD noise between scans of $5 \mu\text{m}$, the MDFD is 1 Jy and 2 Jy, using a matched filter efficiency of 0.5 and 0.4, respectively (Mighell, 2005). The faintest

detectable spectroscopic point source that leads to a spectral SNR = 5 is 25 Jy and 13 Jy, respectively. These are determined for “normal observing”, which consists of co-adding 200 scans in 10 minutes that span the whole 2’x2’ field of view, using a spectral resolution of $\mathbf{R} = 10$ and a nominal OPD noise of 5 μm rms.

At the bottom of the table, we also show the results in case we were using the instrument in an “enhanced sensitivity” mode. This mode is mentioned here to illustrate the flexibility of the interferometer and its observing modes. It consists of increasing the individual integration time for each point in the interferogram by a factor of 3, while reducing the interferometric field of view by the same factor of 3: while the intrinsic field of view is unchanged at the detector, for the same scan time we only cover enough OPD range to cross ZPD for a subset of the pixels of the detector (and obtain a scan of the same length). This mode could be used for example for isolated targets which are located in less crowded star fields, by optimizing the time spent close to ZPD, where there is more signal (as we are interested in low-resolution spectroscopy). BETTII’s observing parameters can be changed during flight so that the instrument stays flexible to optimize the chance of seeing fringes.

Finally, we show the overall sensitivity as a function of point source flux density (Eq. IV.19) for both observing modes and both bands in Figure IV.4. In normal background-limited regime, the sensitivity curves should be straight lines. Here, OPD noise creates a decrease in overall sensitivity as a reduction in coherent power, but also, for brighter targets, from the power lost from the fringe that is converted to white noise (which causes a deviation from straight lines). For very bright targets of 50 Jy or more, it is possible to measure the OPD accurately within each interferogram by tracking the fringes in the science channels themselves (see Appendix C). For sufficiently large SNR, this

process has less error than the assumed 5 μm OPD noise coming from the indirect OPD estimation, so the OPD noise decreases for these very large fluxes to become negligible. This is particularly attractive for in-flight testing and calibration.

It is important to note that for sufficiently faint targets, it is impossible to accurately measure the OPD using single scans or co-adds of scans: we rely on the OPD estimator to have sufficient stability to properly co-add scans until the next calibration measurement. This needs to be considered carefully when planning the observation strategy, as long stretches without calibration could lead to a total loss of the OPD information (hence a total loss in scientific data), due to other OPD noise contributors such as thermal drifts that impact the payload on long timescales.

6 Conclusion

Spatio-spectral interferometry can enable high resolution spectral imaging of wide fields at far-IR wavelengths. Implementation of the technique provides some new instrumental challenges compared to traditional Fourier Transform Spectroscopy, such as the fact that the measured spectrum is a mix of the source's spectral and spatial information.

In a double-Fourier system, the zero path difference for each detector pixel occurs at a different delay setting of the delay line. The delay stroke needed to cover a scientifically interesting field of view is equivalent to a spectral resolving power of 100's to 1000's for the central pixels.

We present an analysis of the impact of Gaussian intensity and OPD noise on the spectral sensitivity. Intensity noise, essentially thermal noise from the optics, sky, astrophysical background, and detector, is similar to noise in FTS systems with the exception

that the longer scan lengths required to cover the spatial field add noise; this can be mitigated by cutting the interferogram for each pixel into smaller arrays centered on each source's ZPD to match the desired spectral resolving power, and by apodizing the interferogram to increase sensitivity to the spectral properties of interest. OPD noise is not usually relevant for FTS systems, but is intrinsic to double-Fourier instruments, since the two incoming beams go through long separate paths before combination. For instruments on balloons or in space, the OPD noise is expected to be dominated by disturbances from the instrument and from pointing errors. On average, OPD noise reduces the coherent power in the interferogram, and converts the power lost from the fringe into additional white noise in the spectrum. We argue that there are three relevant noise timescales: the time to take a single data point, the time to collect a complete interferogram, and the time to co-add M interferograms together in a track. The latter corresponds to the timescale that the source spatial visibility function changes significantly, due to the rotation of the baseline angle on the sky.

We derive the spectral sensitivity of double-Fourier instruments to intensity and OPD noise. The expressions in this paper are derived in the general case and can be used to design any instrument that implements this method.

Applied to the case of BETTII, these equations lead to spectral sensitivity estimates of 25 and 13 Jy in its 30-50 μm and 60-90 μm bands, respectively, to achieve a spectral SNR = 5 in 10 minutes with $\mathbf{R} = 10$ and an assumed OPD noise of 5 μm rms.

Parameter	Band 1	Band 2	Comment
Window emissivity	0.02	0.02	Measured in the lab
Telescope emissivity	0.077	0.077	10 mirrors at 0.992 reflectance
Sky radiance	$0.16 \text{ W.m}^{-2}.\text{sr}^{-1}$	$0.07 \text{ W.m}^{-2}.\text{sr}^{-1}$	Harries, 1980
Window radiance	$0.17 \text{ W.m}^{-2}.\text{sr}^{-1}$	$0.04 \text{ W.m}^{-2}.\text{sr}^{-1}$	Blackbody at 240 K
Telescope radiance	$0.17 \text{ W.m}^{-2}.\text{sr}^{-1}$	$0.04 \text{ W.m}^{-2}.\text{sr}^{-1}$	Blackbody at 240 K
Total optical efficiency	0.3	0.3	Per arm, includes detector
Photon power from the sky	35 pW	36 pW	•
Photon power from the window	40 pW	18 pW	•
Photon power from the telescope	108 pW	38 pW	•
Total absorbed photon NEP	$1.4 \times 10^{-15} \text{ W.Hz}^{-0.5}$	$7 \times 10^{-16} \text{ W.Hz}^{-0.5}$	From each arm
Detector NEP	$3 \times 10^{-16} \text{ W.Hz}^{-0.5}$	$3 \times 10^{-16} \text{ W.Hz}^{-0.5}$	For each detector
Total NEP	$2 \times 10^{-15} \text{ W.Hz}^{-0.5}$	$1 \times 10^{-15} \text{ W.Hz}^{-0.5}$	For the sum of both arms

TABLE IV.1: BETTII noise parameters

Single scan			
	Band 1	Band 2	SNR Target
MDFD	15 Jy	26 Jy	$\text{SNR}_{\mathcal{I}} = 1$
Normal observing (200 scans, 10 min)			
MDFD	1 Jy	2 Jy	$\text{SNR}_{\mathcal{I}} = 1$
Faintest pt. source	25 Jy	13 Jy	$\text{SNR}_k = 5$
Enhanced sensitivity (200 scans, 10 min)			
Faintest pt. source	14 Jy	7 Jy	$\text{SNR}_k = 5$

TABLE IV.2: BETTII sensitivity estimates

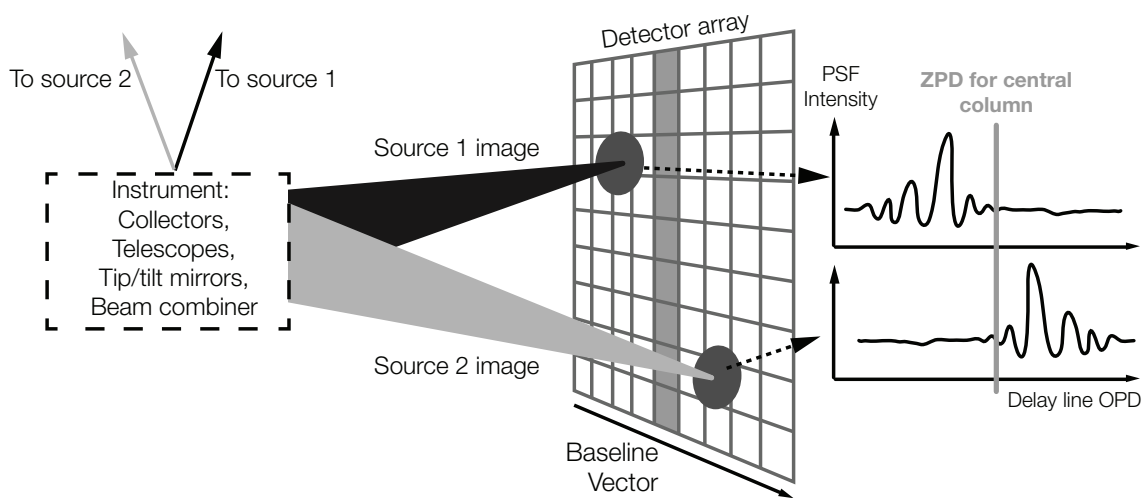


FIGURE IV.1: Concept of wide-field double-Fourier interferometry. Light from the instrument is focused after combination to an image of the sky on the detector array (represented as the grid). Each column of the detector has a distinct ZPD so the interferometric responses (right side) of two sources on different columns are centered around different delay positions. The gray stripe represents the central column on the detector array and its corresponding ZPD on the interferograms.

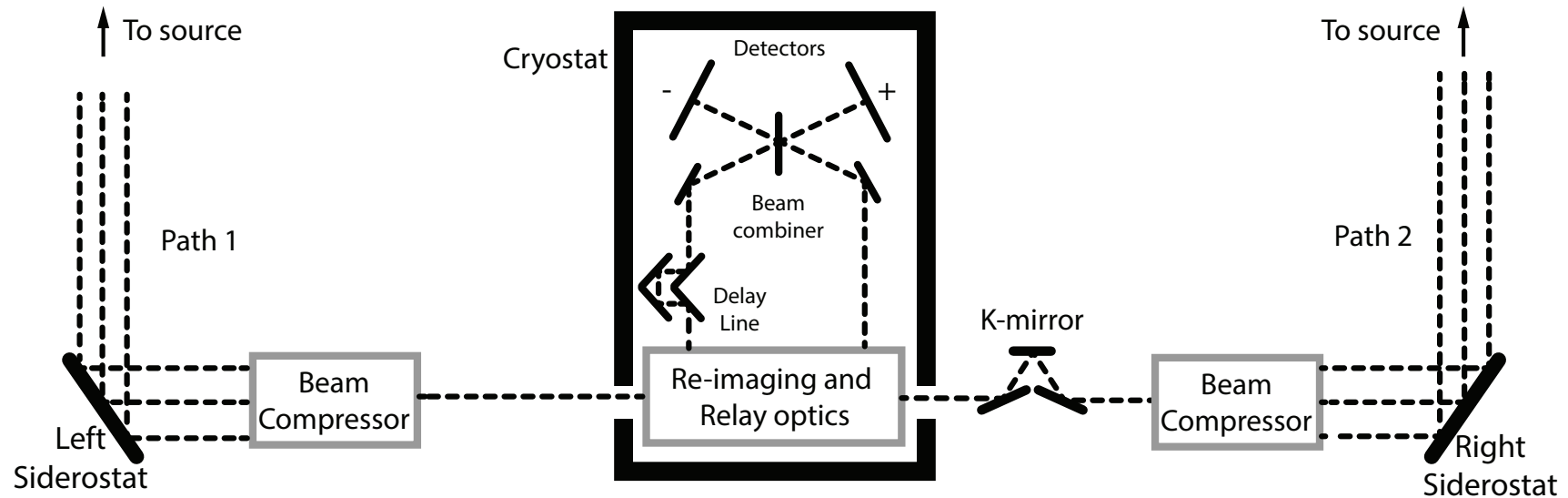


FIGURE IV.2: Optical train diagram of a typical far-IR, double-Fourier instrument. The K-mirror rotates the beam to align the fields of view of the two sides. Inside the cryostat, a set of optics re-image the pupil, implement a controlled instrumental delay between them with the Cold Delay Line, and relay them towards the central beam combiner. After the combiner, the beams are imaged onto the detectors. To see the BETTII-specific implementation of this design, see [2014PASP..126..660R](#)

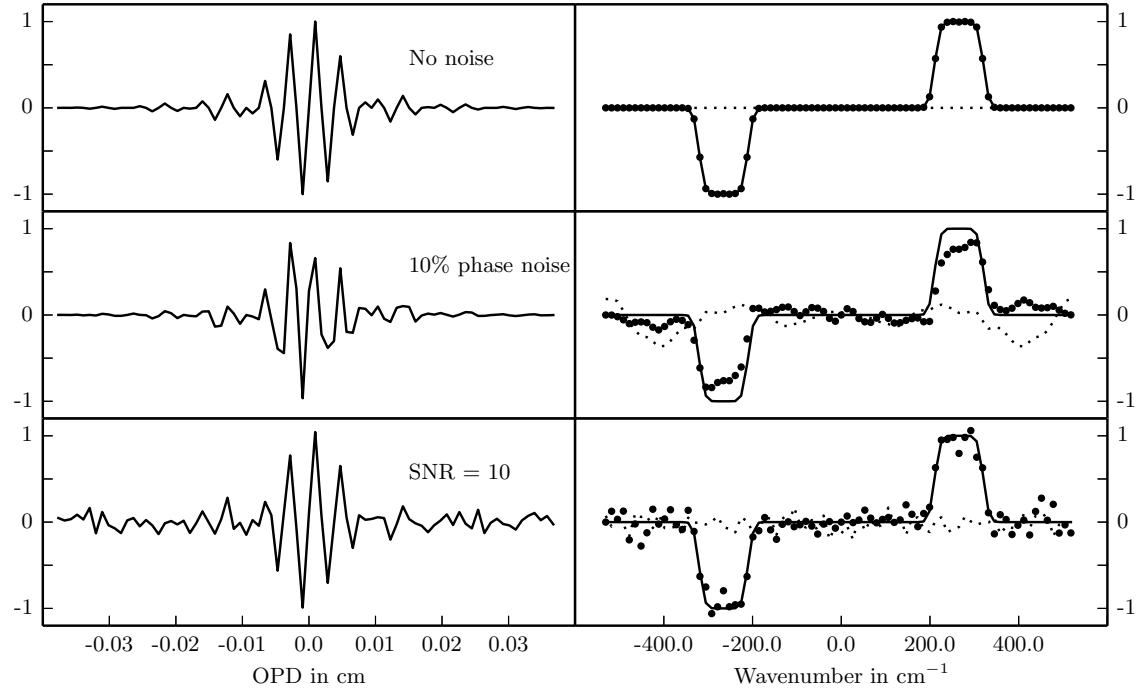


FIGURE IV.3: Effects of phase and intensity noise on the recovered spectrum (single realization of the noise). Left column: normalized interferograms, intensity as function of OPD. Right column: normalized DFT of interferograms. Solid: input spectrum multiplied by anti-symmetric transmission function; Solid circles: Imaginary part of DFT from interferogram; Dotted: Real part of DFT. First row: ideal measured signal, no noise; used for normalization of all other plots. Second row: results with a realization of phase noise of 10% at each point of the interferogram. Third row: results with a realization of intensity noise and $\text{SNR}_{\mathcal{I}} = 10$.

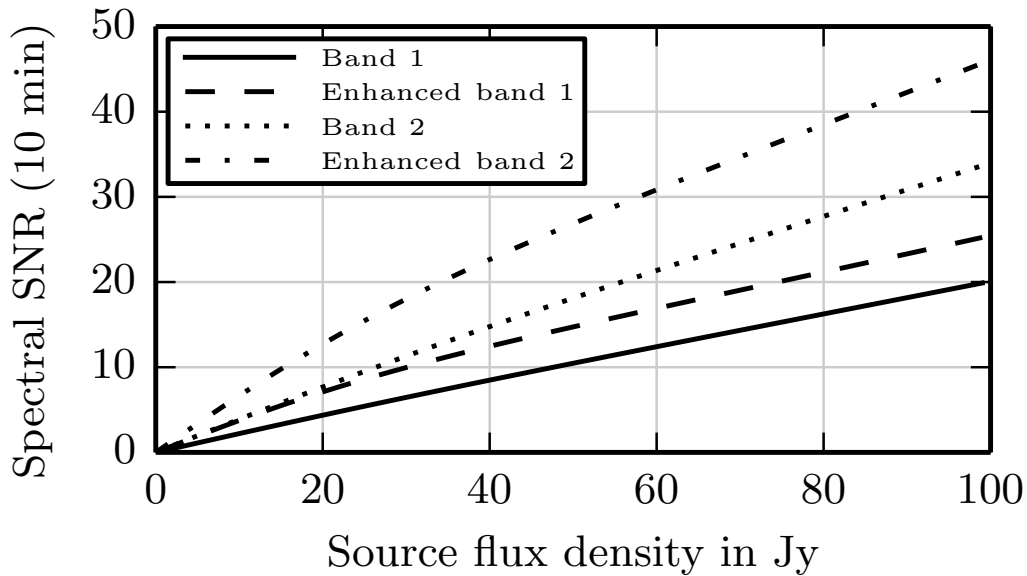


FIGURE IV.4: BETTII's spectral sensitivity. Solid: Normal observing mode, band 1; Dashed: Enhanced sensitivity mode, band 1; Dotted: normal observing mode, band 2; Dot-dashed: Enhanced sensitivity mode, band 2. This plot includes the technique of fringe tracking in the science channel for sufficiently bright sources (see Appendix C). As the source flux rises, the effects of the phase noise become larger and the SNR should reach an asymptotical value. However, with fringe tracking, the phase noise itself becomes smaller since one can see fringes in one single or a few consecutive scans, so the co-adding becomes easier. Thanks to the fringe-tracking, there is no regime where the phase noise is expected to be dominant on BETTII, provided that the control system performs according to expectations.

Chapter V

Attitude estimation and control for BETTII

Don't bother just to be better than your contemporaries or predecessors. Try to be better than yourself.

W. Faulkner

1 Control system architecture

Chapter IV sets the general background to double-Fourier interferometry when used mostly in spectroscopy mode. It sets the mathematical formalism to estimate the spectral sensitivity, given various sources of gaussian noises.

In this section, we see more directly how this applies to BETTII, and how the system is designed to satisfy these requirements in order to guarantee good observations.

1.1 Overall strategy

1.1.1 Requirements

The strategy that we developed aims at satisfying the requirements established in the previous section, under the cost, time and personnel constraints that we were subject to. It fundamentally relies on the fact that *knowledge* is more important than *control*. While several research groups [CITE WASPS] are attempting to provide sub-arcsecond balloon

gondola control, we are not going to. This strategy uses the fundamental advantage that the interferometer has over traditional pointed observatories: the decoupling of the phase with the pointing. This feature of interferometers refers to the possibility of obtaining electromagnetic interference even when the telescopes are slightly mispointed from the target.

There three levels of requirements for our instrument to produce interferograms. First, both arms need to be pointed at the target, so that an image of the target seen through each arm is formed at the detector. For our purpose this will largely be set by the limitation of the field of view of the instrument, which is about 2 arcminutes. When a target is not exactly on-axis with the telescope, it can still fall on the detector if tip/tilt correction happens downstream. The tip/tilt correction will create aberrations, but these are relatively well behaved at our wavelengths. Hence, this requirement can be expressed as an overall pointing requirement of the instrument to some amount that can be corrected in tip/tilt in each individual arms. We set this to $\pm 15''$. This also roughly corresponds to one single pixel on the short band detector, and half a primary beam's FWHM.

Once the instrument is pointed to the desired target to within $\pm 15''$, there needs to be a fine guiding system in each arm that allows for the remaining correction. This level of control needs to overlap the beams to a small fraction of a pixel to get maximum overlap and minimum visibility losses. We set this requirement to $1.5''$ r.m.s., which corresponds to a tenth of a pixel's size. The fine guidance system needs to operate over a range of at least $\pm 15''$ to pick up where the previous level of requirements stops. It also needs to happen with high bandwidth to ensure that only minimum motion is occurring at timescales comparable to a data acquisition timescale. This system is described in section [§].

Finally, an angular mispointing of the baseline vector with respect to the target can be might still exist, even if both beams are overlapped properly. This introduces an unwanted optical delay that can push the fringe packets outside our nominal OPD scanning range. Control of this optical delay is critical for interferometry, as it is required to properly reconstruct the OPD axis of the interferograms that are the elementary data blocks of the instrument. This can be achieved using a delay line . This is commonly done for all interferometers on the ground [CITE], and we will implement a device like this on BETTII as well [section]. For this to work, we need to be able to monitor the changes in OPD accurately, which is equivalent, on short timescales, to accurately estimate the attitude of the payload.

A good estimate of the attitude of our payload can lead to an accurate angular difference between our baseline vector and our target. This angular difference can be converted to an OPD using simple geometric arguments, and can then be fed to the delay line for correction. With an 8 m baseline length, an mispointing of $1''$ along the baseline direction corresponds to an OPD of about $40\text{ }\mu\text{m}$, or one full wavelength of BETTII's short-wavelength band. In order to produce quality interferograms, we will need to know the OPD to a fraction of this [SEE previous section].

1.1.2 Control loop design and operating modes

The three levels of control that we need are:

1. Coarse control of the entire gondola to within $\pm 15''$ of the target,
2. Fine pointing control of each beam to $1.5''$ r.m.s. at the science detector,
3. Fine knowledge of the inertial attitude to $\approx 0.15''$ r.m.s., followed by appropriate OPD control

At its fundamental level, the problem is to implement a system that satisfies these requirements, starting with only the target's location in right ascension (RA) and declination (DEC). Ideally, the system needs to be able to achieve these goals autonomously. All of the operating modes follow from this.

All of the pointing will be done in the reference frame of the gondola, which is tied solidly to the reference frame of the gyroscopes (nominally they are the same) and the star cameras (nominally off by -45° about the \mathbf{y} axis). In the following sections, we describe how the inertial attitude of the gondola is determined. Once it is known, a target's RA and DEC can be converted to a desired local azimuth ϕ_{Az} and elevation ϕ_{El} in the spherical coordinates attached to the gondola reference frame (see Fig. V.1). It is important to note that when we mention "azimuth", we are not referencing to any cardinal directions, as it can be done for other applications. For us, an azimuth is one of the two spherical angles that describe the position of our target in the current gondola reference frame. Note that the elevation angle is defined as being zero in the $(\mathbf{x}_g, \mathbf{y}_g)$ -plane.

Once the turbulence from the ascent have died out, the control system determines where the gondola is currently pointing using the star cameras. For the software to process the star camera image, the payload has to be still to avoid blurring of the stars on the CCD. Hence, the first order of business is to slow down the payload's inertial velocity, which is measured by the gyroscopes. This is also called BRAKE mode.

The first time the system receives a star camera frame and identifies its inertial position, this triggers the estimator algorithm that constantly combines gyroscope and star camera information. From this point on, we have a reasonable estimate of where the gyroscope reference frame is pointed with respect to the inertial frame.

When a new target in RA and DEC is set by the flight computer, the system will

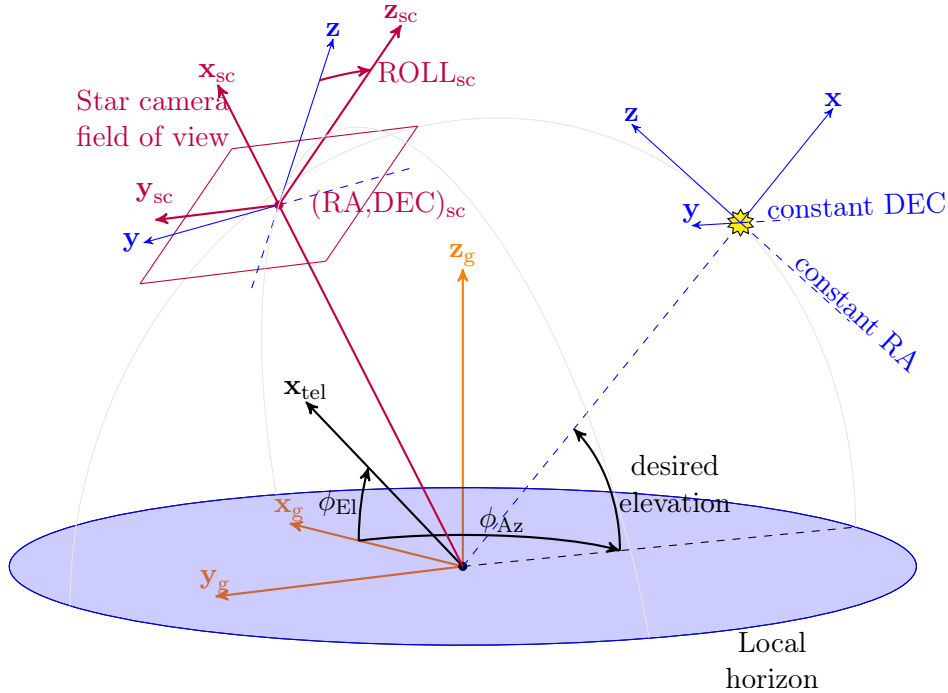


FIGURE V.1

enter the SLEW mode. This creates a profile of desired azimuth position and velocity as a function of time. The software commands the reaction wheels to turn the payload about its z axis. At the same time, it commands the rotation stages that control the telescopes' elevation, to go to the desired elevation. The control in elevation and control in azimuth are entirely decoupled.

When we complete the deceleration phase as we get close to our target, we switch to TRACK mode. This mode is attempting at maintaining control of the telescope within $\pm 15''$ of our target.

Finally, for each of the two arms, we need to acquire a guide star onto our guide camera [section]. This requires a fast imaging capability and a fast-steering tip/tilt correction mechanism to freeze the motion of the sky on the guide camera. This is ACQUIRE mode. Two images of the sky are made on the detector, one from each arm; the guide star is located in each image, and the tip/tilt mechanisms are actuated to center this star onto

a location of the detector that corresponds to maximum overlap at the science detectors. Once the star is centered onto that location, the window size of the camera decreases, and the acquisition speed increases. Ultimately, we will get two patches of 35×35 pixels at ≈ 50 Hz. When this acquisition speed is reached we consider ourselves in LOCKED mode.

In both ACQUIRE and LOCKED mode, the position of the two tip/tilt platforms contains information on the overall mispointing of the optical train: when the actuators are both off in the same direction with respect to their nominal position, it means that the entire truss is off the guide star by this amount. When available, this information is used by the estimator along with the gyroscope and star camera information to compute the best possible attitude estimate. Since the tip/tilt is tied to the actual optics train, its information is heavily weighted compared to the other sensors.

When the two guide star images are centered, this means proper overlap of the far-infrared beams at the science detectors. Hence, we are in a position to spot interferometric signal, which will translate to a modulation of the intensity of the coherently combined image as a function of OPD. The OPD is constantly modulated with the Cold Delay Line [section], independently of the mode in which we are. However, residual mispointings can create large unwanted OPD perturbations. Hence, during TRACK and ACQUIRE mode, the Warm Delay Line mechanism is activated. Its goal is to use the estimated change in baseline position to predict the resulting OPD variations - and correct them directly in OPD space.

During the LOCKED mode, we need to consider what happens if we lose the guide star. Since the field of view is relatively small compared to the expected motions of the gondola, the guide star could technically walk outside the range of the guide camera - at which point the attitude estimation relies temporarily on the gyroscopes as we switch

back to ACQUIRE mode and the guide camera increases its field of view (and decreases its speed) until it finds the guide star.

Mode	Description	Actuators	Sensors
SAFE	All PID gains set to 0; siderostats point towards zenith; azimuth is not commanded; used during ascent, emergencies	– CDL	– Gyros – Star cameras
BRAKE	Used to slow down the payload after undesired motion; derivative gains only, no position loop	– CCMG – Rotators – CDL – Mom. Dump	– Gyros – Star cameras – Elevation encoder – Gimbal encoder
SLEW	Used to move to target with a set velocity profile	– CCMG – Rotators – CDL – Mom. Dump	– Gyros – Star cameras – Elevation encoder – Gimbal encoder
TRACK	Used to stabilize payload after slew, track target coarsely	– CCMG – Rotators – CDL – Mom. Dump – WDL	– Gyros – Star cameras – Elevation encoder – Gimbal encoder – WDL
ACQUIRE	The guide camera grabs images for each arm and identifies the location of a guide star in increasingly smaller quadrant sizes	– CCMG – Rotators – CDL – Mom. Dump – WDL – Tip/Tilts	– Gyros – Star cameras – Elevation encoder – Gimbal encoder – Tip/Tilt encoders – Guide camera
LOCKED	The intensity of the target in the science detector is measured, and the central phase is estimated	– CCMG – Rotators – CDL – Mom. Dump – WDL – Tip/Tilts	– Gyros – Star cameras – Elevation encoder – Gimbal encoder – Tip/Tilt encoders – Guide camera – Science detector

TABLE V.2: BETTII operating modes. Each operating mode has a set of PID gains for each individual loop.

Note that the Cold Delay Line (CDL) is running in closed loop during all the modes. Since the environment inside the cryostat is not changing from test to flight, there is no reason to ever turn the loop off or keep different sets of gains for different operating modes. The CDL is its own closed system.

1.1.3 BETTII Coordinate systems

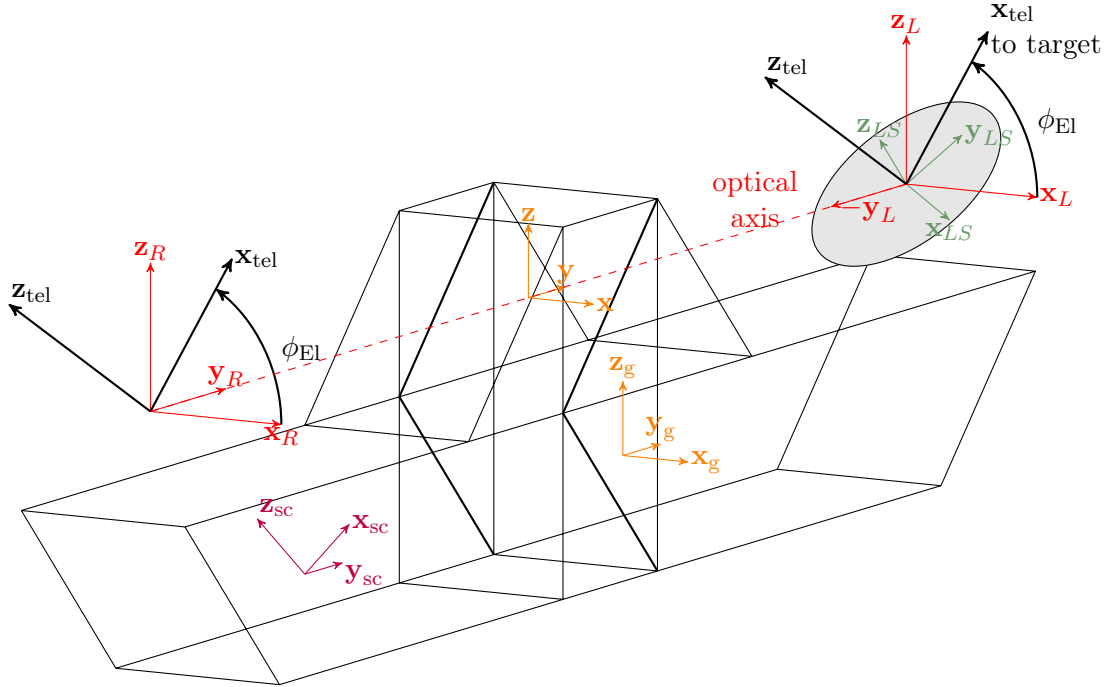


FIGURE V.2

1.2 Subsystems

1.2.1 Gyroscopes

We purchased three SRS-2000 fiber-optic gyroscopes from Optolink. This gyroscope technology uses the Sagnac effect and is the cutting edge in inertial rotational velocity measurements (for a review of the state-of-the-art see, *e.g.* El Badaoui et al., 2014). We chose these devices for their incredibly low angular random walk, which is a measure of their inherent noise. If we were to trust the gyroscope measurement and integrate its velocity to obtain a position estimate, the estimation error we would make after 1 hour of integration has a standard deviation of about 2 arcseconds.

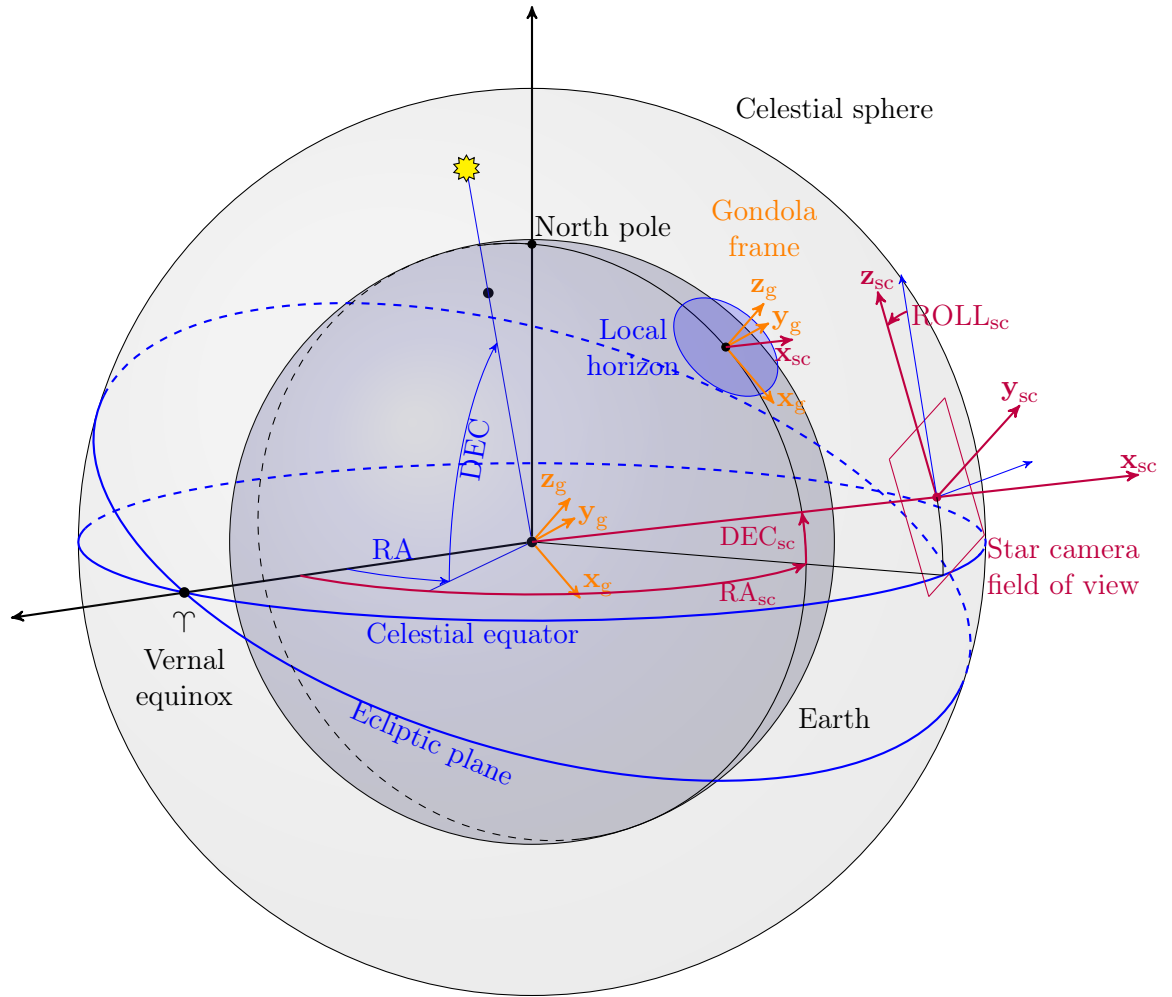


FIGURE V.3

The devices have a bandwidth of 50 Hz, but can be triggered at up to 2000 Hz. Their extreme stability is contingent upon proper temperature stabilization, which is done with a closed-loop set at their calibration temperature of $23.5^{\circ}\text{C} \pm 0.5^{\circ}\text{C}$ using an active built-in Peltier element. This Peltier element transforms electric power into either heating or cooling (Peltier, 1834).

In the following, we describe how we measure the various properties of the gyroscopes, and discuss how they compare to the specifications.

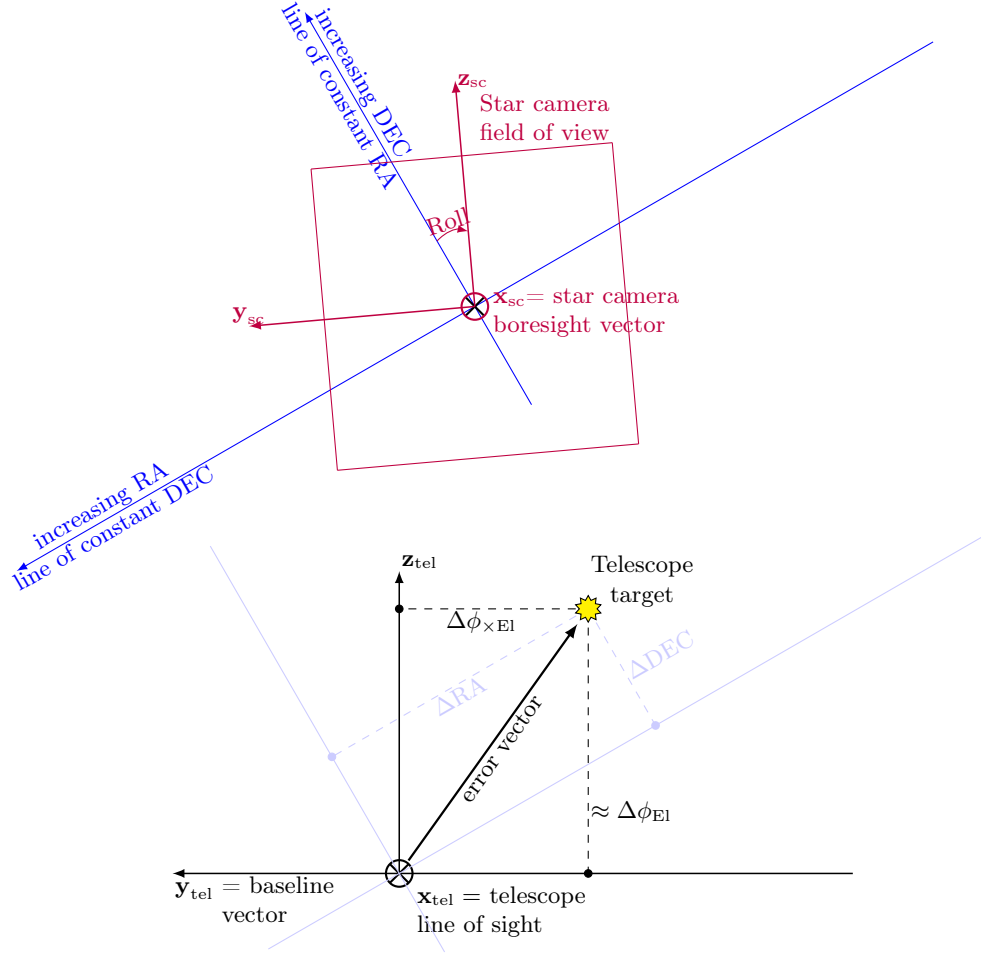


FIGURE V.4

1.2.1.a Sensitivity tests

However, their sensitivity has complicated some of their testing. As soon as we attach a gyroscope to any structure, it measures its vibrational modes, which makes it hard to make a stable measurement of the gyroscope's drift stability. This includes the vibrations that are inherent to the building in which they are placed.

We were successful at measuring the gyroscope properties over long periods of time by attaching them flush to a heavy slab of metal, and putting the slab of metal flush on the vibration-isolating floor of one of NASA Goddard's optics labs in building 34.

We proceeded to an identical series of tests for each gyroscope:

1. We acquired data at 2000 Hz for 10 min to measure a proper power spectral density and characterize the noise;
2. We acquired data at 100 Hz for ~ 8 h to study the drift properties.

The properties that we are looking for are typical instantaneous angular random walk, and the overall drift instability of the gyroscope's mean. When the gyroscopes are set on the floor, they measure a component of the Earth's rotation vector in inertial space. The mean of the measurement depends on the exact angle at which the device is placed with respect to the zenith vector, and is of no importance for this noise study. We seek to understand how much the mean varies over long periods of time. To avoid disturbances from the building vibrations (opening/closing of doors, etc), we operated entirely after regular working hours.

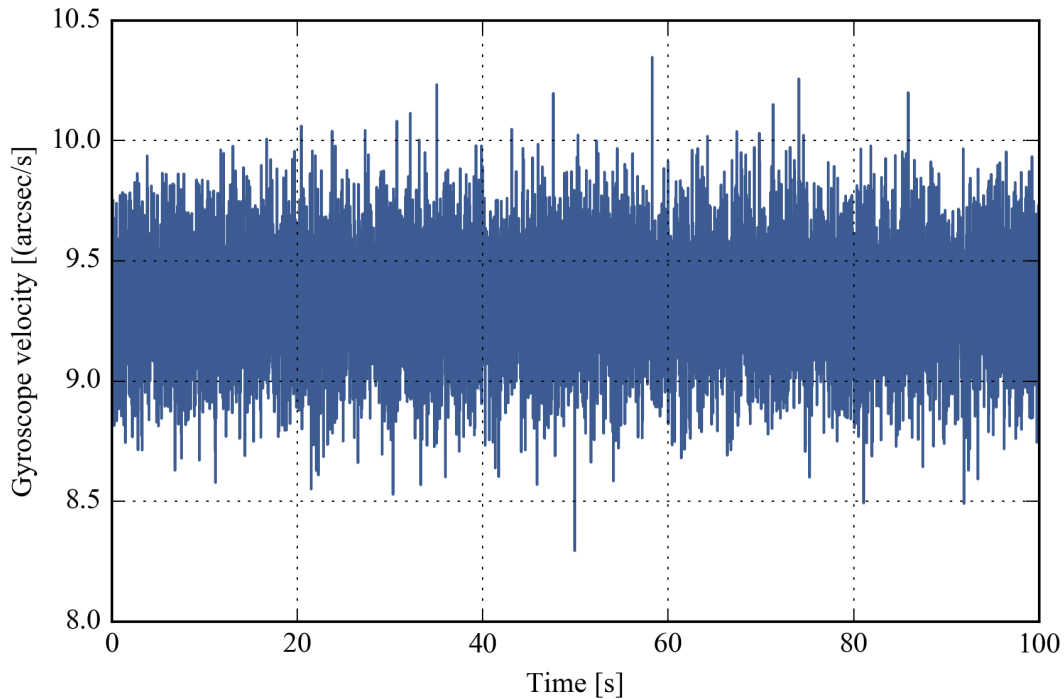


FIGURE V.5: Snapshot of 1000 s of gyroscope data, taken from our 8 h data sample.

The angular random walk (ARW) is a measure of the effects of integrating a noisy velocity measurement. The specification from the manufacturer is $\text{ARW} = 5 \times 10^{-4} \text{ deg h}^{-0.5}$. This means that if we integrate the gyroscope's rate for 1 hour, the $1 - \sigma$ uncertainty on our position would be $5 \times 10^{-4} \text{ deg} \sim 1.8''$. For an integration time of 1 second, it would be $0.03''$. For a single integration time step $\Delta t = 10 \text{ ms}$, it would be $0.003''$.

The manufacturer specification gives a maximum bias instability over a wide range of temperatures less than 0.005 deg h^{-1} . This represents how much the mean angular velocity is expected to vary. These tests are an attempt to verify these numbers.

1.2.1.b Power spectral density

The usual frequency-domain analysis tool is the power spectral density (PSD). This allows us to spot any frequency peaks in the data, and let us look at the $1/f$ noise behavior, which is the typical low-frequency behavior that indicates drifts in the signal. The 100 Hz data is all we need, as the gyroscope's bandwidth is 50 Hz. Hence, the 2000 Hz data does not contain any more information than the 100 Hz. In fact, while plotting the PSD of the 2000 Hz data, we can see clearly the break at 50 Hz characteristic of a 50 Hz low-pass filter.

It is important to note that in their factory settings, the gyroscopes' noise distribution was not normal at all. It exhibited electronic peaks with many harmonics, at frequencies that were varying as a function of the gyroscope inclination (as it was measuring different components of the Earth's rotation). After talking to the manufacturer, we determined that it was caused by the closed-loop algorithms inside the gyroscope electronics. The problem was known by them, and the remedy was to inject a random phase perturbation in the closed loop. This had the effects to get rid of those frequency peaks, at the cost of increasing the overall noise variance by a factor of 4. The noise levels that

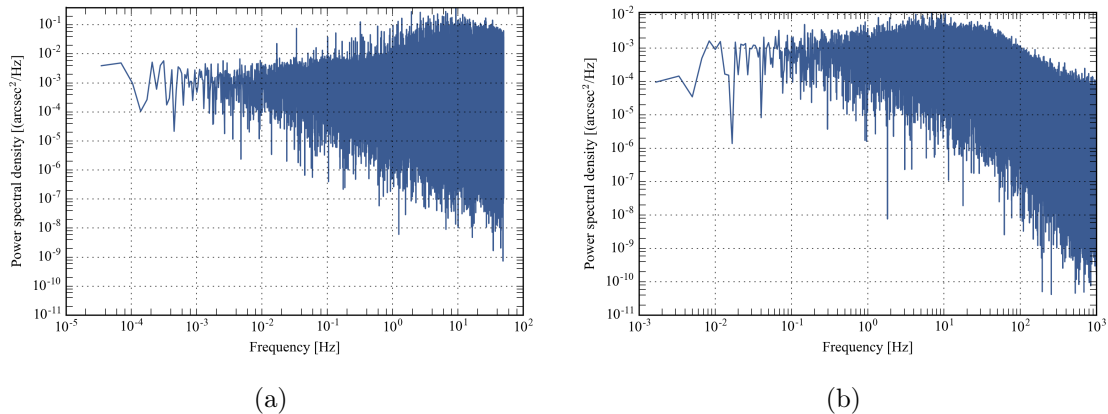


FIGURE V.6: (a): Single-sided power spectral density for gyro 11005, an 8 h sample with a sampling rate of 100 Hz, showing no particular feature (large peaks or resonances). (b): Single-sided power spectral density for gyro 11005, a 10 min sample with a sampling rate of 2000 Hz, showing no electronic resonance peak or other feature. We can notice the -3 dB break at around 50 Hz.

are specified by the company are very close to the noise seen when using that random phase modulation. Hence, if one does not care as much at the frequency content of the gyroscope, it is possible that this device could work even much better than it does for us.

1.2.1.c Normality tests

We ran a few standard normality tests on chunks of the 8-hour data for each gyroscope. While the tests on individual small chunks of data never reject the null hypothesis (that the distribution is normal), the distribution of the total 8 hours does with a very high probability, using both the Anderson-Darling and the Kolmogorov-Smirnov test. It means that it is extremely unlikely that the measured noise over 8 h is coming from a normal distribution. [SHOW TABLE OF TEST RESULTS?]

Since the data is always consistent with being normally distributed over timescales of tens of minutes, after close inspection of the long-term quartile plots and histograms, we determined that it would be safe to consider the distribution as normal for the purpose

of our attitude estimator (see Fig. V.7).

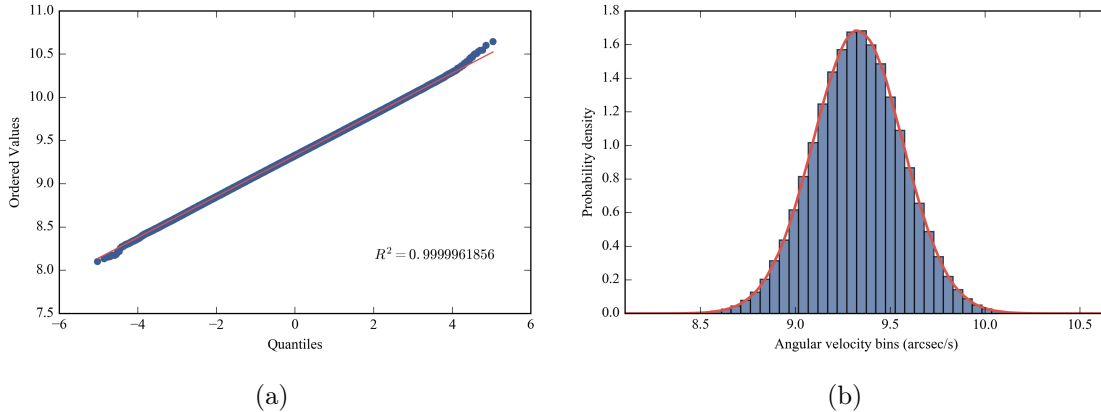


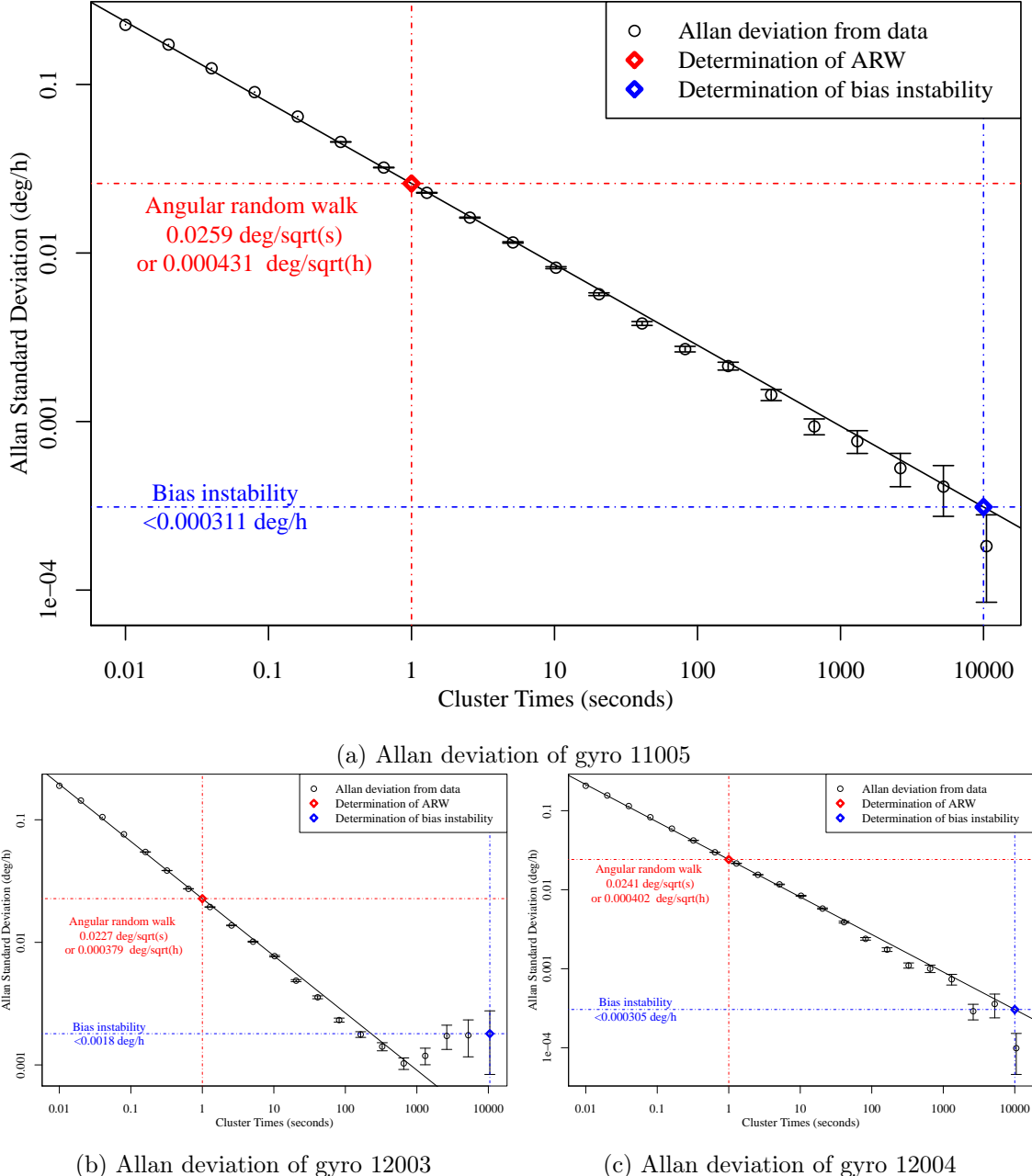
FIGURE V.7: Normality analysis of the gyroscope signal over 8 h of data taken at 100 Hz. (a): Normal quantile-quantile plot for an 8 h sample with a sampling rate at 100 Hz. Here the measured quantiles (fraction of the measured values under a certain value) are plotted against the theoretical quantiles from a normal distribution. The red line is the theoretical distribution if the data were taken from a normal distribution. (b): Probability density distribution for an 8 h sample with a sampling rate at 100 Hz. In red, the theoretical normal distribution we obtain with the measured mean and standard deviation from the sample. While the data is not strictly normally distributed, we consider that it is sufficiently close to a gaussian distribution.

1.2.1.d Allan variance

Another common tool to study of the gyroscope's performance is to plot the Allan variance. The Allan variance gives a time-domain analysis of the gyroscope's noise that is complementary to the power spectral density. [TALK ABOUT HOW TO INTERPRET THE ALLAN VARIANCE GRAPHS]

1.2.1.e Conclusions

The gyroscopes were successfully tested in the environmental chamber, with no noticeable change in performance except a much larger power draw, due to the Peltier element maintaining the fiber temperature.



1.2.2 Star cameras

1.2.2.a Design

We have designed, built and tested a custom star camera setup that provides higher accuracy measurements than commercially available devices. Our collaborators from Cardiff University provided the star camera software, which solves for the inertial orientation from

Measured property	Gyro #11005	Gyro #12003	Gyro #12004
Standard deviation (deg h ⁻¹)	0.237	0.199	0.217
Angular random walk (deg h ^{-0.5})	4.31×10^{-4}	3.79×10^{-4}	4.02×10^{-4}
Bias instability (deg h ⁻¹)	3.11×10^{-4}	1.8×10^{-3}	3.05×10^{-4}

TABLE V.3: Properties of the gyroscopes determined from the Allan variance analysis on an 8 h sample with a sampling rate at 100 Hz. Note that $1 \text{ deg h}^{-1} = 1 \text{ arcsec s}^{-1}$, and the Earth rotates at about 15 arcsec s^{-1} about the line joining the two poles.

a given picture. This software is a C++ set of routines that was originally developed for the EBEX balloon experiment (Oxley et al., 2004).

Our star camera design features an old-generation Nikon Nikkor 300 mm f/2.8 telefocal lens with manual focus and extended hood. These lenses were manufactured between 1977 and 1982 and can be found today online through websites like e-Bay. The lens provides low chromatic aberration, a magnification of $688'' \text{ mm}^{-1}$, a wide field of view ($\approx 10^\circ$) and a collecting area of 90 mm^2 which is larger than most star tracking assemblies. This old lens does not feature a built-in autofocus or any of the image stabilization actuators commonly found in modern lens assemblies: these could have become a liability in the severe balloon environment.

Our camera is a USB3.0 Point Grey Grasshopper3. The CCD is a Sony Pregius IMX174 CMOS sensor with 1920×1200 pixels at $5.86 \mu\text{m}$ pitch. This provides a field of view of $2.14^\circ \times 1.34^\circ$ and a pixel scale of $4.02''/\text{pixel}$. It features a very convenient software suite which works with all the Point Grey camera products, and leaves room for future potential upgrades of the camera. The detector characteristics are summarized in Table V.4.

We have successfully cycled the camera in the environmental chamber all the way until the camera's internal thermometer indicated a temperature of -80°C , and it continued operating nominally.

TABLE V.4: Star camera properties

Property	Value	Description
Quantum efficiency at 525 nm (%)	76	Fraction of incoming photons that create signal
Read noise (electrons)	6.83	Error made when reading the pixel's value
Absolute sensitivity threshold (photons)	9.77	Minimum number of photons required to get a SNR = 1 on a pixel
Well depth (electrons)	32 513	Maximum number of electrons a pixel can store

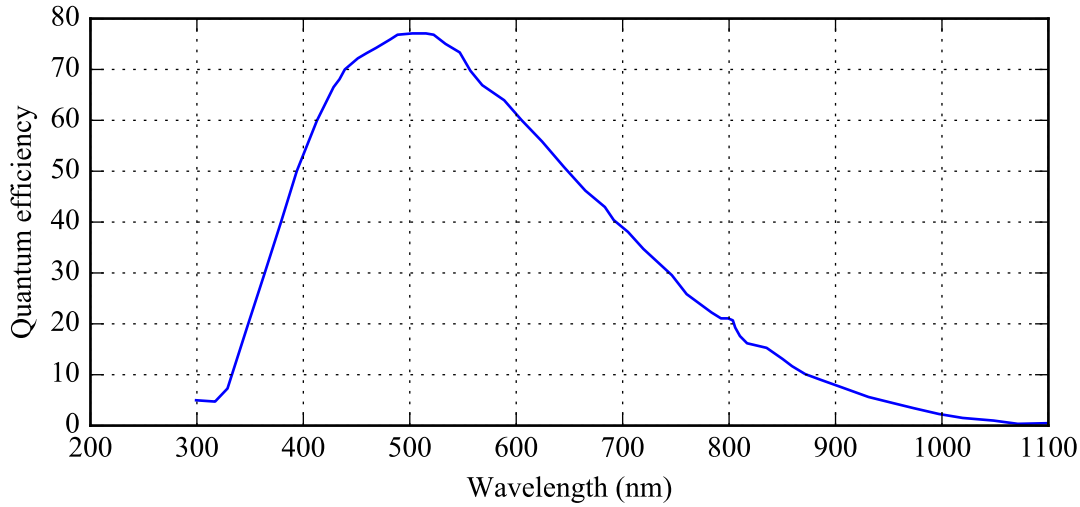


FIGURE V.9: Quantum efficiency of star camera CCD.

1.2.2.b Focusing strategy

Focusing the camera could be required at float due to the change in temperatures that could create a shift of the focal plane. We implemented our own autofocus mechanism, a belt is attached between the lens' focus ring and a stepper motor. When the stepper motor turns, it turns the focus ring. We tested this very simple configuration in our environmental chamber only to realize that the belt was loosing grip when the temperature was too cold. To fix this problem, we added a spring-based belt tensioner which adds a $\approx 20\text{ N}$ of force to the belt.

At cold temperature and low pressure, we noted that the glass in the lens began to exhibit radial cracks, presumably caused by the CTE difference between the steel housing and the glass material. These cracks don't noticeably affect image quality, but of course they could cause the glass to shatter if they become too large. Hence, it was decided to maintain the outside temperature of the lens above 0 °C at all times during flight.

1.2.3 Azimuth control (CCMG)

The CCMG features multiple encoders and motors. First, there is a brushless DC motor that spins each wheel, with a relative 13-bit encoder that monitors where the wheel is in its rotation. Second, there is a Beckhoff AS1050 stepper motor that controls the wheels' shaft angle. On the gimbal, there is a 13-bit absolute magnetic encoder that measures the angle of the wheels from some reference. We use the latter to know where the gimbal is positioned at power-up.

The motion controller that we use to monitor the wheel's speed is a brushless-DC Galil motion controller DMC-4020. It reads out the wheel encoders and controls the current to the wheels accordingly. It directly, independently implements the closed-loop system of the wheels, including all of the gains, acceleration/deceleration, and jogging speeds associated with the desired motion.

The motion controller was modified to accept an external clock pulse in order to synchronize the wheels' motion with our master clock signal. It requires a clock pulse at 1.024 kHz, and deviations from this value will require changing some of the gains - it is our understanding that the controller uses a 1.024 kHz crystal oscillator to generate its time basis, as some of the gains and parameters to the controller can directly be entered as, for example, "steps per second".

At power-up, the wheels immediately start accelerating to their cruising speed of 3000 rpm. They take about 10 minutes to reach their target. The wheels' frequency is set for the entire duration of the flight.

The gimbal is controlled with another Galil Motion controller, a 2-axis stepper driver DMC-4020, which can also be synchronized with an external clock. Only one axis is used for the CCMG, while the second axis is used by the momentum dump motor (see section 1.2.4). The controller operates in micro-stepping mode and has a very smooth response, in contrast to previous controllers we tested which create a lot of vibrations. The controller is set always to use 64 micro-steps per step, and the motor is a [REFERENCE] with 200 steps per revolution. The motor is outfitted with a Beckhoff AG1000 planetary gearhead with a 3.7:1 reduction ratio. The gearbox itself has a ratio of 25, which creates a total gear ratio of 92.5. Hence, a 360° revolution of the stepper corresponds to $360/92.5 = 3.9^\circ$ motion of the shaft. A motion of 1° of the shaft correspond to 3889 motion controller steps. A motion of 90° of the shaft correspond to 296 000 motion controller steps. Finally, the same 90° motion will translate to a 2048 step change in the gimbal magnetic encoder.

In practice, all of the control is done using the regular stepper motor encoder. The magnetic encoder is used for limit-checking and to feed back to the momentum dump mechanism. With this in mind, we can now relate the control signal (stepper motor micro-steps per second) to the physical torque that the wheels provide.

$$\Delta\theta_{[\text{rad}]} = \frac{2\pi}{92.5 \times 200 \times 64} \Delta(\text{micro-steps}) \quad (\text{V.1})$$

$$\sim 5.3 \times 10^{-6} \Delta(\text{micro-steps}) \quad (\text{V.2})$$

$$\Delta\theta_{[']'} \sim 1.09 \Delta(\text{micro-steps}) \quad (\text{V.3})$$

At 3000 rpm, the CCMG has a total stored momentum $M_{CCMG} = 20.8 \text{ N m s}$. Of course, depending on the orientation of the wheels, the momentum along the \mathbf{k} axis is only the projection of this momentum vector,

$$M_{CCMG,z[\text{N m s}]} = 20.8 \sin \theta, \quad (\text{V.4})$$

where $\theta_{[\text{rad}]}$ is the angle between the horizontal axis and the rotation axis of the wheels. This makes sense: when the wheels are horizontal, there is no momentum projected on the \mathbf{k} axis because the rotation vectors of the wheels are orthogonal to \mathbf{k} . When the rotation axes are aligned with \mathbf{k} , we have the maximum momentum.

The torque is the variation of the momentum with time. So we can write:

$$\mathcal{T}_{CCMG[\text{N m}]} = \frac{d}{dt} M_{CCMG,z} \quad (\text{V.5})$$

$$\mathcal{T}_{CCMG[\text{N m}]} = 20.8 \times \dot{\theta}_{[\text{rad s}^{-1}]} \cos \theta \quad (\text{V.6})$$

$$= 1.1 \times 10^{-4} \times n_{[\text{micro-step s}^{-1}]} \cos \theta \quad (\text{V.7})$$

The entire CCMG assembly was tested in a vacuum chamber at cold temperatures. Several heaters are strategically located in the assembly to allow some thermal control for all the electronics in case issues arise.

1.2.4 Momentum dump mechanism

The momentum management strategy consists of using the balloon as a large momentum reservoir. The control system then needs to be equipped with a system that allows a transfer of momentum between the gondola and the balloon, which are connected through the parachute and ladder.

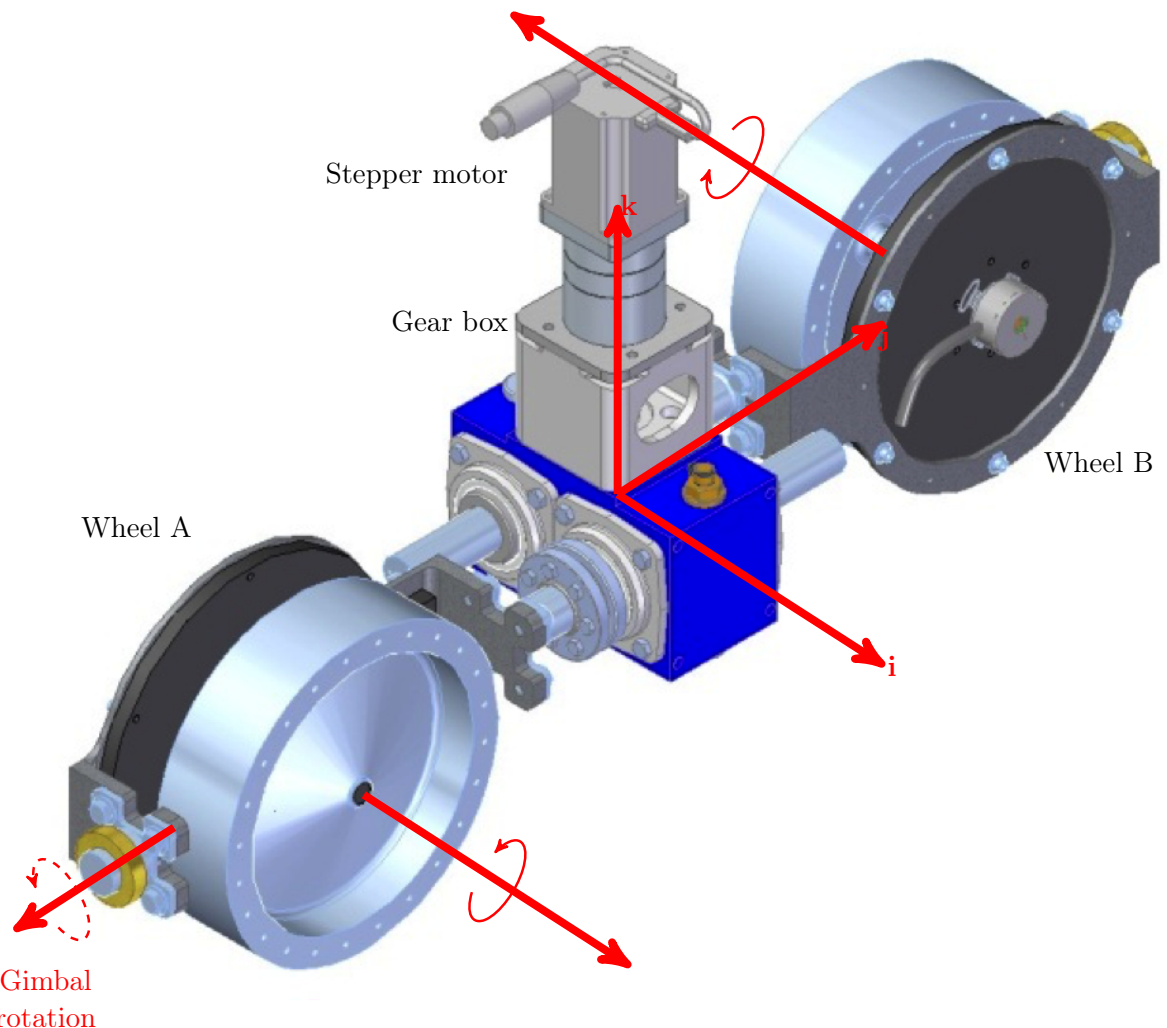


FIGURE V.10

For this purpose, BETTII uses a design which has successfully flown on previous balloon payload (Fig. V.12), with several improvements over its predecessors. It consists of a steel and titanium setup which will make the junction between the bottom of the balloon train (at the very bottom of the ladder) and the very top of the gondola. The critical material is an alloy of steel that has been heat treated and is particularly strong. The setup consists essentially of a pivot and a pin made with this allow, connected together with grade 8 bolts. The top of the pin is attached to the pivot, and has a lip at the bottom on which two circular bearings are stacked: the bottom one uses ceramic balls (for their

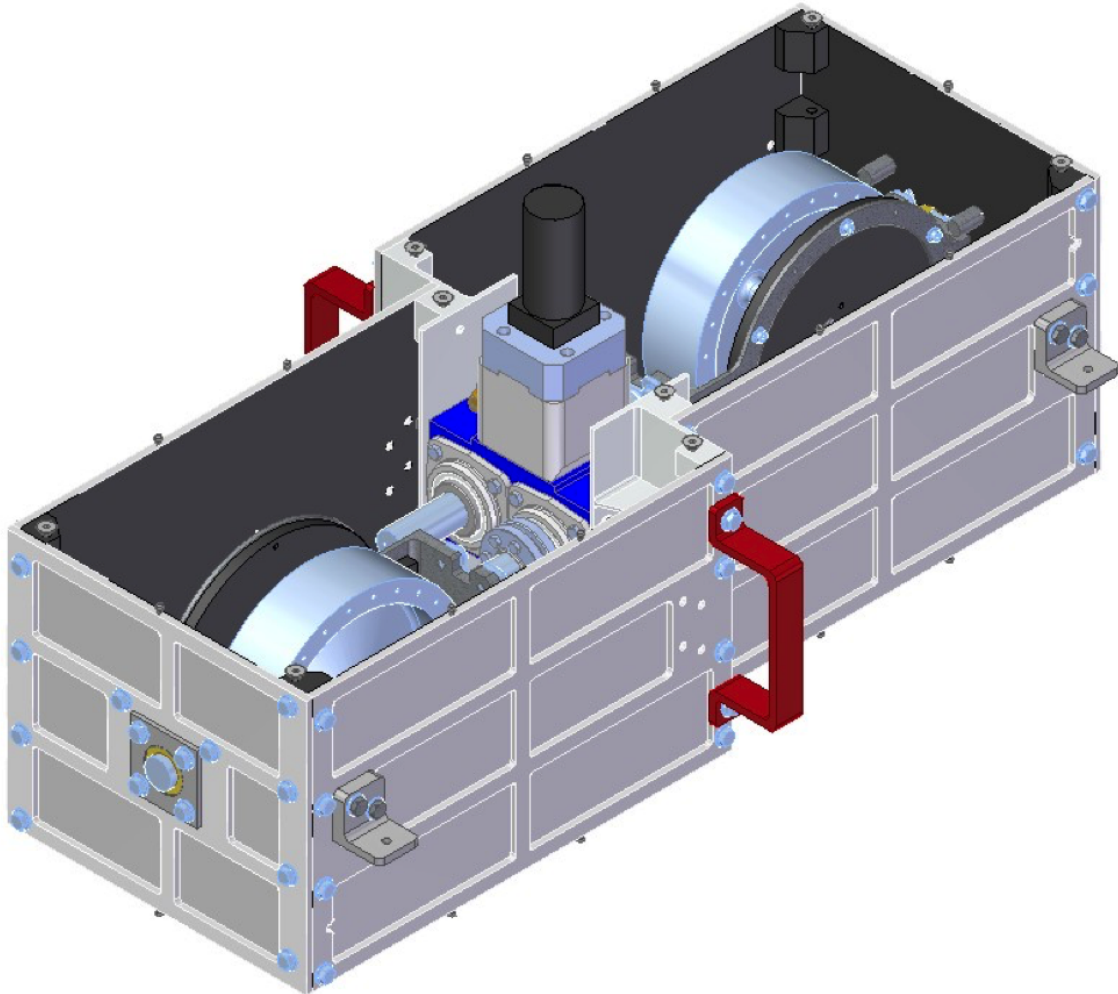


FIGURE V.11

excellent friction properties and long lifetime), and the top one uses steel balls (for their excellent strength). Between the two bearings, there is a metal holder that extends all the way down below the pin. On top of the steel bearing, a titanium case sits, which attaches to the entire gondola.

The momentum dump mechanism is a simple rotary stepper motor. Its housing attaches to the steel case of the assembly - while its shaft attaches to the metal holder between the two bearings. With an assembly like this, when a vertical upward force is exerted, the gondola's weight pushes on the bearings, which then push onto the pin's lip.

When the stepper motor starts spinning, it spins only the top part of the bottom bearing, and the bottom part of the top bearing: the friction force that this exerts allows to slowly dump momentum into the pin, hence into the balloon train.

This configuration seems dangerous since the entire weight of the payload rests on the two bearings and the pin's bottom lip, which can be hazardous during descent when the parachutes open and the payload can experience up to a 10 g vertical load. Hence, this piece of the assembly needs to be thoroughly tested and certified before launch.

In practice, the momentum unloading happens quite slowly due to the very low friction of the bearing. As the stepper turns the bearing, it slowly turns the entire train along with the pivot for a few tens of seconds. When the train has experienced sufficient twist, it then unfurls and gives a slight kick in the opposite direction. We observed this in our data and will discuss this more in [SECTION].

[TALK ABOUT GALIL]

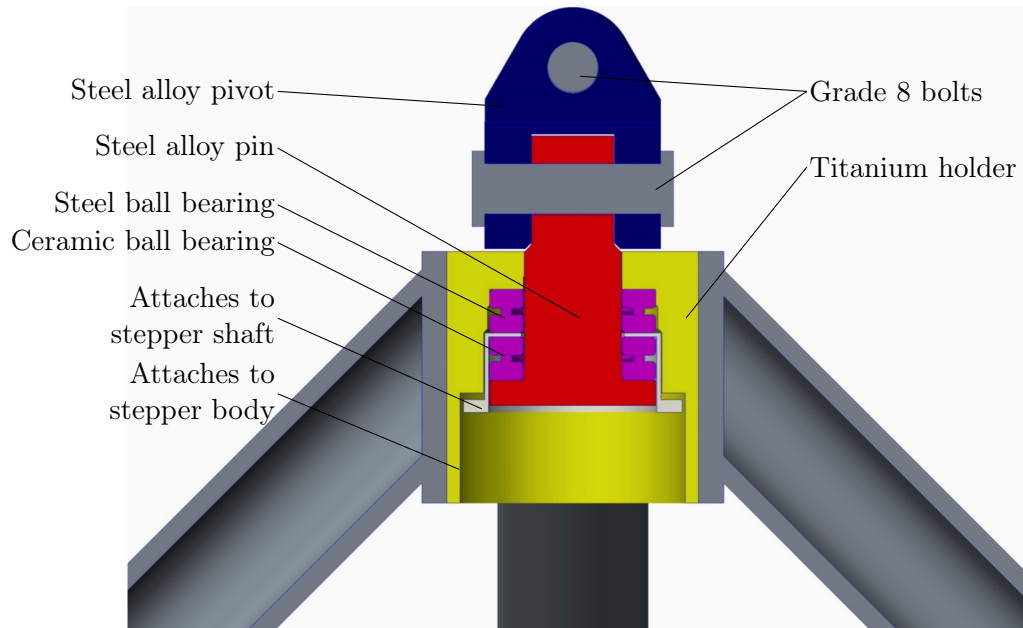


FIGURE V.12: Momentum dump assembly

The momentum dump mechanism has not been tested in the environmental chamber

- however, the stepper motor was rated for vacuum and extreme environments. One of the big unknowns is the value of the bearings' friction coefficients in the balloon environment. When powered, the stepper motor dissipates quite a large amount of heat, which will help maintain the whole assembly to a reasonable temperature.

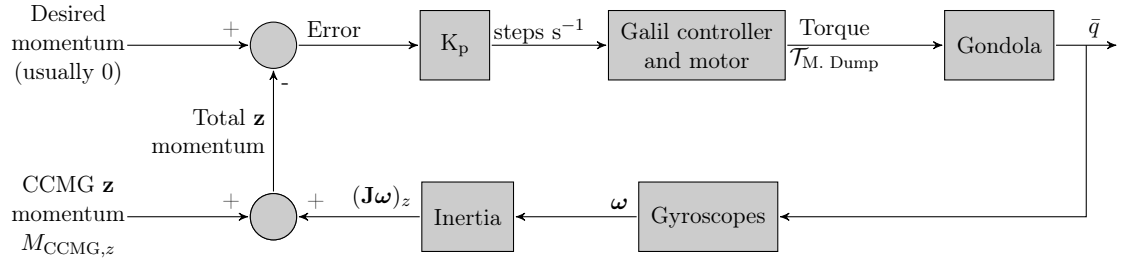


FIGURE V.13: Momentum dump control loop

1.2.5 Elevation control (Rotators)

When put in terms of ground-based telescopes, BETTII is fundamentally an Alt-Az telescope: to reach a target, it has to move in azimuth, and in elevation (also called *altitude*). Instead of moving the entire payload in elevation, which would have conserved the optical setup constant for all targets, we chose to move only the siderostats for increased reliability. We paid one cost: as the siderostat cover different elevations, the fields rotate on the detector, and in opposite directions. So as the elevation changes, an active compensation needs to happen, which consists of a third rotation mechanism located downstream.

These rotation mechanisms have multiple requirements: they need to operate at 90° from the gravity axis; they need to operate well at -40°C ; they need to have an inner clearance to let our 2.5 cm beam through; they need to be able to support many kilograms of cantilevered mass; and they need to have a precise encoder that allows not only smooth motion, but also accurate knowledge of the elevation angle. Griffin Motion LLC makes an industrial rotator that satisfies all of these conditions [Griffin picture].

These are industrial-grade brushless DC rotators. They are controlled by a three-axis Galil Motion controller DMC-4030 with sinusoidal drives. The requirement for sinusoidal drives as opposed to pulsewidth-modulated (PWM) drives stemmed from the fact that these motors were going to be 5 m away from their controller at the end of each arm, and we wanted to avoid creating electromagnetic noise by having high-frequency pulses going through such a large distance. The rotary encoder is a RENISHAW RESOLUTE absolute encoder with 26 bit resolution, which corresponds to a $0.019''$ angular resolution. However, the controller ignores the two bits of lowest significance, effectively giving a 24 bit resolution, corresponding to a $0.08''$ angular resolution.

An old version of these rotation stages was tested in our environmental chamber, but not under load. These devices are rated to operate nominally down to -40°C , but because of their self-heating, we do not expect that they will reach that temperature. During our cold tests of the device, we noted that the friction seemed to change, which required a re-adjustment of the PID coefficients inside the Galil controller.

1.2.6 Delay lines

1.2.7 Tip/tilt

Our tip/tilt mechanisms are Physik Instrumente S330 piezo-electric actuators that move a flat platform in tip and tilt. We attach a mirror to that platform, and put that mirror close to a pupil of the optical system, to correct for angular errors without creating beam walk. After long discussions with the company's engineers, we ordered a custom strain gauge sensor especially tune and tested to resist low temperatures: this sensor tells the angle of the platform, which is important for our control system [see section]. Similar devices

have been successfully used on sounding rocket before to provide milli-arcsecond angular control (Mendillo et al., 2012).

The piezo-electric driver electronics provide the required 100 V to operate the platform, and amplify 10 times an analog 0-10 V command signal. Despite its broad range of motion (≈ 10 mrad), they can still operate at multiple hundred Hz bandwidth, even with a mirror load on top of the platform. The resonant frequency of the structure under load, which needs to be avoided at all costs to avoid severe damage, is at more than 2 kHz, way beyond the frequency at which we need to command the device.

The platform can be controlled in open-loop mode, where there is a simple gain between the command and the voltage applied to the piezo crystals. However, we baseline to use the closed-loop mode during flight. In this configuration, the electronics close the loop using the strain gauge sensor and the command corresponds to an angle rather than simply a voltage. The drawbacks of the closed-loop mode are a slightly decreased bandwidth and overall range of motion. In case more range is needed during flight, it is possible to switch back to open-loop mode.

1.2.8 Fine guidance sensor

The fine guidance sensor is a HAWAII-1RG detector with 1024×1024 pixels that is sensitive to infrared wavelengths between $1\text{ }\mu\text{m}$ and $2.5\text{ }\mu\text{m}$. The device will be operated at a cryogenic temperature of 77 K, at which the expected read noise is 18 electrons r.m.s.

1.2.9 Clocks and timing

Clocks and timings

Computers

Synchronization of the sensors and actuators are of prime importance for our payload.

As an interferometer, we are extremely sensitive to vibrations which could be injected in our system by the motors. While everything was designed to maintain a very good symmetry, slight differences in the inertias or mass distribution of the reaction wheels, for example, could create a beat frequency that would be noticeable in our science data. The existence of multiple clocks, each with their own slight temperature-dependent drift, can dramatically complicate the proper retrieval of the data.

To avoid future complications, all BETTII actuators and sensors are slaved to one single 50 MHz master clock, or an integer divider of that master clock. The cascade of the various clock dividers meets at the common value of 124 800, which corresponds to 2 496 000 ns. This is BETTII's heartbeat. Hence, 124 800 master clock ticks correspond to the elementary cycle of all critical processes:

- The CDL moves of one single step
- The H1RG reads one single frame
- The science detector reads one single frame
- The CCMG wheel position about its axis is checked and a correction is applied.

The advantage of this strategy can be illustrated as follows. The time it takes for a wheel to complete a revolution is set to be an integer multiple of this heartbeat, $998\,400 = 124\,800 \times 8$ master clock ticks (about 50 revolutions per second). Hence, every 8 heartbeats, each wheel is supposed to be in the same position, and it will be controlled 8 times during one revolution to make sure it is. This completely locks in their relative velocities, on average. Let's suppose now that in their 8th position, a mechanical defect in the wheel or the bearing triggers a small vibration. This vibration will occur at a frequency which is locked with respect to our science data, such that we will see its effects every 8

data samples. In the case where these clocks are not synchronized and would unpredictably drift with respect to each other, a perturbation that occurs every 8th of a revolution has repercussions not exactly at every 8 data samples. If we think about this in the frequency domain, it means that the power peak caused by the vibration is now broadened, whereas it is very sharp in the synchronized case.

In practice, however, implementing this "single clock" approach is not straightforward for a project that has modest resources and relies heavily on commercial electronics. Most commercial motion controllers do not allow for external clock synchronization. We came up with a solution with the engineers at Galil Motion, and found a way to change their controller to accept an external TTL signal that would bypass their internal crystal oscillator at 1.024 kHz. The controller normally uses the internal oscillator as a definition of its time basis, so the user can send input in physical units (like acceleration or velocity) - a change in the clock frequency from the introduction of an external signal will have non-trivial repercussions.

The attitude control and sensing occurs every 4 heartbeats, which corresponds to ≈ 100.16 Hz. In the rest of this discussion, we will always refer to this frequency as being at 100 Hz for simplicity of notation - but it important to remember that it is in fact derived from the master clock.

[PUT here the clock diagram]

1.2.10 Computers

BETTII will have two on-board computers (see also diagram [REF]):

1. a computer which operates a real-time Linux kernel will be used to store all the date, process the up/down telemetry, acquire star camera images, solve for inertial

attitude, and process the science detector and H1RG frames. This computer is named *ford*.

2. an FPGA and real-time computer from National Instruments to process the sensor input/outputs, implement the attitude estimation, and synchronize all the control loops. This computer is named *boop*. This is the brain of the control system.

TABLE V.5

Name	Description & tasks
<i>boopFPGA</i>	<ul style="list-style-type: none"> • Generate 50 MHz master clock • Generate all other system clocks derived from master clock • Trigger gyroscopes, star cameras • Read sensors: gyroscopes, galil controllers, <i>ford</i> at 100 Hz • Send actuator commands at 100 Hz • Implement hardware protection (limit, overdrive, etc)
<i>boopRT</i>	<ul style="list-style-type: none"> • Collects all sensors from <i>boopFPGA</i> and estimate gondola's attitude and velocity • Create proper commands to all actuators and sends them to <i>boopFPGA</i> • Manages operating modes [REF SECTION] • Manages FIFOs and communication channels with <i>ford</i>
<i>ford</i>	<ul style="list-style-type: none"> • Processes star camera frames to determine attitude • Processes science detector frames • Processes fine guidance sensor frames • Handles communication with the ground (through the CIP) and from/to <i>boop</i> • Automatically applies observing plan if no commands from the ground: send targets to <i>boopRT</i>

[MAKE DIAGRAM WITH ALL COMPUTERS] *ford* is an Adlink Extreme Rugged Express-IBR 3517UE with a dual-core i7 CPU and 4 GB of ECC (Error Checking and Correction) memory. The ECC memory is helpful in mitigating some of the side effects of cosmic ray hits on the memory chips. The computer has a low power consumption, which allows it to function with a simple radiator instead of a fan. *ford* has been successfully tested at in the environmental chamber, and the temperatures of its cores under maximum CPU stress have been monitored over long periods of time.

boop is a National Instrument cRIO- system. It features a reprogrammable FPGA chip in addition to a dual-core real-time operating system. NI LabView is the software interface to the system. *boop* will generate and distribute BETTII's master clock signal at 50 MHz.

1.3 Software architecture

A diagram showing the flow of the control software is shown in Fig. V.15.

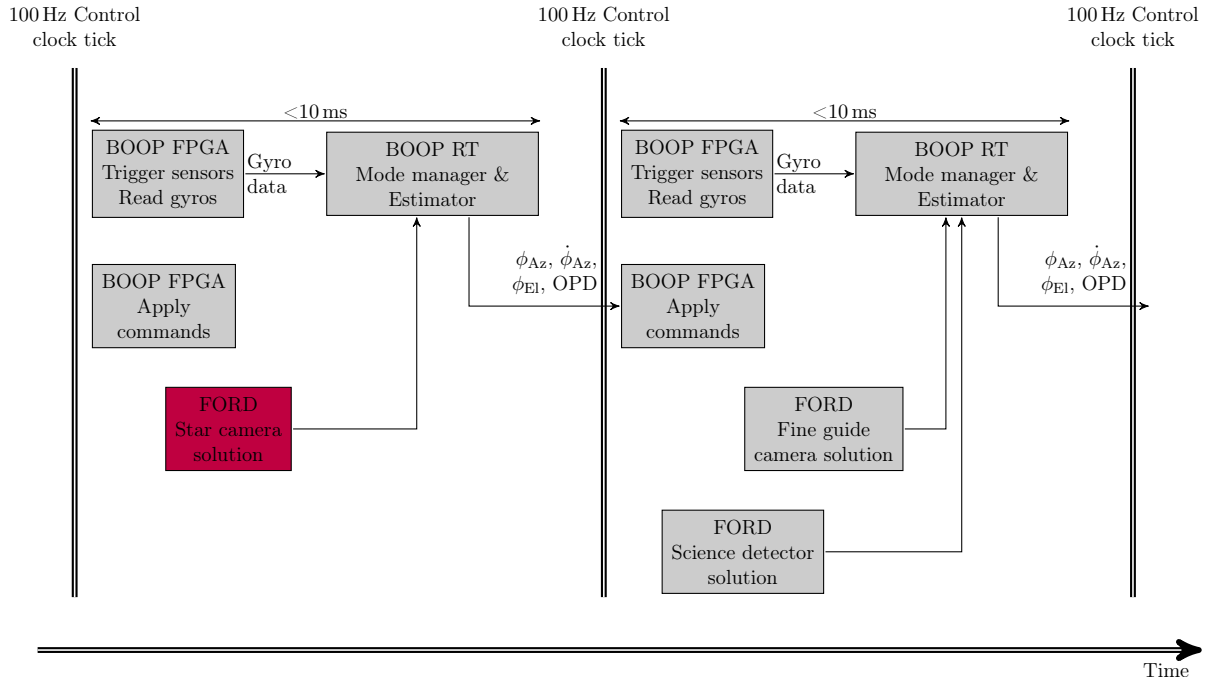


FIGURE V.14: Software layout

2 3D attitude estimation and sensor fusion

The attitude estimation consists of combining high-frequency angular velocity measurements of the payload with low-frequency attitude measurements. The high-frequency measurements, usually from gyroscopes, are relative measurements, and exhibit biases and noise. The attitude measurements are absolute, but they are usually very noisy. The

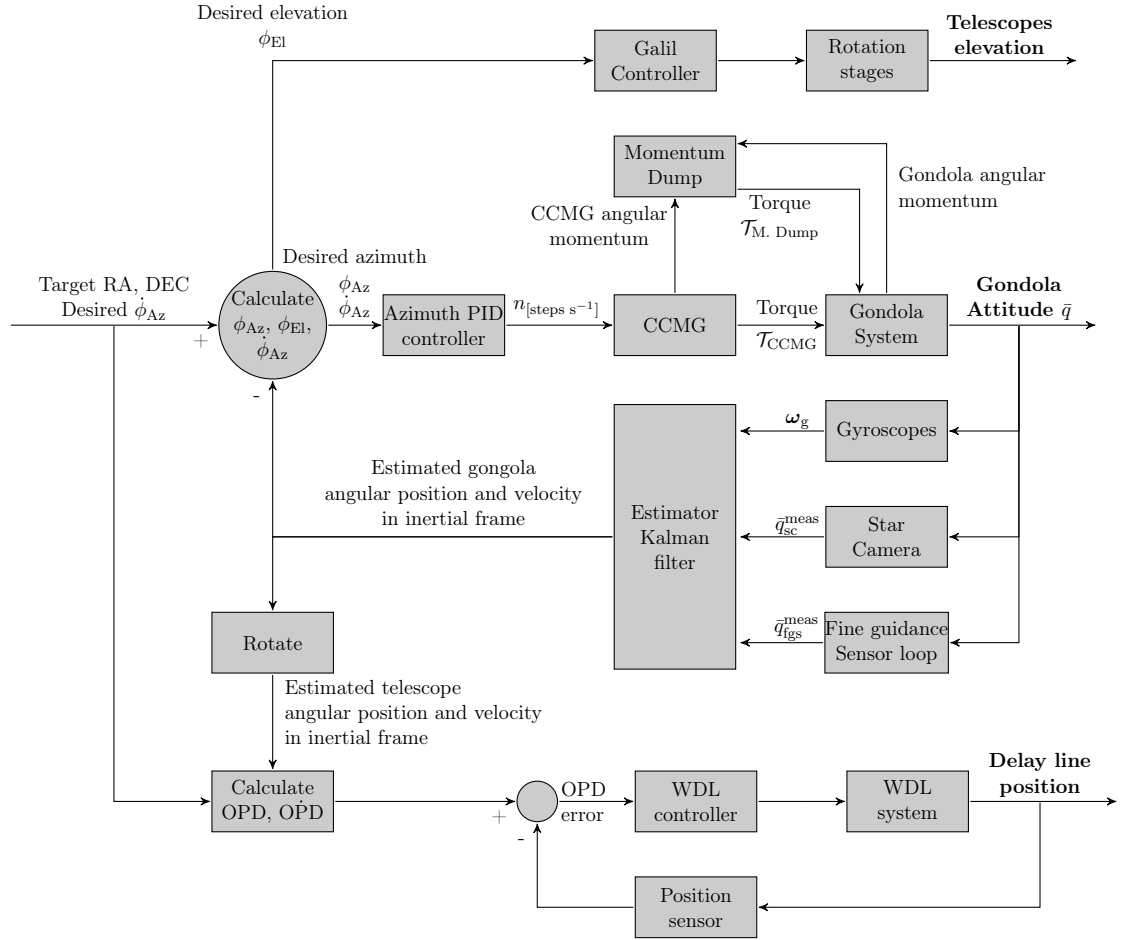


FIGURE V.15: Control system architecture

Kalman filter combines these two measurements in a mathematical formalism that uses the physical relationship between them. The goal of the filter is to estimate the bias of the high-frequency measurements, hence providing bias-corrected, trustworthy dynamical information that can be used to estimate the attitude at all times, even when there is no absolute measurement.

In our situation, gyroscopes will provide high-frequency velocity data (typically at 100 Hz), while star cameras will provide absolute measurements every few seconds. The gyroscopes are much more trustworthy over short periods, so they won't be influenced by just a few star camera measurements. However, on long timescales, the attitude as propagated using the gyroscopes will drift with respect of the star cameras because of the

gyroscopes' inherent biases. The Kalman filter will estimate those biases and provide a bias-corrected angular velocity to make sure that the gyroscopes do not drift away from the star camera results.

This filter is very common for spacecraft attitude and control, although a large number of variations exist. It was first popularized in the 60's [CITE KALMAN original paper?] in the United States during the Apollo missions [reference], when it was used to determine the attitude of the Apollo capsules in inertial space.

[Some paragraph on the theory of the Kalman filter: the fact that it is the optimal filter for gaussian stochastic processes, which means it converges the fastest.]

[Talk about references on Kalman filter. REcent pub: (Crassidis and Junkins, 2011),(Markley and Crassidis, 2014)]

One of the complications of the Kalman filter is that it involves inverting matrices to find the optimal solution when new absolute measurements are received. This has implications in terms of numerical complexity which often will limit the bandwidth of the filter, especially in the context of resource-limit FPGA computers on spacecraft. In practice the trade-off is the following: either limit the bandwidth of the filter, or limit the number of state parameters (*i.e.* limit the rank of the matrix to invert). Fortunately, on the ground, this limitation is usually not an issue. We will be flying a very powerful FPGA computer on our balloon, so we also will not be limited by numerical complexity.

In order to set up the Kalman filter, we choose quaternions to describe our attitude, for the reasons explained in the earlier sections and their advantages in representing all the required information efficiently. In addition, because of their nice behaviour when it comes to small angles, we can use quaternions in their linear, small angle approximation to create a *multiplicative, extended* Kalman filter (MEKF) (Lefferts, Markley, and Shuster,

1982). It is extended because it operates in the small angle approximation, hence it is a local approximation of a non-linear relationship. And it is multiplicative, instead of being additive, because we use the quaternion multiplication operation to describe the "difference" or error between two reference frames. One popular instance where this filter was successfully implemented was on board the WMAP spacecraft [CITE].

First, we need to choose a representation for our sensor suite: the gyroscopes and the star cameras. Second, we describe the equations that govern the physics of our system and connect the sensors together: this is critical for the Kalman filter to produce robust estimates, and the more accurate our representation is, the more accurate our predictions can be. Finally, we discuss the Kalman setup, and two phases of the algorithm: prediction and update.

2.1 Sensor models

2.1.1 Gyroscope model

The gyroscope model that we use is: $\omega^{\text{meas}} = \omega + \mathbf{b} + \mathbf{n}_g$, where ω^{meas} is the measured angular velocity vector, ω is the true angular velocity vector, \mathbf{b} is the bias vector, and \mathbf{n}_g is the angular velocity noise vector (also called the "rate noise"). We consider that \mathbf{n}_g is a white noise process with a diagonal covariance matrix $\mathbf{N}_g = \sigma_{c,g}^2 \mathbf{I}_{3 \times 3}$.

We consider that the derivative of the bias \mathbf{b} is also a white noise process: $\dot{\mathbf{b}} = \mathbf{n}_b$, where \mathbf{n}_b has a diagonal covariance matrix $\mathbf{N}_b = \sigma_{c,b}^2 \mathbf{I}_{3 \times 3}$.

Assuming that the covariance matrices are diagonal help to set up the filter, but is not a necessary assumption in the general case. The following implementation is not relying on this assumption.

Quote this: <http://www.vti.mod.gov.rs/ntp/rad2010/34-10/4/04.pdf> The angular random walk (ARW) specification from the manufacturer is $\text{ARW} = 5 \times 10^{-4} \text{ deg h}^{-1}$. This means that if we integrate the gyroscope's rate for 1 hour, the 1σ uncertainty on our position would be $5 \times 10^{-4} \text{ deg} \sim 1.8''$. For an integration time of 1 second, it would be $0.03''$. For a single integration time step $\Delta t = 0.01 \text{ s}$, it would be $0.003''$.

The units required for σ_g are $[\text{rad s}^{-0.5}]$, so we convert:

$$\sigma_{g[\text{rad s}^{-0.5}]} = \frac{\pi}{60 \times 180} \times \text{ARW}_{[\text{deg h}^{-0.5}]} \sim 1.5 \times 10^{-7} \text{ rad s}^{-0.5}. \quad (\text{V.8})$$

Note that we can relate the ARW to the measured discrete rate noise uncertainty $\sigma(\mathbf{n}_g^{\text{meas}})$ with:

$$\sigma(\mathbf{n}_g^{\text{meas}})_{[\text{deg s}^{-1}]} = \text{ARW}_{[\text{deg h}^{-0.5}]} \times 60 \sqrt{\text{BW}_{[\text{Hz}]}} , \quad (\text{V.9})$$

where $\text{BW}_{[\text{Hz}]}$ is the gyroscope's bandwidth, equal to 50 Hz for our system. We obtain a quantity close to the measured quantity, $\sigma(\mathbf{n}_g^{\text{meas}}) \sim 0.2 \text{ arcsec s}^{-1}$.

The bias instability units are $[\text{rad s}^{-3/2}]$. The manufacturer specification gives a maximum bias instability over a wide range of temperatures equal to 0.005 deg h^{-1} . This is for a bandwidth of 50 Hz, so we obtain the bias instability term, which also corresponds to the process noise of our Kalman filter:

$$\sigma_b_{[\text{rad s}^{-3/2}]} = 0.005 \text{ deg h}^{-1} \times \sqrt{\text{BW}_{[\text{Hz}]}} \sim 1.8 \times 10^{-7} \text{ rad s}^{-3/2}. \quad (\text{V.10})$$

This represents how much what we are trying to estimate is expected to vary. The drift is extremely slow for our gyroscopes, so in practice we will be dominated by the changes in

the alignment of the system for all relevant timescales before the gyroscope bias becomes a problem. [EDIT THIS]

2.1.2 Star camera model

The star camera takes a picture of the sky to make noisy measurements of the right ascension (RA) and declination (DEC) of the boresight, as well as the roll angle (ROLL) in which the frame is taken. The RA and DEC typically are much more accurate than the roll angle. Each angle is can be used as en Euler angle to define the attitude of the payload in the inertial frame (or equivalently, the rotation from the inertial frame to the current attitude). Each angle corresponds to a quaternion rotation about a single axis:

$$\bar{q}_{\text{RA}} = [0, 0, \sin(\text{RA}/2), \cos(\text{RA}/2)]^T, \quad (\text{V.11})$$

$$\bar{q}_{\text{DEC}} = [0, \sin(\text{DEC}/2), 0, \cos(\text{DEC}/2)]^T, \quad (\text{V.12})$$

$$\bar{q}_{\text{ROLL}} = [\sin(\text{ROLL}/2), 0, 0, \cos(\text{ROLL}/2)]^T, \quad (\text{V.13})$$

$$\bar{q}_{\text{sc}}^{\text{meas}} = \bar{q}_{\text{ROLL}} \bar{q}_{\text{DEC}} \bar{q}_{\text{RA}}. \quad (\text{V.14})$$

The errors associated with the three Euler angles are assumed to be a random vector \mathbf{n}^{SC} , also with a diagonal covariance matrix \mathbf{R} . [MENTION TYPICAL STAR CAMERA NOISES]

The star camera is often oriented at a fixed position on the payload, which is not necessarily aligned with the gyroscope reference frame. In that case, the attitude quaternion needs to be rotated by the quaternion representing the transformation between both reference frames. In addition, the covariance matrix needs to be rotated by the direction

cosine matrix corresponding to the same transformation. This would not have an effect if the covariance matrix was a multiple of the identity matrix, but it usually is not the case since the Roll measurement is often much less sensitive. This can have implications while designing the balloon payload and deciding on the placement and orientation of the star camera: the attitude estimation will be less precise about the Roll axis of the star camera.

2.2 Continuous state equation and error

We want to use the Kalman filter to obtain an estimate of the attitude quaternion $\bar{q}_k \equiv {}_I^G\bar{q}(t)$, but also use it to estimate the gyroscope biases $\mathbf{b}(t)$ to improve overall performance. The "state" of our system is described by the vector:

$$\mathbf{x}(t) = \begin{bmatrix} {}_I^G\bar{q}(t) \\ \mathbf{b}(t) \end{bmatrix}. \quad (\text{V.15})$$

The evolution of the state is governed by the two differential equations that follow:

$${}_I^G\dot{\bar{q}}(t) = \frac{1}{2}\boldsymbol{\Omega}(\boldsymbol{\omega}(t)) {}_I^G\bar{q}(t), \quad (\text{V.16})$$

$$\dot{\mathbf{b}}(t) = \mathbf{n}_b(t), \quad (\text{V.17})$$

with $\boldsymbol{\omega} = \boldsymbol{\omega}^{\text{meas}} - \mathbf{b} - \mathbf{n}_g$. These equations represent the exact relationship between our quantities of interest, assuming that the noise values are known. In practice, we will create an *estimator* that is used to evaluate the expected value of these quantities. This

estimator, $\hat{\mathbf{x}} = [\hat{q}(t), \hat{\mathbf{b}}(t)]^T$, is governed by the following equations:

$${}_I^G \dot{\hat{q}}(t) = \frac{1}{2} \boldsymbol{\Omega}(\hat{\boldsymbol{\omega}}(t)) {}_I^G \hat{q}(t), \quad (\text{V.18})$$

$$\dot{\hat{\mathbf{b}}}(t) = \mathbf{0}, \quad (\text{V.19})$$

The Kalman filter's goal is to minimize the variance of the estimator's error - that is, the covariance of the error vector $\mathbf{x} - \hat{\mathbf{x}}$. However, in our case, we have constraints in the system since we force the quaternion to be of unit length: this introduces a singularity in the covariance matrix of the error vector, and is prone to numerical complications. It is possible to circumvent this problem by using the multiplicative properties of the quaternion used in the small angle approximation. This is called a "multiplicative" Kalman filter, as opposed to a more traditional "additive" filter.

To do this, instead of following the evolution of the state $\hat{\mathbf{x}}$ itself, we will follow the evolution of the error vector $\tilde{\mathbf{x}} = [\delta\boldsymbol{\theta}, \Delta\mathbf{b}]^T$, where $\delta\boldsymbol{\theta}$ corresponds to the 3-dimensional angular error between true and estimated attitude quaternion taken from the difference quaternion ${}_{\hat{G}}^G \delta\bar{q} = {}_I^G \bar{q} \otimes {}_I^G \hat{\bar{q}}^{-1} \approx [1, \frac{1}{2}\delta\boldsymbol{\theta}]^T$, and $\Delta\mathbf{b} = \mathbf{b} - \hat{\mathbf{b}}$.

The evolution of $\tilde{\mathbf{x}}$ as a function of time can be obtained by taking the quaternion derivative of the true attitude quaternion $\dot{\bar{q}} = \delta\bar{q} \otimes \hat{\bar{q}} + \delta\bar{q} \otimes \dot{\hat{\bar{q}}}$. With our gyroscope model, we can write:

$$\boldsymbol{\omega}^{\text{meas}} = \boldsymbol{\omega} + \mathbf{b} + \mathbf{n}_g, \quad (\text{V.20})$$

$$\hat{\boldsymbol{\omega}} = \boldsymbol{\omega}^{\text{meas}} - \hat{\mathbf{b}}, \quad (\text{V.21})$$

$$\text{so } \boldsymbol{\omega} = \hat{\boldsymbol{\omega}} - \mathbf{n}_g - \Delta\mathbf{b}. \quad (\text{V.22})$$

After a lengthy derivation to express $\dot{\delta\theta}$ from $\dot{\delta\bar{q}} = [0, \frac{1}{2}\dot{\delta\theta}]^T$ (Trawny and Roumeliotis, 2005), we obtain:

$$\dot{\delta\theta} = -\hat{\omega} \times \delta\theta - \Delta\mathbf{b} - \mathbf{n}_g. \quad (\text{V.23})$$

Note that the cross-product $\hat{\omega} \times \delta\theta$ is equal to the matrix multiplication $[\hat{\omega}_\times] \delta\theta$.

The bias equation is:

$$\dot{\Delta\mathbf{b}} = \dot{\mathbf{b}} - \dot{\hat{\mathbf{b}}} = \mathbf{n}_b. \quad (\text{V.24})$$

The equations representing the evolution of the error $\tilde{\mathbf{x}}$ are then:

$$\dot{\tilde{\mathbf{x}}} = \begin{bmatrix} \dot{\delta\theta} \\ \dot{\Delta\mathbf{b}} \end{bmatrix} = \mathbf{F} \begin{bmatrix} \delta\theta \\ \Delta\mathbf{b} \end{bmatrix} + \mathbf{G} \begin{bmatrix} \mathbf{n}_g \\ \mathbf{n}_b \end{bmatrix}, \quad (\text{V.25})$$

with

$$\mathbf{F} = \begin{bmatrix} [\hat{\omega}_\times] & -\mathbf{I}_{3 \times 3} \\ \mathbf{0}_{3 \times 3} & \mathbf{0}_{3 \times 3} \end{bmatrix}, \quad (\text{V.26})$$

and:

$$\mathbf{G} = \begin{bmatrix} -\mathbf{I}_{3 \times 3} & \mathbf{0}_{3 \times 3} \\ \mathbf{0}_{3 \times 3} & \mathbf{I}_{3 \times 3} \end{bmatrix}. \quad (\text{V.27})$$

Using this error representation allows us to fully describe the state error covariance matrix that will be minimized during the Kalman filter steps.

It is important here to introduce the expression of the covariance matrix of this continuous representation. Writing the noise vector $\mathbf{n} = \begin{bmatrix} \mathbf{n}_g \\ \mathbf{n}_b \end{bmatrix}$, the covariance matrix is the expected value of the product of two noise vectors taken at different times (Trawny

and Roumeliotis, 2005):

$$\mathbf{Q}_c = E[\mathbf{n}(t + \tau)\mathbf{n}^T(t)] = \begin{bmatrix} \sigma_{c,g}^2 \mathbf{I}_{3 \times 3} & \mathbf{0}_{3 \times 3} \\ \mathbf{0}_{3 \times 3} & \sigma_{c,b}^2 \mathbf{I}_{3 \times 3} \end{bmatrix} \quad (\text{V.28})$$

2.3 Integration of continuous equations

Since our system has a fast sampling rate compared to the characteristic times of the system, we consider that \mathbf{F} is constant over a time step. This helps the integration of the state equation between t_{k-1} and $t_k = t_{k-1} + \Delta t$, which has a discrete state transition matrix Φ_k :

$$\Phi_k = \Phi(t_k, t_{k-1}) = \exp(\mathbf{F}\Delta t) \equiv \begin{bmatrix} \Theta_k & \Psi_k \\ \mathbf{0}_{3 \times 3} & \mathbf{I}_{3 \times 3} \end{bmatrix}, \quad (\text{V.29})$$

with $\Theta_k \sim \mathbf{I}_{3 \times 3} - \Delta t [\hat{\omega}_\times] + \frac{\Delta t^2}{2} [\hat{\omega}_\times]^2$ and $\Psi_k \sim \mathbf{I}_{3 \times 3} \Delta t + \frac{\Delta t^2}{2} [\hat{\omega}_\times] - \frac{\Delta t^3}{6} [\hat{\omega}_\times]^2$.

These expressions are now what we need to establish a discrete version of the state equations, which are based on this transition matrix Φ_k .

2.4 Discrete covariance matrices

Since we have a discrete system, it is necessary to also represent the covariance matrix discretely. The discrete system covariance matrix \mathbf{Q} sampled between time t_k and $t_{k+1} = t_k + \Delta t$ is related to the continuous matrix \mathbf{Q}_c through the complicated relationship (Maybeck, 1982):

$$\mathbf{Q} = \int_{t_k}^{t_{k+1}} \Phi(t_{k+1}, \tau) \mathbf{G}(\tau) \mathbf{Q}_c \mathbf{G}^T(\tau) \Phi^T(t_{k+1}, \tau) d\tau.$$

The full result of this equation is given in (Trawny and Roumeliotis, 2005). To the second order in Δt , the equations simplify when $\omega \rightarrow 0$:

$$\mathbf{Q}_{11} = \sigma_g^2 \Delta t \cdot \mathbf{I}_{3 \times 3} \quad (\text{V.30})$$

$$\mathbf{Q}_{12} = -\sigma_b^2 \frac{\Delta t^2}{2} \cdot \mathbf{I}_{3 \times 3} \quad (\text{V.31})$$

$$\mathbf{Q}_{22} = \sigma_b^2 \Delta t \cdot \mathbf{I}_{3 \times 3}, \quad (\text{V.32})$$

with

$$\mathbf{Q} = \begin{bmatrix} \mathbf{Q}_{11} & \mathbf{Q}_{12} \\ \mathbf{Q}_{12}^T & \mathbf{Q}_{22} \end{bmatrix}. \quad (\text{V.33})$$

2.5 Discrete Kalman filter setup

The Kalman filter will estimate the current attitude quaternion and gyroscope bias value, while minimizing the covariance of the error $\tilde{\mathbf{x}}$. Let's summarize the relevant physical equations that are used to set up this filter. This is useful if one wants to build a physical model of the dynamic system.

1. **Velocity estimate:** $\hat{\omega}_k = \omega_k^{\text{meas}} - \hat{\mathbf{b}}_k$,
2. **Attitude propagation:** $\hat{q}_k = \exp\left(\frac{1}{2}\Omega(\hat{\omega}_k)\Delta t\right) \hat{q}_{k-1}$,
3. **Error state evolution:** $\tilde{\mathbf{x}}_k = \Phi_k \tilde{\mathbf{x}}_{k-1} + \mathbf{G}_k \mathbf{n}_k$,
4. **Error covariance to be minimized:** $\mathbf{P}_k = \text{cov}[\tilde{\mathbf{x}}_k]$,
5. **Error covariance evolution:** $\mathbf{P}_k = \Phi_k \mathbf{P}_{k-1} \Phi_k^T + \mathbf{Q}_k$
6. **New attitude measurement:** \bar{q}_k^{meas} ,

7. **State error measurement:** $\tilde{\mathbf{z}}_k = \mathbf{H}_k \tilde{\mathbf{x}}_k + \mathbf{n}_k^{\text{meas}}$.

Note that in that last step, the error measurement $\tilde{\mathbf{z}}_k$ is determined by extracting $\delta\theta_k^{\text{meas}}$ from the difference quaternion $\delta\bar{q}_k = \bar{q}_k^{\text{meas}} \otimes \hat{q}_k^{-1}$ using the small angle approximation. Furthermore, we have $\mathbf{n}_k = [\mathbf{n}_g \quad \mathbf{n}_b]^T$, $\mathbf{n}_k^{\text{meas}}$ is the measurement noise, and in our case $\mathbf{H}_k = [\mathbf{I}_{3 \times 3} \quad \mathbf{0}_{3 \times 3}]$.

At each step, we will attempt to produce our best estimate of the state $\hat{\mathbf{x}}$, and keep track of the evolution of the state error $\tilde{\mathbf{x}}$ and its covariance matrix \mathbf{P} . There are two distinct phases in the Kalman filter: the prediction, and the update.

In the prediction phase, we use our best estimates from the previous step, along with the velocity measurements and the expected propagation relationships to predict what the estimates should be at the current step. If we don't get a new attitude measurement at that step, then these new estimates are the best we can do.

When we do get a new attitude measurement, then in addition to the prediction phase, we also do an update phase. We compare the best estimate from the prediction phase to our new measurement, and use the difference to compute a correction to our state. This uses the weights of the various noise contributors in the system, as we discuss in section [§]. This phase most importantly estimates the bias of the gyroscopes, to allow robust propagation of the state from one step to the next.

For our application, update phases are rare since the star camera can take hundreds of loop cycles to produce an attitude solution. Hence, the last measured star camera occurred at step $k - N$. Until we receive a new measurement, we are trusting our gyroscope model and our bias estimate to propagate the attitude correctly.

In this section, we assume that the attitude measured by the star camera \bar{q}_k^{meas} corresponds to the attitude at the current step. In reality, when we receive the star

camera, it represents an attitude that was taken some number of steps ago. This is due to the slow processing of the star camera images and the catalog search. Our software cannot solve the star camera position in one single loop iteration. We tackle this issue in section [].

2.6 Kalman filter: prediction

The notation $\tilde{\mathbf{x}}_{k|k-N}$ corresponds to the estimate made at step k knowing the value at step $k - N$, where $k - N$ corresponds to the step at which we received the last absolute attitude measurement.

The algorithmic steps for this phase are:

1. **Predict the bias:** $\hat{\mathbf{b}}_{k|k-N} = \hat{\mathbf{b}}_{k-1|k-N}$ since there is no new information to allow us to update the bias.
2. **Estimate the angular velocity:** $\hat{\boldsymbol{\omega}}_{k|k-N} = \boldsymbol{\omega}_k^{\text{meas}} - \hat{\mathbf{b}}_{k|k-N}$.
3. **Predict the attitude:** $\hat{\boldsymbol{q}}_{k|k-N} = \exp\left(\frac{1}{2}\boldsymbol{\Omega}(\hat{\boldsymbol{\omega}}_{k|k-N})\Delta t\right) \hat{\boldsymbol{q}}_{k-1|k-N}$.
4. **Compute the state transition matrix:** $\Phi_k = \begin{bmatrix} \boldsymbol{\Theta}_k & \boldsymbol{\Psi}_k \\ \mathbf{0}_{3 \times 3} & \mathbf{I}_{3 \times 3} \end{bmatrix}$ using $\hat{\boldsymbol{\omega}}_{k|k-N}$ in the expressions of $\boldsymbol{\Theta}_k$ and $\boldsymbol{\Psi}_k$.
5. **Compute the added noise covariance matrix:** \mathbf{Q}_k . This corresponds to the noise that is added by the new gyro measurement.
6. **Update the state covariance matrix:** $\mathbf{P}_{k|k-N} = \Phi_k \mathbf{P}_{k-1|k-N} \Phi_k^T + \mathbf{Q}_k$

We have now propagated our system from step $k - 1$ to step k , and we have three new quantities: the bias $\hat{\mathbf{b}}_{k|k-N}$, the attitude estimate $\hat{\boldsymbol{q}}_{k|k-N}$, and the state covariance matrix $\mathbf{P}_{k|k-N}$. If we do not get any star camera measurement, then at the next step we will just continue propagating with this procedure.

2.7 Kalman filter: update

The star camera information provides us with a measurement of the attitude \bar{q}_k^{meas} , which is compared to our predicted attitude. We use the difference between our prediction and the measurement to update the bias and the state covariance matrix. Under certain circumstances, the Kalman filter is the optimal estimator: it converges towards the correct solution with the minimum amount of iterations.

For the Kalman filter update procedure, we form a measurement vector $\tilde{\mathbf{z}}_k$ that corresponds to the difference of an attitude measurement at step k and the predicted attitude at step k .

7. **Compute the innovation:** $\tilde{\mathbf{z}}_k = \delta\boldsymbol{\theta}_k^{\text{meas}}$ with $\delta\boldsymbol{\theta}_k^{\text{meas}}$ extracted from the difference

$$\text{quaternion } \delta\bar{q}_k = \bar{q}_k^{\text{meas}} \otimes \hat{q}_{k|k-N}^{-1}.$$

8. **Compute the innovation covariance:** $\mathbf{S}_k = \mathbf{H}_k \mathbf{P}_{k|k-N} \mathbf{H}_k^T + \mathbf{R}_k$.

9. **Compute the Kalman gain:** $\mathbf{K}_k = \mathbf{P}_{k|k-N} \mathbf{H}_k^T \mathbf{S}_k^{-1}$.

10. **Update error state:** $\tilde{\mathbf{x}}_{k|k} = \mathbf{K}_k \tilde{\mathbf{z}}_k = \begin{bmatrix} \delta\boldsymbol{\theta} \\ \Delta\mathbf{b} \end{bmatrix} = \begin{bmatrix} 2\delta\mathbf{q} \\ \Delta\mathbf{b} \end{bmatrix}$

11. **Update attitude estimate:** $\hat{q}_{k|k} = \delta\bar{q} \otimes \hat{q}_{k|k-N}$ with $\delta\bar{q} = \begin{bmatrix} \sqrt{1 - \delta\mathbf{q}^T \delta\mathbf{q}} \\ \delta\mathbf{q} \end{bmatrix}$ if $\delta\mathbf{q}^T \delta\mathbf{q} \leq 1$, or $\delta\bar{q} = \frac{1}{\sqrt{1 + \delta\mathbf{q}^T \delta\mathbf{q}}} \begin{bmatrix} 1 \\ \delta\mathbf{q} \end{bmatrix}$ otherwise.

12. **Update the bias:** $\hat{\mathbf{b}}_{k|k} = \hat{\mathbf{b}}_{k|k-N} + \Delta\mathbf{b}$.

13. **Update the angular velocity estimate:** $\hat{\boldsymbol{\omega}}_{k|k} = \boldsymbol{\omega}_k^{\text{meas}} - \hat{\mathbf{b}}_{k|k}$

14. **Update state covariance matrix with Joseph's form:** $\mathbf{P}_{k|k} = (\mathbf{I}_{6 \times 6} - \mathbf{K}_k \mathbf{H}_k) \mathbf{P}_{k|k-N} (\mathbf{I}_{6 \times 6} - \mathbf{K}_k \mathbf{H}_k)^T + \mathbf{K}_k \mathbf{R}_k \mathbf{K}_k^T$.

2.8 Delayed star camera solution

In general, the star camera takes much longer than one single loop cycle to produce an attitude estimate. Between the time we trigger the star camera frame and the time we receive the attitude measurement, we need to keep track of the propagation matrices that will allow to express both the attitude and its covariance matrix in the current reference frame, where the measurement can be combined with the a priori estimate from the Kalman filter.

While no new star camera measurement is available, the attitude transition is expressed by $\hat{q}_k = \exp\left(\frac{1}{2}\boldsymbol{\Omega}(\hat{\omega}_k)\Delta t\right) \hat{q}_{k-1}$, and the new covariance is $\mathbf{P}'_k = \boldsymbol{\Phi}_k \mathbf{P}_{k-1} \boldsymbol{\Phi}_k^T + \mathbf{Q}_k$, where we assume that \mathbf{Q}_k is a constant. We can consider that the gyroscope bias does not change significantly during the time between two star camera measurement (typically on the order of a few seconds). With this we can create a recursive relationship and $\bar{q}_k = [\boldsymbol{\Pi}_{i=k-N}^k \exp\left(\frac{1}{2}\boldsymbol{\Omega}(\hat{\omega}_i)\Delta t\right)] \bar{q}_{k-N}^{\text{meas}}$ where $k - N$ again represents the index at which the star camera image was taken. Similarly, we have: $\mathbf{P}_k = \mathbf{A}_k \mathbf{P}_{k-N} \mathbf{A}_k^T + \mathbf{B}_k$ where \mathbf{A}_k and \mathbf{B}_k are defined recursively as $\mathbf{A}_k = \boldsymbol{\Phi}_k \mathbf{A}_{k-1}$ with $\mathbf{A}_0 = \mathbf{I}_{6 \times 6}$, and $\mathbf{B}_k = \mathbf{Q}_k + \boldsymbol{\Phi}_k \mathbf{B}_{k-1} \boldsymbol{\Phi}_k^T$ with $\mathbf{B}_0 = \mathbf{0}_{6 \times 6}$. \mathbf{A}_k can also be written $\mathbf{A}_k = \boldsymbol{\Phi}_k \boldsymbol{\Phi}_{k-1} \cdots \boldsymbol{\Phi}_{k-N} = [\boldsymbol{\Pi}_{i=k-N}^k \boldsymbol{\Phi}_i]$.

Hence, once we trigger the star camera, we need to start keeping track of the matrices \mathbf{A}_k , \mathbf{B}_k , and $\mathbf{C}_k = \boldsymbol{\Pi}_{i=k-N}^k \exp\left(\frac{1}{2}\boldsymbol{\Omega}(\hat{\omega}_i)\Delta t\right)$, appropriately reset them when a new star camera trigger has occurred, and propagate them until the estimator receives the star camera value.

Chapter VI

Implementation and on-sky testing

*Ever tried. Ever failed. No matter.
Try again. Fail again. Fail better.*

S. Beckett, *Worstward Ho!*

1 Key pre-flight procedures

1.1 Inertia measurement

While CAD models allowed to us to estimate the moment of inertia of the payload, this is only an approximation. For testing and for launch, the payload will be different than the model we have: we will either miss some components because they are not yet installed, or have additional components such as the ballasts, the crush pads, or the weights that are used to balance the payload.

We use a simple procedure to estimate the moment of inertia about \mathbf{z}_g of the payload while hanging from a crane. For this purpose, we command the CCMG to input a torque to the payload by moving the gimbal at a constant velocity. According to Eq. V.7, $\mathcal{T}_{CCMG} = 20.8 \times \dot{\theta} \cos \theta$. According to conservation of angular momentum, the rate of change of the total angular momentum about \mathbf{z}_g is $(\mathbf{J}\dot{\omega})_z = \mathcal{T}_{CCMG} = 20.8 \times \dot{\theta} \cos \theta$.

We measure the inertia \mathbf{J}_z by averaging measurements of the angular acceleration $\dot{\omega}_z$, divided by the instantaneous input torque, which is numerically more stable than averaging its inverse since the accelerations, expressed in rad s^{-1} are typically very small. A measure of the inertia is then the inverse of this average. By repeating the measurement over multiple accelerations and deceleration cycles, we can also obtain an uncertainty to this estimate.

[PUT HERE A TABLE WITH MEASURED INERTIA AND UNCERTAINTIES]

1.2 Sensor alignment and calibration

While the intrinsic noise of our sensors has been characterized in Section 1.2.1, it is important to test them while mounted to the payload, align their axes to the other reference frames, and study their spectral energy distribution. Mounting the gyroscopes in a 3-dimensional mount on the truss will inevitably lead to alignment errors and the contribution of new vibration frequencies present in the structure and excited by the moving parts on the payload.

1.2.1 Gyroscope spectral analysis in flight configuration

1.2.2 Orthogonalization of gyroscope mount

1.2.3 Alignment of gyroscope mount to star camera mounts

BETTII will have two flight star cameras for redundancy. It is important to understand the transformation between the gyroscope reference frame and the two star camera reference frames to minimize the propagation errors within the Kalman filter.

A first transformation matrix can be estimated roughly by assuming that the star camera is in the $(\mathbf{x}_g, \mathbf{z}_g)$ plane. The elevation of the star camera, nominally around 45° , can

be estimated if \mathbf{z} is assumed to be aligned with the gravity vector while the payload is sitting on the ground, which is a good approximation. By taking some star camera measurements, solving the fields, and converting these fields to a local azimuth and elevation (using the time at which the frames were taken and the geographical location), the elevation can be estimated, which corresponds to the angle of the line of sight vector of the star camera with respect to the horizontal plane. This gives us a first estimate of our star camera-to-gyroscope reference frame rotation, but is not very precise given our assumptions. This rotation is critical during the update phase of the Kalman filter when combining the star camera measurement with the propagated estimate.

But if this matrix is slightly off, the Kalman filter will attribute the difference between estimated position and measured position as an additive bias error in the gyroscope velocity measurement, which should converge to a steady-state value after a few tens of star camera measurements, depending on the Kalman filter gains. The filter then uses this additive bias to reconstruct an estimated velocity at each time step. Admittedly, this value of the bias also contains the value of the real gyroscope bias - but we anticipate this bias value to be very small compared to the potential effects of misalignments.

Our procedure involves calculating the quaternion representing the rotation from the steady-state estimated angular velocity vector, and the measured, orthogonalized angular velocity vector. While sitting on the ground, this corresponds to measuring the Earth's angular velocity. This uses the mathematical technique that we derived in Appendix 5.2. Each star camera measurement shall be further rotated by this quaternion to ensure that it is properly expressed in the gyroscope reference frame.

Below, we summarize the steps to properly align the gyroscopes to the star camera:

1. Orthogonalize the gyroscope mount according to Appendix 1.2.2, and find M_{orth} .

This now gives a velocity vector in an orthogonal gyro reference frame, $\omega_g = M_{\text{orth}} \omega_g^{\text{meas}}$.

2. While the truss is sitting horizontal on the ground, calculate the elevation of the star camera by converting solutions to the local East-North-Up reference frame, using the sidereal time and the geographical latitude. This gives a matrix M_{coarse} or a quaternion \bar{q}_{coarse} representing the transformation from the star camera reference frame to the gyroscope reference frame.
3. Still while sitting on the ground, use M_{coarse} or \bar{q}_{coarse} in the flight Kalman filter to estimate the gyro bias vector. Record the steady-state value of the estimated velocity vector.
4. Calculate the transformation between the estimated and measured angular velocity vector, this is a matrix M_{fine} or a quaternion \bar{q}_{fine} .
5. For each star camera reference frame solution, rotate the solution $\bar{q}_{\text{fine}} \bar{q}_{\text{coarse}}$.
6. Use this new matrix in the flight Kalman filter to make sure the estimated biases are close to zero.

1.3 Star camera

1.3.1 Tuning tests

TABLE VI.1: Star camera exposure time tests.

	Exposure time (ms)	Number of images in run	Fitted exposure time (ms)	Number of matching stars	Fit ra & dec error (arcsec)	Fit roll error (arcsec)	Processing time (s)	Solution success rate (%)
Exp1	250	118	260 ± 92	9.12 ± 1.67	1.46 ± 0.43	114 ± 40	1.48 ± 0.77	98
Exp2	125	36	113 ± 13	9.75 ± 1.95	1.46 ± 0.39	118 ± 32	1.05 ± 0.26	100
Exp3	62	49	70 ± 53	8.43 ± 1.55	1.72 ± 0.64	155 ± 66	1.01 ± 0.21	96
Exp4	62	132	66 ± 23	7.32 ± 1.34	1.75 ± 0.65	151 ± 55	1.22 ± 0.59	76
Exp5	31	35	44 ± 53	6.54 ± 0.84	2.33 ± 0.79	180 ± 65	1.19 ± 0.48	37

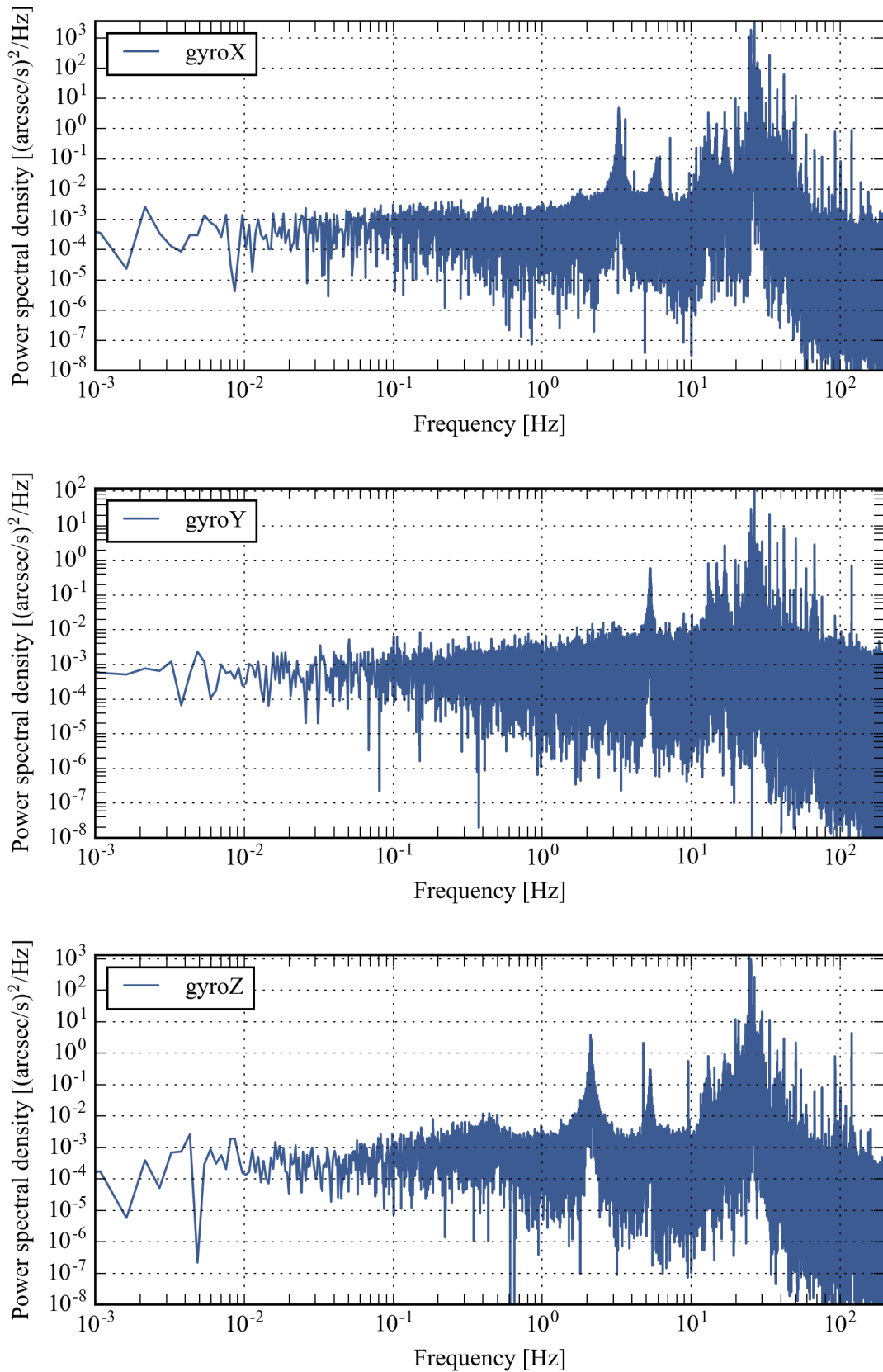


FIGURE VI.1: Gyro PSD with payload on the ground

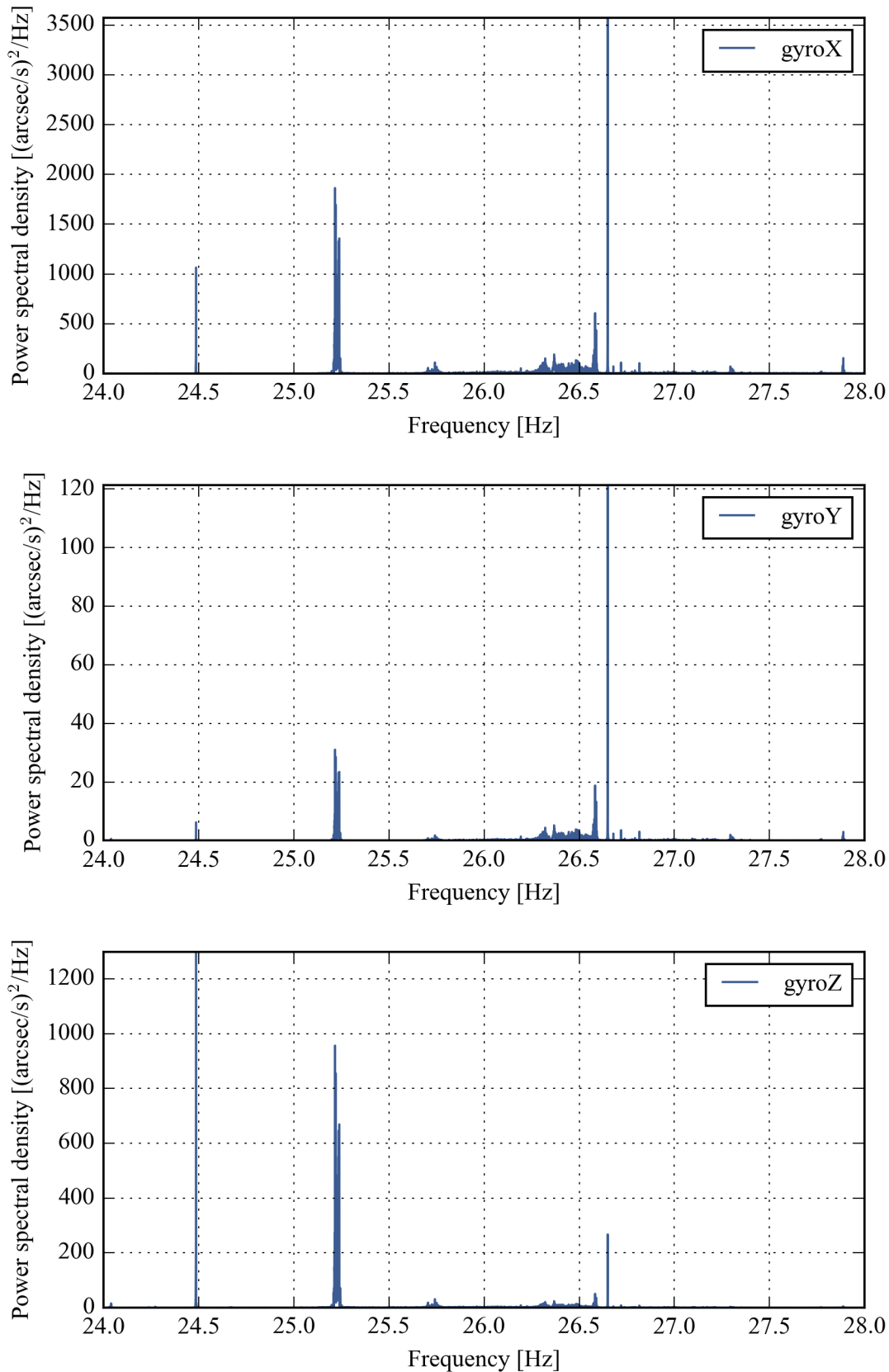


FIGURE VI.2: Gyro PSD with payload on the ground - main peaks.

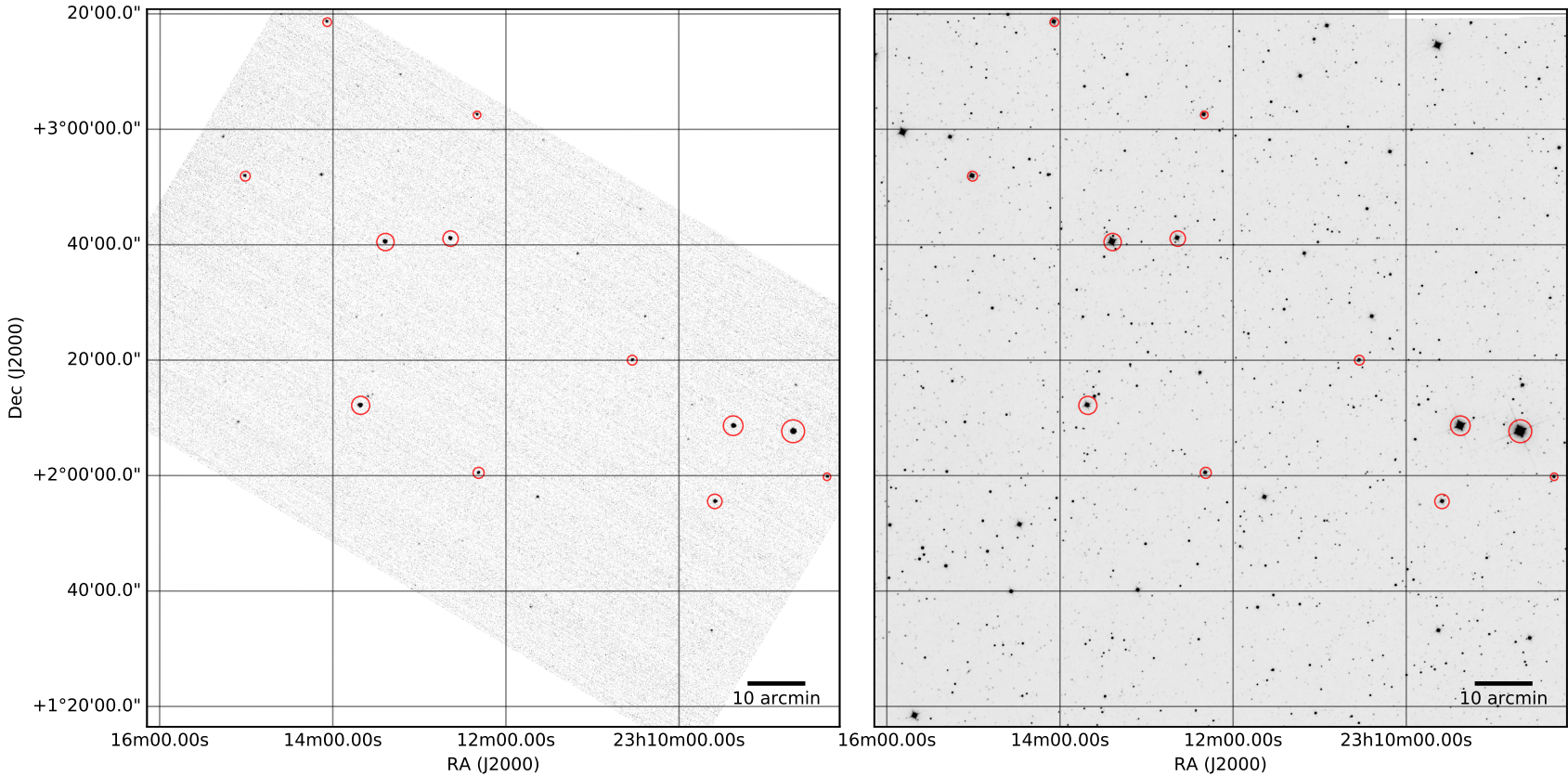


FIGURE VI.3: *Left:* Example of a background-subtracted star camera image with identified $> 5\sigma$ sources circled in red. The orientation of the image on the celestial sphere is the one provided by BETTII's embedded star camera solver. This image corresponds to a field in the Scorpius constellation. *Right:* WISE 3.4 μm mosaic from the online archive, centered on the same location. This image is composed of 9 individual WISE images that we patched into a mosaic using the *Montage*[CITE] software package.

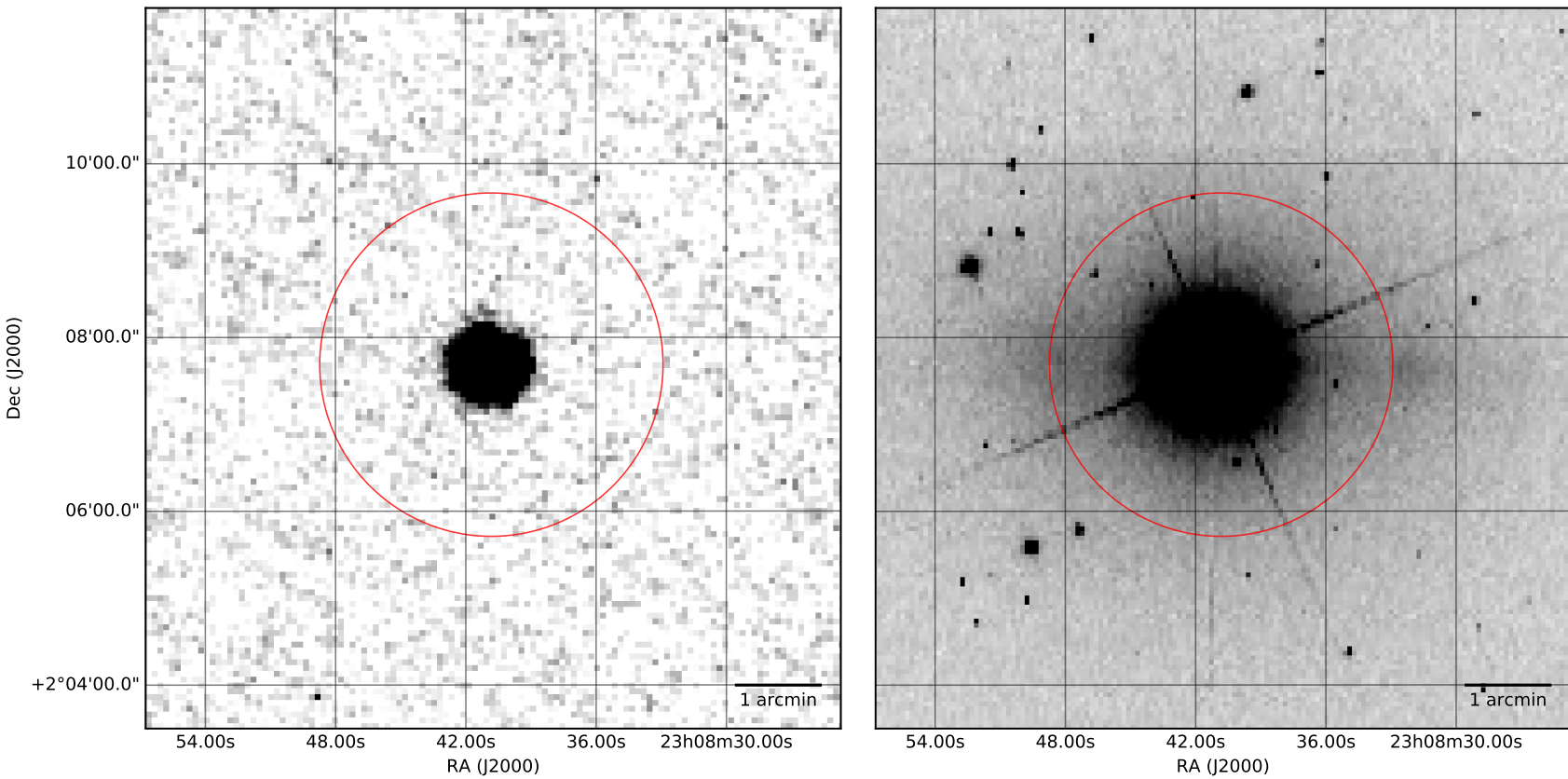


FIGURE VI.4: *Left:* Snapshot of a bright star seen within the background-subtracted star camera frame. *Right:* Snapshot taken at the same location from the WISE 3.4 μ m archive.

Discuss about tuning, catalog, filters, etc

Table with the star camera parameters

Show mean deviation of star camera image with optimized parameters; show time, statistics, etc.

1.3.2 Final parameters

2 Test setups and limitations

2.1 Talk about the way we test in the high bay, etc

2.2 List of test setups: gyro only, gyro+star camera, gyro+star camera+tip/tilts with CCD cameras, gyro+star camera with H1RG;

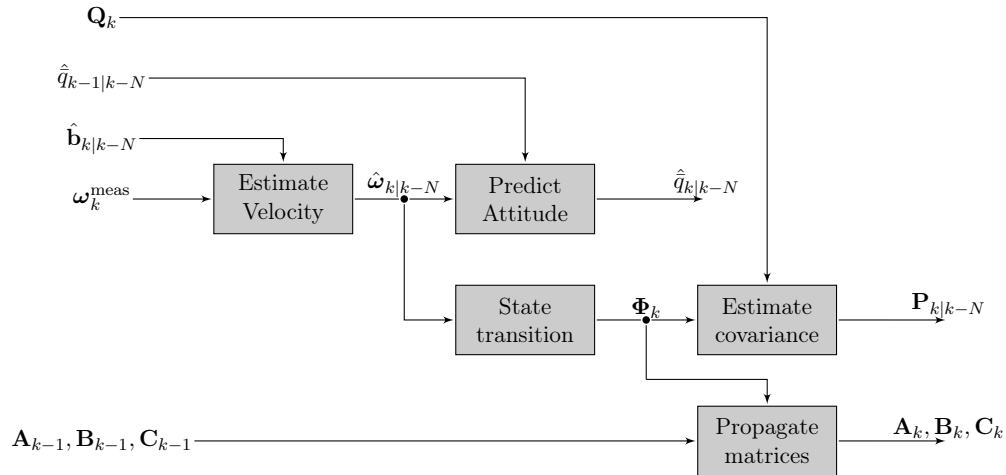
2.3 Explain the communication/data recording approach

2.4 Autofocus algorithm and performance

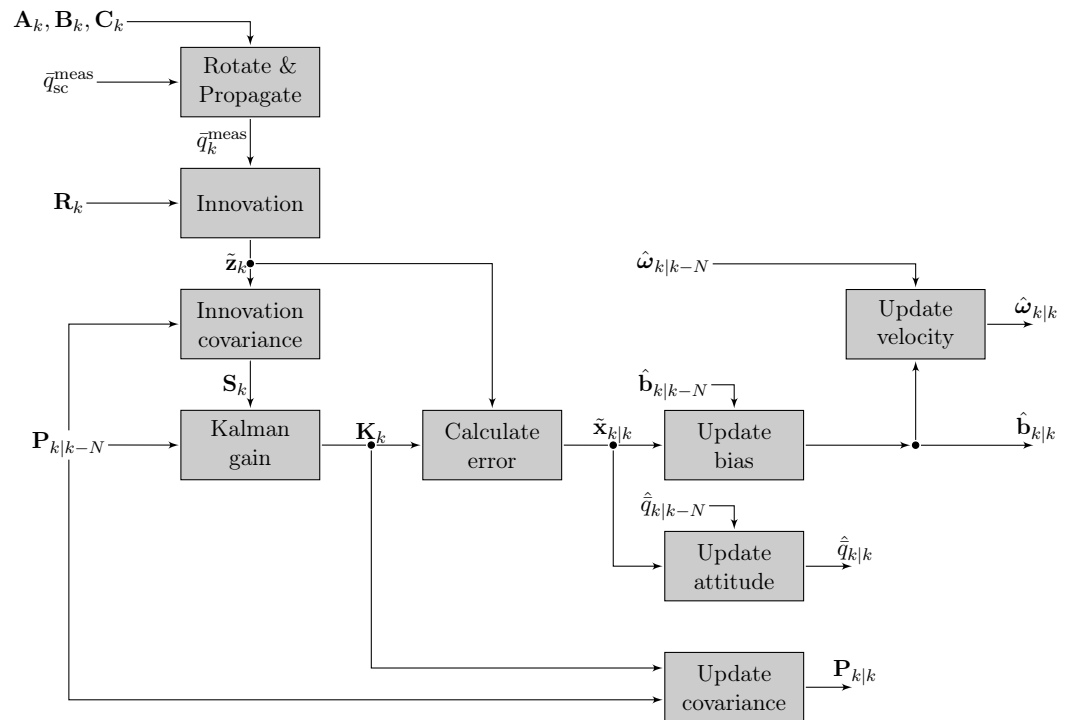
3 Estimator implementation

3.1 Gyro attitude estimator

Kalman Filter: Prediction



Kalman Filter: Update



3.1.1 Testing the Kalman filter software with simulated data

3.1.2 Test results when sitting on the ground

3.2 Telescope attitude estimator

Link to cross-elevation

3.3 Phase estimator [is that Arnab's realm?]

4 Operating modes

4.1 Track mode

Gain tuning Show wheel angle for long time

4.2 Slew mode

4.3 Acquire mode [this one is contingent on the telescopes working, and is not perfectly representative when only using one single side of the payload]

5 Pointing tests and performance results

5.1 Gondola pointing stability

5.1.1 In the high bay

show azimuth stability data show telescope rolling rms

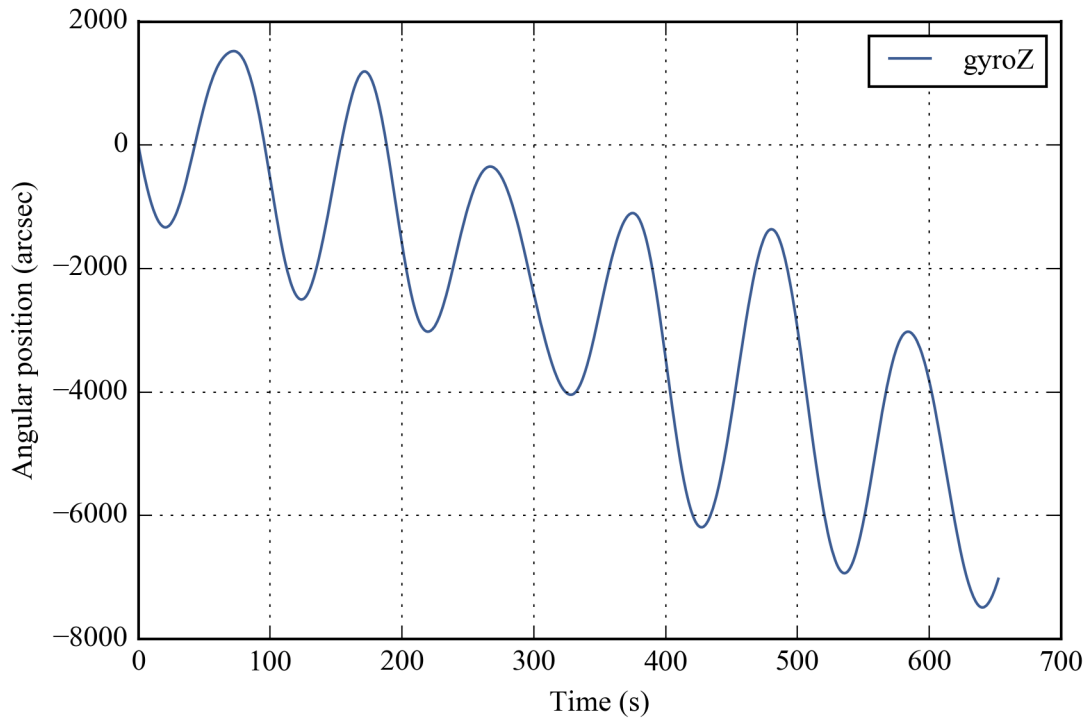


FIGURE VI.5: Integrated gyro time series while hanging and no motor on.

5.1.2 With the door open

5.2 Kalman filter performance

Show data with the door open with the star camera acquiring frames

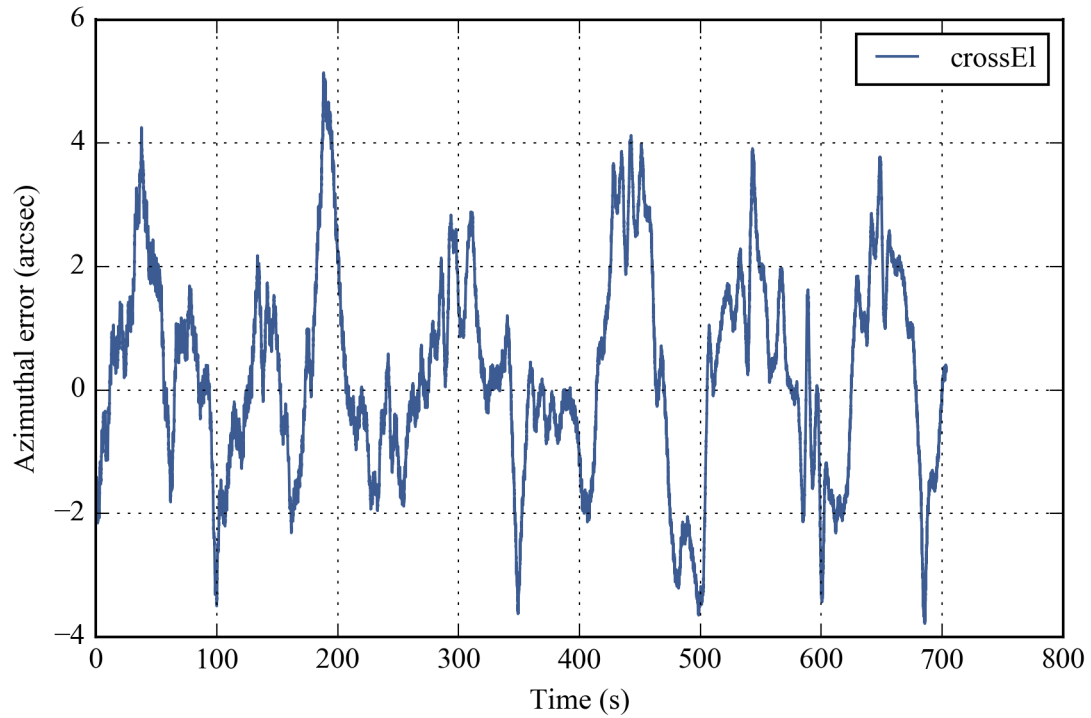


FIGURE VI.6: Cross-elevation with control loop on (gyroscopes only).

5.3 gyro+star camera+tip/tilts with CCD cameras

5.4 gyro+star camera with H1RG;

6 Using the test results to estimate the flight performance

(have to think more about that section)

6.1 Perturbation rejection estimates

6.2 Pointing knowledge predictions

6.3 Pointing control predictions

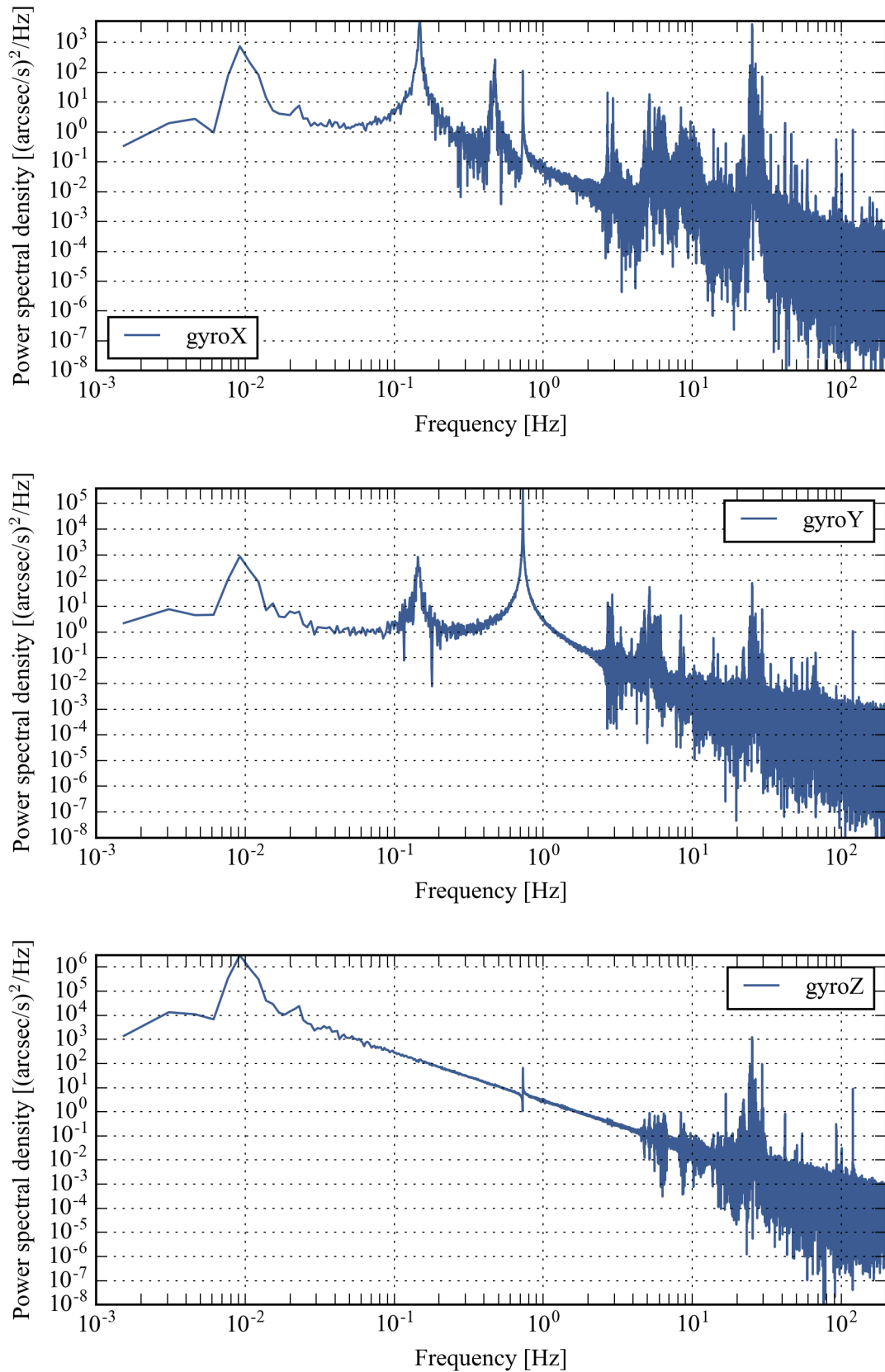


FIGURE VI.7: Gyro PSD with payload lifted.

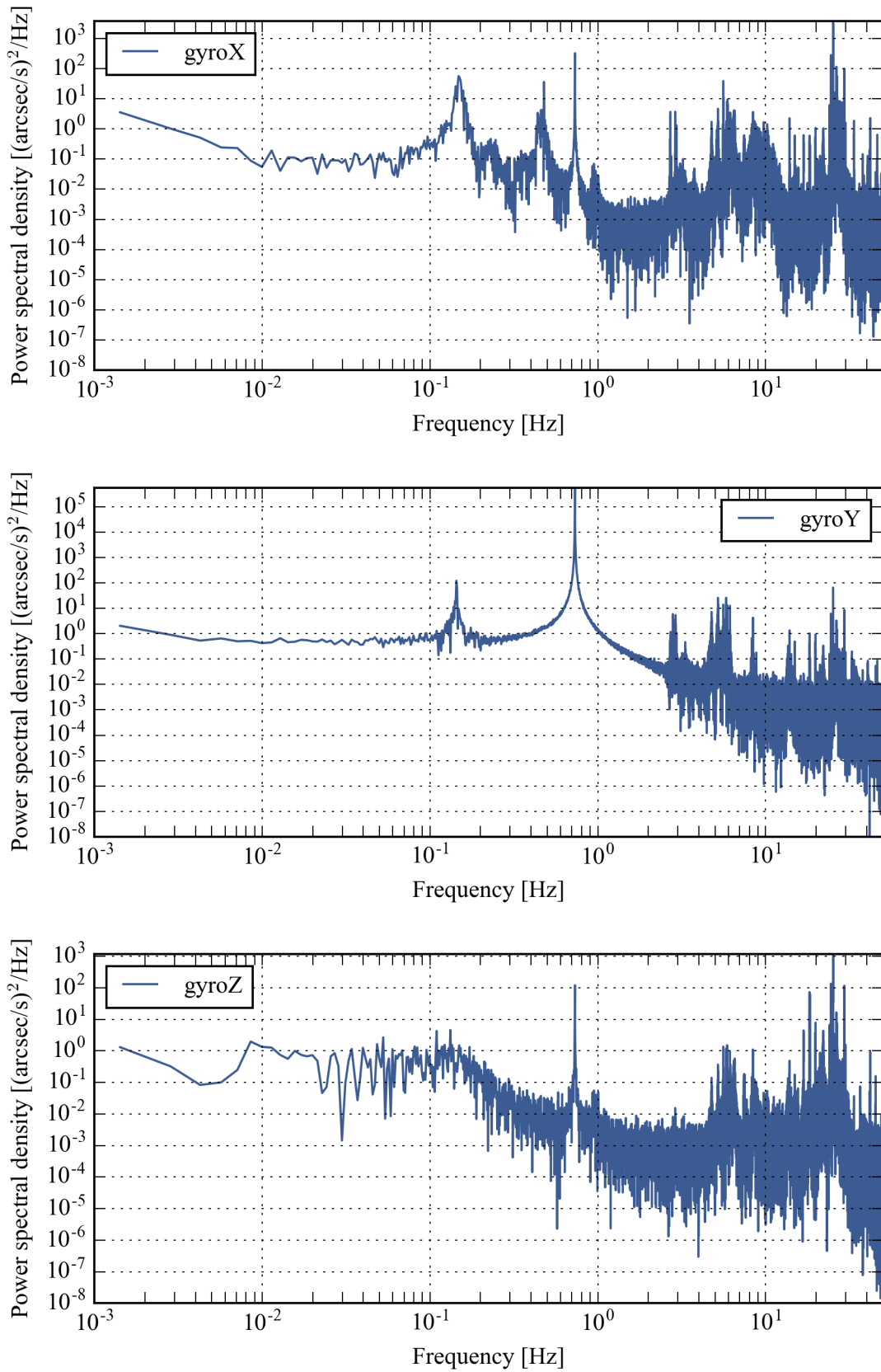


FIGURE VI.8: Gyro PSD with payload under azimuth control.

Chapter VII

Conclusion

There is nothing like a dream to create the future.

V. Hugo

Appendix A

Attitude representation in three dimensions

There are three common representations of the orientation, or *attitude*, of an object in a 3-dimensional Euclidian reference frame: in the following we will discuss the Tait-Bryan angles (which are very similar to, and sometimes confused with proper Euler angles), rotation matrices, and quaternions. All of them can be understood as a rotation of the initial reference frame $I = \{\mathbf{I}, \mathbf{J}, \mathbf{K}\}$ into the object's local reference frame $L = \{\mathbf{i}, \mathbf{j}, \mathbf{k}\}$.

The reference frame I is assumed to be fixed while L is allowed to move. We can write each unit vector as follows: $\mathbf{I} = {}^I[1, 0, 0]^T$, $\mathbf{J} = {}^I[0, 1, 0]^T$, $\mathbf{K} = {}^I[0, 0, 1]^T$, and $\mathbf{i} = {}^L[1, 0, 0]^T$, $\mathbf{j} = {}^L[0, 1, 0]^T$, $\mathbf{k} = {}^L[0, 0, 1]^T$. $\{\mathbf{I}, \mathbf{J}, \mathbf{K}\}$ and $\{\mathbf{i}, \mathbf{j}, \mathbf{k}\}$ are orthonormal bases to I and L , respectively. The subscript before the vector indicates in which reference frame the vector is expressed, and the T after the vector indicates the transpose operation. We will keep this formalism for all vectors and matrices in this work.

1 Tait-Bryan/Euler angles

The Tait-Bryan formalism [CITE] corresponds to a sequence of three angles, each corresponding to a rotation about one of the object's main axes: these are also called "intrinsic" rotations. They differ from "extrinsic" rotation, sometimes called "Euler angles", which correspond to a rotation about one of the axes of the global (fixed) reference frame. In the following, we will focus on using exclusively intrinsic rotations, as they are more intuitive. Note that sometimes people call this formalism "Euler angles" as well, so it is important to understand how this works. With this formalism, we start in the global reference frame and rotate the reference frame three times to end up in the *body* reference frame, which describes the final orientation of an object. We will most often choose a well-known sequence of rotation such as the $z - y' - x''$ order, which corresponds to the angles used to describe the heading, elevation and bank of an aircraft with respect to a reference frame attached to the Earth, for example the North-East-Down reference frame. The first rotation about **k** will transform I into L' . The second rotation, about the **j** axis of the rotated frame L' , transforms L' into L'' . The third and last rotation, about the **i** axis of L'' , will transform L'' into the final orientation, L , of the object (see Fig. A.4).

This sequence of rotation can be used to represent the rotation matrix that describes the attitude of an image of the sky. Celestial coordinates are usually given in terms of right ascension, declination. To fully describe the image of a patch of sky, we need another degree of freedom, which is the roll of the image about the boresight. When given these three angles: RA, DEC, and ROLL, one can reconstruct the attitude using the Tait-Bryan angles in the $z - y' - x''$ order, where the first, second and third elementary rotations correspond to the rotations in right ascension, declination and roll, respectively.

2 Rotation matrices

Perhaps the most common way to express the orientation of an object within a given reference frame is to use the matrix that describes the rotation from one reference frame to the other. Since rotations are linear transformations of \mathcal{R}^3 , there always exists a matrix to represent it. If we choose an orthonormal basis to \mathcal{R}^3 , matrices representing rotations are 3×3 orthogonal matrices. When given the traditional matrix multiplication operation, 3×3 orthogonal matrices with determinant of +1 form a group which is an isomorphism of the group of all 3-D rotations of Euclidian space (subsequently called SO(3) for "special orthogonal group") [REFERENCE?]: it means that each rotation can always be represented by exactly one 3×3 orthogonal matrix. This theorem is the mathematical translation of the sometimes obvious intuition that rotation matrices always exist, are unique for a given rotation, and that the composition of two rotations is still a rotation. It also expresses the requirement that the corresponding rotation matrices have a determinant of +1, which can be useful when we consider numerical implementations of these matrices, as rounding errors might require a periodic normalization of the matrices to ensure they stay in this group. Note that the group of rotation is a cyclic group, since a rotation of an angle θ is the same as a rotation of $\theta + 2\pi$.

We are interested in matrices describing rotations of entire coordinate systems, which are also called *passive* rotations. This is different from matrices describing rotations of vectors within a given coordinate system (called *active* rotations), and an important distinction that can often lead to confusion. Let's suppose that we have an initial coordinate system I of basis $\{\mathbf{I}, \mathbf{J}, \mathbf{K}\}$, and a second coordinate system L of basis $\{\mathbf{i}, \mathbf{j}, \mathbf{k}\}$. For example, this applies when L is the body reference frame, and we want to understand its

orientation with respect to an initial reference frame, such as the inertial reference frame. The basis vectors of L can all be expressed by a linear combination of the basis vector of I . This transformation can be described using the *direction cosine matrix*, which has the following expression:

$${}^I_L \mathbf{R} = \begin{bmatrix} \mathbf{i} \cdot \mathbf{i} & \mathbf{j} \cdot \mathbf{i} & \mathbf{k} \cdot \mathbf{i} \\ \mathbf{i} \cdot \mathbf{j} & \mathbf{j} \cdot \mathbf{j} & \mathbf{k} \cdot \mathbf{j} \\ \mathbf{i} \cdot \mathbf{k} & \mathbf{j} \cdot \mathbf{k} & \mathbf{k} \cdot \mathbf{k} \end{bmatrix}. \quad (\text{A.1})$$

The columns of this matrix correspond to the expression of the basis vectors of I expressed in the basis of L . This is what we call the *rotation matrix* between I and L , and transforms vectors expressed in I into their representation in L . With this convention, the matrix pre-multiplies the vector. For example, if we have some vector ${}^I \mathbf{u}$ expressed in the initial reference frame I , its expression in the reference frame L will be ${}^L \mathbf{u} = {}^I_L \mathbf{R} {}^I \mathbf{u}$.

Note that the rotation matrix ${}^I_L \mathbf{R}$ is an orthogonal matrix of determinant +1: each columns are orthogonal with each other and of unit norm. Hence, the inverse of this matrix is its transpose, which also corresponds to the rotation of a vector from frame I to frame L : $({}^I_L \mathbf{R})^{-1} = ({}^I_L \mathbf{R})^T = {}^L_I \mathbf{R}$.

Let's take an example and consider the unit vector ${}^I \mathbf{u} = {}^I(1, 0, 0)$, expressed in I originally. Now, let's rotate the coordinate frame I by an angle θ with respect to the axis \mathbf{k} . The new reference frame is $L' = \{\mathbf{i}', \mathbf{j}', \mathbf{k}'\}$. For simplification, let's consider that $\theta = +90$ degrees. It is clear that the vector \mathbf{i} is now equal to $-\mathbf{j}'$, and ${}^{L'} \mathbf{i} = {}^{L'}(0, -1, 0)$.

In the more general case, let's suppose that the local reference frame L' is rotated by an angle θ about the \mathbf{k} axis (Fig. A.2) with respect to the reference frame I . The

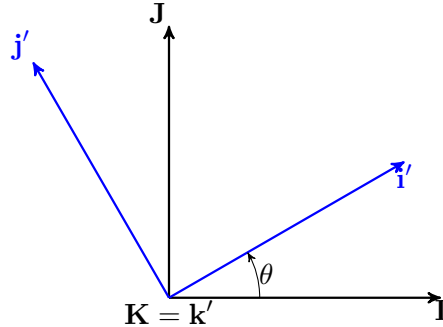


FIGURE A.1: The $\{i', j', k'\}$ reference frame (in blue) is rotated with respect to $\{I, J, K\}$ (in black). The rotation is about the axis K by an angle $\theta = 30$ degrees.

convention we adopt sets the rotation matrix for this transformation as being:

$${}_{I'}^L \mathbf{R} = \mathbf{R}_k(\theta) = \begin{bmatrix} \cos \theta & \sin \theta & 0 \\ -\sin \theta & \cos \theta & 0 \\ 0 & 0 & 1 \end{bmatrix}, \quad (\text{A.2})$$

where \mathbf{k} indicates the third axis of the current basis (\mathbf{i} and \mathbf{j} represent the first and second axes, respectively). This will transform vectors from I to L' . Suppose now that we further rotate our reference frame by an angle ϕ about the newly-rotated j' axis. The rotation for this elementary transformation is:

$${}_{L'}^{L''} \mathbf{R} = \mathbf{R}_j(\phi) = \begin{bmatrix} \cos \phi & 0 & -\sin \phi \\ 0 & 1 & 0 \\ \sin \phi & 0 & \cos \phi \end{bmatrix}. \quad (\text{A.3})$$

And let's do one last rotation about i'' , of an angle ψ , for which the transformation matrix is:

$${}_{L''}^L \mathbf{R} = \mathbf{R}_i(\psi) = \begin{bmatrix} 1 & 0 & 0 \\ 0 & \cos \psi & \sin \psi \\ 0 & -\sin \psi & \cos \psi \end{bmatrix}. \quad (\text{A.4})$$

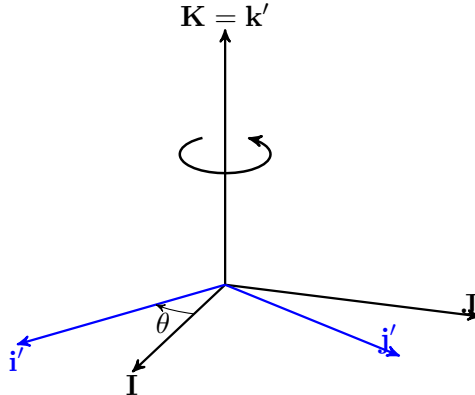


FIGURE A.2: The $\{i', j', k'\}$ reference frame (in blue) is rotated with respect to $\{I, J, K\}$ (in black). The rotation is about the axis K by an angle $\theta = -30$ degrees.

The matrix that corresponds to the active transformation of I to L will multiply vectors expressed in I and express them in L . Hence, this matrix can be written:

$${}_I^L \mathbf{R} = {}_{L''}^L \mathbf{R}_{L'}^{L''} \mathbf{R}_I^{L'} \mathbf{R} = \mathbf{R}_i(\psi) \mathbf{R}_j(\phi) \mathbf{R}_k(\theta), \quad (\text{A.5})$$

where we pre-multiply the matrix for each consecutive rotation of reference frames. This corresponds to the "natural order" of rotations [CITE], and is especially relevant when related to quaternions. While the first axis of rotation, \mathbf{k} , is defined in the initial reference frame, it is important to realize that the axes corresponding to the second and third rotations are defined in the intermediate frames L' and L'' , respectively. We can understand this by thinking that the transformations follow the *body*, as each rotation is done in the body reference frame, and is a particularly useful approach to our problem.

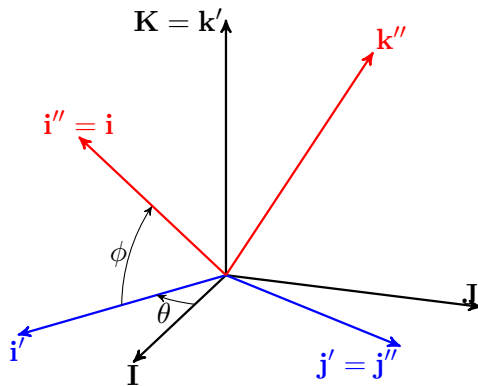


FIGURE A.3: The $\{i'', j'', k''\}$ reference frame (in red) is rotated with respect to $\{i', j', k'\}$ (in blue). The rotation is about the axis j' by an angle $\phi = -45$ degrees.

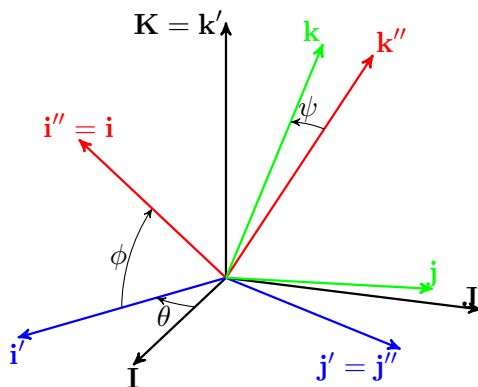


FIGURE A.4: The $\{i, j, k\}$ reference frame (in green) is rotated with respect to $\{i'', j'', k''\}$ (in red). The rotation is about the axis i'' by an angle $\psi = 15$ degrees.

3 Quaternions

Quaternions are a more modern way to describe the orientation of a reference frame with respect to another, and are today widely used to describe spacecraft orientation [QUOTE]. From a strictly mathematical point of view, quaternions form a normed algebra over the real numbers that is an extension of traditional complex numbers. The quaternion normed algebra has four dimensions, instead of just two for the complex numbers. At its fundamental level, the basis for the quaternion algebra consists of one real axis and three imaginary axes $\{1, \mathbf{i}, \mathbf{j}, \mathbf{k}\}$. Like complex numbers (which have a basis $\{1, \mathbf{i}\}$), there are fundamental relations between the basis elements that govern the multiplication operation, such as the well known identity $\mathbf{i}^2 = -1$, that we will discuss at length later in this section. In this document, we will write a quaternion using one of the following equivalent notations (Coutsias 1999) and (Schmidt 2001) :

$$\bar{q} = q_r \times 1 + q_i \mathbf{i} + q_j \mathbf{j} + q_k \mathbf{k} = q_r + \mathbf{q} = \begin{bmatrix} q_i \\ q_j \\ q_k \\ q_r \end{bmatrix} = \begin{bmatrix} \mathbf{q} \\ q_r \end{bmatrix} = \begin{bmatrix} \mathbf{q}^T & q_r \end{bmatrix}^T, \quad (\text{A.6})$$

where we make a clear distinction between the quaternion's real part q_r , and its 3-dimensional imaginary part that we choose to represent as a vector $\mathbf{q} = q_i \mathbf{i} + q_j \mathbf{j} + q_k \mathbf{k}$.

Like complex numbers, quaternion have a conjugate operation, which negates the imaginary part: $\bar{q}^* = \begin{bmatrix} \mathbf{q}^T & q_r \end{bmatrix}^T$.

Quaternions are interesting beyond their pure mathematical definition because the subset of quaternions of unit norm can be used to represent a coordinate frame rotation in three dimensions. The Euler rotation theorem states that any coordinate frame rotation

can be described by a rotation of an angle θ about an appropriately-chosen unit vector $\mathbf{u} = x\mathbf{i} + y\mathbf{j} + z\mathbf{k}$ (also called the "Euler axis" or "Euler vector"). This formalism has 3 degrees of freedom, the minimum needed to describe a rotation between two reference frames: two degrees of freedom in the vector (which is constrained to be of unit norm), and one in the rotation angle. If we encode this information in a quaternion using Euler's exponential notation for vectors [need references here], this precisely defines the quaternion:

$$\bar{q} = \exp \left[\frac{\theta}{2} (x\mathbf{i} + y\mathbf{j} + z\mathbf{k}) \right] = \cos \frac{\theta}{2} + (x\mathbf{i} + y\mathbf{j} + z\mathbf{k}) \sin \frac{\theta}{2}. \quad (\text{A.7})$$

This quaternion completely describes the rotation between the two reference frames and has unit norm. Conversely, every quaternion of unit norm can be decomposed like this and represent a rotation in three-dimensional Euclidian space. Like rotation matrices, the unit quaternions form a group under the quaternion multiplication operation, which is isomorphic to the special unitary group $SU(2)$ [reference]. It is known that $SU(2)$ is a surjective 2:1 homomorphism of $SO(3)$. This means that each element in $SO(3)$ can be described by exactly two elements in $SU(2)$, or equivalently, two distinct unit quaternions: the quaternion \bar{q} , and its opposite $-\bar{q}$.

Quaternions use 4 numbers to describe 3 degrees of freedom: an advantage over matrices (9 elements), but an apparent disadvantage over Tait-Bryan angles, which consist of an optimal number of 3 elements. However, Tait-Bryan angles can be shown to exhibit a phenomenon called *gimbal lock* [references], which leads to a degeneracy when describing the set of angles corresponding to rotations when the pitch angle (second rotation angle, about \mathbf{j}) is $\pm\pi/2$. This creates situations where some rotations and sequences of rotation would have to be avoided by fear of creating numerical issues caused by gimbal lock [footnote: for an example of gimbal lock, refer to the Apollo program!]. Quaternions, while

needing an extra number to represent the rotation, are free of this concern. This is one of the main reasons that they were originally preferred to Tait-Bryan angles early in the spaceflight era [WERTZ 1985?]. [talk more about the advantages of quaternions: number of multiplications, etc - see Shuster et al 1993]

3.1 Quaternion multiplication

In order to form the unit quaternion group, one has to define an appropriate multiplication operation. We warn that the formulation that we use and present in the next few paragraphs does not correspond to the commonly accepted rules for quaternion operations (also called "Hamilton notation", from W. R. Hamilton who is attributed the discovery of quaternions). We use a formalism that was popularized by Caley [CITE] and adopted in most of the aerospace community [cite JPL quaternion standard], mostly to describe the orientation of satellites in inertial space. Its main advantage is that consecutive transformations using quaternions consist of multiplying elementary quaternions in a "natural order", exactly in the same order as the rotation matrices mentioned at the end of the previous section.

[Add more philosophical dwelling on the hows and whys of this notation; including references still on page]

To avoid confusion, we will not mention the original Hamilton rules in this work.

Instead, we define the quaternion elementary multiplication rules as follows[CITE]:

$$\begin{aligned} \mathbf{i}^2 &= \mathbf{j}^2 = \mathbf{k}^2 = -1; \\ \mathbf{ji} &= -\mathbf{ij} = \mathbf{k}; \\ \mathbf{kj} &= -\mathbf{jk} = \mathbf{i}; \\ \mathbf{ik} &= -\mathbf{ki} = \mathbf{j}. \end{aligned} \tag{A.8}$$

Using the relations in Eq. A.8, we define the general quaternion multiplication operator \otimes :

$$\begin{aligned} \bar{p} \otimes \bar{q} &= (p_r + p_i\mathbf{i} + p_j\mathbf{j} + p_k\mathbf{k}) \times (q_r + q_i\mathbf{i} + q_j\mathbf{j} + q_k\mathbf{k}) \\ &= (p_r q_r - p_i q_i - p_j q_j - p_k q_k) \\ &\quad + (p_r q_i + p_i q_r - p_j q_k + p_k q_j) \mathbf{i} \\ &\quad + (p_r q_j + p_j q_r - p_k q_i + p_i q_k) \mathbf{j} \\ &\quad + (p_r q_k + p_k q_r - p_i q_j + p_j q_i) \mathbf{k} \end{aligned} \tag{A.9}$$

To express a vector ${}^I\mathbf{v} = {}^I(x, y, z)$ in the new frame L , we construct a purely imaginary quaternion from this vector: $\bar{q}_{\mathbf{v}} = 0 + x\mathbf{i} + y\mathbf{j} + z\mathbf{k}$, and we use the quaternion multiplication to obtain:

$$\begin{bmatrix} {}^L\mathbf{v} \\ 0 \end{bmatrix} = {}_I^L \bar{q} \otimes \bar{q}_{\mathbf{v}} \otimes {}_I^L \bar{q}^{-1}, \tag{A.10}$$

and extract the vector ${}^L\mathbf{v}$ from the resulting quaternion.

Note that the quaternion inverse operation for quaternions of unit norm is the same as the conjugate operation.

3.2 Relationship with matrices and elementary quaternions

Using this formalism, a quaternion is behaving in the same way as the corresponding *passive* transformation matrix to describe a reference frame rotation. This means that consecutive rotations are multiplying in the "natural order", which makes it more intuitive.

For example, let's consider the elementary rotation described in Fig A.2 that represents a rotation of the initial reference frame I into a reference frame L about \mathbf{k} . Using the "left-hand" rule, the angle θ of rotation about \mathbf{k} is now $\theta = +30$ degrees. This quaternion is ${}_I^L\bar{q} = \bar{q}_{\mathbf{k}}(\theta) = \cos \frac{\theta}{2} + \sin \frac{\theta}{2}\mathbf{k}$, and represents the same rotation as the passive rotation matrix $\mathbf{R}_{\mathbf{k}}(\theta)$ discussed in Section ???. [WORK OUT THE MATHS FOR THE VECTOR TRANSFORMATION] If the rotation of the reference frame is described by three consecutive rotations of angles θ , ϕ and ψ about \mathbf{k} , \mathbf{j}' , and \mathbf{i}'' , respectively [see some figure], we can write:

$$\begin{aligned} {}_I^L\bar{q} &= \bar{q}_{\mathbf{i}}(\psi)\bar{q}_{\mathbf{j}}(\phi)\bar{q}_{\mathbf{k}}(\theta) \\ &= \begin{bmatrix} 0 \\ \sin \frac{\psi}{2} \\ 0 \\ \cos \frac{\psi}{2} \end{bmatrix} \begin{bmatrix} 0 \\ 0 \\ \sin \frac{\phi}{2} \\ \cos \frac{\phi}{2} \end{bmatrix} \begin{bmatrix} 0 \\ 0 \\ \sin \frac{\theta}{2} \\ \cos \frac{\theta}{2} \end{bmatrix}, \end{aligned} \quad (\text{A.11})$$

which forms a quaternion that is equivalent to the rotation matrix multiplication $\mathbf{R}_{\mathbf{i}}(\psi)\mathbf{R}_{\mathbf{j}}(\phi)\mathbf{R}_{\mathbf{k}}(\theta)$. Note that the order of the quaternions is the same as the order of the matrices. This is one of the advantages of choosing this "natural order" convention [cite

Shuster].

4 Quaternion derivative and integration

Properly defining the derivative and integral of quaternions is necessary for our purpose.

We will need a derivative to describe our dynamic system as its orientation changes over time; and we will need to integrate (or *propagate*) those equations to find a numerical solution to the attitude estimation problem.

In the following, we consider the body reference frame $L(t)$ which evolves as a function of time with respect to a fixed, inertial reference frame I .

The mathematical derivations leading to those results can be found elsewhere [CITE].

Over an infinitesimal time step dt , the local frame is rotating by an angular vector $\delta\theta$. The instantaneous angular velocity, expressed in the body reference frame $\mathbf{L}(t)$, is ${}^{L(t)}\boldsymbol{\omega}(t) = \lim_{dt \rightarrow 0} \frac{\delta\theta}{\delta t}$. It can be shown [CITE TRAWN] that with this formalism, the quaternion derivative is defined using either a quaternion multiplication, or an equivalent matrix multiplication:

$${}^I_L \dot{\bar{q}}(t) = \frac{1}{2} \begin{bmatrix} \boldsymbol{\omega} \\ 0 \end{bmatrix} \otimes {}^I_L \bar{q} = \frac{1}{2} \boldsymbol{\Omega}(\boldsymbol{\omega})_I^{L(t)} \bar{q}, \quad (\text{A.12})$$

where the matrix

$$\boldsymbol{\Omega}(\boldsymbol{\omega}) = \begin{bmatrix} 0 & \omega_z & -\omega_y & \omega_x \\ -\omega_z & 0 & \omega_x & \omega_y \\ \omega_y & -\omega_x & 0 & \omega_z \\ -\omega_x & -\omega_y & -\omega_z & 0 \end{bmatrix} \quad (\text{A.13})$$

is going to play an important in the later sections.

The integrator formulas are derived in []. The problem is to find a matrix Θ to integrate a quaternion ${}_I^{L(t)}\bar{q}(t)$, and estimate attitude at time $t + \Delta t$, knowing the instantaneous angular velocity $\omega(t)$:

$$\bar{q}(t + \Delta t) = \Theta(t, t + \Delta t)\bar{q}(t) \quad (\text{A.14})$$

A zeroth-order solution assumes that the angular velocity ω is a constant over the timestep Δt , an important special case since it describes the typical discrete representation that we will use in our software. The solution can be expressed as:

$$\Theta(t, t + \Delta t) \equiv \Theta(\Delta t) = \exp\left(\frac{1}{2}\Omega(\omega)\Delta t\right), \quad (\text{A.15})$$

where the matrix exponential is defined using a Taylor expansion [give reference for that].

A first-order solution is given in [TRAWNY] and uses knowledge of two previous ω values to estimate the integral.

5 Covariance matrices in different reference frames

In the following, we will be describing our attitude using quaternions or rotation matrices in a Kalman filter with a state-space representation. This means that we will be make estimates of physical quantities, as well as estimates of our estimation error. These errors are represented using covariance matrices.

Covariance matrices contain information about the cross-correlation of the variables in the state vector. The diagonal elements represent the auto-covariance of a given variable, while the terms off the diagonal indicate the degree of covariance (or correlation) between the different variables. For example, we will have three gyroscopes which will be mounted orthogonally from each other, each measuring the angular velocity about three different

axes. In the ideal case, all gyroscopes are independent and the covariance matrix associated to the set of three angular velocities is diagonal, with the variances of each gyroscope on the diagonal.

If we rotate the gyroscopes' frame with a rotation matrix \mathbf{R} , the new covariance matrix \mathbf{Q} needs to be rotated as well: $\mathbf{Q}' = \mathbf{R}\mathbf{Q}\mathbf{R}^T$.

5.1 Small angle approximation

Quaternions become more intuitive in the small angle approximation. Indeed, when all angles are small with respect to π , we can write:

$$\overset{L}{I}\bar{q} \approx \begin{bmatrix} \frac{1}{2}\delta\boldsymbol{\theta} \\ 1 \end{bmatrix}, \quad (\text{A.16})$$

where $\frac{1}{2}\delta\boldsymbol{\theta} = \frac{1}{2}[\delta\theta_i, \delta\theta_j, \delta\theta_k]^T$ corresponds to three small rotations about all the three axes of the initial reference frame. Because we are in the small angle approximation, the order of the rotations does not matter. Hence, if the imaginary part of a quaternion has small values q_i, q_j, q_k , and if $q_r \approx 1$, this quaternion represents a rotation of the reference frame by an angle $\delta\theta_i = 2q_i$, then by an angle $\delta\theta_j = 2q_j$, and finally by an angle $\delta\theta_k = 2q_k$, where all the angles are expressed in radians.

More simplifications can also be found. For example, in the limit where $\boldsymbol{\omega} \rightarrow \mathbf{0}$, the matrix exponential defined in Eq. A.15 simplifies into:

$$\boldsymbol{\Theta}(\Delta t) \xrightarrow{\boldsymbol{\omega} \rightarrow \mathbf{0}} \mathbf{I}_{4 \times 4} + \frac{\Delta t}{2} \boldsymbol{\Omega}(\boldsymbol{\omega}). \quad (\text{A.17})$$

5.2 Finding the rotation between two vectors

To measure misalignments between reference frames, it is useful to know how to find matrices between two vectors that would be determined using different methods. For example, this can be used when determining the misalignment between the star camera reference frame and the gyroscope reference frame. The raw velocity measured in the orthogonalized gyro reference frame corresponds to one measure of the inertial velocity, while the estimated values using the Kalman filter and the star camera consist of a second measure of the same inertial velocity. In the Kalman filter, this is corrected for by using an additive bias, but this assumes that the two reference frames are already aligned. In reality, there can be a residual misalignment between the gyro reference and the star camera reference frame.

Our approach is to treat the estimated inertial velocity of the gyroscope reference frame as an entirely new measurement of the velocity ω^{sc} (where the superscript indicates that we are using the information from the star camera to improve our measurement), and solve for the quaternion that transforms it into the raw velocity vector measured by the gyros, ω^{meas} .

The process of finding the appropriate unit quaternion is simple, and corresponds to finding the unique angle θ and unit Euler vector \mathbf{e} which corresponds to the axis of the rotation. We have:

$$\theta = \arccos \left(\frac{\omega^{\text{sc}} \cdot \omega^{\text{meas}}}{\|\omega^{\text{sc}}\| \|\omega^{\text{meas}}\|} \right) \quad (\text{A.18})$$

$$\mathbf{e} = \frac{\omega^{\text{sc}} \times \omega^{\text{meas}}}{\|\omega^{\text{sc}}\| \|\omega^{\text{meas}}\|}, \quad (\text{A.19})$$

which lead to the quaternion:

$$\bar{q}(\boldsymbol{\omega}^{\text{sc}}, \boldsymbol{\omega}^{\text{meas}}) = [\mathbf{e} \sin \theta, \cos \theta]^T. \quad (\text{A.20})$$

Appendix B

The PID control loop

Before we elaborate on the control architecture of the entire system, let's first discuss the elementary controls block: the PID.

A Proportional-Integral-Derivative (PID) control loop is one of the most basic, yet most used method to build systems with active control. The problem that these systems try to solve is simply to make an object reach a desired state: a sensor is used to measure the current state, and the difference between the desired state and the current state is fed to an apparatus capable of changing the state. Most commonly, this uses motors and either position or velocity sensors, but it can also be used for example for temperature control in a cryogenic environment, where heaters are used to change the temperature. For simplicity, in the rest of this work, we will always consider a loop with sensors and actuators.

In its most simple expression, the PID can be reduced to a simple proportional loop. That is, the command is proportional to the error between the desired and measured state. The value of this proportional coefficient usually sets the dynamics of the response, as a large proportional gain K_p will mean that even a small deviation from our desired state will trigger a large response. Sometimes, a purely proportional system can lack stability.

A proportional-derivative loop adds the information of the speed at which the error varies. If the error is growing quickly, we can increase our command. If the error is being reduced quickly, it is time to slow down the command to avoid overshooting our target. This uses the time derivative of the error that multiplies a gain, K_d , and has the effect to damp the motion. A PD loop usually will help with the system's stability.

But even then, a proportional-derivative does not guarantee that you will reach your desired state. We then complete the PID loop with an integral gain K_i , which multiplies the integral of the error over some length of time. While the K_p and K_d gains mostly control the dynamics of the response, the integral term will control the steady-state error and ensure it converges to zero. While useful, this term needs to be considered with precaution, as some situations can lead to a diverging response.

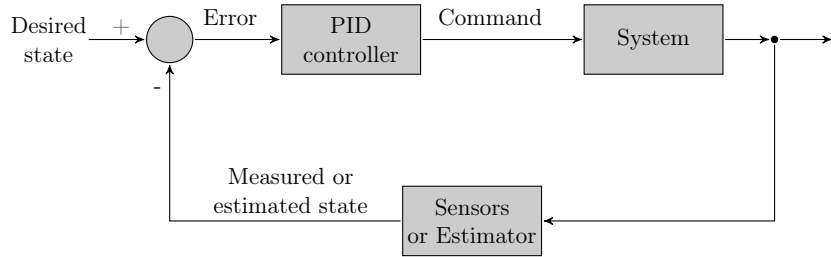


FIGURE B.1

A simple PID loop diagram is shown in Fig B.1, with the desired input state at the entrance of the loop and the real state at the output of the loop. It is often the case that the state cannot be directly measured: this require the use of an *estimator* or *observer*, in which various indirect measurements will feed a mathematical model of the system to estimate its parameters. The relevant example for us is a scenario where we only measure a velocity measurement, while we want to close the loop on the position. Simply put, we know that the position has an integral relationship with the velocity, and the observer's role is to estimate the integration constants.

The estimator is also used to realize *sensor fusion*. This consists of combining various types of measurements to provide the best estimate of the state to feed back to the control loop. The various measurements often happen at different discrete rates, with different lag times, which can lead to rather complex implementations. One of the most well-known estimation algorithms is the Kalman filter, which we will discuss at length in Section [].

For BETTII, each subsystem has its own PID control loop. Each PID loop structure consists of 7 variables: the K_p , K_d , K_i gains, and overall scaling factor, an upper and a lower limit on the command, and a boolean value that is used to reset the content of the integral term used to multiply K_i .

Bibliography

- Allamandola, L J, A G G M Tielens, and J R Barker (1985). “Polycyclic aromatic hydrocarbons and the unidentified infrared emission bands - Auto exhaust along the Milky Way”. In: *Astrophysical Journal* 290, pp. L25–L28.
- Allen, L et al. (2007). “The Structure and Evolution of Young Stellar Clusters”. In: *Protostars and Planets V*, p. 361.
- Anglada, Guillem et al. (1998). “On the Exciting Sources of the L723 and IRAS 20050+2720 Quadrupolar Molecular Outflows”. In: *Star Formation with the Infrared Space Observatory* 132, p. 303.
- Anthony-Twarog, B. J. (1982). “The H-beta distance scale for B stars - The Orion association”. In: AJ 87, pp. 1213–1222. DOI: [10.1086/113204](https://doi.org/10.1086/113204).
- Astropy Collaboration et al. (2013). “Astropy: A community Python package for astronomy”. In: A&A 558, A33, A33. DOI: [10.1051/0004-6361/201322068](https://doi.org/10.1051/0004-6361/201322068). arXiv: [1307.6212](https://arxiv.org/abs/1307.6212) [astro-ph.IM].
- Bachiller, R, A Fuente, and M Tafalla (1995). “An extremely high velocity multipolar outflow around IRAS 20050 + 2720”. In: *Astrophysical Journal* 445, pp. L51–L54.
- Bachiller, Rafael (1996). “Bipolar Molecular Outflows from Young Stars and Protostars”. In: *Annual Review of Astronomy and Astrophysics* 34.1, pp. 111–154.
- Bally, J. (1982). “Energetic activity in a star-forming molecular cloud core - A disk constrained bipolar outflow in NGC 2071”. In: ApJ 261, pp. 558–568. DOI: [10.1086/160366](https://doi.org/10.1086/160366).

- Beltrán, M T et al. (2008). “On the nature of outflows in intermediate-mass protostars: a case study of IRAS 20050+2720”. In: *Astronomy and Astrophysics* 481.1, pp. 93–105.
- Bevington, Philip Raymond and D Keith Robinson (2003). *Data Reduction and Error Analysis for the Physical Sciences*. McGraw-Hill.
- Bonnell, I A et al. (1997). “Accretion and the stellar mass spectrum in small clusters”. In: *Monthly Notices of the Royal Astronomical Society* 285, p. 201.
- Bonnell, Ian A and Matthew R Bate (2002). “Accretion in stellar clusters and the collisional formation of massive stars”. In: *Monthly Notice of the Royal Astronomical Society* 336.2, pp. 659–669.
- (2006). “Star formation through gravitational collapse and competitive accretion”. In: *Monthly Notices of the Royal Astronomical Society* 370.1, pp. 488–494.
- Bracco, A et al. (2011). “Herschel-ATLAS: statistical properties of Galactic cirrus in the GAMA-9 Hour Science Demonstration Phase Field”. In: *Monthly Notices of the Royal Astronomical Society* 412.2, pp. 1151–1161.
- Buckle, J. V. et al. (2010). “The JCMT Legacy Survey of the Gould Belt: a first look at Orion B with HARP”. In: MNRAS 401, pp. 204–222. DOI: [10.1111/j.1365-2966.2009.15619.x](https://doi.org/10.1111/j.1365-2966.2009.15619.x). arXiv: 0908.4162.
- Butner, H. M. et al. (1990). “High-resolution, far-infrared observations of NGC 2071”. In: ApJ 364, pp. 164–172. DOI: [10.1086/169398](https://doi.org/10.1086/169398).
- Cardelli, Jason A, Geoffrey C Clayton, and John S Mathis (1989). “The relationship between infrared, optical, and ultraviolet extinction”. In: *Astrophysical Journal* 345, pp. 245–256.

- Carrasco-González, C. et al. (2012). “Multiplicity, Disks, and Jets in the NGC 2071 Star-forming Region”. In: *ApJ* 746, 71, p. 71. doi: 10.1088/0004-637X/746/1/71. arXiv: 1111.5469.
- Chen, H et al. (1997). “IRAS 20050+2720: An Embedded Young Cluster Associated with a Multipolar Outflow”. In: *The Astrophysical Journal* 475.1, pp. 163–172.
- Chernin, L. and C. Masson (1993). “Observations of SO and SiO in the outflow from NGC 2071”. In: *ApJ* 403, pp. L21–L24. doi: 10.1086/186712.
- Chini, R et al. (2001). “Mm/Submm images of Herbig-Haro energy sources and candidate protostars”. In: *Astronomy and Astrophysics* 369.1, pp. 155–169.
- Clauset, Aaron, Cosma Rohilla Shalizi, and M E J Newman (2007). “Power-law distributions in empirical data”. In: *arXiv.org* 4, pp. 661–703. arXiv: 0706.1062v2 [physics.data-an].
- Crassidis, John L and John L Junkins (2011). *Optimal Estimation of Dynamic Systems, Second Edition*. CRC Press.
- Davis, Sumner P, Mark C Abrams, and James W Brault (2001). “Fourier transform spectrometry”. In: *Fourier transform spectrometry by Sumner P. Davis et al. San Diego*.
- Di Francesco, J et al. (2007). “An Observational Perspective of Low-Mass Dense Cores I: Internal Physical and Chemical Properties”. In: *Protostars and Planets V*, pp. 17–32.
- Dunham, Michael M et al. (2010). “Evolutionary Signatures in the Formation of Low-Mass Protostars. II. Toward Reconciling Models and Observations”. In: *The Astrophysical Journal* 710.1, pp. 470–502.
- El Badaoui, Noad et al. (2014). “Towards a solid-state ring laser gyroscope”. In: *Comptes Rendus Physique* 15.10, pp. 841–850.
- Elias, Nicholas M et al. (2007). “The Mathematics of Double-Fourier Interferometers”. In: *The Astrophysical Journal* 657.2, pp. 1178–1200.

- Evans II, N. J. et al. (2009). “The Spitzer c2d Legacy Results: Star-Formation Rates and Efficiencies; Evolution and Lifetimes”. In: *ApJS* 181, 321, pp. 321–350. DOI: 10.1088/0067-0049/181/2/321. arXiv: 0811.1059.
- Evans, Neal J et al. (2009). “The Spitzer c2d Legacy Results: Star-Formation Rates and Efficiencies; Evolution and Lifetimes”. In: *The Astrophysical Journal Supplement* 181.2, pp. 321–350.
- Ferrière, Katia M (2001). “The interstellar environment of our galaxy”. In: *Reviews of Modern Physics* 73.4, pp. 1031–1066.
- Fixsen, D J and Eli Dwek (2002). “The Zodiacal Emission Spectrum as Determined by COBE and Its Implications”. In: *The Astrophysical Journal* 578.2, pp. 1009–1014.
- Fixsen, D J et al. (1996a). “A Balloon-borne Millimeter-Wave Telescope for Cosmic Microwave Background Anisotropy Measurements”. In: *Astrophysical Journal v.470* 470, p. 63.
- Fixsen, D J et al. (1996b). “The Cosmic Microwave Background Spectrum from the Full COBE FIRAS Data Set”. In: *Astrophysical Journal v.473* 473.2, pp. 576–587.
- Fixsen, D J et al. (1998). “The Spectrum of the Extragalactic Far-Infrared Background from the COBE FIRAS Observations”. In: *The Astrophysical Journal* 508.1, pp. 123–128.
- Flaherty, K. M. and J. Muzerolle (2008). “Evidence for Early Circumstellar Disk Evolution in NGC 2068/71”. In: *AJ* 135, pp. 966–983. DOI: 10.1088/0004-6256/135/3/966. arXiv: 0712.1601.
- Fontani, F, R Cesaroni, and R S Furuya (2010). “Class I and Class II methanol masers in high-mass star-forming regions”. In: *Astronomy and Astrophysics* 517, A56.

- Forman, Michael L, W Howard Steel, and George A Vanasse (1966). “Correction of Asymmetric Interferograms Obtained in Fourier Spectroscopy”. In: *Journal of the Optical Society of America* 56, p. 59.
- Gillett, F C, W J Forrest, and K M Merrill (1973). “8 - 13-micron spectra of NGC 7027, BD +30 3639, and NGC 6572.” In: *Astrophysical Journal* 183, pp. 87–93.
- Grainger, William F et al. (2012). “Demonstration of spectral and spatial interferometry at THz frequencies”. In: *Applied Optics* 51.12, pp. 2202–2211.
- Griffiths, Peter R and James A De Haseth (2007). *Fourier Transform Infrared Spectrometry*. John Wiley & Sons.
- Günther, H M et al. (2012). “IRAS 20050+2720: Anatomy of a Young Stellar Cluster”. In: *The Astronomical Journal* 144.4, p. 101.
- Gutermuth, R A et al. (2009). “A Spitzer Survey of Young Stellar Clusters Within One Kiloparsec of the Sun: Cluster Core Extraction and Basic Structural Analysis”. In: *The Astrophysical Journal Supplement* 184.1, pp. 18–83.
- Gutermuth, R A et al. (2011). “A Correlation between Surface Densities of Young Stellar Objects and Gas in Eight Nearby Molecular Clouds”. In: *The Astrophysical Journal* 739.2, p. 84.
- Gutermuth, Robert A et al. (2005). “The Initial Configuration of Young Stellar Clusters: A K-Band Number Counts Analysis of the Surface Density of Stars”. In: *The Astrophysical Journal* 632.1, pp. 397–420.
- Harries, J E (1980). “Atmospheric radiometry at submillimeter wavelengths”. In: *Applied Optics* 19.18, p. 3075.
- Harvey, P. M. et al. (1979). “Infrared observations of NGC 2071/IRS/ and AFGL 490 - Two low-luminosity young stars”. In: ApJ 229, pp. 990–993. DOI: 10.1086/157033.

- Harwit, Martin, David Leisawitz, and Stephen Rinehart (2006). “A far-infrared/submillimeter kilometer-baseline interferometer in space”. In: *New Astronomy Reviews* 50.1-3, pp. 228–234.
- Helmich, Frank P and R J Ivison (2009). “FIRI—A far-infrared interferometer”. In: *Experimental Astronomy* 23.1, pp. 245–276.
- Herter, T L et al. (2012). “First Science Observations with SOFIA/FORCAST: The FORCAST Mid-infrared Camera”. In: *The Astrophysical Journal Letters* 749.2, p. L18.
- Herter, T L et al. (2013). “Data Reduction and Early Science Calibration for FORCAST, A Mid-Infrared Camera for SOFIA”. In: *Publications of the Astronomical Society of the Pacific* 125.933, pp. 1393–1404.
- Johnstone, D. et al. (2001). “Large Area Mapping at 850 Microns. III. Analysis of the Clump Distribution in the Orion B Molecular Cloud”. In: *ApJ* 559, pp. 307–317. DOI: [10.1086/322323](https://doi.org/10.1086/322323).
- Kato, Eri et al. (2010). “Far-Infrared Interferometric Telescope Experiment : I. Interferometer Optics”. In: *Transactions of Space Technology Japan* 7.ists26, pp. 47–53.
- Kennicutt, R. C. and N. J. Evans (2012). “Star Formation in the Milky Way and Nearby Galaxies”. In: *ARA&A* 50, pp. 531–608. DOI: [10.1146/annurev-astro-081811-125610](https://doi.org/10.1146/annurev-astro-081811-125610). arXiv: [1204.3552](https://arxiv.org/abs/1204.3552).
- Kennicutt, Robert C and Neal J Evans (2012). “Star Formation in the Milky Way and Nearby Galaxies”. In: *Annual Review of Astronomy and Astrophysics* 50.1, pp. 531–608.
- Kessler, M F et al. (1996). “The Infrared Space Observatory (ISO) mission.” In: *Astronomy and Astrophysics* 315, pp. L27–L31.

- Kim, Sang-Hee, P G Martin, and Paul D Hendry (1994). “The size distribution of interstellar dust particles as determined from extinction”. In: *Astrophysical Journal* 422, pp. 164–175.
- Lada, Charles J and Elizabeth A Lada (2003). “Embedded Clusters in Molecular Clouds”. In: *Annual Review of Astronomy & Astrophysics* 41.1, pp. 57–115.
- Lada, E. A. et al. (1991). “A 2.2 micron survey in the L1630 molecular cloud”. In: ApJ 371, pp. 171–182. DOI: 10.1086/169881.
- Larson, R B (1994). “The Evolution of Molecular Clouds”. In: *The Structure and Content of Molecular Clouds* 439. Chapter 2, pp. 13–28.
- Launhardt, R. et al. (1996). “Dust emission from star-forming regions. IV. Dense cores in the Orion B molecular cloud.” In: A&A 312, pp. 569–584.
- Lawson, Peter R (2000). “Principles of Long Baseline Stellar Interferometry”. In: *Principles of Long Baseline Stellar Interferometry. Course notes from the 1999 Michelson Summer School*.
- Lefferts, E J, F L Markley, and M D Shuster (1982). “Kalman Filtering for Spacecraft Attitude Estimation”. In: *Journal of Guidance* 5.5, pp. 417–429.
- Leisawitz, David et al. (2007). “The space infrared interferometric telescope (SPIRIT): High-resolution imaging and spectroscopy in the far-infrared”. In: *Advances in Space Research* 40.5, pp. 689–703.
- Leisawitz, David et al. (2012). “Developing wide-field spatio-spectral interferometry for far-infrared space applications”. In: *Optical and Infrared Interferometry III. Proceedings of the SPIE*. Ed. by Françoise Delplancke, Jayadev K Rajagopal, and Fabien Malbet. NASA Goddard Space Flight Ctr. (United States). SPIE, 84450A.

- Li, Aigen and B T Draine (2001). “Infrared Emission from Interstellar Dust. II. The Diffuse Interstellar Medium”. In: *The Astrophysical Journal* 554.2, pp. 778–802.
- Mariotti, J-M and S T Ridgway (1988). “Double Fourier spatio-spectral interferometry - Combining high spectral and high spatial resolution in the near infrared”. In: *Astronomy and Astrophysics (ISSN 0004-6361)* 195, p. 350.
- Markley, F Landis and John L Crassidis (2014). *Fundamentals of Spacecraft Attitude Determination and Control*. New York, NY: Springer.
- Mathis, J S, W Rumpl, and K H Nordsieck (1977). “The size distribution of interstellar grains”. In: *Astrophysical Journal* 217, pp. 425–433.
- Mathis, John S (1990). “Interstellar dust and extinction”. In: *IN: Annual review of astronomy and astrophysics. Vol. 28 (A91-28201 10-90). Palo Alto* 28.1, pp. 37–70.
- Matsumoto, T, S Matsuura, and M Noda (1994). “2.4 micrometer sky brightness at balloon altitude”. In: *Astronomical Society of the Pacific* 106, p. 1217.
- Maybeck, Peter S (1982). *Stochastic Models, Estimation, and Control*. Academic Press.
- McKee, Christopher F and Eve C Ostriker (2007). “Theory of Star Formation”. In: *Annual Review of Astronomy and Astrophysics* 45.1, pp. 565–687.
- McKee, Christopher F and Jonathan C Tan (2003). “The Formation of Massive Stars from Turbulent Cores”. In: *The Astrophysical Journal* 585.2, pp. 850–871.
- Megeath, S. T. et al. (2012). “The Spitzer Space Telescope Survey of the Orion A and B Molecular Clouds. I. A Census of Dusty Young Stellar Objects and a Study of Their Mid-infrared Variability”. In: AJ 144, 192, p. 192. DOI: 10.1088/0004-6256/144/6/192. arXiv: 1209.3826.
- Mendillo, Christopher B et al. (2012). “Flight demonstration of a milliarcsecond pointing system for direct exoplanet imaging”. In: *Applied Optics* 51.29, p. 7069.

- Meynart, Roland (1992). "Sampling jitter in Fourier-transform spectrometers - Spectral broadening and noise effects". In: *Applied Optics (ISSN 0003-6935)* 31.30, p. 6383.
- Mighell, Kenneth J (2005). "Stellar photometry and astrometry with discrete point spread functions". In: *Monthly Notices of the Royal Astronomical Society* 361.3, pp. 861–878.
- Mitchell, G. F. et al. (2001). "A Submillimeter Dust and Gas Study of the Orion B Molecular Cloud". In: *ApJ* 556, pp. 215–229. DOI: 10.1086/321574.
- Molinari, S et al. (1996). "A search for precursors of ultracompact HII regions in a sample of luminous IRAS sources. I. Association with ammonia cores." In: *Astronomy and Astrophysics* 308, pp. 573–587.
- Murakami, H et al. (2007). "The Infrared Astronomical Mission AKARI". In: *Publications of the Astronomical Society of Japan* 59.sp2, 369–S376.
- Myers, P C and E F Ladd (1993). "Bolometric temperatures of young stellar objects". In: *Astrophysical Journal* 413, pp. L47–L50.
- Myers, Philip C (2011). "Star Formation in Dense Clusters". In: *The Astrophysical Journal* 743.1, p. 98.
- Neugebauer, G et al. (1984). "The Infrared Astronomical Satellite (IRAS) mission". In: *Astrophysical Journal* 278, pp. L1–L6.
- Offner, Stella S R and Christopher F McKee (2011). "The Protostellar Luminosity Function". In: *The Astrophysical Journal* 736.1, p. 53.
- Ossenkopf, V and Th Henning (1994). "Dust opacities for protostellar cores". In: *Astronomy and Astrophysics (ISSN 0004-6361)* 291, pp. 943–959.
- Oxley, Paul et al. (2004). "The EBEX experiment". In: *Infrared Spaceborne Remote Sensing XII. Edited by Strojnik* 5543, pp. 320–331.

- Palla, F et al. (1991). "Water masers associated with dense molecular clouds and ultracompact H II regions". In: *Astronomy and Astrophysics (ISSN 0004-6361)* 246, pp. 249–263.
- Peltier, JCA (1834). *Investigation of the heat developed by electric currents in homogeneous materials and at the junction of two different conductors*. Ann. Chim. Phys.
- Persson, S. E. et al. (1981). "High Velocity h2 Line Emission in the NGC2071 Region". In: *ApJ* 251, p. L85. DOI: 10.1086/183699.
- Pilbratt, G L et al. (2010). "Herschel Space Observatory. An ESA facility for far-infrared and submillimetre astronomy". In: *Astronomy and Astrophysics* 518, p. L1.
- Porras, Alicia et al. (2003). "A Catalog of Young Stellar Groups and Clusters within 1 Kiloparsec of the Sun". In: *The Astronomical Journal* 126.4, pp. 1916–1924.
- Press, William H et al. (1992). "Numerical recipes in C. The art of scientific computing". In: *Cambridge: University Press*.
- Richards, M A (2003). "Coherent integration loss due to white gaussian phase noise". In: *IEEE Signal Processing Letters* 10.7, pp. 208–210.
- Rinehart, S A et al. (2014). "The Balloon Experimental Twin Telescope for Infrared Interferometry (BETTII): An Experiment for High Angular Resolution in the Far-Infrared". In: *Publications of the Astronomical Society of the Pacific* 126, pp. 660–673.
- Rizzo, Maxime J et al. (2012). "Tracking near-infrared fringes on BETTII: a balloon-borne, 8m-baseline interferometer". In: *Optical and Infrared Interferometry III. Proceedings of the SPIE* 8445, 84451T.
- Robitaille, T P (2011). "HYPERION: an open-source parallelized three-dimensional dust continuum radiative transfer code". In: *Astronomy and Astrophysics* 536, A79.

- Robitaille, Thomas P et al. (2006). “Interpreting Spectral Energy Distributions from Young Stellar Objects. I. A Grid of 200,000 YSO Model SEDs”. In: *The Astrophysical Journal Supplement Series* 167.2, pp. 256–285.
- “Self-similar collapse of isothermal spheres and star formation” (1977). In: *Astrophysical Journal* 214, pp. 488–497.
- Sellgren, K (1994). “Tiny Grains, Large Molecules, and the Infrared Cirrus”. In: *The First Symposium on the Infrared Cirrus and Diffuse Interstellar Clouds. ASP Conference Series* 58, pp. 243–.
- Shirley, Yancy L et al. (2000). “Tracing the Mass during Low-Mass Star Formation. I. Submillimeter Continuum Observations”. In: *The Astrophysical Journal Supplement Series* 131.1, pp. 249–271.
- Skinner, S. L. et al. (2009). “Chandra and Spitzer Imaging of the Infrared Cluster in NGC 2071”. In: ApJ 701, pp. 710–724. doi: 10.1088/0004-637X/701/1/710. arXiv: 0906.2428 [astro-ph.SR].
- Spezzi, L. et al. (2015). “The VISTA Orion mini-survey: star formation in the Lynds 1630 North cloud”. In: *ArXiv e-prints*. arXiv: 1505.04631 [astro-ph.SR].
- Sromovsky, Lawrence A (2003). “Radiometric Errors in Complex Fourier Transform Spectrometry”. In: *Applied Optics OT* 42.10, p. 1779.
- Staguhn, Johannes G et al. (2014). “The GISMO Two-millimeter Deep Field in GOODS-N”. In: *The Astrophysical Journal* 790.1, p. 77.
- Stecher, T P and B Donn (1965). “On Graphite and Interstellar Extinction”. In: *Astrophysical Journal* 142, pp. 1681–.
- Stojimirović, I., R. L. Snell, and G. Narayanan (2008). “Multiple Parsec-Scale Outflows in the NGC 2071 Cluster”. In: ApJ 679, pp. 557–569. doi: 10.1086/586688.

- Strom, K. M., S. E. Strom, and F. J. Vrba (1976). “Infrared surveys of dark-cloud complexes. I. The Lynds 1630 dark cloud.” In: *AJ* 81, pp. 308–313. DOI: [10.1086/111888](https://doi.org/10.1086/111888).
- Tan, J C et al. (2014). “Massive Star Formation”. In: *Protostars and Planets VI*, pp. 149–172.
- Terebey, S, F H Shu, and P Cassen (1984). “The collapse of the cores of slowly rotating isothermal clouds”. In: *Astrophysical Journal* 286, pp. 529–551.
- Thompson, A Richard, James M Moran, and Jr George W Swenson (2008). *Interferometry and Synthesis in Radio Astronomy*. John Wiley & Sons.
- Trawny, N and S I Roumeliotis (2005). “Indirect Kalman filter for 3D attitude estimation”. In:
- Ulrich, R K (1976). “An infall model for the T Tauri phenomenon”. In: *Astrophysical Journal* 210, pp. 377–391.
- van Kempen, T. A. et al. (2012). “The Small-scale Physical Structure and Fragmentation Difference of Two Embedded Intermediate-mass Protostars in Orion”. In: *ApJ* 751, 137, p. 137. DOI: [10.1088/0004-637X/751/2/137](https://doi.org/10.1088/0004-637X/751/2/137). arXiv: [1203.3718](https://arxiv.org/abs/1203.3718).
- Weingartner, Joseph C and B T Draine (2001). “Dust Grain-Size Distributions and Extinction in the Milky Way, Large Magellanic Cloud, and Small Magellanic Cloud”. In: *The Astrophysical Journal* 548.1, pp. 296–309.
- Werner, M W et al. (2004). “The Spitzer Space Telescope Mission”. In: *The Astrophysical Journal Supplement Series* 154.1, pp. 1–9.
- Whitney, B A et al. (2013). “Three-dimensional Radiation Transfer in Young Stellar Objects”. In: *The Astrophysical Journal Supplement* 207.2, p. 30.

- Whitney, Barbara A et al. (2003a). “2-D Radiative Transfer in Protostellar Envelopes: I. Effects of Geometry on Class I Sources”. In: *arXiv.org* 2, pp. 1049–1063. arXiv: astro-ph/0303479v1 [astro-ph].
- Whitney, Barbara A et al. (2003b). “Two-dimensional Radiative Transfer in Protostellar Envelopes. II. An Evolutionary Sequence”. In: *The Astrophysical Journal* 598.2, pp. 1079–1099.
- Wilking, B A et al. (1989). “A millimeter-wave spectral-line and continuum survey of cold IRAS sources”. In: *Astrophysical Journal* 345, pp. 257–264.
- Williams, J P, L Blitz, and C F McKee (2000). “The Structure and Evolution of Molecular Clouds: from Clumps to Cores to the IMF”. In: *Protostars and Planets IV (Book - Tucson: University of Arizona Press; eds Mannings,* pp. 97–.
- Wright, Edward L et al. (2010). “The Wide-field Infrared Survey Explorer (WISE): Mission Description and Initial On-orbit Performance”. In: *The Astronomical Journal* 140.6, pp. 1868–1881.
- Yusef-Zadeh, F, M Morris, and R L White (1984). “Bipolar reflection nebulae - Monte Carlo simulations”. In: *Astrophysical Journal* 278, pp. 186–194.
- Zhou, S., N. J. Evans II, and L. G. Mundy (1990). “An NH₃ ring around the infrared sources in NGC 2071”. In: *ApJ* 355, pp. 159–165. DOI: 10.1086/168749.